Unsteady Flow Around Bluff Bodies Spanning Thin Rectangular Ducts

David George Harland

A thesis submitted for the degree of

Doctor of Philosophy of Imperial College London

Department of Mechanical Engineering

October 15, 2017

Abstract

This project consists of a two-pronged computational and experimental approach to the study of flow in closed, thin rectangular ducts with a partial cubic blockage. Results are presented at three different bulk Reynolds numbers, $Re_D = 5600$, 10400 and 15600, based on the channel height, which is also the blockage dimension. The new experimental data produced consists of fluctuating pressure measurements at the cube surface, with 2D-2C PIV snapshots captured simultaneously in the wake region. In addition to this, DNS data is produced at the lowest Reynolds number of $Re_D = 5600$, allowing more detailed comparisons where PIV laser access was not possible. Comparisons are drawn between the data and URANS CFD simulations. A literature review and preliminary testing process narrowed down the considered URANS models to the two-layer $k - \varepsilon$ model and the Elliptic Blending Reynolds Stress Model, or $EBRSM$. In the light of the new data, these two URANS models are compared in order to better understand their strengths and weaknesses. Particular regard is given to the prediction of large-scale unsteady behaviour, with a focus on vortex shedding. This unsteady phenomenon was found to be present and to have a significant effect on the flow in the near-cube and wake regions. Results show that certain aspects of this behaviour are captured with only limited accuracy by the URANS models tested. As a result, inaccuracies are also found in the mean simulated velocity fields. The shortcomings appear more pronounced at higher flow rates. At a given flow rate, they are more severe in regions of the flow where organised unsteadiness is large relative to the mean values. It is suggested that inaccuracies in mean URANS predictions are a result of limitations in model capability for unsteady flows, and that validation cases may be pertinent to address this.

Declarations

The work contained within this thesis has been carried out by the author David Harland, any exceptions to this are appropriately referenced or otherwise acknowledged. For a summary of these instances, readers are directed to the "References" (Section 9) and the "Acknowledgements" (Section 10).

Contents

Tables and Figures

List of Tables

List of Figures

Nomenclature

Most abbreviations, notation and definitions are defined in context; the list given here is by no means exhaustive. Items are presented if they appear within the text far separated from their definitions.

Abbreviations

- CAD - Computer Aided Design
- CFL - Courant-Friedrichs-Lewy stability criterion
- DFT - Discrete Fourier Transform
- DNS - Direct Numerical Simulation
- EBRSM - Elliptic Blending Reynolds Stress Model
- FFT - Fast Fourier Transform
- RANS/URANS - Steady/Unsteady Reynolds-Averaged Navier-Stokes methodology
- RMS - Root Mean Square
- RSM - Reynolds Stress Model

Notation and Definitions

- ϕ - Phase
- ε - Turbulence dissipation rate
- $(0, 0, 0)$ - Centre of coordinate system, at geometric centre of blockage
- $A_{pt\phi}$ - Peak-trough amplitude characterising the spread in phase-averaged pressure values
- D - characteristic dimension, for example, cylinder diameter, cube dimension
- H - rectangular channel height, smaller of the two dimensions

- N_ϕ - Number of phase bins
- N_c - Number of cells in the computational domain
- N_p - Number of periods
- N_s - Number of snapshots
- Re_D - Reynolds number based on the characteristic diameter of the cube, D, which is also the channel height
- Re_{Dh} - Reynolds number based on the hydraulic diameter of the channel, $Dh = 4A/P$
- Re_t - turbulent Reynolds number based on the local turbulent conditions
- Re_{yw} - Reynolds number based on the wall distance
- St - Strouhal number, the non-dimensionalised shedding frequency
- St_{cp} - Strouhal number using constant period method
- St_{nccp} - Strouhal number using using constant period method accounting for flow constriction past block
- St_{vp} - Strouhal number using variable period method
- T_{cp} - Mean period using constant period method
- T_t - Turbulent timescale
- T_{vp} - Mean period using variable period method
- U, V, W - Mean u, v, w velocities
- U_b - Bulk velocity, integral of u with respect to y and z across channel cross-section
- W - rectangular channel width, larger of the two dimensions
- f_{FT} - Frequency based on the spectral peak from the Fourier Transform
- f_{cp} - Estimated shedding frequency, from mean period using constant period method

- f_{ncvp} - Strouhal number using using variable period method accounting for flow constriction past block
- f_{shed} - Dominant shedding frequency
- f_{snap} - Rate at which velocity snapshots were recorded
- f_{vp} - Estimated shedding frequency, from mean period using variable period method
- k - Turbulent kinetic energy
- n_ϕ - Phase bin number
- n_p - Period number
- n_s - Snapshot number
- n_x, n_y, n_z - Number of cells in the x, y, z directions
- u, v, w - Velocity in x, y, z directions
- x, y, z - Streamwise direction, short dimension separating two large plates, wide dimension spanning between small channel sides
- y^+ - Normalised wall distance
- y_w - Distance to the nearest wall

1 Introduction

1.1 Project Aims

The principal aim of this project was to perform a study on computational methodology for the prediction of single-phase flow within nuclear reactor sub-channels. The focus is placed on issues that may arise from the presence of partial blockages in a rectangular duct of relevance to the nuclear industry. Major turbulence modelling strategies that are commonly used in industry are tested to see how well they fare under conditions that are known to raise certain difficulties despite the absence of phase change, namely highly unsteady flows around bluff bodies. Acknowledging first of all that the realistic prediction of mean heat transfer within convection-dominated flows is heavily dependent on the correct representation of mean flow structure, the need to scrutinise in detail mean flow predictions from the chosen models is considered paramount. Under certain conditions, unsteady components of the flow exist on scales so large as to be comparable to the mean flow structures themselves. These exist across time-scales much longer than those associated with turbulent eddies. Furthermore, the periodic regularity of such phenomena may raise issues of resonance and unwanted acoustic noise. As a result, the ability of the models to accurately predict the largest, most ordered fluctuations in velocity and pressure needs to be tested.

1.2 Rectangular Ducts of High Aspect Ratio

The prediction of flow in closed ducts is clearly of interest across a broad range of engineering domains, applying to ventilation systems, heat exchangers, jet engines and heat transfer in industrial processes among many others. As a result, much work has been done to provide the engineer with the tools to calculate important quantities such as pressure drops, bulk flow velocities and heat exchange rates, often constructed using experimental correlations and applied via interpolation or extrapolation to a broad range of similar cases. While these may be useful as a quick point of reference, deviation from the appropriate conditions of application may result in incorrect predictions, even for cases that seem intuitively quite simple.

As an illustration of this point, one may regard the prediction of pressure drop within straight rectangular ducts; a classical approach based on the hydraulic diameter [22] is known to diverge from reality for thin ducts where the aspect ration $R_a = W/H$ is large. The authors of [14] designed an approach based on using the square root of the cross-sectional area rather than the hydraulic diameter to provide some generality with regards to duct shape, but even this approach was limited to smaller aspect ratios. One example where these correlations may be limited is the coolant channel geometry of an MTR type reactor [71], a rectangular duct with an aspect ratio of approximately 30. Partial blockage of these ducts due to a hypothetical fuel plate buckling scenario was investigated in [68] in order to ascertain the likelihood of boiling under such conditions; the coolant flow became 3D due to the duct's changing shape. Fully 3D RANS methodology was employed accordingly, using the realizable $k - \varepsilon$ model [74]. Validation of the model's predictive capabilities for temperature was provided in an earlier paper by the same author [69] for the case of an unblocked duct of constant cross-section. In that study, the average temperature across transverse sections of the flow was compared with that generated under steady conditions by MTRTHA, a 1D systems code designed for Thermal Hydraulics in the nuclear industry. Effective extrapolation from this is clearly dependent on the ability of the code to accurately represent the redistribution of coolant across the channel cross-section. Due to the smooth, steady changes in geometry this extrapolation seems very reasonable, but it is worth highlighting that the predicted coolant temperature was nevertheless a strong function of the location across the channel width. If geometry

changes were sharper this assumption may have been unfounded.

Another difficulty is well known to arise in the process of predicting turbulent flows in straight rectangular ducts, that of corner vortices. Experimental data relating to this subject may be found in [7], [58] and [20]. These studies are accompanied by a thorough explanation of the origins of such secondary flows within a Reynolds Averaging theoretical framework; mean measurements of turbulent quantities are used to show how crucial it is to allow for anisotropy of the Reynolds Stress Tensor. Early attempts to simulate these resulted in the development of Explicit Algebraic Reynolds Stress Models [28], where an experimental correlation was used to define the values of turbulence intensity components within the duct cross section as a function of position and bulk velocity, with successful results. For a discussion on more general methods of closure for the Reynolds Stress components that do not require such a priori knowledge, readers are directed to [75]. This same author was also able to produce secondary flows in a rectangular duct using a modified version of the $k - \varepsilon$ model [76]. The interested reader is directed to [61], for the details of a theoretical framework for a sub-set of "effective-viscosity" models that are capable of dealing with anisotropy in the Reynolds Stress fields, although this will not be discussed here. Finally, attention is drawn to [59] where DNS was used to directly observe turbulent structures in the wall and corner regions. In that work, the mean secondary flows were shown conclusively to be a manifestation of the statistically preferential location of low speed streaks near the walls and of instantaneous vortices aligned with the streamwise direction. These coherent structures are small in size and exist over short time-scales, but their combined effect establishes the secondary flows in the mean, which are typically $\sim 1\%$ of the bulk velocity.

Concluding this discussion on rectangular ducts, many of the details required to successfully model turbulent flow in the simple case of a straight rectangular channel are non-trivial, from correlations for pressure-drop to simulation of velocity components. Even without the introduction of any blockage, in fully-developed flow where all velocity gradients in the streamwise direction vanish, care is needed in the selection of turbulence models to represent secondary flows. Where smooth, gradual changes are present, the accurate prediction of flow distribution can have consequences of industrial importance. As will be demonstrated in what follows, the effect on flow fields of the presence of small blockages is significant. Larger scale unsteady structures may have more drastic con-

sequences on the mean flow prediction of turbulence models, as will be outlined in the following section.

1.3 Bluff Body Interactions

1.3.1 Long Cylinders

The computational study of flow around blockages has had some success in the case of very long cylinders in cross flow, relevant to objects such as tethers for oil rigs and bridge struts. In these cases, the geometry far from the cylinder ends is effectively two-dimensional. In cases where cylinders are shorter, the proximity of these end walls may be important, and their effect on the flow within the central symmetry plane is essential to consider before making assumptions about the degree to which the flow is 2D or 3D in nature. The authors of [78] had performed experiments on a long cylinder with end plates attached at the ends, which they moved to cover plate separations from $0.25D$ to $12D$ at Reynolds numbers of 8,000 to 140,000. The researchers found that at fixed Reynolds numbers near the upper end of the range, both Strouhal numbers and fluctuating lift may be modified quite significantly by a change in L/D, the ratio of the cylinder length over the diameter. They concluded that this was probably due to an an increase of the correlation in the pressure across the cylinder length in general; for longer cylinders the shedding from the cylinder surface was found to be out of phase with the fluctuating pressure in the centre. What is more, this triggered a disturbance in the primary shedding cycle roughly every 1-20 cycles such that it appeared dampened over several shedding periods each time, resulting in reduced lift. They also found that the effect of changes in aspect ratio was dependent on Reynolds number, regular shedding and hence lift disappeared for L/D from 1-3. At lower Reynolds numbers there was little effect of aspect ratio changes. As a result, it was suggested that complex interactions between the end plates and the flow resulting in cross flows aligned with the cylinder might have been the cause.

This helped to motivate the work carried out in [53], using the same end-plate design. One of the stated aims of that study was to provide guidelines for choosing large enough aspect ratio, in order to help following researchers design experiments with negligible dependency on the third dimension aligned with the cylinder axis. The minimum cylinder length studied was about five cylinder diameters. At all Reynolds numbers and all aspect

ratios, the Strouhal number was roughly 0.2, but it varied with both. It peaked around 0.21 for a certain Reynolds number at all aspect ratios; with decreasing aspect ratio this critical Reynolds number increased. For $10,000 < Re < 40,000$, the minimum required cylinder length to achieve independence of the end-plates was estimated to be about $L/D = 25$. At $4,000 < Re < 10,000$ they estimated it to be about 60. Noting that these were conservative estimates, they suggested that the key parameter influencing these results might be an "undisturbed axial correlation length", and suggested making cylinders four or five times as long as this, despite noting that obvious direct effects from the end plates extended only about $5D$ from each plate.

In the same year, [45] made an experimental study of a square cylinder of length $9.75D$ spanning a closed rectangular duct, so based on the work of [53] the effect of the cylinder walls was likely to be noticeable but not dominant. They collected LDA measurements in the central plane near to the cylinder face that was side-on to the flow in order to construct profiles of mean velocity and also of the fluctuations. In addition to this, they simultaneously measured the pressure at the centre of the cylinder side face in order to provide a reference point for the time dependency of the fluctuations. Once the turbulent component had been filtered out from the pressure, it was possible to phase-average the velocity data based on the time of its capture relative to the large scale pressure fluctuations. This detail regarding mean structure, chaotic turbulence and also organised fluctuation made it useful as a reference point for further studies, including the set of LES studies detailed in [66] and the DNS study made in [79]. In the former of these two, all the independent contributors used either periodic or slip conditions and the domain span along the cylinder axis was $4D$, whereas in [79] the cylinder length was πD with periodic conditions on the boundaries at the cylinder ends. In all of these cases the flow was treated as if no walls existed near the cylinder ends, nevertheless, comparisons were drawn between these and the results in [45]. One of the principal conclusions of the authors of [66] was that more difficulty was found in simulating flow around a long cylinder than around a wall-attached cube, and it was suggested that this was down to the transitional nature of the flow.

The DNS study in [79] argued that the domain was sufficiently long in the direction of the cylinder axis by calculating two-point correlations of the velocity; a separation of about half the domain span resulted in a drop in the values to near zero. This argument was

pertinently used to show the suitability of the domain size for simulating flow without end walls, but it did not prove that the simulation was perfectly equivalent to the experiments where end walls were present. Discrepancies found between the results in [79] and [45] were small, but present nonetheless. The clearest differences were in the magnitude of streamwise velocities along the domain centreline in the region behind the cylinder, where experimental values were consistently lower than the DNS ones. In particular, the DNS predicted a lower magnitude for the maximum negative streamwise velocity here, although profiles of streamwise velocity showed a good match further away from the centreline. It is possible that the discrepancy is due to instantaneous cross-stream flows normal to both the mean stream and the cylinder due to the flapping motion; these might have been stronger in the experiments than in the DNS, and would not have shown up in the mean if they were averaged out. However, there is no direct evidence to suggest this.

One experimental study of turbulent flow around a circular cylinder where lateral wall effects were significant, [5], used a circular cylinder of length $4.8D$ spanning a duct of rectangular cross section such that the blockage coefficent D/H was approximately 0.2. This study was carried out with an aim to generate data for validation of turbulence models at a high Reynolds number of 140,000. The authors deliberately chose a geometry that would not result in "infinite-span" conditions, therefore accepting the presence of strong 3D effects from the channel walls. Nevertheless, velocity data was presented only in the central plane normal to the cylinder axis, meaning that interactions between structures near the measurement plane and those near the wall could not be studied. This work has been recently used as a reference point for studies on nominally 2D flow, for example [2], where periodic boundary conditions were employed in the direction along the cylinder axis, which measured only $(\pi D)/2$, under the assumption that these wall effects were not important. Given the arguments made above that wall effects may be consequential for $L/D = 9.75$, and the express acceptance in [5] that wall effects were likely to be consequential at $L/D = 4.8$, this assumption seems to be rather tenuous, and may well be the cause of discrepancies between the predicted pressure on the cylinder surface and the experimental results. Despite a larger difference in Reynolds number, the match with experimental data from [9] was better; an experiment with a cylinder having $L/D = 29.3$ where the ends were shielded from the boundary layers at the wind-tunnel walls with end-plates.

Since the work of [78] and [53] described above, it has been shown that significant 3D structure exists in the near wake of cylinders in cross flow, even when the flow is largely two-dimensional. At relatively low Reynolds numbers, such a flow may undergo a fairly sudden transition to a turbulent state [33]. These authors were able to clearly demonstrate the onset of a secondary instability which appeared between $Re = 175$ and $Re = 225$ through direct numerical simulation within a small domain. Triggered by an initiating perturbation introduced by the researchers, a third component of spanwise velocity appeared and amplified itself at the higher of the two Reynolds numbers but at the lower it died out. Raising the Reynolds number further, to 300, then 333, and finally to 500 where the flow became chaotic, the path towards fully turbulent flow was observed, seeming to follow the classical "period doubling" route. The third component of velocity was approximately 2 orders of magnitude smaller than the streamwise one, but the authors questioned the validity of performing 2D simulation after the onset of 3D behaviour. Using LES simulations at up to $Re = 10,000$, the authors of [32] were able to simulate the aerodynamic forces on such a cylinder. The values that they reported for Strouhal number and time-averaged drag coefficient matched well with experiments, but no comparison was made for fluctuating lift. The fluctuating shear forces in the direction of the cylinder axis were approximately 2 orders of magnitude lower than those in the cross-stream direction, but the 3D instability was seen to occur in the cylinder wake. By visualising vorticity contours, the authors were able to clearly show large scale 3D structure developing in the near-cylinder wake.

As the flow around long cylinders can be shown to have a significant third velocity component at low Reynolds numbers, it might be remiss to not take this into account, with or without the presence of walls. One clear feature of these type of flows is the appearance of velocity components aligned with the cylinder. There is an interplay between the parameters of Reynolds and L/D that may result in changes in the fluctuating quantities due to the degree to which shedding is synchronised along the cylinder length, and this may only be captured with 3D simulations.

1.3.2 Wall-attached Blockages

Rather than placing end plates at both ends of a cylinder or confining it to span a channel from wall to wall, a large number of studies have focussed on the flow around objects attached to a flat floor with the upper end open to the free-flow, simulating how wind may interact with tall structures or other types of protrusions from larger surfaces. One such example of this is [29]. In this particular study, the object was not entirely contained within the boundary layer, which reached approximately 10% of the cylinder height, $3D$, where D is the cylinder diameter. Pressure tappings were made at various locations on the cylinder's lateral walls and the free upper surface, and hot wire measurements were made downstream of the cylinder at various heights from the floor. Strong periodic shedding was evident at only $0.33D$ away from the wall in frequency spectra of the velocity and pressure, that gradually decreased approaching the cylinder's free end where it was much weaker. Its strength was greatly reduced halfway up the cylinder height, apparently due to the influence of the free surface as opposed to the effect of the wall. This conclusion appears to be backed up by [81], where the width of the mean wake gradually decreased from a peak around $1D$ away from the wall towards the cylinder's free end at $4D$. Rather than being a feature of a steady flow structure, this is probably due to a decrease in the size of the flapping motion nearing the free stream, where the flow over the top of the cylinder tucks back in behind it. Due to the strength of the shedding in the lower section of these cylinders and the strong effect of the top surface, it is quite logical to ask what might happen when the cylinder height is of the order of its width; will an organised periodic component remain or will it be too disturbed by the free end to be significant? Flow around a wall-attached cube has been a focus of attention since at least 1991, where visualisation of the flow structure through several means was used to build up a good picture of the highly three-dimensional structures present in flow around a cube [39], and an extension to that work was carried out in [49] where flow around wider cuboidal objects was measured and visualised. In both cases, the channel was twice as high as the cube. Key mean features included upstream vortices near the corner between the channel floor and the cube, an area of flow separation after the leading edge and horseshoe shaped vortices both behind the cube and stretching from upstream of the cube out past the sides and further downstream. The highly three-dimensional flow behind the cube was present

up to a cuboid width/height ratio of approximately $W/H > 6$ beyond which point there was a region of flow that was largely 2D; the horseshoe shaped vortices no longer joined together downstream of the cube but remained separate. Following on from this, LDA measurements in the wake were collected to directly measure the production, convection and transport of turbulent kinetic energy, and to infer indirectly the dissipation rate. This detailed dataset has been used as a benchmark for several studies including LES [73] and unsteady RANS [27], where the latter study also drew on the former as a reference point. The work of [73] was able to provide some insight into a phenomenon that had been noted by the original experimentalists; a strong bimodality in the velocity upstream near the symmetry plane at the origins of the horseshoe vortex. They were able to show that in certain regions of the flow, the solution jumped back and forth between two states quasi-periodically. Performing spectral analysis of the force on the cube side, they found that for a very long data collection time a clear peak did not exist at any particular frequency. This is quite different to findings from long square cylinders without free ends [45], where a clear dominant frequency was found at a Strouhal number consistent with other studies of flow around long square cylinders. In addition to the study of flow around a long cylinder, the authors of [66] applied LES to the study of flow around a cube at $Re = 3,000$ and $40,000$, and in [65], several steady $k - \varepsilon$ variants were compared with these results. One of the principal conclusions of this paper was that unsatisfactory predictions were made by the steady simulations, particularly with regards to the length of the recirculation region. The author of [27] was able to show that a very good match to experiments for the mean flow profiles could be achieved using unsteady RANS methodology, which could not be achieved with a steady version of the same model, concluding that it was the vortex shedding that made the difference. These authors found that a periodic back and forth motion was manifest in several ways within the cube vicinity including movement of the arch vortex behind the cube, a major 3D flow feature. In [66], it was noted that in general better agreement with experiments was found for the flow around the cube than for a long cylinder. This was despite the fact that in both cases the boundaries were not resolved at one set of lateral walls, where either periodic or slip conditions were applied. The match for mean stream-wise velocity profiles above the cube and in the recirculation region beteween the LES and the experiments was very good at both $Re = 3,000$ and $Re = 40,000$.

In conclusion, it is clear that the unsteady flow associated with vortex shedding produces certain challenges that have been the focus of attention right up to the present day. Crucially, it is essential to take into account the unsteady nature of the flow; mean velocity predictions are significantly affected by the unsteady components, even in geometrical symmetry planes. The tempting assumption of 2D shedding around long cylinders, with the simplifications and associated economies in computational resources that may be made, has been shown to be too restrictive. This modelling neglects 3D phenomena that are present across the Reynolds number range from when laminar 2D shedding occurs right up to highly turbulent flows where $Re = O\left(10^5\right)$; such 3D phenomena are inherent to these flows and make up significant parts of the flow physics. In cases where a cylinder is set between the walls of closed rectangular ducts, it may be seen that discrepancies arise in the prediction of such important quantities as stream-wise velocity in the recirculation region behind the bluff body, wherever careful consideration is not given to the effects of the lateral wall boundary layers. Such effects have not been taken into account, even in recent years, probably due to reasons of computational cost. These effects may be present at L/D ratios near 10 and 5 and there is reason to assume that they may become more dominant as this ratio reduces further; interactions between 3D structures near the duct walls and those near the cylinder surfaces would inevitably cover a larger part of the flow domain. In cases where a cylinder length approaches its diameter, and the walls within which it is embedded become much closer together than those parallel to it, it is unknown to what degree these interactions would change the physics of the flow. To the knowledge of the current author, such a case has not been reported on either experimentally or computationally.

1.4 Contributions Made

During this study, two complementary approaches are followed, one computational and one experimental, and conditions are carefully controlled so as to make them equivalent for comparison. The computational calculations include high-fidelity DNS simulation as well as unsteady RANS methodology, and the experimental study makes use of time-resolved pressure recordings as well as instantaneous capture of sections of the flow using PIV methodology. Key points of interest are summarised below:

- Turbulent flow within a new geometry is studied in detail: a cubic partial blockage spans the smaller of the two dimensions in a wide, thin rectangular channel at three different Re_D numbers, 5600, 10400 and 15600 based on the channel height/blockage size. Flow around this object results in previously unseen structure, and the effect on shedding is scrutinised

- PIV measurements in the wake region provide 2D velocity snapshots as a point of reference for velocity predictions at all three Reynolds numbers, both mean and instantaneous flow structure is made available

- Time-resolved pressure tapping at the cube side provides a point of reference for scrutinising the frequency and amplitude of organised fluctuations at all three Reynolds numbers, and is phase-matched with the velocity data

- DNS simulation provides a further point of reference at the lowest of the three Reynolds numbers, from which details of both the instantaneous and mean flow are extracted for comparison.

- URANS predictions using different models are compared with both the experiments and DNS in order to build up a picture of their various strengths and failings; during this process they are also compared with each other in order to propose explanations for the differences in predictions.

- Recommendations are made relating to the use of turbulence models for single-phase flow in non-circular ducts, with a particular focus on the flow around partial blockages

- Avenues for further work are suggested in the light of the comparisons made, including important areas of development for URANS methodology

1.5 Outline of Thesis

The introduction section above provides context for the work, including project aims and a background study of available literature on the subject. In all of what follows, descriptions of more specific techniques, concepts and formulae are embedded within the appropriate sections, with references given within each chapter.

Firstly, description of the experimental apparatus is given, with a focus placed on facilitating any further related research. To this end, references are made to relevant studies that may provide insight into flow-rig design. In addition to this, details of the particular components is given, with specification where appropriate.

Secondly, in-depth detail of the experimental methodology is presented. The process followed to capture the data is explained in detail. As part of this, some qualitative results from preliminary experiments are given, with an intention to set the scene for the final set of experiments. Where they are considered useful to show the suitability of the set-up, or where they may be used to demonstrate details of the data-treatment process, some analysed results are given.

The results of the experiments are presented next; fluctuating pressure and 2D-2C PIV data is presented in the recovery region of the cube. Mean averaging and phase-averaging of the flow is used to highlight quantities of interest, including phase-averaged pressure amplitude and structure of the velocity fields.

Moving on to computational work, the turbulence models used are introduced after a brief discussion of their origins. Attention is drawn where possible to the motivations and reasoning for specific developments made by the respective authors, in order to give an intuitive idea of how models might be expected to perform in the context of the present study. Details of the mesh refinement and time-step selection process are explained, with appropriate results shown to argue the suitability of the final choices.

Computational results are presented next, alongside each other in order to highlight similarities and differences, with a focus on the most readily visible discrepancies and on particular details in the modelling that may help to explain them. An overall picture of flow structure is given alongside some specific phenomena of interest.

Validation of the URANS methodologies used is carried out by comparison to the experimental results and the DNS; all results are non-dimensionalised by appropriate

quantities. Key points regarding modelling strengths and weaknesses that have been alluded to previously are focussed on using the new benchmarks. Successes and failures to represent accurately the physics are discussed. Wherever the DNS or experiments are considered unreliable or imperfect, caution is given with reasoning attached.

Final conclusions are drawn in order to draw together useful comments on the URANS models; how suitable are they and what are their relative strengths and weaknesses? Where conclusions agree with the scientific literature, this is highlighted, and any differences are discussed.

Lastly, suggestions for further work are outlined. These suggestions are targeted where conclusions drawn from the current study are insufficiently evidenced and also where phenomena of interest have been highlighted, particularly with regards to turbulence modelling shortcomings.

2 Experimental Apparatus

2.1 Flow Rig Design

In order to help inform the choices of materials and geometries in the design process, a simple MATLAB program was created to help predict the pressure drop in different sections of the circuit for given fluid properties. The friction factor estimate used for predicting pressure drop in the main channel was that suggested in [14] for narrow, smooth ducts of non-circular cross-section. For pressure drop in the pipes, that given by [22] was applied. "K" factors from an online database [60] were used to find estimated coefficients for various pipe fittings. Classic stress-strain formulae for flat plates with clamped edges were used to estimate deflection of the main channel faces, and double checked against results from a more detailed and well-defined Finite Volume Stress Analysis using Star-CCM+. This program allowed quick and easy trial-and-error of different flow rates, channel geometries and other parameters for setting useful bounds in the design criteria before a more detailed, finalised design was produced. The hydraulic circuit (Figure 1) was driven by a constant level overhead reservoir, with a free surface open to the atmosphere approximately $4m$ above the main channel. This overhead tank had a nested design consisting of two constituent tanks such that the water level in the internal tank was held constant and the outer tank collected the overflow. The working fluid was tap water from the mains supply, with bleach at $5ppm$ to prevent microbe development. Smooth plastic piping having an internal diameter of 3" was used to direct the main flow from the overhead tank to a cubic inlet box of $380mm$ internal width (Figure 3). Solidworks by Dassault Sytemes was used to design the inlet box and main channel, and to produce 3D CAD files that were sent to the manufacturers. The inlet box was made of clear acrylic plastic. Flow rate through the channel was controlled with a ball valve set into the main flow pipe, also having a 3" internal diameter. The main flow passed from the pipe into this box via a sudden expansion through a hole made in the top face, slowing down as it did so.

The inlet box (Figure 3) is conceived in such a way that the convergence guide piece is easily accessible. It may be removed from the box in one piece, modified then replaced. Within this box, baffles were used to direct the flow through a smooth change in cross

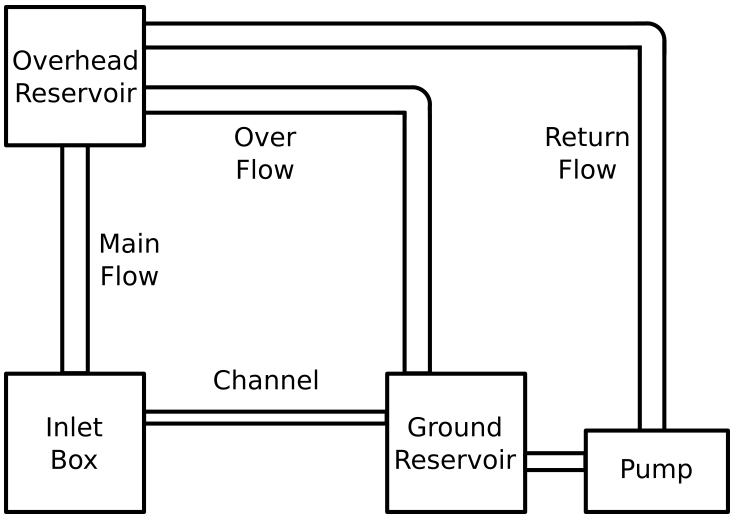

Figure 1: Hydraulic circuit design

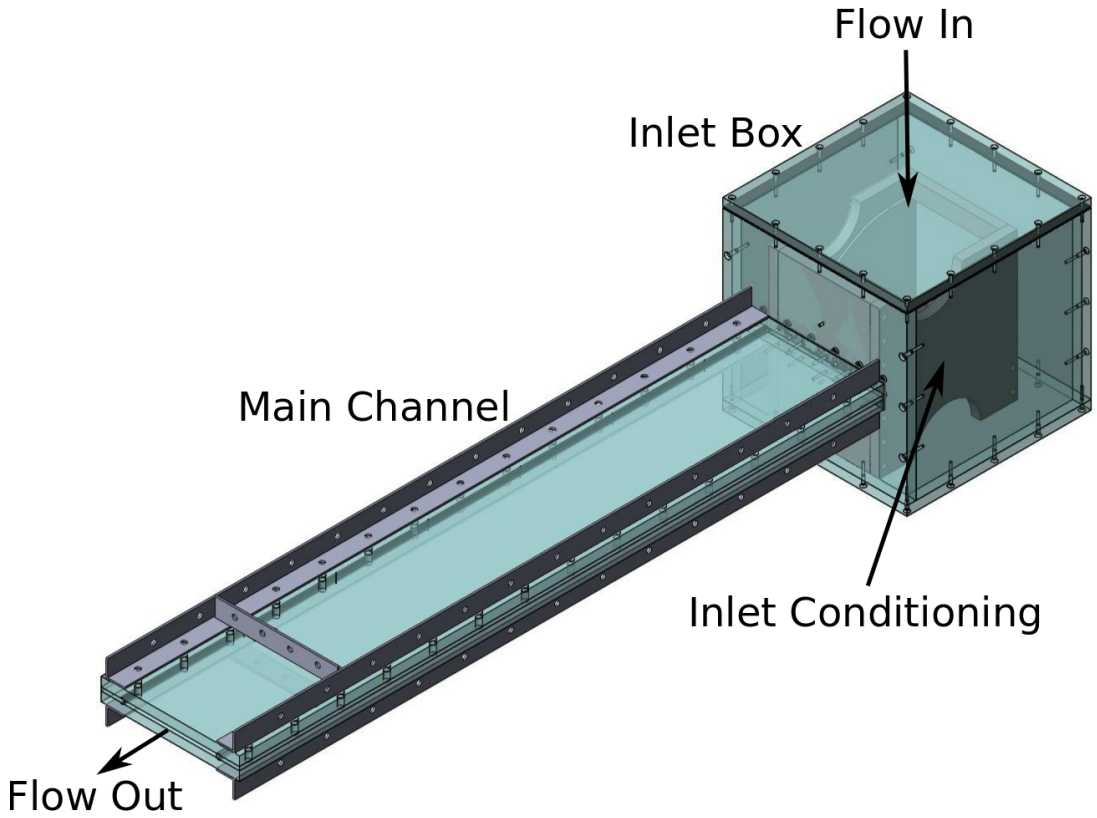

Figure 2: Assembly of main channel including inlet box for inlet and support struts

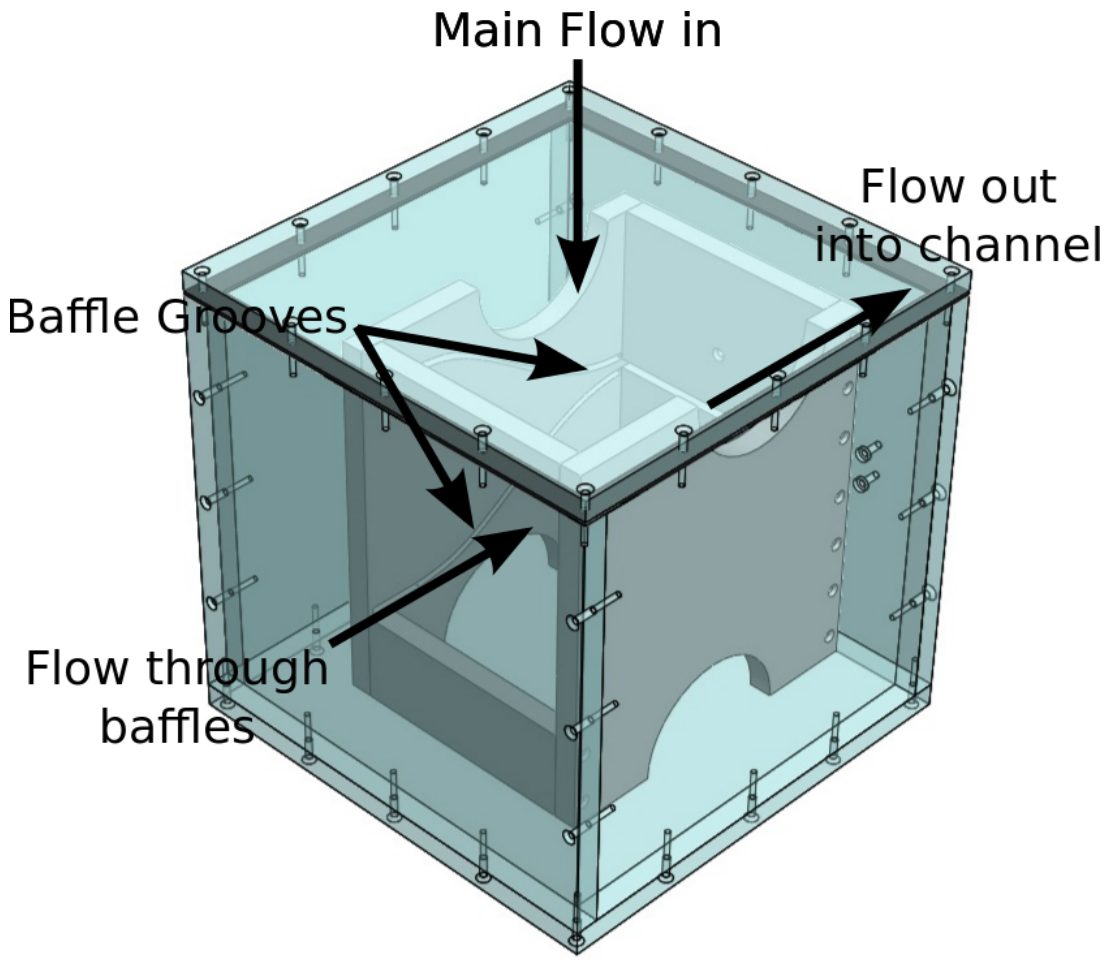

Figure 3: Flow conditioning box before main channel inlet, with baffles removed

section, following the form of a cubic spline with both ends having a zero gradient. The baffles are not explicitly displayed in Figure 2 or Figure 3, they were located in the grooves that are shown. This form is similar to that used in the wind tunnel design outlined in [3]. Regarding the contraction ratio, defined as $R_c = A_{inlet}/A_{outlet}$, consideration was given to the findings in [6]. That study investigated the effect of contraction ratio on vortices as they pass through, where large eddies may be amplified by vortex stretching. Both streamwise-normal components of vorticity were generated by vortices of similar strength due to careful inlet conditioning giving nearly homogeneous inlet turbulence. The authors found that the contraction ratio and the inlet turbulence level are the parameters which most significantly affect the turbulence level through the contraction. It was discovered that for increasing contraction ratio from $R_c > 4$, the level of isotropy of turbulence far from the wall increased until the turbulence became almost isotropic at $R_c \sim 8$. Based on these findings, a high contraction ratio was considered desirable so as not to emphasise any large vortices that may be present at the inlet. A large inlet area also entails another added benefit; a lower inlet velocity results in lower vortex-producing velocity gradients near the inlet lip.

The baffles were symmetric about the channel's central xy and xz planes and had a constant side-on cross section. They were positioned such that they prevented fast-moving fluid from the inlet pipe from entering directly into the main channel, the flow was forced to change direction by 90° and align itself with the main channel after having slowed down greatly. The reduction in cross-sectional area of the convergence baffle section was from $40,000mm^2$ to $1,600mm^2$ between inlet and outlet, giving a ratio in the bulk velocities across these surfaces that was the inverse of the contraction ratio of $R_c = 25$. The final cross-section had a width of $W = 200mm$ and a height of $H = 8mm$. Rather than a perfectly smooth transition between the baffles and the main channel, there was a lip protruding by a fraction of a mm. This remained to served as a trip to aid the development of turbulence. Following this, the flow passed straight through the channel wall for $40mm$ with no further change in cross-section, entering the main channel, which also had the same width and a height of $H = 8mm$, corresponding to an aspect ratio of $R_a = W/H = 25$. The assembly of the inlet box, main channel and support struts was tested before commissioning (Figure 2). The straight section of the main duct was $1,400m$ long, or $175H$, and measurements were eventually made about $125H$ downstream

of the duct inlet. For comparison, [50] reported that fully-developed flow was attained in a square duct at only $37H$ downstream of the inlet and [26] reported that flow in a rectangular duct having $R_a = 12$ was fully developed by $47H$. Adjustable feet were fitted to the channel's Aluminium support legs in order to facilitate laser beam alignment. The acrylic side piece faces were meticulously polished in the region where measurements took place using a wet/dry sanding kit which consisted of many sheets having decreasing grain size, the finest of which was $1\mu m$. Spray polish was finally used to fill in any remaining micro-scratches. After this treatment the side pieces were extremely transparent; looking through them one could see a clear picture on the other side with very few apparent aberrations. The refractive index of the acrylic was ~ 1.49, whereas for the water it was ~ 1.33.

Water exited from the duct by squirting directly out into a large main reservoir held at atmospheric pressure. This main reservoir served as the water storage tank when the circuit was not in operation, and had a capacity of $\sim 400l$. When the circuit was in operation, overflow from the overhead tank also returned directly to this main reservoir via a 3" plastic pipe. Such a large diameter was chosen to ensure that the overflow could cope with a high flow rate when the main valve was completely closed, to prevent accidental overfilling of the overhead reservoir. Water was recirculated from the main reservoir to the overhead tank with a Grundfos NBE series centrifugal pump, via 2" smooth plastic piping. This pump was configured to order; it could provide a high enough flow rate to maintain the level in the overhead tank with the ball-valve fully open, without overflowing the overhead tank when the the valve was fully closed. The pump throughput was managed via a rotary control on the power supply, which had an automatic start-up transient to protect the pump from damage.

The main duct consisted of two large faces of $20 \times 300 \times 1400mm$ and two sidepieces of $8 \times 50 \times 1400mm$, fabricated entirely from clear acrylic plastic. The side pieces were sandwiched between the two larger plates at the sides to leave a large straight internal duct of $8 \times 200mm$ cross section. This design allowed for the modification of the channel cross section via the side pieces. Waterproofing was ensured by placing rubber O-ring type piping in grooves running the length of the channel. A neoprene seal was placed between the convergence box and the main channel, and a small amount of silicone bath sealant was used in crucial places to ensure that there were no leaks.

2.2 Blockage Design

Two blockages were manufactured from different materials, having very precise dimensions of $8mm^3$ (Figure 5). This characteristic dimension D was precisely the same as the channel height H so that it could form a partial blockage spanning between the large channel plates. Two different methods were used to manufacture the blockages. For the first, precise milling machinery was used to fabricate a cube from a block of aluminium. The absolute precision of the machinery movement was just $0.01mm$. Holes were carefully drilled to produce a small pressure tap in one of the cube faces. The diameter of the drill bit used for the hole in the cube face was $1mm$. The connection between the gauge and the cube face was made by way of a $2mm$ diameter hole drilled through from below the cube, forming a 90° angle with the small $1mm$ hole drilled through the cube wall. This connection then passed through the channel wall, where the pressure gauge was threaded in using PTFE tape to ensure a watertight connection. The differential pressure gauge had one port open to the atmosphere, the other was connected to the hole in the cube face. Both of these ports were pre-threaded, making their connection easier. In general, the finish of the cube was imperfect due to very small chips that broke off from the cube corners during milling. Although great care was taken and although these chips seemed very small in absolute size, relative to the cube size they appeared significant enough to disturb the flow somewhat. Moreover, despite careful blackening of the surface of the aluminium cube, small scratches were easily introduced such that the silver colour showed through, introducing a risk of hazardous laser reflections. For these reasons, a second cube was manufactured before experiments with lasers were carried out.

The second cube was made to order in matte black plastic by high precision 3D printing equipment, with a maximum spatial manufacturing error of $42\mu m$. Visual inspection under a microscope showed that this cube was very evenly manufactured, with neat edges and flat surfaces. Reflections were greatly suppressed by the black finish allowing a laser to be shone in the vicinity of the cube with minimal safety implications. A free passage from the lower cube face to one of the cube side faces allowed pressure tapping. The diameter of the hole for the pressure tapping was just $0.5mm$, resulting in minimal disturbance to the flow, and a point-like pressure reading. A syringe full of water was used to force water through the pressure tapping prior to each experimentation in order to remove air

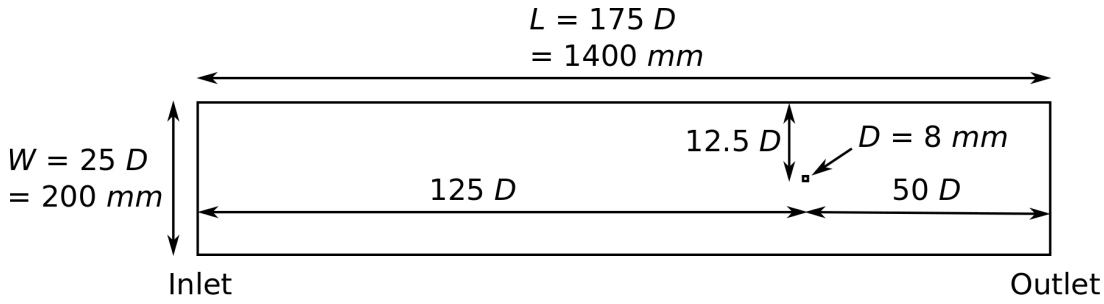

Figure 4: Channel dimensions and cube location

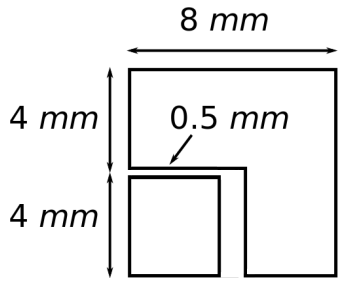

Figure 5: Cube dimensions, section showing 0.5 mm pressure tapping which was centrally located in a face parallel to the flow

bubbles. The blockages were inserted into the channel $125D$ downstream of the inlet, or $50D$ upstream of the outlet, (Figure 4), and were prevented from moving laterally with a small pin. There were no noticeable movements in the cube at any flow rate. A very small amount of bath sealant was placed on the lower surface of the cube before it was wedged into the channel to ensure airtightness of the pressure tapping.

2.3 Pressure Transducer

In order to characterise the time-dependent periodic shedding phenomenon, a Kistler 4264A series differential pressure gauge was used. This piezoresistive pressure sensor has a quoted accuracy of $\pm 0.2\%$ across a range from $0-1.5\,PSI$, or $0-10343\,Pa$, corresponding to $20.7Pa$. The high accuracy was important as a high degree of pressure resolution was predicted to be necessary by the preliminary simulations, in order to resolve the small pressure differences associated with vortex shedding. What is more, the transducer was calibrated at the factory before shipping, to ensure its fidelity to the quoted accuracy. The frequency response of the transducer was $2kHz$, ~ 57 times that of the shedding frequency expected at the highest Reynolds number. The transducer was powered by two $9V$ batteries, chosen for the stability of their output relative to that of a mains power pack. Capture of the signal was done by way of a National Instruments USB 6002

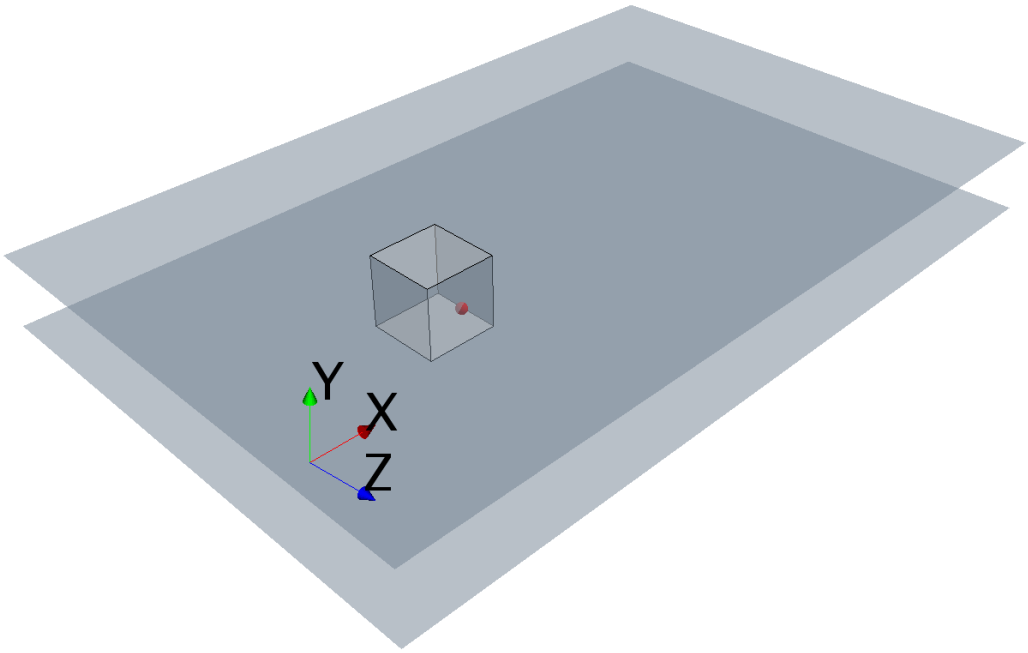

Figure 6: Pressure tap location at the centre of the cube face parallel to the mean flow in the x direction

Digital Acquisition Device (DAQ). This piece of equipment was capable of reading voltages across a range from $-10V$ to $+10V$ with 16 bit resolution, corresponding to a resolution of $\sim 3 \times 10^{-4}V$. Using the factory calibration curve, this corresponds to a change of about $0.3Pa$, beyond what the transducer is capable of. The maximum sampling rate of this device was $50Ks/s$ meaning that the DAQ was more than adequate for resolving the signal output by the transducer; this was the case both in terms of response time and pressure resolution.

2.4 Particle Image Velocimetry Apparatus

2.4.1 Laser

The light source used was a New Wave Research Solo PIV Nd:YAG dual pulse laser, with a dedicated power supply. The laser had an integrated harmonic generator which took the infra-red light generated at $1024nm$ and converted it to visible, green light at $532nm$. The laser pulse duration was $3-5ns$, and the maximum pulse energy was $\sim 124mJ$. Optical pumping for this laser was provided by two flash lamps, one for each of the dual Nd:YAG rods, and firing was initiated by "Q-switch" triggering, described below in Section 2.4.4. For safety, care was taken to enclose the laser beam and reduce surface reflectivity as

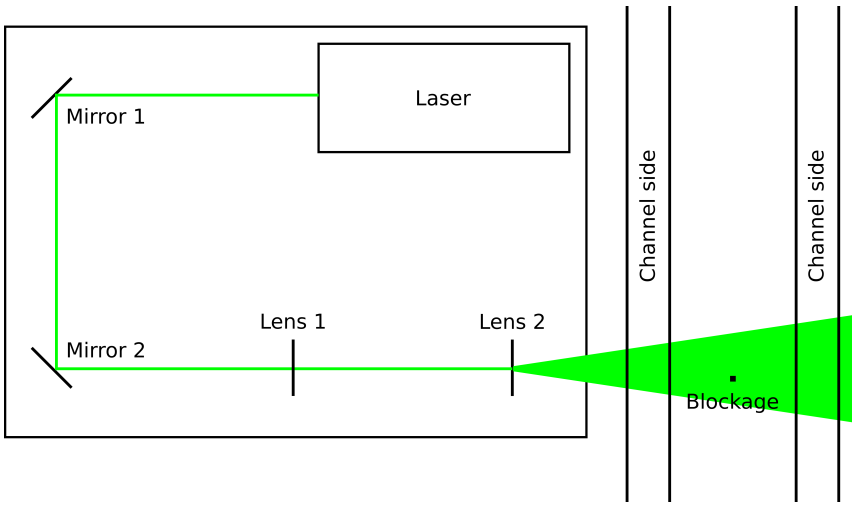

Figure 7: Basic layout of optical equipment on bench, not to scale

much as possible.

2.4.2 Beam Manipulation

A large, sturdy optical bench with pre-drilled and threaded holes was acquired in order to mount the mirrors and lenses needed. A mounting frame for the bench was constructed from extruded Aluminium profiles, with adjustable feet that had rubber pads to dampen vibrations. Metal mounts were used for the optical components, and these mounts were firmly fixed to the bench. It was possible to make minute changes in the positioning and orientation of the optical components using adjustment screws without loosening them from the bench, which allowed for fine-tuning of the beam path. Four main optical components were used (Figure 7). Mirrors 1 and 2 were used for changing the beam direction. Lens 1 was a plano-convex lens used for flattening the beam into an elliptical shape. Its focal length was chosen in order that the ellipse was as flat as possible in the cube vicinity. Lens 2 was a plano-concave lens, used for spreading the ellipse out in the direction of its major axis in order to form a wide, thin laser sheet. The laser bench, mounts and optical components were acquired from Thor Labs, and were optimised for use in a narrow wavelength range corresponding to that of the laser used.

2.4.3 Camera

A LaVision Imager Pro Plus camera was used to capture the raw images of the illuminated particles. This camera had a 4 MP resolution, or 2048×2048 pixels. In addition, it had CCD capability, which made possible the capture of two images in very quick succession.

Image data for each of the two snapshots was transferred from the camera buffer memory to the computer in the time between image pair capture. An adjustable camera lens was used to allow the camera to be focussed in the region of interest. Addition of a filter allowed all light outside of a narrow band comprising $532nm$ to be removed. In tandem with the intensity of the laser light relative to that ambient in the lab, this filtering allowed optical noise to be greatly reduced. The effects of any remaining optical noise, along with any extra electrical noise from the CCD circuit, were further reduced by subtracting the mean intensity reading for each pixel across 100 frames, see Section 3. In addition to removing the mean of the noise component, this pixel by pixel treatment allowed for any systematic variations due to inconsistencies in the CCD chip. For experiments at all three Reynolds numbers, the field of view that was captured was very similar. For the downstream measurements, the field of view included most of the cube and extended to $\sim 2.7D$ downstream, from $x \sim -4mm$ to $x \sim 21.5mm$. Despite slight differences in the field of view captured, the equivalent size of a pixel was $0.05mm \pm 0.002mm$ across all downstream measurements.

2.4.4 Laser-Camera Synchronisation and Control

In order to manage the synchronisation of the the laser firing and the image capture, DaVis 8 specialised PIV software was used, in conjunction with an external Programmable Triggering Unit (PTU). These two elements comprise the "timing management system" referred to in the following. All external triggering signals were sent by the PTU unit, according to parameters communicated to it via the DaVis software. Feedback signals from the laser firing unit were returned to this PTU in order to provide it with the information it needed during experimental runtime. Triggering and timing was very precisely controllable due to a two step process consisting of flash-lamp triggering followed by "Q-switch" triggering, which fired the laser. The flash-lamp firing was triggered by an external "top-hat" shaped pulse of $\sim 5V$ in height which was $> 100\mu s$ in length. Illumination of the cavity put the lasing medium into an excited state, making the laser prone to fire. The emission of a $\sim 110\mu s$, $\sim 5V$ top-hat pulse via a "Lamp Synch OUT" channel $\sim 120ns$ later allowed the timing of the lamp firing to be known precisely by the external timing management system. The process of stimulated emission began with the rising edge of the external Q-switch triggering from the timing management system. The delay length between the "Lamp Synch OUT" pulse and the Q-switch triggering could be adjusted within the timing management system, and was typically $180 - 200\mu s$. Approximately $120ns$ after receipt of this second external input signal, a "Q-switch Synch" signal was output to the timing management system, having the same $\sim 110\mu s$, $\sim 5V$ top-hat form. The Q-switch Synch OUT trigger line was fed in to a T-connector after which it passed to the timing management system; it was also connected into the DAQ device alongside the pressure transducer. Both channels were recorded simultaneously with the DAQ at a rate of $20kHz$, high enough to reliably catch each $\sim 110\mu s$ pulse so that the time at which the images were recorded relative to the pressure signal could be known. The maximum error in the time of receipt of this signal by the timing management system was $\sim 5 \times 10^{-5}s$, which was much greater than the delay between the signal's emission and the firing of the laser pulse. As a result, the error on the time-stamping of the laser pulse was also taken to be $\sim 5 \times 10^{-5}s$. This level of precision was more than sufficient to time-stamp each velocity snapshot relative to pressure fluctuations, whose frequency of the order of $10Hz$. A total of 1000 velocity snapshots were recorded for each experiment.

3 Experimental Methodology

3.1 Dye Flow Visualisation

In order to make qualitative observations of the condition of the flow past the blockage, blue ink was injected at two separate locations, using a syringe with a thin needle. Firstly, ink was injected by syringe $10mm$ downstream of the channel inlet on the centreline. Dye was injected by hand in bursts of varying duration from half a second to a few seconds. There were pauses between bursts in order to ensure that all ink from one burst was washed out of the channel before the next, and the same process was carried out at different flow rates. The dye was immediately convected downstream in a straight line past the cube, verifying that there was no span-wise yaw in the mean flow following the z direction. The width of the region that was coloured by the ink increased gradually with distance downstream, initially at an equal rate in the positive and negative z directions, and it exceeded no more than a few cube widths by the time it passed the cube 125 cube widths downstream of the inlet. This verified that there were no large vortices aligned in the y direction that were being advected in through the inlet convergence section. The second injection location was at the pressure tapping hole in the side cube face. White card was placed below the channel in order to make the ink more visible, and the cube region was floodlit. Short bursts were produced by hand gently, as it was considered important to not disturb the boundary layer any more than necessary by the process of the injection itself. Care was taken not to place too much pressure on the syringe so as not to force the ink through too quickly. A digital video camera with a frame rate of 128 frames per second was used to record the ink being washed away from the cube side, into the recirculation region, and finally being dragged downstream in the form of Von-Karmann type vortices in a cone-shape of increasing width (Figures 8 and 9). Using a simple stop-watch and counting the number of vortices that were apparently produced, one could calculate the shedding period to be roughly $10Hz$, which corresponded to the Strouhal number of 0.2 expected for shedding at the same flow parameters with a long cylinder [54]. These preliminary experiments were useful in order to ensure the quality of the flow conditioning and also to show that periodic shedding did occur in a pattern qualitatively similar to that of flow past long cylinders.

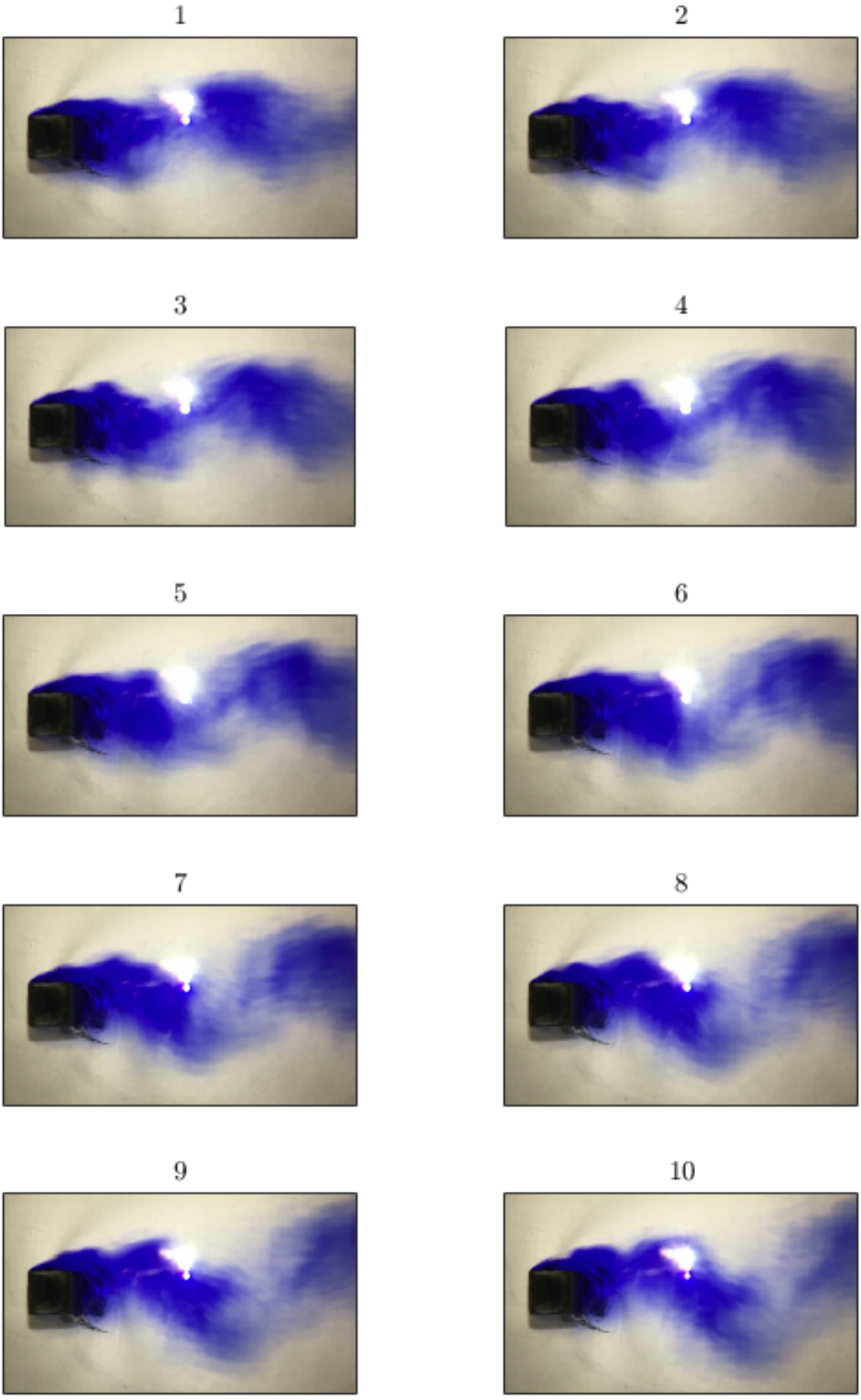

Figure 8: Video recording at 128 frames/second, frames 1-10

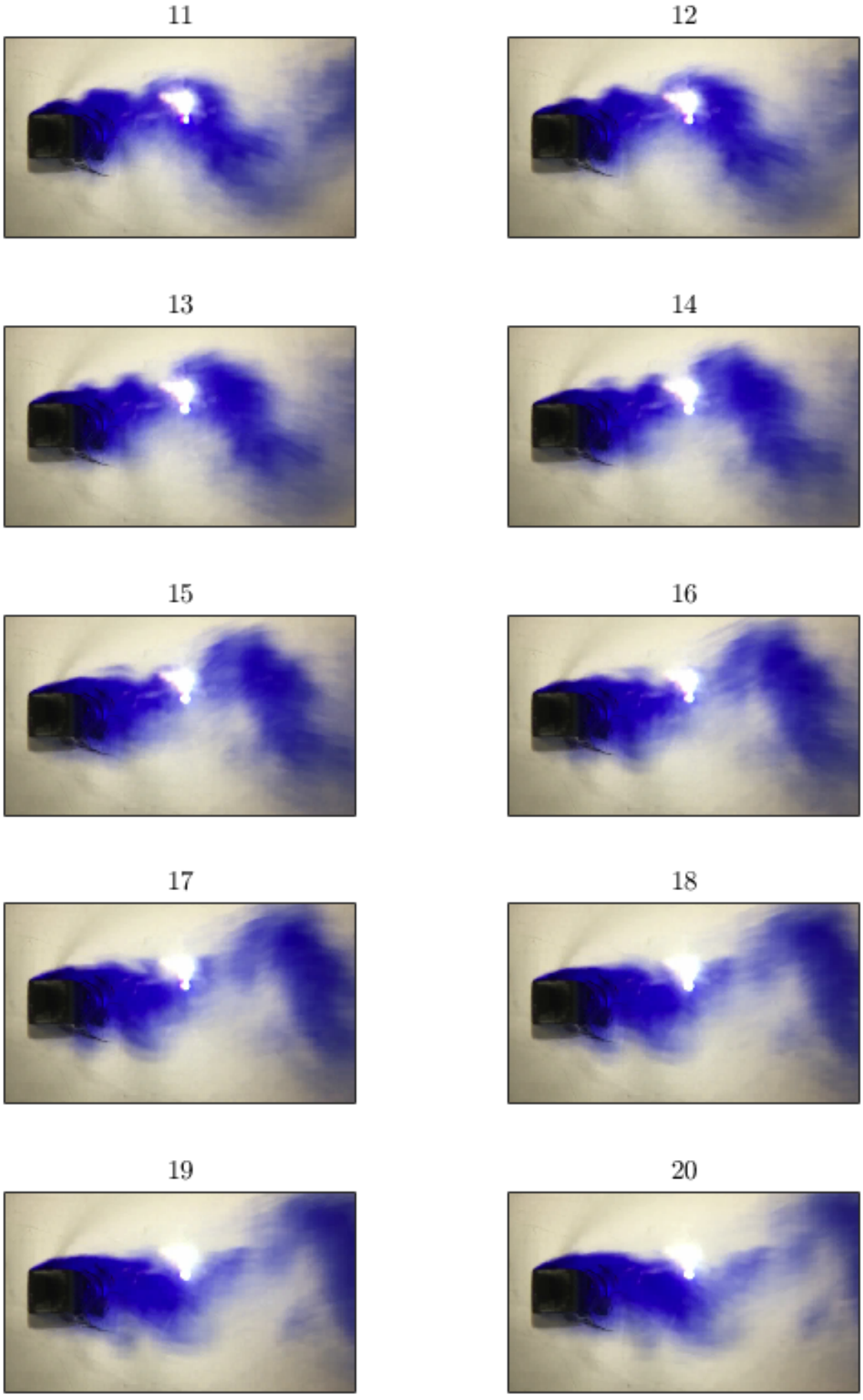

Figure 9: Video recording at 128 frames/second, frames 11-20

3.2 Flow Rate Measurement and Control

Measurements were carried out based on three separate target Reynolds numbers. Based on the hydraulic diameter of the channel, these Re_{Dh} numbers were 10800, 20000 and 30000. This corresponded to a Re_D based on the channel height H of 5600, 10400 and 15600 respectively. The blockage was cubic and of dimension D, spanning the plate separation fully, so $D = H$. The primary focus will be on the flow in the vicinity of the cube far from the side walls where the physics is dictated by the geometry of characteristic dimension D. For this reason, Re_D will be used in what follows to characterise the flow as opposed to Re_{Dh}. In order to test the repeatability of the flow rate as governed purely by valve position, marks were drawn on the valve handle and flow rates were measured and re-measured while changing back and forth between the marked positions. Flow rates were measured by timing the filling of a bucket with a stopwatch. Several such measurements were taken with each valve position change to reduce statistical error. The process of measuring the flow rate took a few minutes and resulted in unavoidable small amounts of spillage, so for some preliminary tests the target Reynolds numbers were not matched accurately; where this is the case, it is clearly noted. The weight of the bucket was measured with a luggage scale, accurate to $\pm 1\%$. The value of the relative standard deviation over these measurements was typically $\sim 2\%$ at $Re_D = 5600$, (Figure 10). Where estimated errors in flow rate are given, they are based on the standard deviation in the measurements taken.

The relative standard deviation was typically $\sim 4\%$ at both $Re_D = 10400$ and $Re_D = 15600$. This was likely to be due to the more rapid filling of the bucket at the higher flow rate. The temperature in the lab varied by several $^\circ C$ according to the time of year, corresponding to a change in water viscosity of over 10%. It would have been possible to iteratively adjust the valve position and re-measure the flow rate whenever the temperature had changed, to reach a target flow rate corresponding to each fixed Re_D number at the current temperature. However, this was undesirable as an adjusted flow rate would correspond to a different Strouhal number despite the match in Reynolds number. In addition to the differences in ambient temperature, during prolonged experimentation the temperature in the circuit was found to rise by several $^\circ C$ due to the heating provided by the pump action. For these reasons, the temperature was maintained as steady as

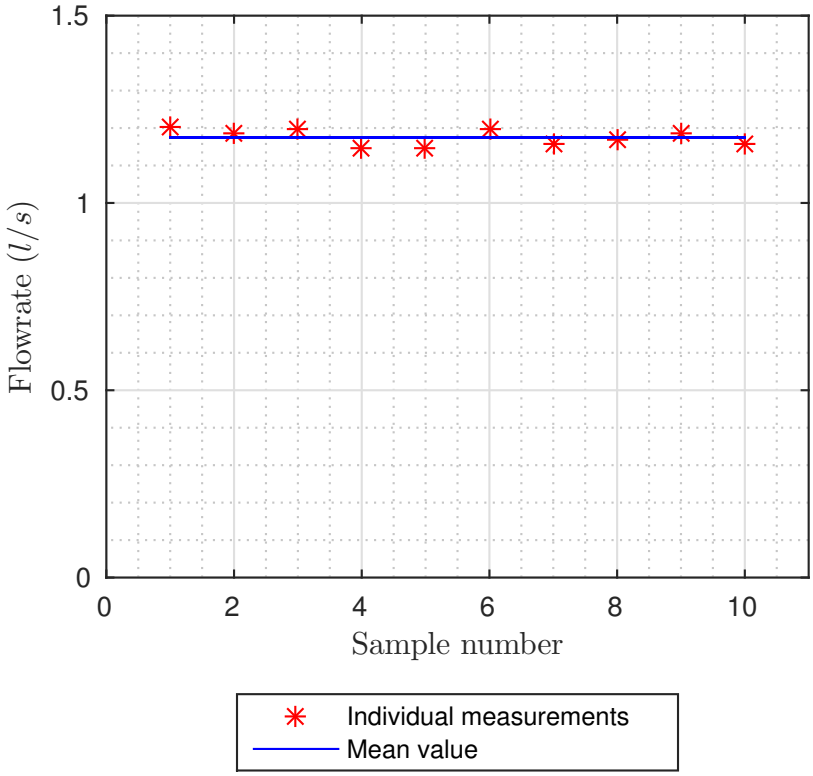

Figure 10: Flow rate measurement data, $Re_D = 5600$

possible during experiments. A thermometer was immersed in the main reservoir to measure water temperature to within 0.5 °C, corresponding to an accuracy of ∼1.5% in the value for viscosity taken from lookup tables, provided by the International Association for the Properties of Water and Steam [1]. Ice was used to cool the water whenever the temperature was seen to have risen in order to maintain the temperature near 19.5 $°C$. In order to prevent dilution of the circuit water, and hence a change in concentration of seeding particles, the ice was placed inside a plastic bag that was partially submerged in the main reservoir. This prevented it from entering the water in circulation, but still allowed effective cooling. All data presented were taken with the temperature reading between 19 $°C$ and 20 $°C$, corresponding to a maximum change in water viscosity of $\sim 3\%$. Relative density changes were far smaller than this, at $\sim 0.1\%$.

3.3 Pressure Transducer Measurements

In order to quantify the background noise present, a total of four 10s test runs were carried out, two with the power to the transducer switched off, and two with the power switched

on but without any water flow. The noise was converted from voltage to an equivalent pressure reading according to the calibration data, from which the typical RMS of the noise was found to be equivalent to $\sim 4Pa$. No discernible difference was seen between the signals from the transducer while powered up and powered down in the absence of the water flow. Having a maximum response frequency of $2kHz$, the gauge was more than sufficient to capture shedding frequencies of the order of $10Hz$. In order to confirm the reliability of the factory calibration, a test was carried out using a simple water column, in order to ensure that there were no problems caused during transit. The estimated pressure resolution attainable by this test was $\sim 20Pa$, near that of the quoted accuracy for the transducer, and the factory calibration curve matched within this margin of error over the range $100 - 1000Pa$.

3.3.1 Preliminary Tests - Pressure

Readings were taken at three Re_D numbers, 5600, 10900 and 15500, close to the target Re_D numbers of 5600, 10400 and 15600. These experiments were carried out using Cube 1, which was fabricated from Aluminium. The pressure signals appeared quite noisy and complex to the eye, such that the the periodic behaviour was obscured, see Figure 11. In order to extract the periodic shedding behaviour, a Fast Fourier Transform (FFT) algorithm was first applied to the raw signal to calculate the DFT. MATLAB was chosen for this purpose due to its versatility. In this first stage of the analysis, for some of the experiments the spectrum was somewhat cluttered at low frequencies, where a single clear peak was not seen but rather a cluster of peaks of the order of $1Hz$, see Figures 13 and 14. This inconsistency was probably due to low-frequency changes in pressure that were not captured in sufficient number within the short experimental time. In all cases there was a much clearer peak at higher frequency, albeit at a slightly lower power. The appearance of this clear peak scaled roughly linearly with Reynolds number as evident in Figures 12, 13 and 14. This is exactly what would be expected from periodic shedding around a long cylinder [54].

The Strouhal number dependency at these three Re_D numbers is summarised in Table 1.

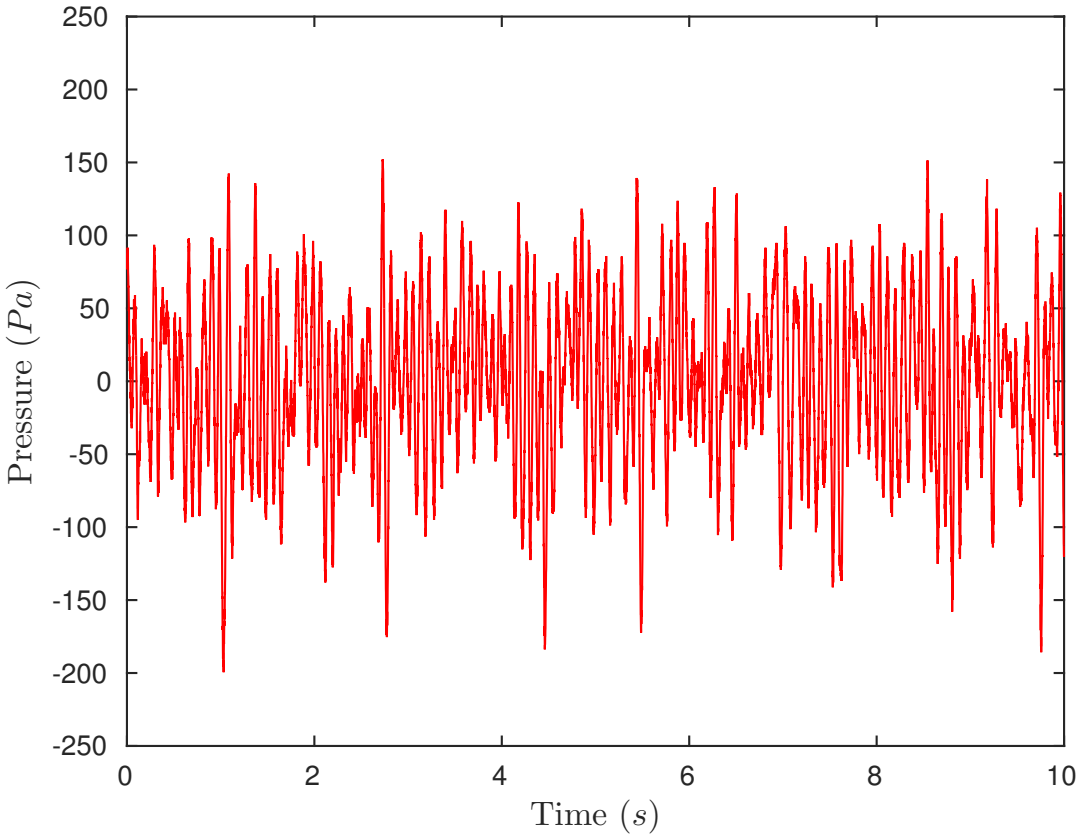

Figure 11: Pressure signal as captured by the pressure transducer at $Re_D = 5600$

Re_D	5600	10900	15500
$U_{bulk}(m/s)$	0.734 $\pm$2%	1.44 $\pm$3%	2.04 $\pm$5%
Re_{Dnc}	5800	11300	16100
f_{FT}	12.5 $\pm$1	25 $\pm$1	35 $\pm$2
St_{cp}	0.136 $\pm$0.01	0.139 $\pm$0.005	0.138 $\pm$0.008
St_{nccp}	0.131 $\pm$0.01	0.133 $\pm$0.005	0.132 $\pm$0.008
$St_{Okajima}$	0.129	0.134	0.134

Table 1: Periodic shedding behaviour at three different bulk velocities

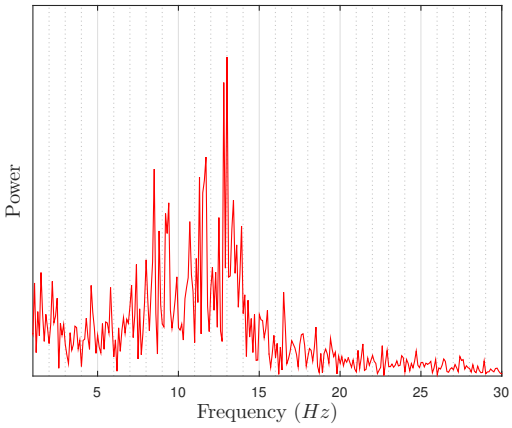

(a) Run 1

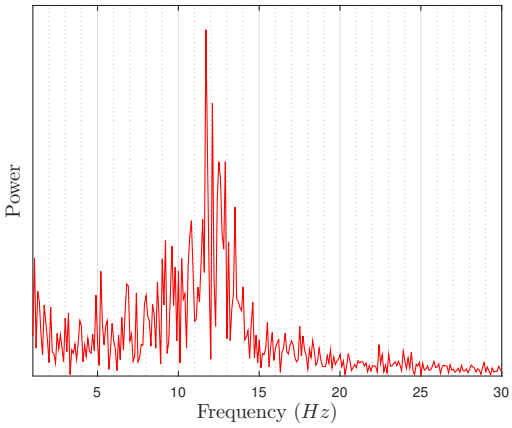

(b) Run 2

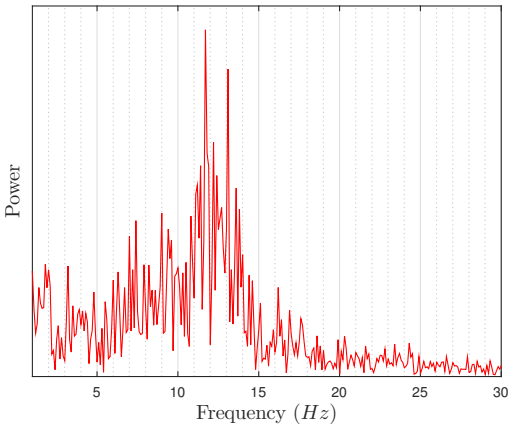

(c) Run 3

Figure 12: Discrete Fourier Transform of the fluctuating pressure signal at $Re_D = 5600$, $U_b = 0.734m/s$, $Re_{Dnc} = 5800$, three separate runs each of $10s$ capture time

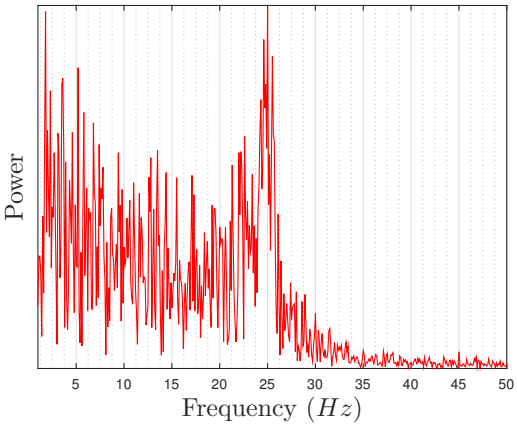

(a) Run 1, capture time $10s$

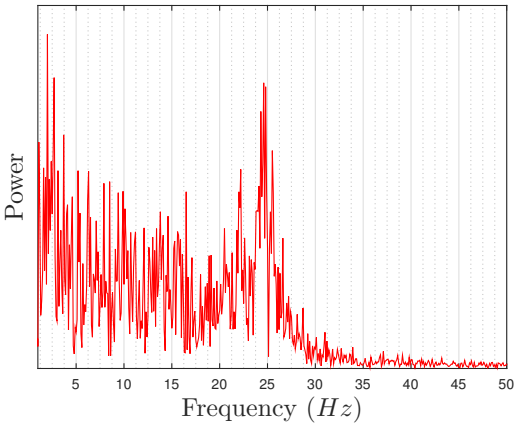

(b) Run 2, capture time $10s$

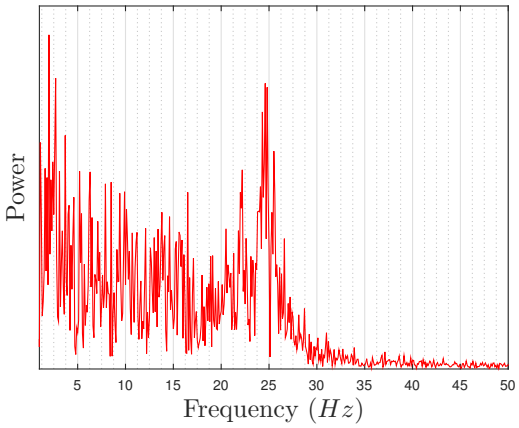

(c) Run 3, capture time $10s$

Figure 13: Discrete Fourier Transform of the fluctuating pressure signal at $Re_D = 10900$, $U_b = 1.44m/s$, $Re_{Dnc} = 11400$, three separate runs each of $10s$ capture time

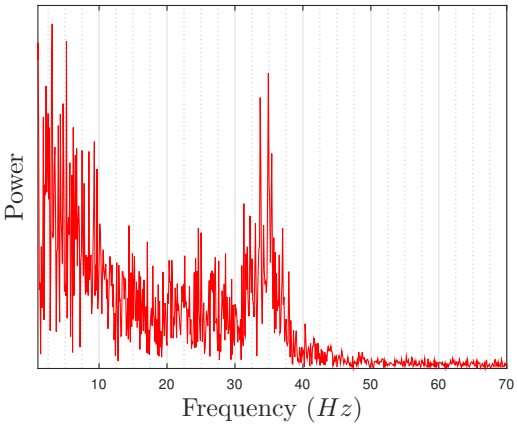

(a) Run 1

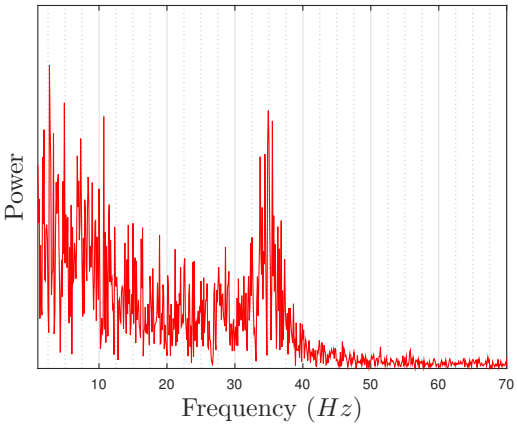

(b) Run 2

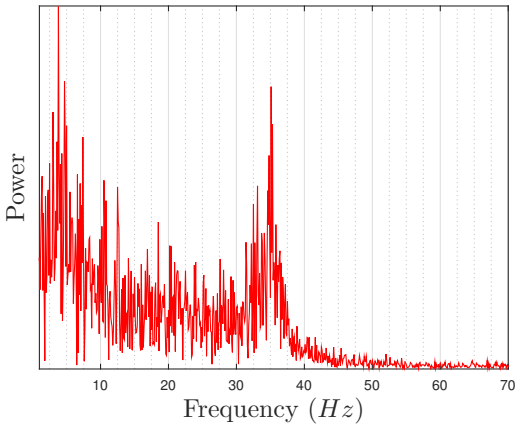

(c) Run 3

Figure 14: Discrete Fourier Transform of the fluctuating pressure signal at $Re_D = 15500$, $U_b = 2.04m/s$, $Re_{Dnc} = 16100$, three separate runs each of $10s$ capture time

Comparisons of the Strouhal number for each Reynolds number were made using data from a study of flow around a long square cylinder reported by [54], also placed in Table 1. A piecewise-cubic spline method was used to interpolate between the data to draw better equivalence between the two sets. The Strouhal numbers calculated with the channel bulk velocity are denoted St_{cp} and the numbers calculated with the bulk flow through the slightly constricted section past the cube are denoted St_{nccp}. The slight modification in velocity required to account for flow constriction within the channel as the flow passes the cube made only a small difference to the Strouhal number. However, the multiplication by 25/24 made the result approach that in the quoted study. In conclusion, all Strouhal numbers calculated from the current data are similar to those expected in [54], and match within the margins of error. In [54], a very slight increase in Strouhal number with increasing Re_D number was observed over the range of Reynolds number in question, but the size of the error margins in the data makes it impossible to draw conclusions on whether or not this was the case with the preliminary experiments described above.

3.3.2 Constant Period Method

Taking the frequency obtained from the DFT as a starting point, it is possible to perform a phase-averaging on the data in order to estimate the amplitude of the periodic component of the shedding. Two different methods were applied in order to do this. The simplest method of phase-averaging began with separating the entire continuous signal into a number N_p of periods of equal length T_p, which were timestamped, and which corresponded to the period of the primary oscillations. Following this, each period was further separated into a number N_ϕ of sub-divisions, or "phase-bins" of equal length, which were also timestamped. All data points were then sorted into the appropriate phase-bin among the $N_p \times N_\phi$, according to their capture time relative to these threshold times. A mean, or ensemble average, was taken across the N_p periods for each phase-bin. Denoting the phase by ϕ, the initial time by t_0, and the period number by n_p, the phase-averaged pressure at a given phase ϕ may be expressed as:

$$\overline{p(t_0 + \phi + 2n_p\pi)} = \overline{p_\phi} = \frac{1}{N_p} \sum_{n_p=1}^{N_p} p(t_0 + \phi + 2n_p\pi) \tag{1}$$

where the bar signifies an arithmetic mean, in this case, the phase-average. In some of what follows, this will be referred to as the "phase-averaged" pressure. As it is presented in Equation 1, ϕ could represent an exact phase, but in the analysis described it represents one of the finite number of discrete bins of finite width. In the limiting case, each individual phase-bin may in practice only include one sample per cycle, and represent as precise a phase as is possible. At a limiting N_p, the phase-average is therefore calculated by taking one sample per bin per period. This threshold is identified here by:

$$N_{thresh} = T_p f_s \tag{2}$$

where f_s is the sampling frequency. f_s was equal to $2kHz$ in the experiments on which this "Constant Period" analysis was done such that in the cases of the three experiments, N_{thresh} was approximately 169, 80 and 57 at Re_D =5600, 10900 and 15500. Some results are presented with the arithmetic mean across the N_ϕ phase-averages subtracted. This mean may be written as

$$1/N_\phi \sum_{n_\phi=1}^{N_\phi} \overline{p_\phi} \tag{3}$$

where each of the N_ϕ phase-averages is identified by an n_ϕ number. This average of the separate phase-averages is not equivalent to the time-averaged mean, and is used only for the purpose of making the amplitude of the phase-averaged pressure more readily identifiable in the data presented.

A plot of the ensemble averages may be made, using the phases of the bins as the independent variable. The size of the spread in the phase-averages may be represented by the peak-trough amplitude of the phase-average plot, denoted by $A_{p\phi}$. It is worth noting that for a number of phase bins lower than N_{thresh}, (Equation 2), the amplitude calculated is expected to be slightly lower than for the case $N_{phi} = N_{thresh}$ due to averaging across the bin width, a phenomenon known as "phase-blurring". For each analysis, an increasing number of phase-bins was used until this phase-blurring became unnoticeable. However, in real unsteady flows the Constant Period method may have severe limitations. Such a method is highly sensitive to frequency or phase change, such that a small error in the prediction of the primary period or a small discontinuity in the periodic phenomenon will yield results that appear anomalous in so much as they fail to adequately represent the

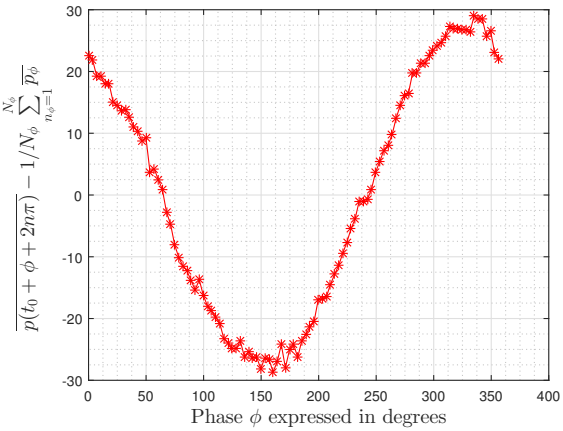

(a) Phase-averaging at $34.6Hz$

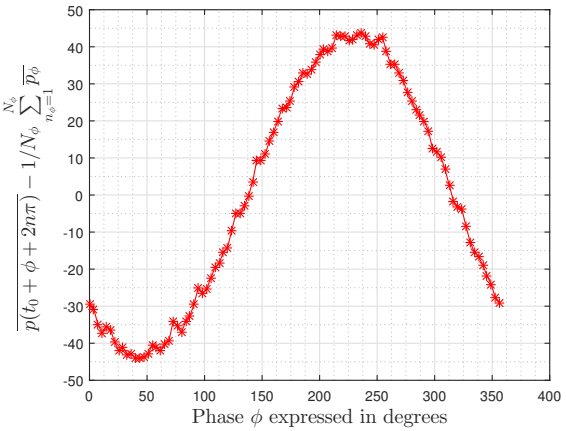

(b) Phase-averaging at $35.1Hz$

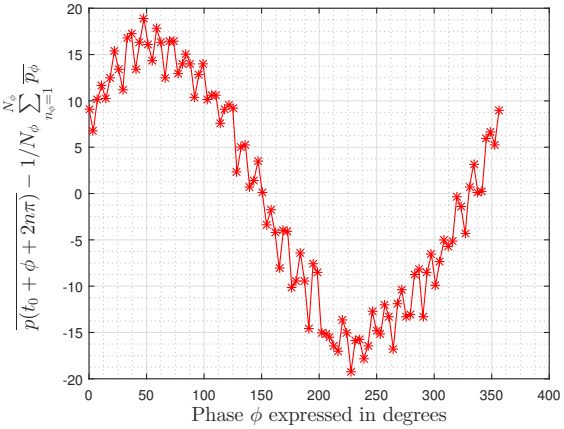

(c) Phase-averaging at $35.6Hz$

Figure 15: Ensemble-averages of the captured pressure signal using periods defined by three different guess frequencies, $Re_D = 15500$

size of the fluctuations. This phenomenon may be used to an advantage in some respect. A simple trial and error process will allow the establishment of a more precise average period by searching for the period that yields the highest amplitude, under the condition that the plot looks "clean", for example Figure 15, where a slight change in frequency either side of $35.1Hz$ results in a less clear phase-averaged pressure plot. The starting point for the period determined by this trial and error process was taken to be the inverse of the peak frequency returned by a DFT of the data. The estimated frequency that was eventually found following this "Constant Period" method will be denoted by f_{cp} from here onwards.

Another advantage of this form of analysis is that it allows for an estimate of the amplitude of the organised fluctuations simply by inspecting a plot of the ensemble averages in much the same way as one might read from a graph of any roughly sinusoidal function, see for example Figure 16, such as those which are typically produced by URANS simu-

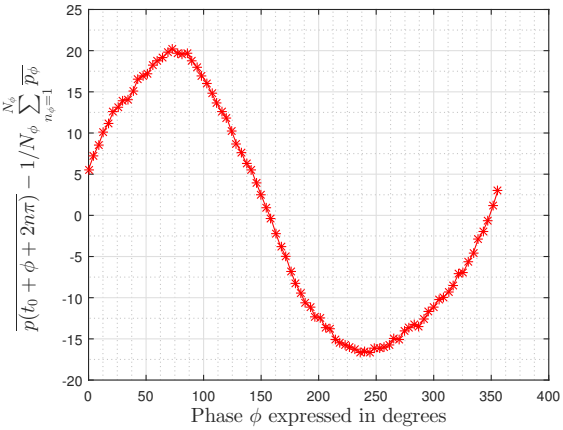

(a) $Re_D = 5600$

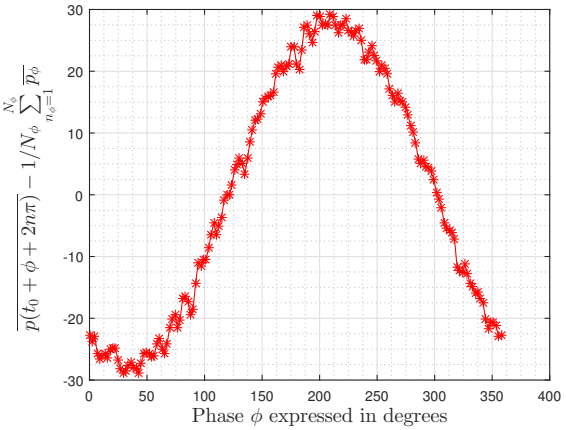

(b) $Re_D = 10900$

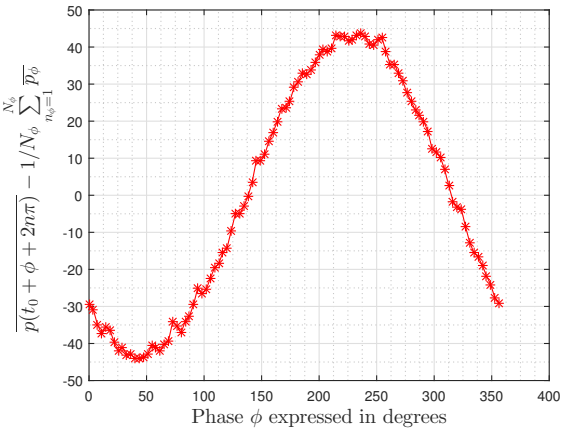

(c) $Re_D = 15500$

Figure 16: Phase-averaging of the captured pressure signal at three separate Re_D numbers

Re_D	5600	10900	15500
$U_{bulk}(m/s)$	0.734 ±2%	1.44 ±3%	2.04 ±5%
$f_{cp}(Hz)$	11.8 ±0.2	24.9 ±0.1	35.1 ±0.5
St_{cp}	0.129 ±2%	0.14 ±3%	0.138 ±5%
St_{nccp}	0.123 ±2%	0.138 ±3%	0.138 ±5%
Amplitude (Pa)	36 ±3	56 ±4	90 ±5

Table 2: Analysis of the Periodic shedding behaviour at three different bulk velocities using the constant period method

lations. Results shown were selected to show the cleanest phase-average plots extractable from the data sets using this method. Some otherwise similar test runs produced data from which such clean sinusoidal patterns of high amplitude could not be produced, and results for these are not included here. In the light of longer test runs, as will be described below, this inconsistency appears to be due to low-frequency changes in pressure that were not captured within the short experimental time. The results of this analysis are summarised in Table 2.

The results for Strouhal number presented in Table 2 appear to show a trend consistent with that in the preliminary tests and with the data - there is a slight increase in Strouhal number between the lowest Reynolds number and the higher two, where it levels off. However, the calculated value of Strouhal number is lower at the lowest Reynolds number than that in [54] and that taken straight from the peak in the Fourier Transform in Table 1. At the highest Reynolds number, the Strouhal number is higher than that shown in [54] and in Table 1. As the study [54] was conducted with a long cylinder, it is not necessarily to be expected that the results would match perfectly. What is more, the degree of arbitrariness that is inherent in the Constant Period method analysis may have been responsible for a small error that would be impossible to estimate. The flow exiting the channel appeared to maintain a steady rate, but it is important to reiterate that measurement of the instantaneous channel bulk flow rate was not possible. In fact, a mean flow rate was used, the measurement of which took a few minutes. Due to the error in the measurement of volume in each bucket several measurements were required, each of which took roughly 30 seconds. It was therefore not possible to quantify accurately the steadiness of the flow rate over smaller periods of time. Apparent limitations in the "Constant Period" phase-averaging technique used suggested that the flow rate may be changing slightly, or that small phase changes may have occurred in the shedding. An

unsteady free surface in the overhead reservoir is one possible cause of small pressure fluctuations. Observation of the water level during operation suggests that it was constant to within $1mm$ in general, equivalent to $\sim 10Pa$, but small splashes and unevenness in the free surface due to impingement of the flow from the replenishment pump against the inner reservoir wall may be responsible for slightly higher pressure fluctuations of a few 10s of Pa. For reference, at $Re_D = 5600$, the pressure drop in the unblocked channel may be estimated at $\sim 420Pa$, using the correlation-based equation given in [14]. This calculation suggests that a change of $10Pa$ to a new steady channel pressure-drop would correspond to a change in bulk flow rate of only $\sim 1.3\%$, and at higher flow rates the relative change in bulk flow rate would be lower still. Fluctuating pressure changes of this size would not be sufficient to accelerate the flow very quickly, a simple force balance suggests they would result in an acceleration of the fluid in the channel of less than $0.01m/s^2$. As a result, these pressure fluctuations are not likely to have caused a significant shift in bulk velocity, or consequently in shedding frequency. If other uncontrolled pressure fluctuations did occur that were larger than this, for example due to slug flow in the main flow pipe, the flow rate may have been modified. Overall, the magnitudes of the phase-averaged fluctuations were small compared to those of the URANS simulations; this will be further discussed in Section 4. The sinusoidal type forms appeared quite messy in general; despite many shedding periods of data being recorded, results were not consistent. It is considered likely that the lower frequency pressure fluctuations, manifest in the spectra shown in Figures 13 and 14, were responsible for changes in the flow rate. As a result, they may have affected the shedding period. In order to fairly represent these lower frequency fluctuations, much longer experiment times would be needed to capture an adequate number of cycles.

3.3.3 Variable Period Method

The second method used for estimation of the primary shedding frequency was designed to allow for the possibility of a slight variation of flow rate and hence shedding period from cycle to cycle, and is similar to that used by [45]. The process of data treatment requires several steps:

- Read raw data

- Identify dominant frequencies present using FFT
- Identify range of frequencies associated with periodic shedding
- Create filter isolating these frequency components only
- Reconstruct filtered signal from selected range of components
- Find peaks in filtered signal
- Phase-average raw data according to peaks

This method was able to adjust for the effects of any small changes in bulk flow rate as a range of frequencies could be used to represent the shedding rather than a single frequency. As before, the calculation of the Discrete Fourier Transform using a Fast Fourier Transform (FFT) algorithm was carried out using MATLAB. Data was collected using Cube 2, captured simultaneously with the PIV data. As the flow rates were adjusted more carefully, the Reynolds numbers were Re_D = 5600,10400 and 15600 with error margins of ±2%, ±4% and ±4% respectively. Simple application of the FFT algorithm to the raw signal resulted in a spectrum with many peaks, and the frequency resolution of $5 \times 10^{-5} Hz$ was far higher than needed due to the large sample size. This was probably due to slower fluctuations that were not captured over the shorter experimentation times of the preliminary tests.

3.3.4 Windowing Function

In order to maximise statistical convergence with the available data, the "Method of Overlapping Segments" was applied. This consists of dividing the discretised signal into overlapping sections, for which the individual power spectra are calculated, before performing a mean average of the individual segments to produce one single spectrum. Two different methods were used to calculate the FFT, characterised by a "Boxcar" and a "Hanning" window function in the time domain. The Boxcar type function corresponds to the simple application of an FFT to an entire recorded signal, whereas the Hann method requires the application of a smoothing function to the data before the FFT. The Hann function that was used is alternatively known as the "Raised-Cosine" function in some literature, and is that described in [55]. It is known that the simpler Boxcar method

results in "frequency leakage". Within the power spectrum, this manifests itself as power apparent at frequencies that do not exist in the original input waveform, and as such is an undesirable non-physical phenomena associated purely with the analysis. In order to minimise frequency leakage, each of the individual segments had a Hann windowing function applied to it before calculation of the FFT. In order to calculate the number of samples to place within each segment, it was first necessary to decide on a desired frequency resolution Δf_{sreq}. This was initially chosen to be around $0.3Hz$. Estimation of the required number of samples N_{sreq} for each segment followed from this desired frequency resolution, and the closest number of of the type $N_s = 2^n$ was selected to give N_{sreq} before the signal was split up and the window function applied. The sample time required for a resolution of Δf_{sreq} with a Hann type window function was calculated from:

$$T_{sreq} = \frac{4}{\Delta f_{sreq}} \tag{4}$$

As the FFT algorithms work best with sample numbers of the type $N_s = 2^n$, 262,144 samples were used as a starting point, corresponding to a window length of $T_{sreq} = 13.1s$ and an estimated frequency bandwidth of $\Delta f_{sreq} = 0.305Hz$. This same analysis was applied with higher and lower frequency bandwidths, keeping N_{sreq} of the form $N_s = 2^n$, with estimated Δf_{sreq} ranging from 0.15 to 1.2 Hz. Graphs of the power spectrum were plotted side by side to observe any changes in Figures 17, 18 and 19. At this stage of the analysis, relative peak heights are sufficient to provide the necessary information; the frequency at which the peak heights occur, the breadth of the peak clusters and their relative heights are important to the filter design process. For this reason, the power axis is presented as a linear scale with no values. Results are presented from the pressure signals that were recorded simultaneously along with the PIV data. The bulk flow velocities were measured to be $0.716m/s \pm 2\%$, $1.32m/s \pm 2\%$ and $2.07m/s \pm 4\%$, matching the three target Re_D numbers of 5600, 10400 and 15600 respectively within the quoted error margins.

Results showed that mitigating frequency leakage did not appear to significantly change the breadth of the peaks. In each case, the lower frequency peak was higher than the higher frequency one. With increasing Reynolds number, this effect was prominent such that at the highest Reynolds number the low frequency peak was ~ 3 times the

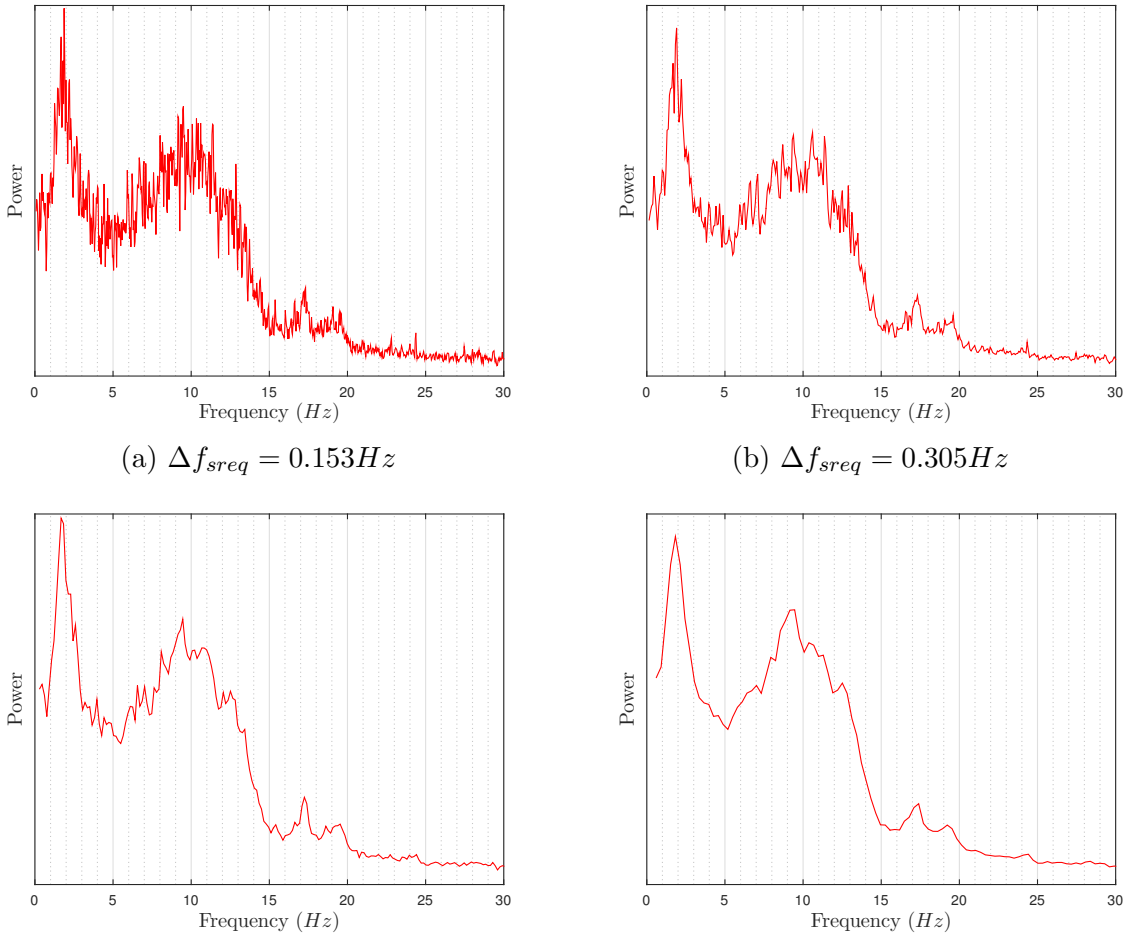

(a) $\Delta f_{sreq} = 0.153Hz$

(b) $\Delta f_{sreq} = 0.305Hz$

(c) $\Delta f_{sreq} = 0.610Hz$

(d) $\Delta f_{sreq} = 1.22Hz$

Figure 17: Spectra produced by the method of overlapping segments, with increasing frequency bandwidth estimates, $Re_D = 5600$

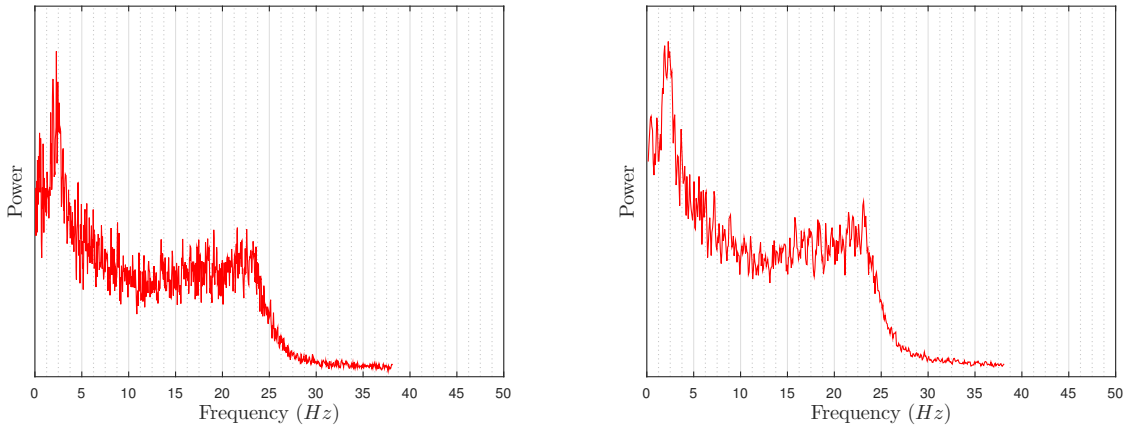

(a) $\Delta f_{sreq} = 0.153Hz$ (b) $\Delta f_{sreq} = 0.305Hz$

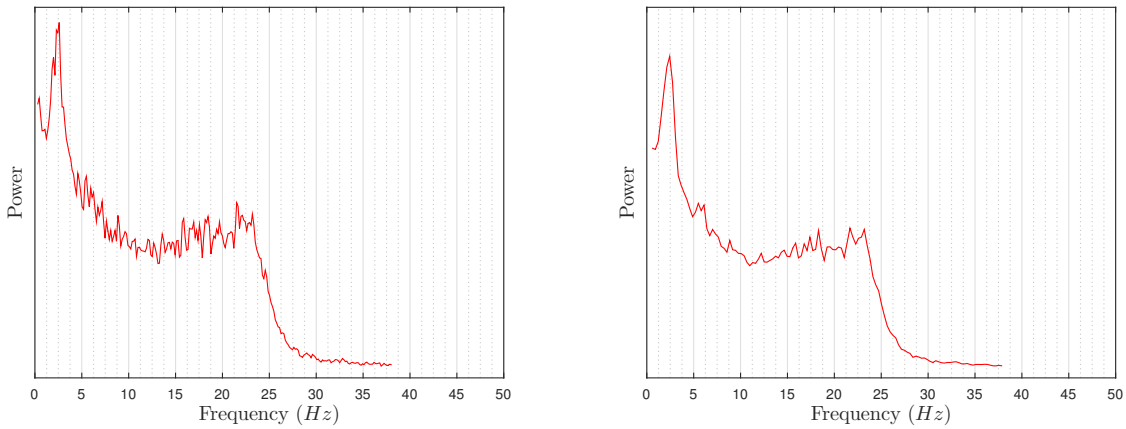

(c) $\Delta f_{sreq} = 0.610Hz$ (d) $\Delta f_{sreq} = 1.22Hz$

Figure 18: Spectra produced by the method of overlapping segments, with increasing frequency bandwidth estimates, $Re_D = 10400$

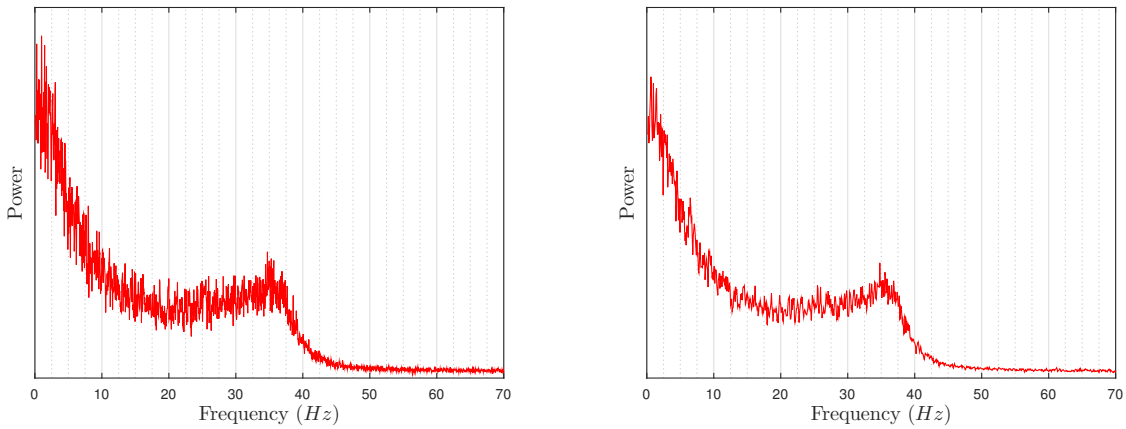

(a) $\Delta f_{sreq} = 0.153Hz$

(b) $\Delta f_{sreq} = 0.305Hz$

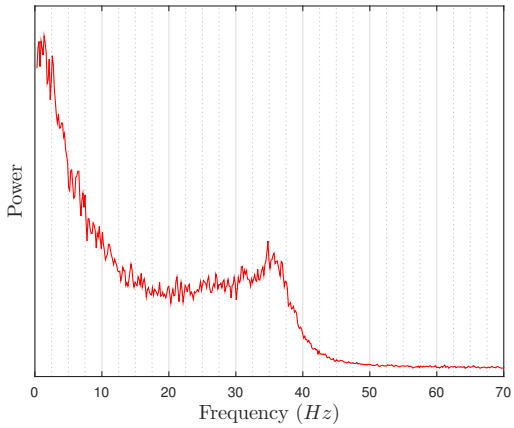

(c) $\Delta f_{sreq} = 0.610Hz$

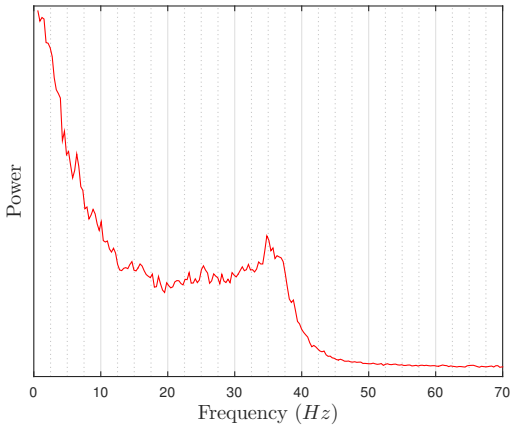

(d) $\Delta f_{sreq} = 1.22Hz$

Figure 19: Spectra produced by the method of overlapping segments, with increasing frequency bandwidth estimates, $Re_D = 15600$

Re_D	5600	10400	15600
U_{bulk}	0.716 ±2%	1.32 ±4%	2.07 ±4%
Re_{Dnc}	5800	10800	16300
f_{FT}	9.5 ±5%	23 ±2%	35 ±1%
St_D	0.106 ±5%	0.139 ±4%	0.135 ±4%
St_{nc}	0.102 ±5%	0.134 ±4%	0.130 ±4%
$St_{Okajima}$	0.129	0.134	0.134

Table 3: Periodic shedding behaviour at three different bulk velocities, picking only the second highest peak after Hann windowing analysis

magnitude of that at the higher frequency, whereas at $Re_D = 5600$ it was only ~ 3 times larger. For all three Re_D, the low frequency peak appeared around the same frequency of $\sim 2Hz$, whereas the higher frequency peak scaled roughly linearly with Reynolds number, and hence U_b. For shedding at the higher frequency peak, the Strouhal number behaviours as a function of Reynolds number are summed up in Table 3. The origin of these lower frequency peaks is unknown.

3.3.5 Filter Design

Bandpass filters were designed to only allow through frequencies around the peak associated with the periodic shedding near the Strouhal number frequency, (the higher of the two peaks), while filtering out the large lower frequency fluctuations. A "Butterworth" type bandpass filter of order 2 was used first of all, (see Figure 20 for an illustration of the frequency response of the filter). This filter was applied to the raw signal to reconstruct a filtered signal only from the retained components. Such a filter is associated with a phase shift in the reconstructed signal; it was visually evident that some of the peaks in the filtered signal appeared to be shifted relative to the peaks in the raw signal. In an attempt to improve upon this, a "zero-phase" filtering technique was used based on the original Butterworth filter. In order to remove phase-shift, the signal is first filtered as before, then the filtered sequence is reversed and filtered again. The effect of this was that the positions of the peaks in the signal filtered using the zero-phase technique appear to match the original signal better than those of the original Butterworth filter, (Figures 21a 20).

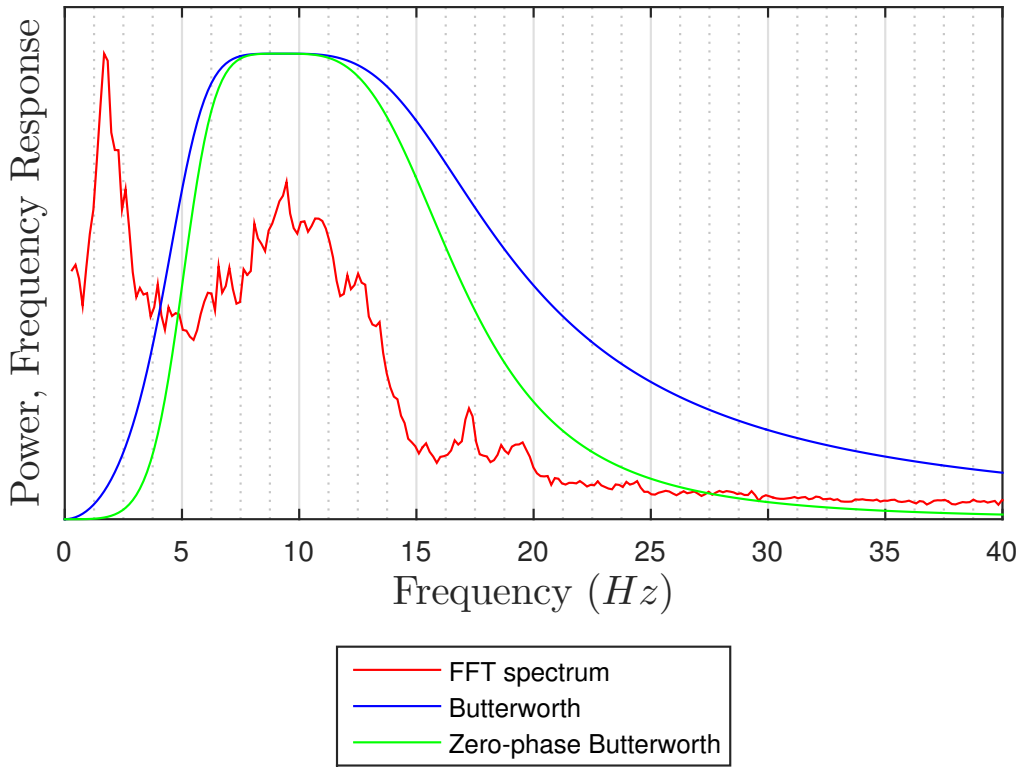

Figure 20: FFT power spectrum and Filter frequency response overlaid to illustrate properties of the bandpass filters, $Re_D = 5600$

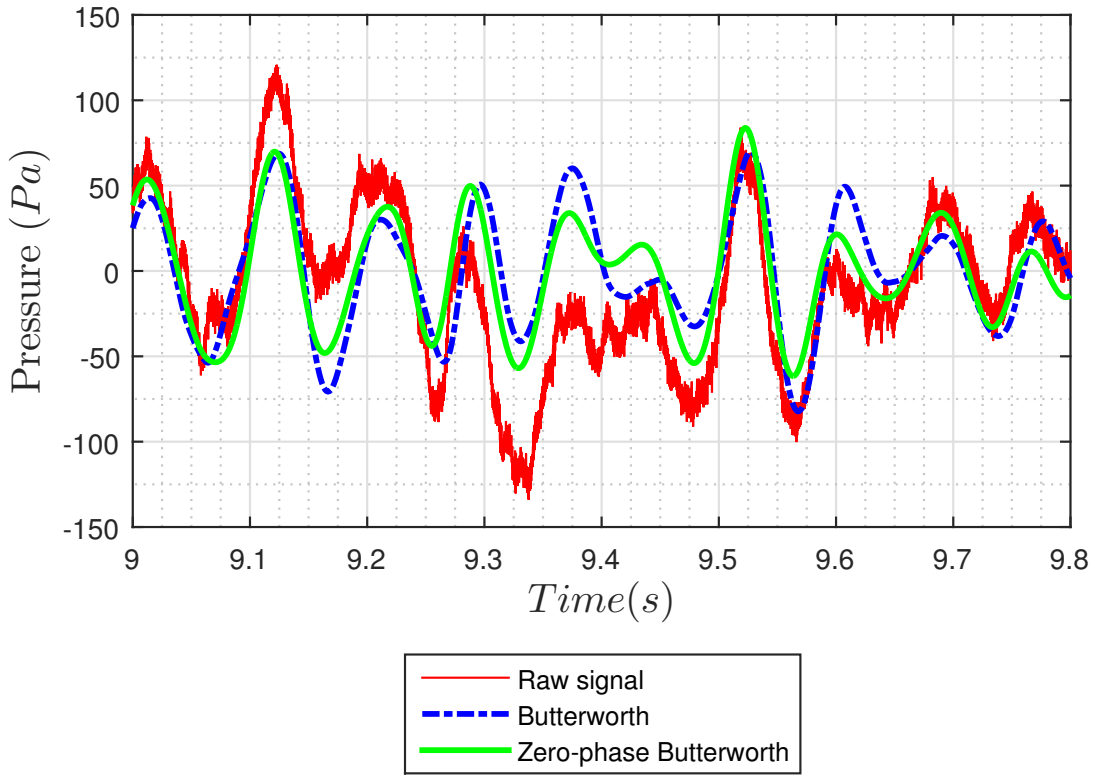

(a) Effect on filtered signal of two different filtering methods

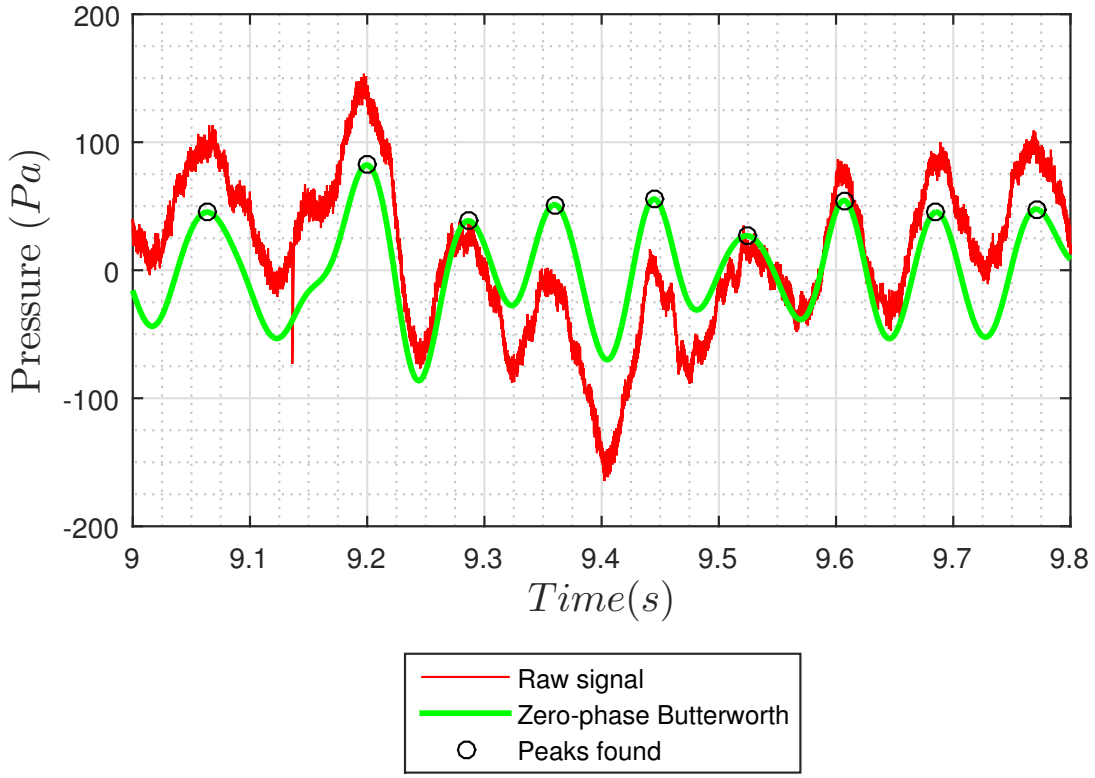

(b) Peaks found from filtered signal relative to raw signal

Figure 21: Typical segments of raw and filtered signal illustrating the phase-identification process, $Re_D = 5600$

3.3.6 Period Identification

A peak finding algorithm was employed to find the peaks of each local period in the filtered signal, which were time-stamped, see Figure 21b. These time-stamps are referred to as "peak times". The periods between the peak times were calculated and the standard deviations of these period lengths were also calculated in order to provide an estimate for the error on this mean period. Using this method, the mean period lengths were $0.0910s \pm 0.0213$, $0.045s \pm 0.0077$ and $0.0282s \pm 0.0028$ at $Re_D = 5600$, $Re_D = 10400$ and $Re_D = 15600$ respectively. In order to provide a second estimate, the peaks of the inverted signal were time-stamped using the same algorithm, which are referred to as "trough times" from here onwards. Calculating the local time periods based on the trough times resulted in the same mean period length and standard deviations for all three datasets. A third method consisted of taking an average of each period length from the peak times and its corresponding nearest period length from the trough times, with the standard deviation calculated from the averaged period length set. There was still no change in the first three significant figures for the mean period using this third method, although the standard deviation was reduced slightly. The mean periods with these smaller standard deviations are summarised in Table 4, where the error is quoted as being $\pm$ half the standard deviation. Strouhal numbers are also presented based on these mean period lengths. Histograms showing the spread in period length are presented in Figure 22, which give a description of the final period lengths identified after the filtering process. The histograms are broader at the lower Reynolds numbers, suggesting a larger spread in period lengths, although the spectral peak was less easily identifiable at the higher flow rates. This is a consequence of the effect of the filtering, which was designed after an extensive trial and error process, and is not directly representative of the original pressure signal.

3.4 Particle Image Velocimetry

Particle Image Velocimetry, or PIV, is a well established tool used for capturing instantaneous velocity fields over a measurement region that may be 2D or 3D, unlike Laser Doppler Anemometry (LDA) which focusses on a very small point-like region. The particular variant of this technique that was implemented was "2D-2C" PIV, or two dimensional,

Re_D	5600	10400	15600
$U_{bulk}(m/s)$	0.722 ±1%	1.34 ±4%	2.01 ±4%
$T_{vp}(s)$	0.0910 ±0.0096	0.0463 ±0.00355	0.0280 ±0.0013
$f_{vp}(Hz)$	11.0 ±1.1	21.6 ±1.6	35.7 ±1.7
St_{vp}	0.122 ±0.012	0.123 ±0.0096	0.143 ±0.0068
St_{ncvp}	0.117 ±0.012	0.118 ±0.0096	0.137 ±0.0068

Table 4: Analysis of the Periodic shedding behaviour at three different bulk velocities using the variable period method

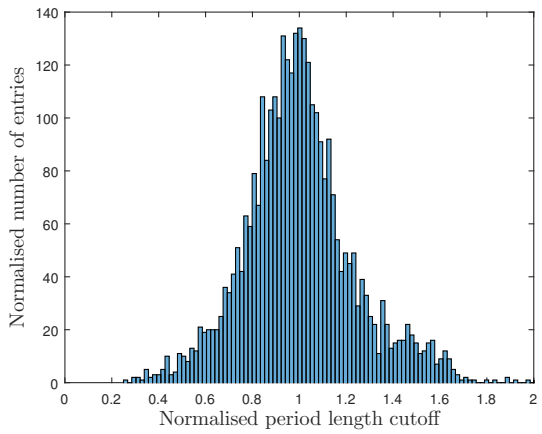

(a) $Re_D = 5600$

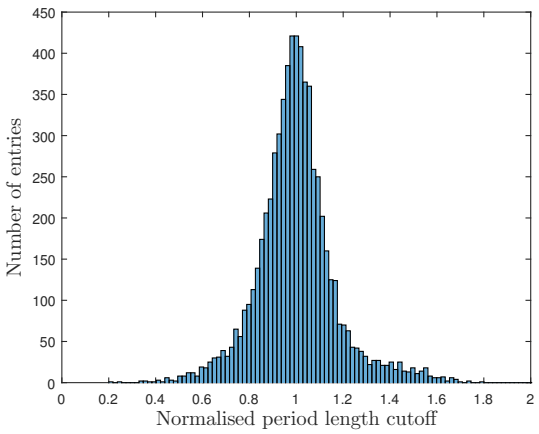

(b) $Re_D = 10400$

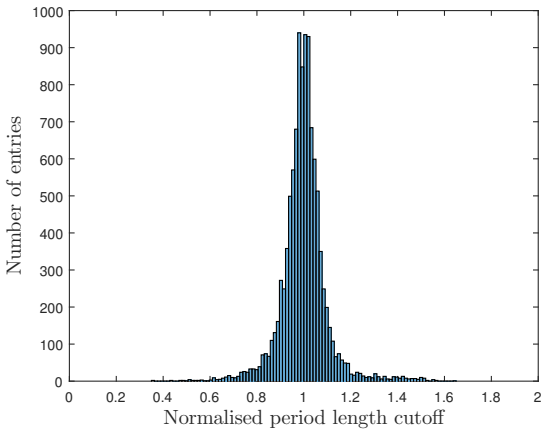

(c) $Re_D = 15600$

Figure 22: Histograms showing the spread in mean period length calculated using the Variable Period method at three Re_D numbers

two component PIV. Firstly, a two-dimensional field was illuminated by a flattened and diverged laser beam formed into a light sheet, which shone into the measurement field where it reflected from seeding particles. Secondly, a single CCD chip camera placed perpendicular to the light sheet enabled the capture of two frames in very quick succession. Next, an automated process of local velocity determination was performed by comparing the values of an auto-correlation function between the pairs of images. By determining the value of the auto-correlation function between small "interrogation windows" in the first image and many different interrogation windows in the second image, which are offset in different directions by different distances, the best match can be found. This corresponds to the flow direction, and the velocity magnitude depends on the shift. A good reference regarding this technique and its practical implementation may be found in [62], from which many of the following points are drawn. One of the first practical considerations to take into account is the alignment of the laser light plane. The positioning of the lenses and their focal lengths was chosen in such a way that the light sheet was as thin as possible when passing the cube. The shape, orientation and positioning of the light was determined just before entry to the perspex side pieces by observing through safety goggles its reflection from white card covered in a luminous marker fluid. The emergent light sheet from the other side could also be visualised in this way, allowing estimates of the error in thickness and positioning. It was estimated from this procedure that the position of the illuminated region in the cube vicinity was no more than $0.5mm$ away from the central plane in the z direction across the whole measurement area. In order to obtain measurements close to the cube, the light sheet encompassed the blockage itself. As a result, there were reflections from the cube, so it was not possible to obtain velocity readings in some areas close to it, see for example Figure 23. However, the matte black plastic finish to the cube greatly reduced the intensity of these reflections such that the area where velocity readings were not possible was quite small. Another important practical point to consider was the ability of the seeding particles to follow the flow in a natural manner, effectively acting like fluid particles. They should react to velocity gradients in the same manner in all directions. Their tendency to be convected along with the flow must far outweigh their tendency to sink or float. For spherical particles, a ratio between the force magnitudes from Stokes' drag law and the particle's buoyancy may be written

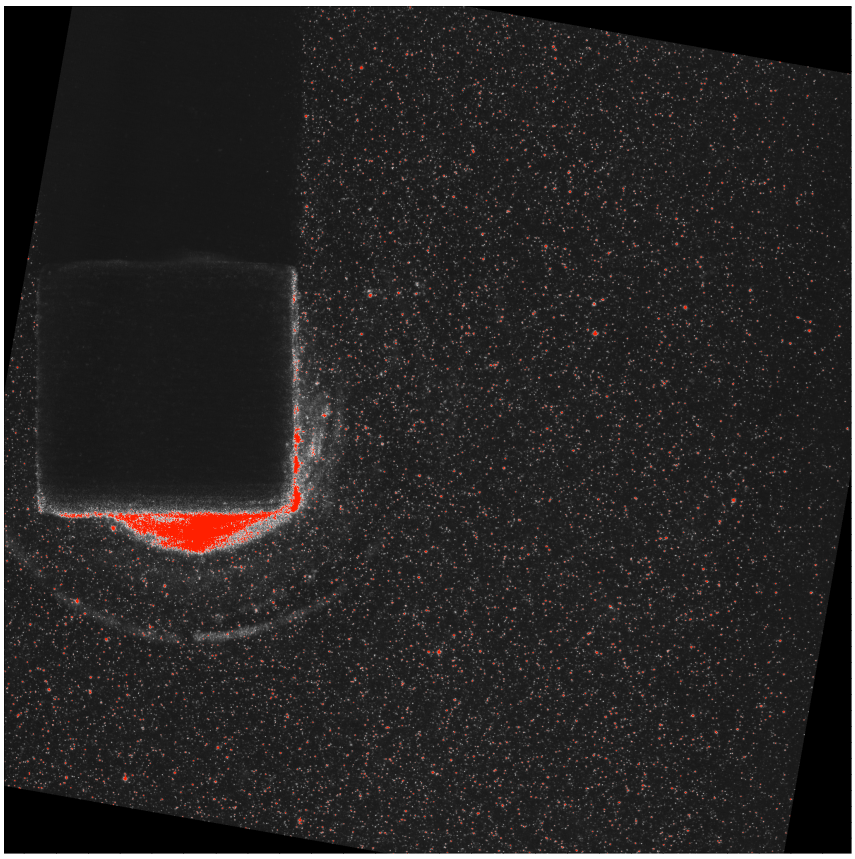

Figure 23: Single PIV image , encompassing cube and extending $3D$ downstream

as

$$\frac{|\mathbf{F_{drag}}|}{|\mathbf{F_{buoy}}|} = \frac{3}{2}\frac{\mu_f\,|\mathbf{U_p} - \mathbf{U_f}|}{(\rho_p - \rho_f)\,r^2\,|\mathbf{g}|} \tag{5}$$

where the subscripts p and f denote the particle and the fluid, and a ratio $\gg 1$ is desirable. Following [62], the velocity lag of a spherical particle in a continuously accelerating fluid may be given by

$$\mathbf{U_p} - \mathbf{U_f} = \frac{2}{9}r_p^2\frac{(\rho_p - \rho_f)}{\mu}\mathbf{a} \tag{6}$$

In the case of non-continuously accelerating particles, a characteristic time taken for particles to attain velocity equilibrium with the surrounding fluid is given by

$$\tau_{epf} = \frac{2}{9}r_p^2\frac{\rho_p}{\mu} \tag{7}$$

Taking into consideration these factors, the particles should be chosen such that $\rho_f \sim \rho_p$ and such that r is small. However, it is essential that enough light be scattered from the particles in order for their location to be captured by the camera, and this is a function of r. As the beam-particle-camera triplet forms an approximate right-angle, backscattering

is not as important as scattering at 90 deg. The direction of light scattering by a spherical glass particle in water at $\lambda = 532nm$ is summarised in Mie diffraction patterns shown in [62], suggesting that particle sizes larger than $10\mu m$ might be preferable at this viewing angle. In addition to this, scattering from the particles occurs in all directions, meaning that particles out of the laser plane may be sufficiently illuminated to register on the camera for a high density of seeding particles. With all these considerations in mind, the chosen seeding particles were hollow glass spheres of mean diameter $10\mu m$, with a size distribution of $2 - 20\mu m$. Initially, a single heaped teaspoon of seeding particles was added to the water in the main reservoir and allowed to mix around the circuit, driven by the pump. Individual PIV images were captured periodically in order to gauge by eye the suitability of the seeding density. A zoom function was used to view close-ups of small areas in the vicinity of the cube in order to ascertain that there was a large enough number of seeding particles to populate the images. The cube itself was visible in the images, so the location of it's corners was used to define the origin of the coordinate system, and it's side length was used to define the scale. In fact, it was the image of the upper cube face that was visible to the camera, rather than it's cross-section in the central plane. However, the error in side length introduced by this was calculated to be no more than $D/125$. The length covered by a pixel side was equivalent to $\sim 0.01mm$. Due to lack of sharpness of the cube image, which was very slightly out of focus, positioning of the cube could not be determined more accurately than to within ~ 8 pixels. Therefore, $\sim 8\mu m$ is the final estimate of the maximum error in vector placement for each map produced. This was considered to be more than adequate for the comparisons made, and much smaller than $0.5mm$, the estimated laser plane thickness. Optimisation of the time separation of the frames was carried out automatically by the PIV software (Davis 8 by LaVision) based on the average movement of the entire image by a fixed number of pixels. Processing of the raw PIV images was carried out using this same software, and is similar to that described in [72]. The first stage consisted of shift correction and rotation, removing the effects of vibrations in the rig, and rotating them so that the cube sides were parallel to the image window edges. Next, intensities of the images were normalised to ensure that any differences in intensity of the light produced by the two separate laser cavities were accounted for. A multi-level iterative method similar to that described in [25] was then applied, beginning with an interrogation window of 512×512 pixels, and ending with an

Re_D	5600	10400	15600
U_{bulk} (m/s)	0.722 ±1%	1.34 ±4%	2.01 ±4%
Minimum detectable pixel shift	0.04	0.04	0.04
Uncertainty in velocity (m/s)	0.006	0.011	0.016

Table 5: Estimated uncertainty in PIV measurements using integrated tool within software

8×8 window. A 50% overlap was used so that the auto-correlation process was applied also on a staggered grid, offset by 4 pixels. Post-processing consisted of multiple passes of a routine which improved the quality of the generated results by applying an adaptive filtering process; each of these passes included several stages. Firstly, vector calculations that are deemed to be unreliable due to having a low value of cross-correlation peak ratio are removed. Secondly, where calculated vector values are considerably different to the RMS values of those in the surrounding area, the vectors are assumed to be spurious and substituted for interpolated ones. Finally, a smoothing filter is applied. The multiple passes of the routine are conducted with increasingly stringent requirements on cross-correlation peak ratios and matches with the RMS values of the vectors in the surrounding area, which shrinks with the window size, following the basic methodology in [25]. The complexity of the routine makes it extremely difficult to keep track of error estimates, but an automated tool for error estimation is included in the Davis 8 package. The estimated uncertainties in the detectable shift between images are well below the size of a pixel. As a result, the estimated velocity uncertainties are only $\sim 0.8\%$ of the bulk velocities in each case (Table 5).

Re_D	5600	10400	15600
$U_b(m/s)$	0.722 ±1%	1.34 ±4%	2.01 ±4%
$A_{pt\phi}(Pa)$	84 ±4	108 ±4	156 ±4
$\frac{A_{pt\phi}}{\rho U_b^2}$	0.161	0.0603	0.0387

Table 6: Peak-trough amplitude of the phase-averaged pressure signal

4 Experimental Results

4.1 Phase-averaged Pressure

Once the period timestamps had been identified following the Variable Period Method (Section 3), they were used to define the separation of the pressure signal into phase-bins. Results are presented for the three different Reynolds numbers (Figures 24a, 24b and 24c).

There is an increase in magnitude of the phase-averaged pressure fluctuations with increasing Reynolds number (Table 6). In addition to this, a non-dimensionalised pressure amplitude is also presented using ρU_b^2. The amplitude of the this non-dimensionalised phase-averaged pressure decreases with increasing Reynolds number. These results characterise the average size of the pressure fluctuations that took place at frequencies near the dominant shedding frequency. It is worth recalling that the analysis process filtered out the large amplitude fluctuations at lower frequencies in order to define the period cut-offs, (Section 3). The phase-averaging took place on the original signal so these large fluctuations were not completely discarded, however, they may have simply been averaged out. As a result, the phase-averaged amplitudes are smaller than the largest fluctuations as read directly from the original signal.

4.2 Mean Velocity

The velocity at a point described by the vector $\mathbf{x}$ at the moment of a snapshot n_s is denoted by $\mathbf{u}(\mathbf{x}, n_s)$. As the measurement plane was 2D with a constant y value in the coordinate system used, the components of the vector $\mathbf{x}$ are denoted x and z. Velocity components were measured only in this plane and are denoted by u and w. The mean velocity field $\mathbf{U}(\mathbf{x})$, where the value at each point described by $\mathbf{x}$ is the arithmetic mean

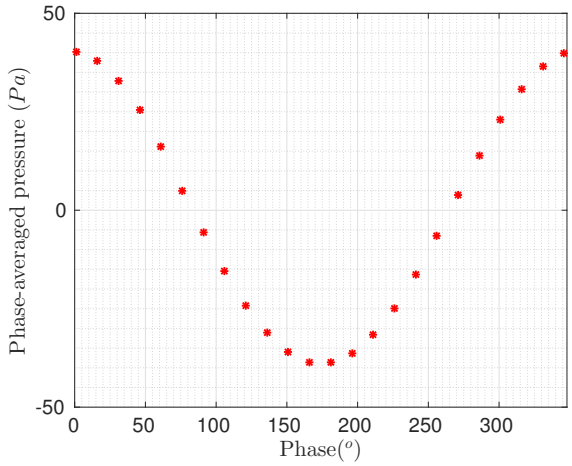

(a) $Re_D = 5600$

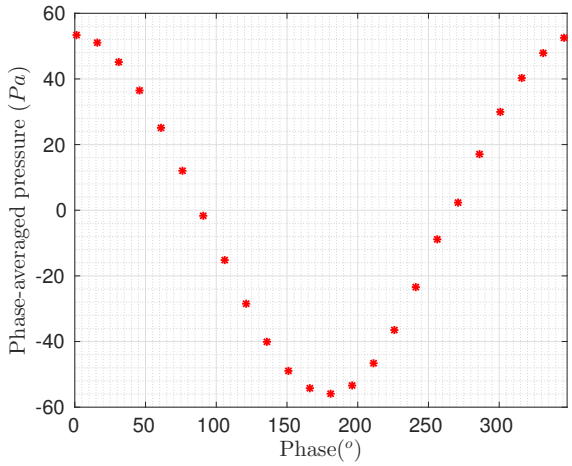

(b) $Re_D = 10400$

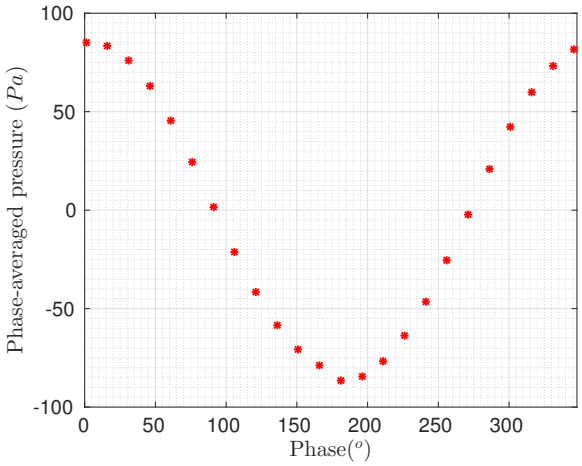

(c) $Re_D = 15600$

Figure 24: Phase-averages in Pa of pressure signal using variable period method, 24 phase bins

at that location across a number N_s of snapshots is denoted by:

$$\mathbf{U}_{N_s}(\mathbf{x}) = \frac{1}{N_s}\sum_{n_s=1}^{N_s}\mathbf{u}(\mathbf{x}, n_s) \tag{8}$$

where N_s is very large. Assuming that the mean flow is stationary over the experimentation time and that N_s is sufficiently high, $\mathbf{U}$ remains effectively constant with any further increase in number of snapshots. The required number N_s of snapshots is to be determined. In order to characterise the captured field of the velocity across all $\mathbf{x}$ between the limits x_1, x_2, z_1 and z_2 at any given snapshot n_s one may define:

$$I_{\mathbf{u}_{n_s}} = \frac{1}{(x_2 - x_1)(z_2 - z_1)}\int_{x_1}^{x_2}\int_{z_1}^{z_2}\sqrt{\mathbf{u}(\mathbf{x}, n_s) \bullet \mathbf{u}(\mathbf{x}, n_s)}\, dx\, dz \tag{9}$$

where the square root of the dot product is used to characterise the velocity at $\mathbf{x}$ using its magnitude. The velocity field was measured at a high number $N_x \times N_z$ of discrete points (x_{n_x}, z_{n_z}), so a good approximation to this integral may be written as

$$I_{\mathbf{u}_{n_s}} = \frac{1}{N_x \times N_z}\sum_{n_x=1}^{N_x}\sum_{n_x=1}^{N_z}\sqrt{\mathbf{u}(x_{n_x}, z_{n_z}, n_s) \bullet \mathbf{u}(x_{n_x}, z_{n_z}, n_s)} \tag{10}$$

In order to characterise the mean field of the velocity magnitude across all measured x and z points one may define

$$I_{\mathbf{U}_{N_s}} = \frac{1}{N_x \times N_z}\sum_{n_x=1}^{N_x}\sum_{n_x=1}^{N_z}\sqrt{\mathbf{U}(x_{n_x}, z_{n_z}) \bullet \mathbf{U}(x_{n_x}, z_{n_z})} \tag{11}$$

where the square root of the dot product is used to characterise the mean velocity at (x_{n_x}, z_{n_z}) using its magnitude. The frequency of firing of the laser pulse $f_{snap} = 4Hz$ was much lower than the shedding frequency $f_{shed} = O(10)Hz$, so two consecutive velocity fields were assumed to uncorrelated. However, it was considered that there may be an effect associated with the fact that the velocity measurements took place at a fixed frequency and that the shedding also took place at a roughly constant frequency. Although separated well in time a string of consecutive measurements may have a tendency to represent only certain phases of the shedding cycle for a low number N_s. In order to remove the effect of such a phenomenon and to therefore realistically characterise the decrease

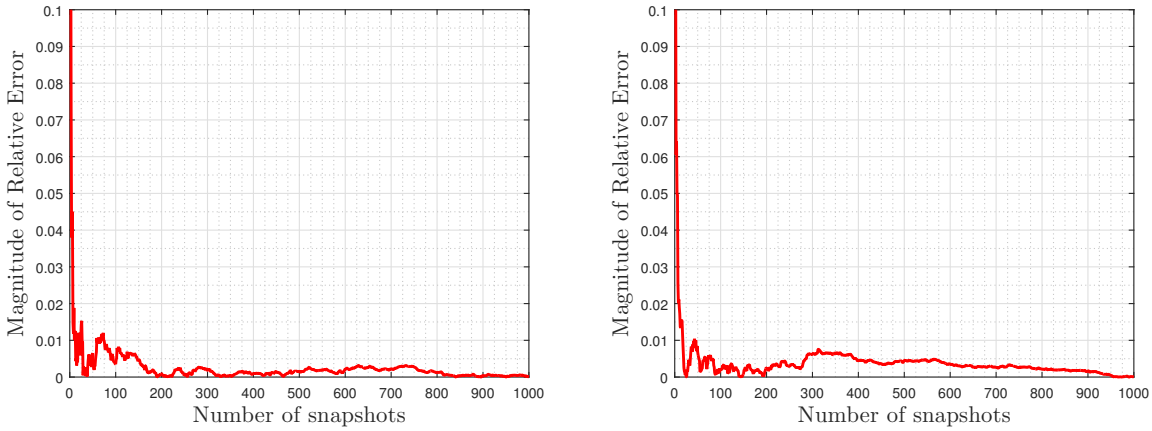

(a) Unmodified snapshot order

(b) Random snapshot order

Figure 25: Convergence of $I_{\mathbf{U}_{N_s}}$ - snapshots added in an unmodified order compared with a random order

in statistical error associated purely with an increase in the number of snapshots, the snapshots were selected in a random order. With each additional snapshot, $I_{\mathbf{U}_{N_s}}$ was calculated over the new N_s and the values recorded for $N_s = 1$ to $N_s = 1000$. For comparison, results were also produced using the same method but with snapshots selected sequentially in the order they were captured (Figure 25). The magnitude of the relative error in $I_{\mathbf{U}_{N_s}}$ as a function of the number of snapshots is presented in Figure 26. The results are similar across the three Reynolds numbers, that is to say that the value of $I_{\mathbf{U}_{N_s}}$ drops sharply within 100 snapshots. In all three cases the relative error in $I_{\mathbf{U}_{N_s}}$ dropped to $\sim 2\%$ within 50 snapshots. Within 100 snaphots, it had dropped to $\sim 1\%$. The slope had levelled of well before $N_s = 1000$, indicating that the number of captured snapshots was more than sufficient. Four different mean plots were calculated using an increasing number of randomly-selected snapshots (Figure 27). These show that a roughly symmetric mean field forms between $N_s = 12$ and $N_s = 100$. By using all 1000 snapshots in each case, a clearly symmetric mean field was generated for the experiments at each Reynolds number. These converged mean velocity fields are shown in Figure 28.

Defining the length of the recirculation region, L_r, as the distance from the rear of the cube to the point on the centreline where the mean velocity magnitude is equal to 0, we see a decrease with increasing Reynolds number (Table 7). The difference in L_r between the low and mid Reynolds numbers is $1.7mm$, and only $0.9mm$ between the mid and upper Reynolds numbers, suggesting a convergence towards a high Reynolds number asymptote, although with only three different Reynolds number datasets this is not well

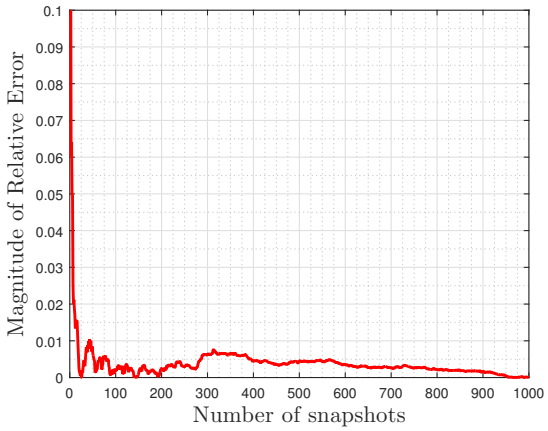

(a) $Re_D = 5600$

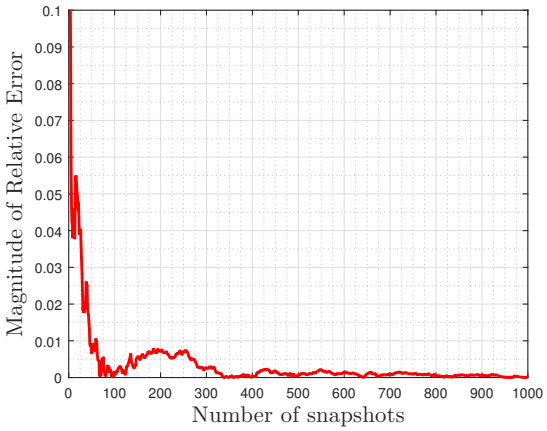

(b) $Re_D = 10400$

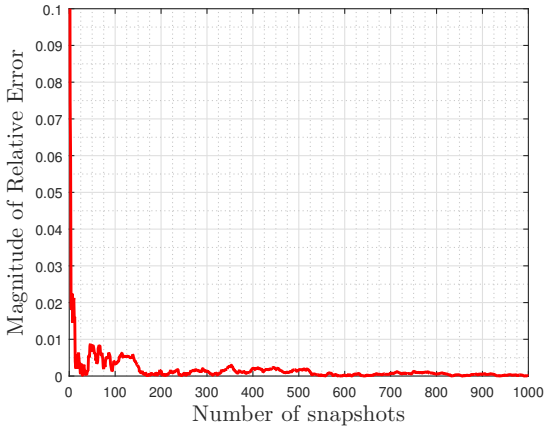

(c) $Re_D = 15600$

Figure 26: Magnitude of the relative error in the $I_{\mathbf{U}_{N_s}}$ integral for increasing N_s, characterising the convergence with number of snapshots of the mean velocity magnitude across the entire measurement domain.

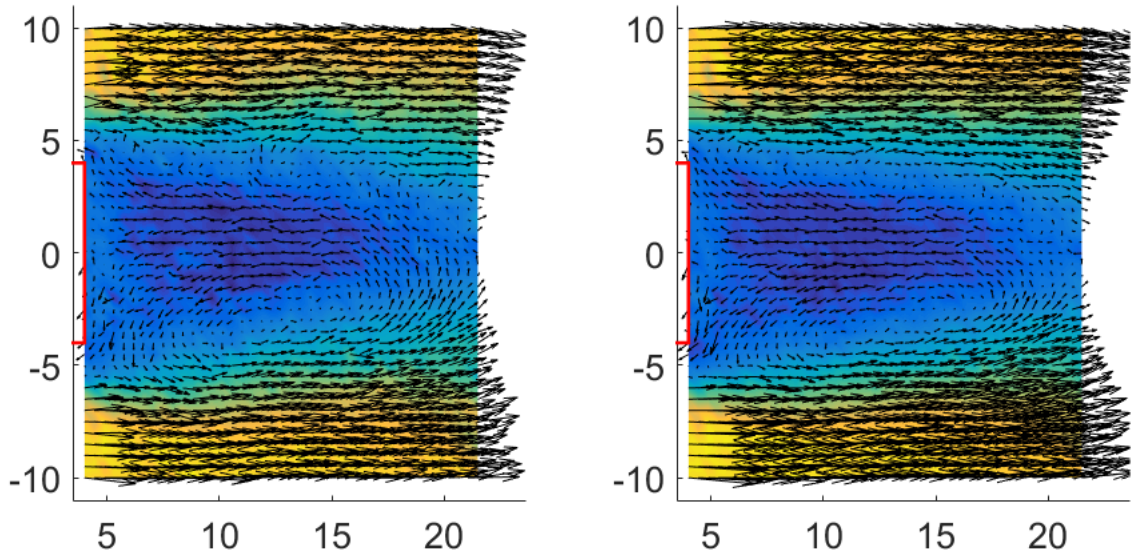

(a) $N_s = 12$

(b) $N_s = 25$

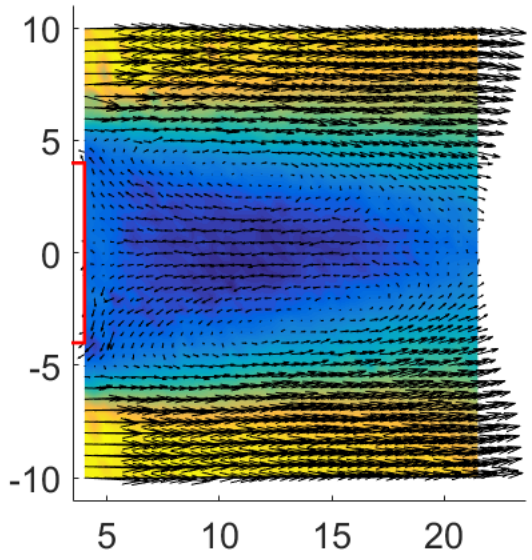

(c) $N_s = 50$

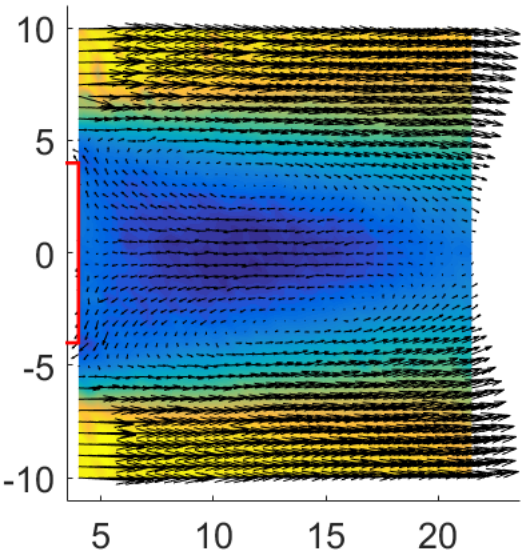

(d) $N_s = 100$

Figure 27: Mean velocity field calculated from an increasing number N_s of snapshots, $Re_D = 5600$

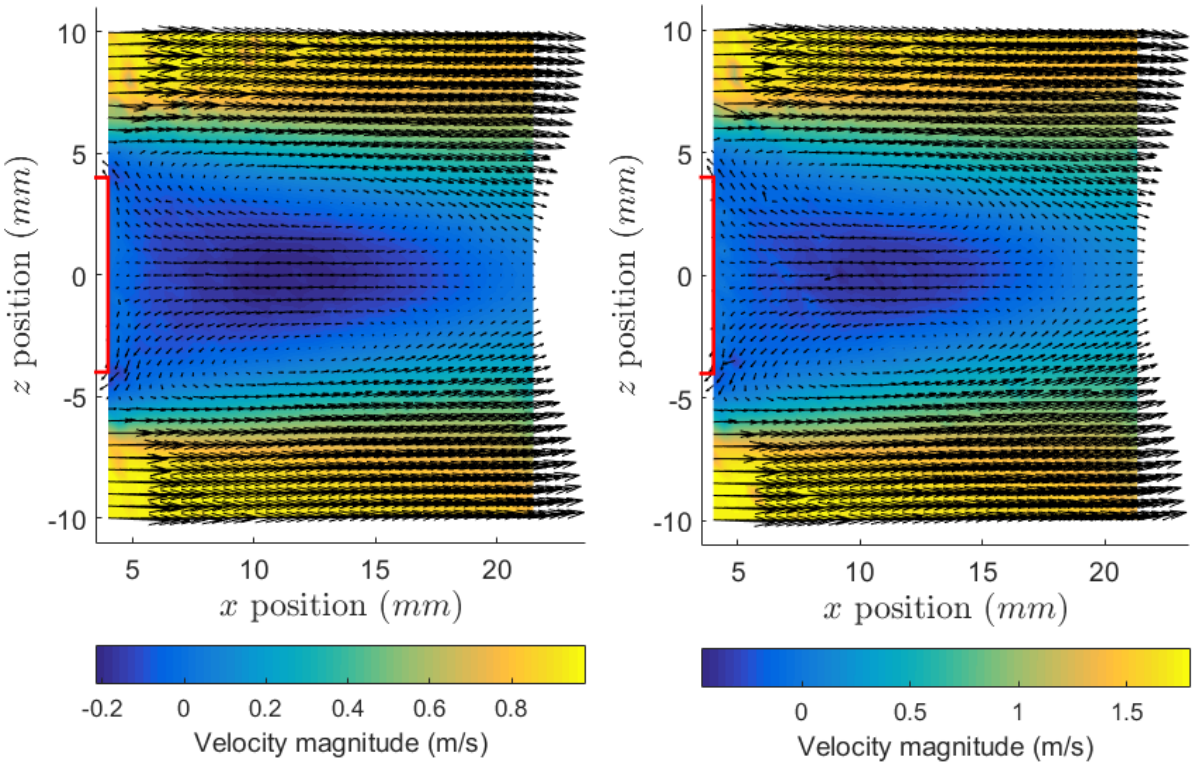

(a) $Re_D = 5600$

(b) $Re_D = 10400$

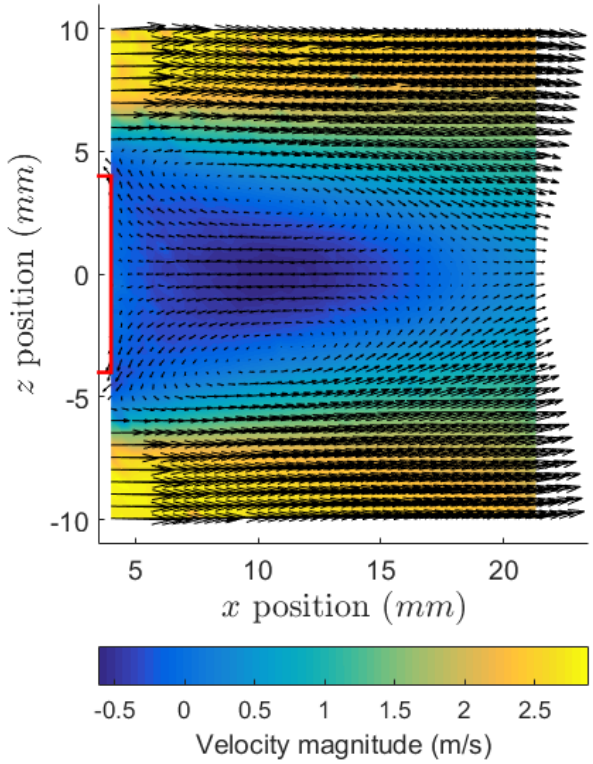

(c) $Re_D = 15600$

Figure 28: Mean velocity in cube wake within the plane $y = 0$, PIV measurements

Re_D	5600	10400	15600
L_r	$20.2mm \pm 0.1mm$	$18.7mm \pm 0.1mm$	$17.8mm \pm 0.1mm$

Table 7: Recirculation length, from the experimental mean velocity

characterised. The size of this recirculation region may also be visualised by plotting an iso-velocity contour at $U = 0m/s$, (Figure 29). It may be seen that the recirculation regions decrease slightly in length following x with a small increase in width following z for a given x. The increased velocity gradients co-linear with z must result in increased static pressure gradients in the opposite directions; at the higher Re_D numbers negative U values are also higher inside the recirculation zone.

4.3 Phase-Averaged Velocity

Using the same period cut-off points that were used to phase-average the pressure signal, each of the velocity snapshots was allocated a phase-bin number corresponding to the relative phase of its time-stamp. It was necessary to use a high number of individual snapshots for each phase-averaged field to reduce the statistical error, but also important to use phase-bins that were narrow enough to reduce phase-blurring. The best possible balance between these two conflicting criteria was judged by trial-and-error. The same method of analysis was followed to generate phase-averaged velocities for different numbers of phases, and coherent patterns in velocity structure were searched for by eye. Before this analysis was carried out, it was hoped that the recirculation region for the different phases would show a clear pattern of moving side to side with phase change, analogous to the flapping motion often observed within studies for flow past long cylinders. Such a pattern was seen to be present in the Dye Flow Visualisation carried out as a preliminary study, although the larger field of view made it easier to discern and the frame rate was much higher than the shedding frequency. It was not possible to clearly discern such a pattern phase-averaging the data by the trial-and-error method. As the first phase began at the peak of the filtered signal, and the last phase directly preceded it, it is not expected that there should be a large difference between the two phases. For each set of velocity measurements, an uneven number of phases was used such that the central phase would represent the phase that was as far separated as possible from the first and last phases. Results are presented for the 5 phase analysis in Figures 30, 31 and 32. In

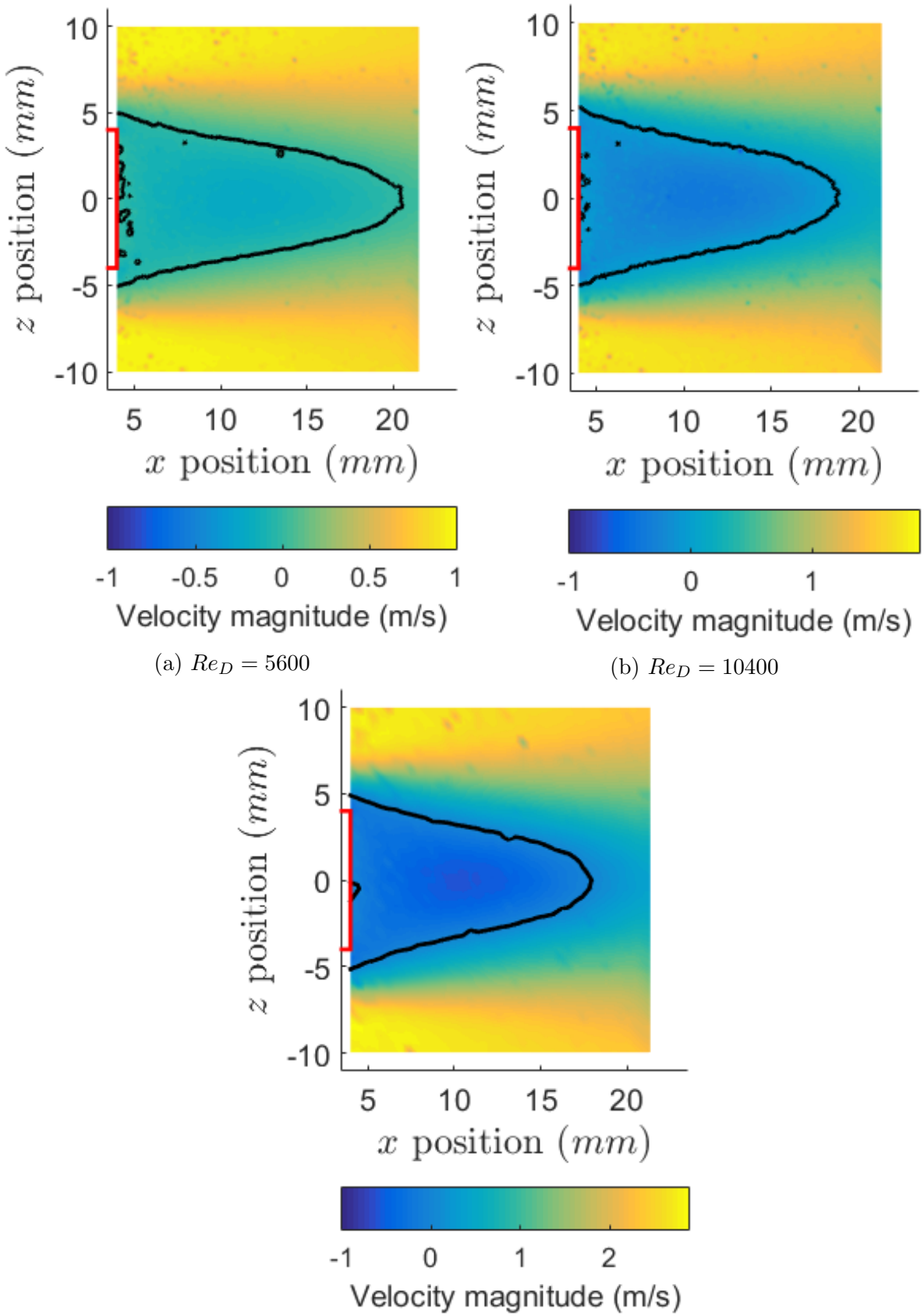

(a) $Re_D = 5600$

(b) $Re_D = 10400$

(c) $Re_D = 15600$

Figure 29: Mean streamwise velocity, showing iso-velocity contour at $U = 0$

each case there were an average of 200 snapshots per phase and no single phase contained less than 140 snapshots. It is not clear that the recirculation region has moved a great distance from side to side between phases in a consistent manner. In Section 4.1 it was shown that 100 randomly selected snapshots was sufficient to show a clear resemblance in the mean velocity to that produced using 1000 snapshots. This was first demonstrated via convergence of the $I_{\mathbf{U}_{N_s}}$ integral. In addition to this, the mean velocity vector maps confirmed that this convergence with increasing N_s was also noticeable by eye. It is not known why similarly clear patterns could not be observed in the phase-averaged velocity. The phase relationship between the pressure at the cube side face and the velocity in the recirculation region may have been much more complex than was expected, perhaps 3D effects were significant. It is also possible that the influence of the larger pressure fluctuations discussed in Section 3 obscured the relationship.

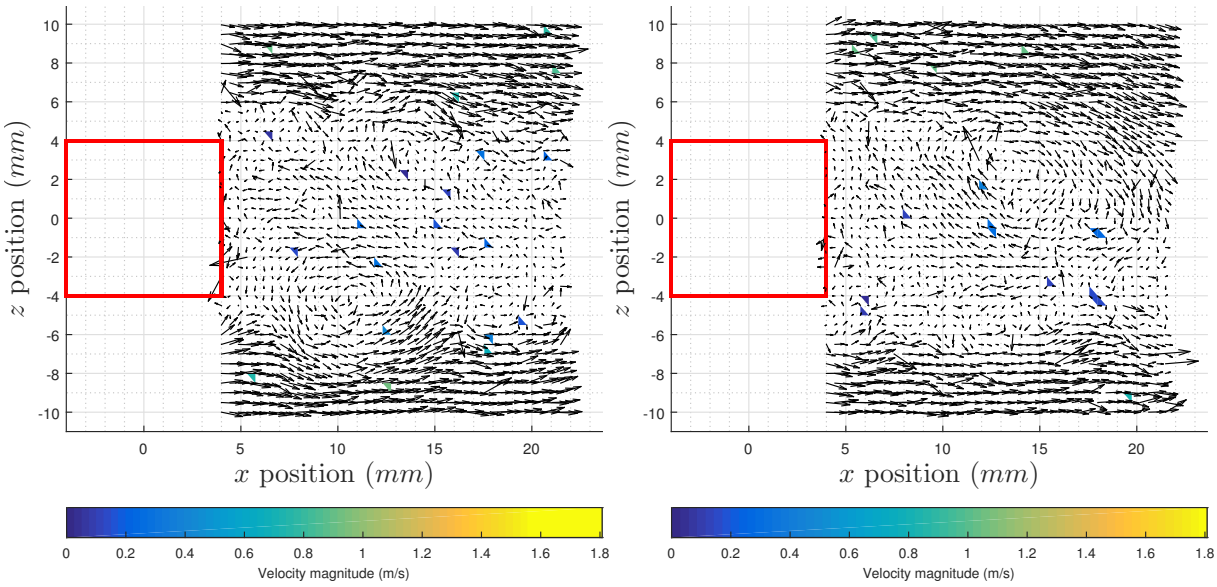

(a) Phase 1

(b) Phase 2

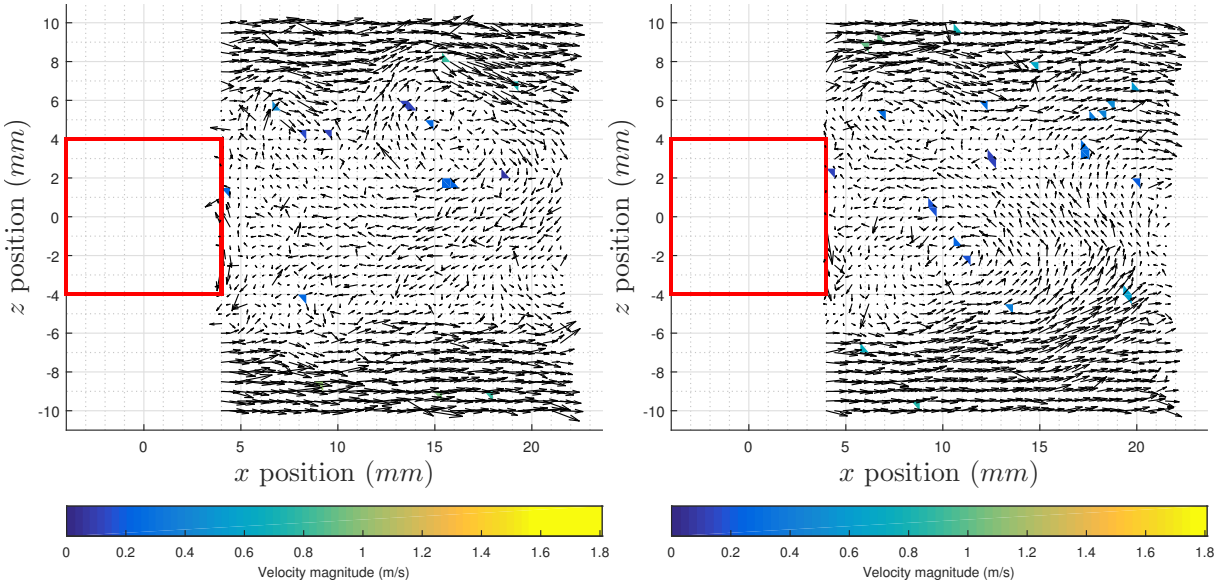

(c) Phase 3

(d) Phase 4

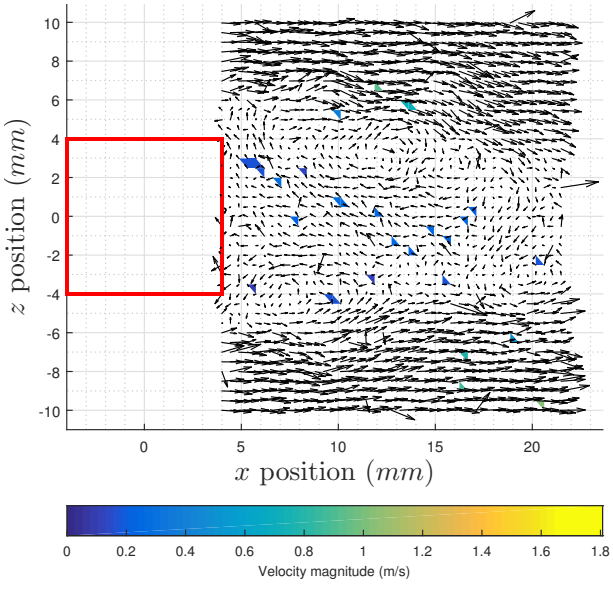

(e) Phase 5

Figure 30: Phase-averaged velocity field, $Re_D = 5600$

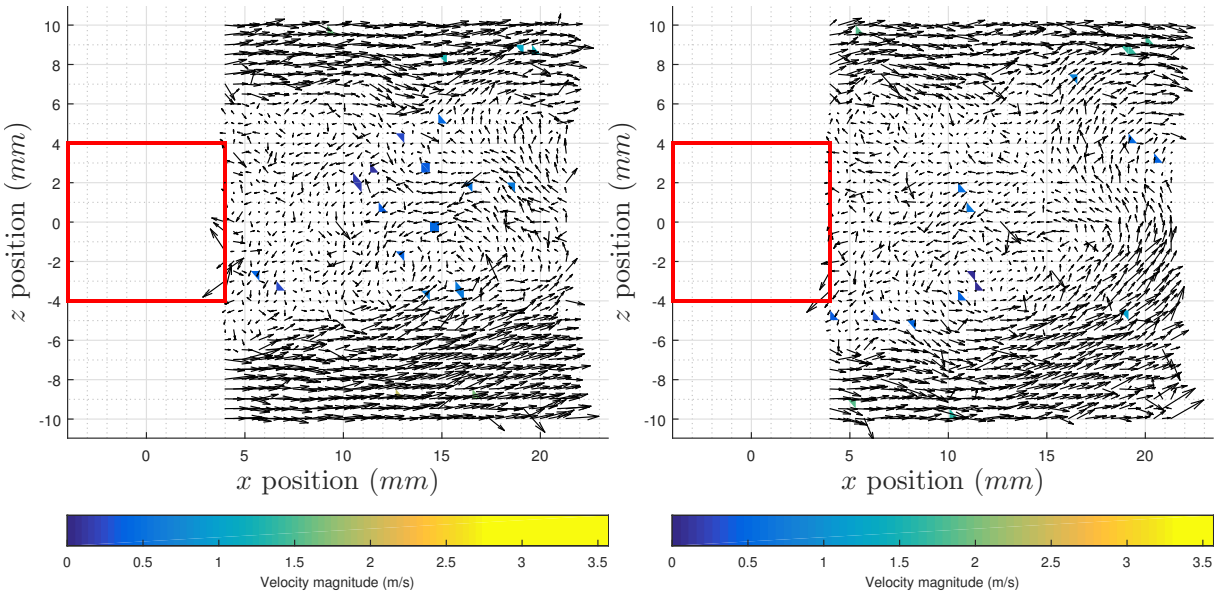

(a) Phase 1

(b) Phase 2

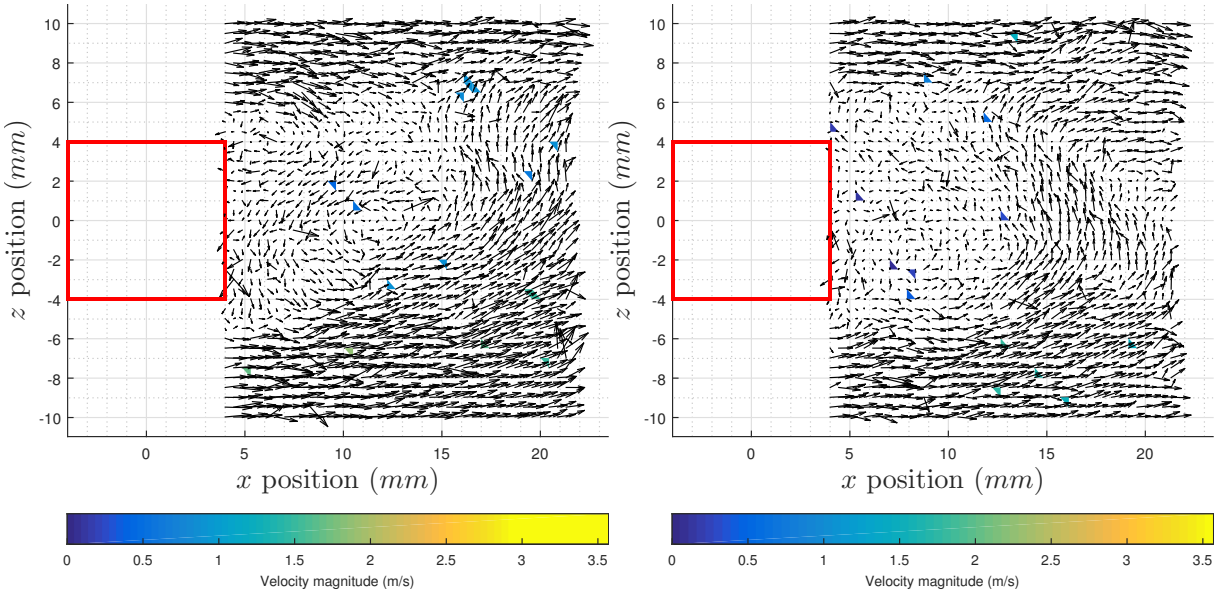

(c) Phase 3

(d) Phase 4

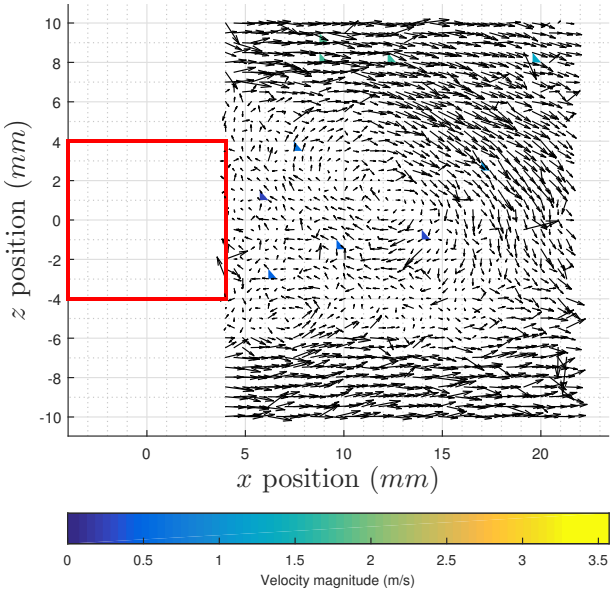

(e) Phase 5

Figure 31: Phase-averaged velocity field, $Re_D = 10400$

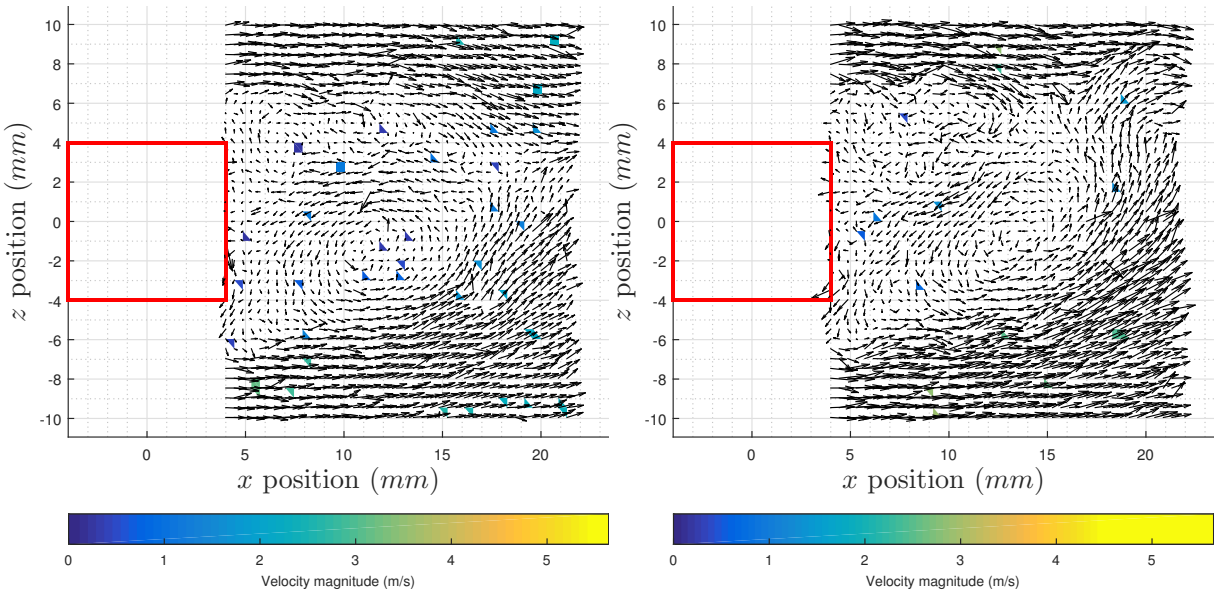

(a) Phase 1

(b) Phase 2

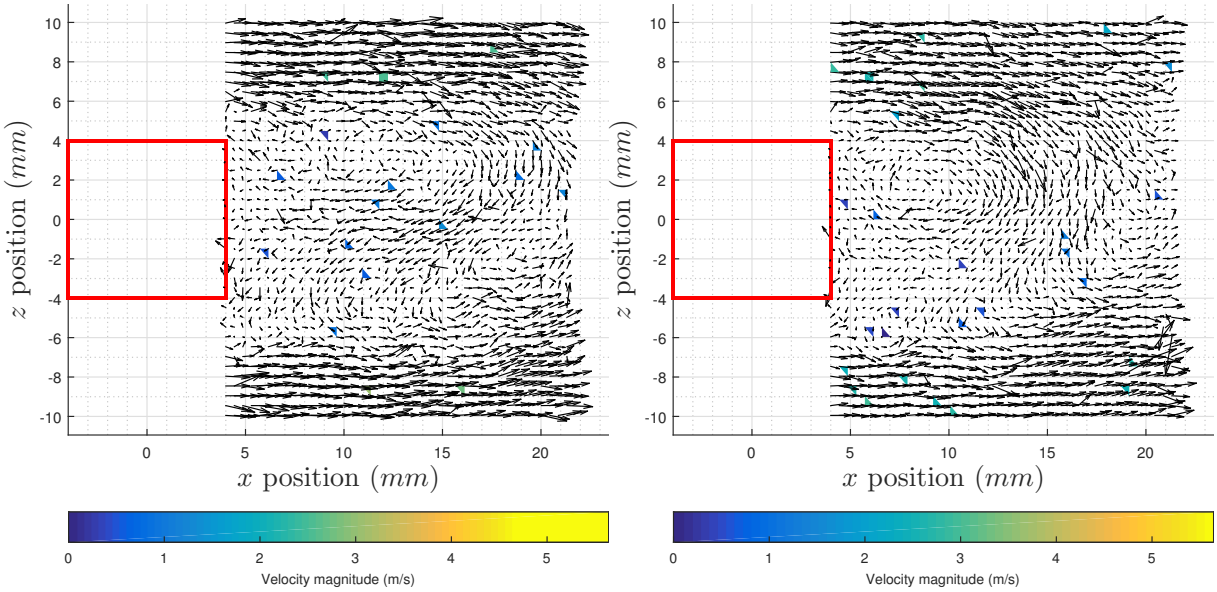

(c) Phase 3

(d) Phase 4

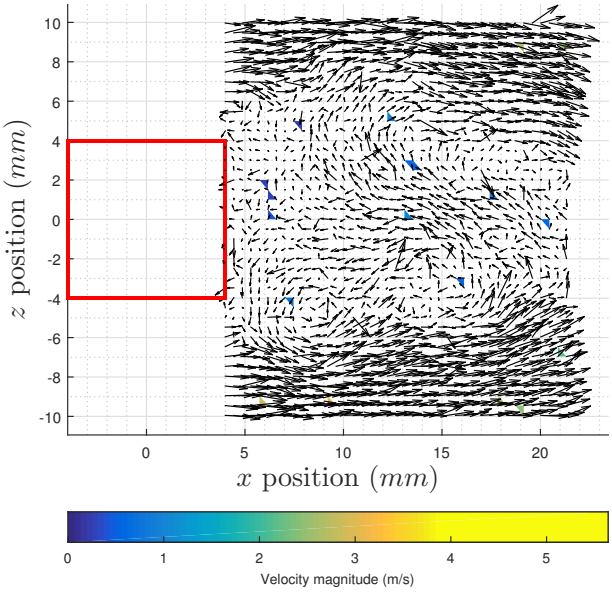

(e) Phase 5

Figure 32: Phase-averaged velocity field, $Re_D = 15600$

5 Computational Modelling

5.1 Incompressible Navier-Stokes Equations

The Navier-Stokes equations for incompressible flow in the absence of body forces may be written as:

$$\frac{\partial u_i}{\partial x_i} = 0 \tag{12}$$

$$\rho \frac{\partial u_i}{\partial t} + \rho u_j \frac{\partial u_i}{\partial x_j} = -\frac{\partial p}{\partial x_i} + \frac{\partial \tau_{ij}}{\partial x_j} \tag{13}$$

where τ_{ij} is the viscous stress tensor. Using the Stoke's relation, this may be defined as:

$$\tau_{ij} = 2\mu s_{ij} - \frac{2}{3}\mu \frac{\partial u_k}{\partial x_k}\delta_{ij} \tag{14}$$

δ is the Kronecker symbol, and s_{ij}, the rate of strain tensor, is given by:

$$s_{ij} = \frac{1}{2}\left(\frac{\partial u_i}{\partial x_j} + \frac{\partial u_i}{\partial x_j}\right) \tag{15}$$

5.2 Reynolds Decomposition and the RANS Equations

Time-averaging of a scalar quantity ϕ is defined as:

$$\overline{\phi} = \Phi = \frac{1}{\Delta T}\int_{t=0}^{\Delta T} \phi(t)dt \tag{16}$$

where the uppercase Φ is used to denote the time averaged mean quantity. When Φ no longer changes for any further increase in ΔT, ΔT is said to be sufficiently large. The ensemble mean of a scalar quantity is calculated by collecting a number N_s of discrete samples, each of which may be denoted by a unique number n. This mean is defined as:

$$\langle\phi\rangle = \Phi = \frac{1}{N_s}\sum_{n=1}^{N_s} \phi_n \tag{17}$$

when Φ no longer changes for any further increase in n, the sample size N_s is sufficiently large and the average is said to be statistically converged. In some of what follows, the upper-case notation will be used to denote a mean without making a precise distinction

between time averaging and ensemble averaging, enabling the notation to be made more concise. The Reynolds decomposition splits each component of the velocity field into its ensemble mean value and a fluctuating part:

$$u_1 = U_1 + u_1' \tag{18}$$

$$u_2 = U_2 + u_2' \tag{19}$$

$$u_3 = U_3 + u_3' \tag{20}$$

The pressure is decomposed in the same fashion:

$$p = P + p' \tag{21}$$

These relations may be substituted into the Navier-Stokes equations, after which "Reynolds Averaging" is carried out, taking the ensemble mean values of each of the terms. Assuming constant physical properties ρ and μ, one arrives at the Reynolds Averaged Navier-Stokes, or RANS equations:

$$\frac{\partial U_i}{\partial x_i} = 0 \tag{22}$$

$$\rho U_j \frac{\partial U_i}{\partial x_j} = -\frac{\partial P}{\partial x_i} + 2\mu \frac{\partial S_{ij}}{\partial x_j} - \rho \frac{\partial \left(\overline{u_i' u_j'}\right)}{\partial x_j} \tag{23}$$

where S_{ij} is the ensemble mean of the strain rate:

$$S_{ij} = \frac{1}{2}\left(\frac{\partial U_i}{\partial x_j} + \frac{\partial U_j}{\partial x_i}\right) \tag{24}$$

The RANS equations resemble the Navier-Stokes equations, but the appearance of a new set of terms on the right require additional models for the closure of the system. These terms are usually called "Reynolds stresses", they are turbulent terms which must be modelled:

$$T_{ij} = -\rho \overline{u_i' u_j'} \tag{25}$$

where T_{ij} is a "Reynolds Stress Tensor". This is perfectly valid in cases of "steady" flow, which consists of a steady mean component with small, chaotic fluctuations superimposed over it. For unsteady flows, Unsteady RANS, or "URANS" methodology is used. URANS

is based on the RANS framework, in the sense that the instantaneous components are separated into turbulent and non-turbulent parts.

5.3 Normalised Wall Distance

In order to correctly predict the flow in the boundary layer where gradients are sharp, it is necessary to follow one of two general approaches. Either one must use a large number of grid points near the wall, such that the details of the boundary layer are directly resolved, or one must use "wall-functions" to prescribe quantities of interest based on a knowledge of their behaviour within boundary layers across a broad range of flows. In order to help characterise the flow behaviour across such a broad range, it is useful to cast the distance to the nearest wall, y_w, in a non-dimensionalised form using quantities of relevance in the near-wall region. This new wall-distance y^+ is formed using a reference velocity, the "friction velocity" u^*, and the kinematic viscosity ν to form a non-dimensionalised group:

$$y^+ = \frac{u^* y_w}{\nu} \tag{26}$$

where u^* is given by:

$$u^* = \sqrt{\frac{\tau_w}{\rho}} \tag{27}$$

and τ_w is the wall shear stress. This y^+ may be used in order to help judge how the wall-cell height compares to the thickness of the boundary layer, and therefore facilitate choice of wall treatment. The velocity in the region of wall-influence may be non-dimensionalised using u^* following:

$$u^+ = \frac{u}{u^*} \tag{28}$$

The wall treatment used in this study depends on a blending factor that is a function of the wall-distance based Reynolds number Re_{yw}; this factor is used to define u^*. It is used to blend between the classical High-Reynolds wall function approach and Low-Reynolds number approaches, which will be described below after an introduction to the eddy-viscosity modelling concept.

5.4 Eddy-Viscosity Modelling

In real flows, the transition from laminar to turbulent flow is associated with an increased effective viscosity of the fluid μ_e, and this effective viscosity is traditionally modelled as the sum of two separate contributions in order to reflect this effect:

$$\mu_e = \mu_l + \mu_t \tag{29}$$

where μ_l is the molecular viscosity and μ_t is the effective turbulent viscosity associated with the additional turbulent eddies. Eddy-viscosity models make use of this turbulent viscosity concept by modelling T_{ij} in an analogous way to modelling the stresses in laminar flow, thus:

$$T_{ij} = 2\mu_t S_{ij} - \frac{2}{3}\left(\mu_t \frac{\partial U_l}{\partial x_l} + \rho k\right)\delta_{ij} \tag{30}$$

In incompressible flow the divergence vanishes. Dimensional analysis reveals that the turbulent viscosity μ_t might be expected to depend on a velocity scale u_t and a length scale l_t, that would be somehow characteristic of the eddies, in the following way:

$$\mu_t \sim \rho u_t l_t \tag{31}$$

5.4.1 $k - \varepsilon$ Models

To outline the rationale for the $k - \varepsilon$ class of models, one may use dimensional analysis to express u_t and l_t in terms of k and ε as follows:

$$u_t \sim k^{1/2} \tag{32}$$

$$l_t \sim \frac{k^{3/2}}{\varepsilon} \tag{33}$$

resulting in:

$$\mu_t = C_\mu \rho \frac{k^2}{\varepsilon} \tag{34}$$

The $k - \varepsilon$ model consists of the solving of two transport equations for these k and ε variables in addition to the four that are solved for Continuity and Conservation of Momentum, and is therefore often said to belong to the class of turbulence modelling

strategies known as "two equation" models.

One early example of the $k-\varepsilon$ model may be seen in [30]. There are two variants of the $k-\varepsilon$ model detailed in [30]. The first set are sometimes referred to as the Standard-$k-\varepsilon$ model, and sometimes as the High-Reynolds number $k-\varepsilon$ model. The second set are normally referred to as the Low-Reynolds number $k-\varepsilon$ model; it was the latter which were the main contribution of the paper. The authors focussed on the accurate prediction of "laminarisation" which may occur when a boundary layer is strongly accelerated. Under these conditions, the viscous sublayer of the boundary layer may thicken. Although it will not be discussed within this project, this may have important effects on the prediction of heat-transfer. The authors cited previous work by [56], which had prescribed turbulent viscosity via an algebraic formula dependent on wall distance. However, under certain conditions the boundary layer may behave differently, changes in turbulent quantities may depend on stream-wise position as well as wall-normal position. The authors of [30] were able to improve upon the High-Reynolds number formulation in the case of flow accelerating through converging plates, showing a better match with experimental data. They did this by introducing their Low-Reynolds Number approach, which comes into effect in the viscous sub-layer near the wall. Within their formulation, algebraic functions that were explicitly dependent on wall distance were not employed. Rather, a new set of algebraic functions acted on two coefficents, taking their original values from the High-Reynolds number formulation and modifying them according to local turbulent Reynolds number $Re_t = \rho k^2/\mu\varepsilon$. As a result, localised areas of low turbulence activity near the walls could be predicted.

Tests of the $k-\varepsilon$ model under a broad range of conditions were compiled together in [41]. Here, details were included of its application to a plane jet in a moving stream, a wall jet on a conical surface, pipe flow, the boundary layer on a turbine blade, a wall jet where a recirculation region was present after a backward-facing step, coaxial jets, a cavity flow, flow along a twisted tape where a swirling motion was induced and flow within square ducts. Results across these vastly different scenarios were mixed and will not be described in detail here, but certain themes were evident. The model performed well where its ability to transition between laminar and turbulent flow was tested, for example the development of a boundary layer over a turbine blade with differing levels of free stream turbulence upstream. In the case of backward-facing step flow, with a recirculation region, the Low-

Reynolds number variant gave much better predictions for ε immediately after the step. This was supposed to be because fluid from downstream moved back up towards the step face, and that as a result ε was dependent on the downstream values, not wall distance. Notably, the models fell short in the prediction of corner flows in straight rectangular ducts, these being turbulent in origin. As a result, the authors remarked that there may be a need for further development of models which calculate explicitly the Reynolds Stress fields.

Two-layer $k-\varepsilon$ models Since the aforementioned paper [41], many modifications and tweaks have been made to the $k-\varepsilon$ model, such that it would be very difficult to cover them all. However, one milestone that is certainly worth mentioning is that of "two-layer" models covered in [64]. In this type of model, the near-wall region is resolved by applying a one-equation model with wall distance dependency and a two-layer model is applied further out into the bulk region. Of particular interest in the context of the current project, the article covered application to a range of separated flows and also to vortex shedding around a square cylinder. In all of the cases of separated flow where the flow was largely steady, the two-layer $k-\varepsilon$ variant model improved predictions throughout the recirculation region when compared to the Standard $k-\varepsilon$ model with wall functions. This was evident in every comparison presented including wall-friction, mean velocity and turbulent kinetic energy comparisons. For the case of flow throughout the separation zone past a large axisymmetric body of revolution, the two-layer $k-\varepsilon$ model improved predictions relative to the Low-Reynolds variant of the $k-\varepsilon$ model; The Low-Reynolds model failed to predict separation that was present in the experiments, but the two-layer model did. What is more, the two-layer model was shown to be successfully applicable to flow past a sphere, where a very small separation zone was observed in experiments. In the separation zone and wake, velocity profiles were a good match. In the case of flow around a square cylinder described in [64], which summarised some results from [18], the Standard-$k-\varepsilon$ model with wall functions failed to reproduce the vortex shedding at all. This could be seen as a serious failure; the vortex shedding phenomena is of practical significance in many engineering contexts as well as being of academic interest. It is not clear what effect the mesh-refinement had on this, it may be the case that the use of the wall-functions tempted the researchers to apply too coarse a mesh. The two-layer model

that was introduced did reproduce the shedding phenomenon, although it under-predicted the strength of it. The authors remarked that there was an over-prediction of the length of the recirculation region, and explained this by the under-prediction in the strength of the shedding; a lower degree of momentum exchange due to less cross-stream movement would result in an extension of the low-velocity bubble. Two RSM models that account for transport of the Reynolds Stresses, one with wall-functions and one with the two-layer blending approach were also tested. These did not show clearly better mean-velocity results than the $k-\varepsilon$, they will be discussed later on (Section 5.5), but of the two, the two-layer model showed better agreement with the results.

As part of the process of constructing a two-layer model, it is necessary to have a means of defining what constitutes "near-wall" and what constitutes "bulk" regions. One method of doing this was outlined in [31], in which the final equation set was the same throughout the domain, and in which a blending parameter was used to blend between the High-Reynolds two-equation model in the bulk and a one-equation model right next the wall. This was achieved by means of a blending factor that could be tuned to move from a smooth to a sharp transition between the two-layers, making it flexible. The author found that by doing this they were able to reduce numerical stiffness, which is associated with matching the solution in two layers at explicitly defined positions, and also that they could increase the wall-cell height relative to the Low-Reynolds approach. Also, the author was able to obtain better predictions of the pressure recovery within the divergence section of a diffuser, relative to the High-Reynolds and Low-Reynolds number approaches that were tested.

5.4.2 Final $k-\varepsilon$ model

The model used for the calculations presented here [10] is of the two-layer type as discussed above. It is based on that of [64], combining a High-Reynolds and a Low-Reynolds approach via blending functions.

As given in [10], the transport equations for the turbulent kinetic energy and turbulent dissipation rate far from the wall are:

$C_{\varepsilon 1}$	$C_{\varepsilon 2}$	C_l
1.44	1.92	2.556

Table 8: Coefficients appearing in the $k-\varepsilon$ model

k transport equation

$$\rho\frac{Dk}{Dt} = \frac{\partial}{\partial x_j}\left[\left(\mu + \frac{\mu_t}{\sigma_k}\right)\frac{\partial k}{\partial x_j}\right] + \mu_t\left(\frac{\partial U_i}{\partial x_j}\right)^2 - \rho\varepsilon \tag{35}$$

ε transport equation

$$\rho\frac{D\varepsilon}{Dt} = \frac{\partial}{\partial x_j}\left[\left(\mu + \frac{\mu_t}{\sigma_\varepsilon}\right)\frac{\partial \varepsilon}{\partial x_j}\right] + \frac{1}{T_t}\left[C_{\varepsilon 1}\mu_t\left(\frac{\partial U_i}{\partial x_j}\right)^2 - C_{\varepsilon 2}\rho\varepsilon\right] \tag{36}$$

These have their origins in the two-layer $k-\varepsilon$ model described above, found in [64]. However, they are applicable in three dimensions, hence the i, j sub-indices. The characteristic timescale of the turbulence, is given by:

$$T_t = max\left(\frac{k}{\varepsilon}, \sqrt{\frac{\nu}{\varepsilon}}\right) \tag{37}$$

The constants that appear are given in Table 8.

An "all-y^+" formulation is used, which makes use of a blending factor. Within [10] this blending factor is defined as:

$$\beta = exp\left(-\frac{Re_{yw}}{11}\right) \tag{38}$$

and the wall-distance Reynolds number is:

$$Re_{yw} = \frac{\sqrt{k}y}{\nu} \tag{39}$$

This is used to calculate u_* in the near-wall cell as follows:

$$u_* = \sqrt{\beta\frac{\nu U}{y} + (1-\beta)C_\mu^{\frac{1}{2}}k} \tag{40}$$

where U is the velocity in the wall-cell parallel to the wall. This reference velocity goes

towards calculating y^+ for post-processing, and also is used as an input to the equation:

$$P_k = \beta\mu_t \left(\frac{\partial U_i}{\partial x_j}\right)^2 + (1-\beta)\frac{1}{\mu}\left(\rho u^* \frac{U}{u^+}\right)^2 \frac{\partial u^+}{\partial y^+} \tag{41}$$

This equations governs the wall-cell production of turbulent kinetic energy P_k, replacing the simpler, non-blended term (Equation 35) within the wall-cell only. Next, the question of how to prescribe the dissipation of turbulence in the near-wall cell must be addressed. The final model used for this [10] is a blending of the traditional High-Reynolds number and Low-Reynolds number approaches, following a method like that described above from [31]. Near to the wall, the value for the turbulent dissipation rate ε is calculated from:

$$\varepsilon = \frac{k^{3/2}}{l_\varepsilon} \tag{42}$$

which is blended with the solution in the bulk from Equation 36. The precise details of the blending process necessitate description of the numerical solution procedure, which will not be covered here. Based on the work of Wolfshtein [83], the length scale l_ε is dependent on the wall-distance Reynolds number:

$$l_\varepsilon = C_l \left[1 - exp\left(\frac{-Re_{yw}}{2C_l}\right)\right] \tag{43}$$

In [10], $C_l = 2.556$ to three decimal places. In a similar fashion, also based on the work of [83], the near-wall turbulent viscosity is:

$$\frac{\mu_t}{\mu} = 0.2300 Re_{yw}\left[1 - exp\left(-\frac{Re_{yw}}{70}\right)\right] \tag{44}$$

The constant 0.2300 which appears here is correct to four decimal places.

Following [31], a hyperbolic function is used to indicate wall proximity, which is also based on the wall distance Reynolds number:

$$\lambda_{2l} = \frac{1}{2}\left[1 + tanh\left(\frac{Re_{yw} - 60}{4.352}\right)\right] \tag{45}$$

where the coefficients 4.352 and 60 are produced from default values [10]. This function allows for a smooth transition between the values in the near-wall cell and those farther out. Using this blending function the turbulent viscosity is calculated with:

$$\mu_t = \lambda_{2l}\mu_t\Big|_{k-\varepsilon} + (1-\lambda_{2l})\mu\left(\frac{\mu_t}{\mu}\right)\Big|_{2l} \tag{46}$$

The left-most $k-\varepsilon$ term is similar to that of the Standard-$k-\varepsilon$ model above (Equation 34). The additional element on the right is the Kolmogorov timescale, which provides a lower threshold based on constant fluid properties:

$$\mu_t = C_\mu \rho k \, max\left(\frac{k}{\varepsilon}\,,\,\sqrt{\frac{\nu}{\varepsilon}}\right) \tag{47}$$

whereas the $2l$ term to the right uses the near-wall turbulent viscosity ratio from (Equation 44). Therefore, the turbulent viscosity that is finally calculated is blended between the two.

5.5 Reynolds Stress Transport Modelling

5.5.1 Reynolds Stress Models

Reynolds Stress Models (RSM) fall into a category known as second-order closures, the simplest category of the higher order closure models originally derived by Chou in 1945 [12]. Rather than representing the Reynolds stresses purely in terms of turbulent viscosity and mean or quasi-steady flow quantities an exact transport equation for them is derived. In the process, unknowns are introduced at a level one deeper than the now solved-for stresses, for example, triple-correlations of fluctuating components appear. In addition to these, the "pressure rate-of-strain" correlation is introduced. The main advantage of Reynolds Stress Models is the ability to account for certain effects associated with anisotropy in the Reynolds Stress tensor. As discussed previously, this may be important for the simulation of corner vortices in straight ducts, for example [28], where an explicit relationship for the Reynolds Stress distribution was created from experimental data. However, this "Explicit Algebraic" approach is too case specific to be of use as a general tool for industry, and as a result it will not be discussed in detail. An early example of a successful closure and numerical solution of this set of equations is found in [24]; these authors presented the exact Reynolds Stress Transport equations in the following form:

$$\frac{D\overline{u_i'u_j'}}{Dt} = \underbrace{-(\overline{u_i'u_k'}\frac{\partial U_j}{\partial x_k} + \overline{u_j'u_k'}\frac{\partial U_i}{\partial x_k})}_{Production} + \underbrace{\overline{\frac{p'}{\rho}(\frac{\partial u_i'}{\partial x_j} + \frac{\partial u_j'}{\partial x_i})}}_{Redistribution} + \underbrace{\frac{\partial}{\partial x_k}[\nu\frac{\partial\overline{u_i'u_j'}}{\partial x_k} - \overline{u_i'u_j'u_k'} - \overline{\frac{p'}{\rho}(u_i'\delta_{jk} + u_j'\delta_{ik})}]}_{Diffusion} \underbrace{-2\nu\overline{\frac{\partial u_i'}{\partial x_k}\frac{\partial u_j'}{\partial x_k}}}_{Dissipation} \quad (48)$$

The "Production" terms are solved for directly at this level of closure, representing the production of the stresses by shearing of the Reynolds-Averaged velocity. Within "Diffusion", only the triple correlation $\overline{u_i'u_j'u_k'}$ requires modelling. The authors demonstrated that it could be calculated using only second-order correlations under certain assumptions. Firstly, the third-order velocity correlations were written in terms of the exact transport equation for the fourth-order correlations. Some of the fourth order correlations were written in terms of second-order ones, and certain terms were neglected. The "Dissipation" term was assumed to be isotropic, and consequently that it may be represented using a scalar vale, ε in the following manner:

$$2\nu\overline{\frac{\partial u_i'}{\partial x_k}\frac{\partial u_j'}{\partial x_k}} = \frac{2}{3}\delta_{ij}\varepsilon \quad (49)$$

Under this assumption of isotropy, they also neglected the viscous diffusion term. Finally, they turned their attention to the "Redistribution" term, also often referred to as the "pressure-strain" correlation. Physically, it accounts for the movement of the Reynolds stresses due to interactions between the fluctuating pressure and the strain in fluctuating velocity:

$$\phi_{ij}^* = \overline{\frac{p'}{\rho}\left(\frac{\partial u_i'}{\partial x_j} + \frac{\partial u_j'}{\partial x_i}\right)} \quad (50)$$

It may be noted at this point that the pressure-strain correlation term is traceless due to continuity; this means that it does not contribute directly to the kinetic energy of the turbulence. Due to its anisotropic nature it serves to redistribute energy between the off-diagonal stress components, rather than increasing the kinetic energy components. Hence, it is labelled as a "redistribution" term. In order to determine accurately the level of anisotropy in the Reynolds stresses one must effectively model it. These terms were modelled under the assumption that inhomogeneity in the turbulence did not affect

the outcome much. In reality, such inhomogeneity is quite strong in near-wall regions, but this was not taken into account. Modelling of this pressure-strain term has been the focus of much work since [24]. Of note, [40] addressed wall-effects on the pressure-strain correlation. Drawing on published experimental data they remarked that the streamwise stress component is much larger near the wall than it is in flow where turbulence was nearly homogeneous. Inversely, the wall-normal component is smaller near the wall than in homogeneous turbulence. This "blocking" effect of the wall on the fluctuating wall-normal velocity is felt out to $y^+ \sim 100$ in some instances. They also remarked that, in light of data for fully developed flows in between two planes, wall effects make the normal stresses unequal even near the mean velocity maximum in some cases. As a result, they then took into account the wall effect on this pressure-strain rate, modelling it separately for the near-wall and bulk regions. Compared with the data of [11], the new model gave much better predictions for the streamwise stresses than the [24] model, with slightly better predictions of the overall kinetic energy k. In all other comparisons made, they did not find a superior performance. They suggested that further work on the modelling of ε might prove fruitful, although admitting that it was possible that improvements in the modelling of the pressure-strain rate may also be crucial. [64] summarised some results of [18] for vortex shedding around a long cylinder, who used the Reynolds Stress model of [40]. In order to calculate ε the author applied wall-functions for one test, and also used a two-layer model for ε in order to compare the outcomes. Mean velocity predictions were clearly improved throughout the recirculation region behind the cylinder by the application of the two-layer model, they overpredicted it less compared to the RSM with wall-functions. Results for total fluctuating energy in the same region were not able to show a clear advantage for either, the two-layer model overpredicted it and the model with wall-functions underpredicted it. However, as the mean velocity predictions were improved by the two-layer approach this is less important. It may hint that the greater degree of fluctuation in the cylinder wake improved predictions by increasing momentum exchange between the bulk and the recirculating fluid; this would serve to reduce the level of overprediction of velocity when using the two-layer approach.

Another notable paper in this year which focussed on the modelling of the pressure-strain rate, [77], tested a new method against four independent points of reference. These references were designed such that they provided differing levels of anisotropy in the

Reynolds Stress tensor, and measurements thereof, thereby making them particularly useful for testing the ability of the model. The rationale behind the modelling strategy was that the time-evolution for the decay of and return to isotropy should be accurately reproduced. One of the reference points was a DNS simulation [43], focussed on turbulent flow under high strain rates in one direction, so as to be applicable near flat walls. Beginning from an initial state of isotropy, these simulations evolved in time so that the move towards anisotropy could be recorded. The new model predicted a very similar time-evolution for k to the [40] model, both models matched well with the DNS data and neither was clearly better. However, the new model showed slightly better agreement with the data regarding time-evolution of the anisotropy tensor components, predicting a higher degree of anisotropy which was more in line with the data. Its predictive capabilities in homogeneous turbulence under plane strain were essentially unchanged with respect to the [40] model, showing that a disadvantage had not been introduced in the bulk of the flow. However, within an axisymmetric contraction, the new model showed clearly better predictions for both k and the anisotropic components relative to the DNS data, particularly regarding the evolution of k. In an axisymmetric expansion, k predictions were very similar from the two models but the newer one showed much better predictions of the anisotropic components. In summary, the development with respect to time towards anisotropy from an artificially imposed isotropic initial condition was better mapped with the new model. However, no results were presented that showed the variation within space of the Reynolds Stresses, which leave some questions unanswered. The need to account for anisotropy within the Reynolds Stress tensor near walls was one of the motivations behind [16], who managed to allow for the strong wall effect via a different means. An elliptical blending equation which progressively changed the model behaviour from that of the simpler quasi-homogeneous model in the bulk to a near-wall behaviour; boundary conditions could be imposed on the blending equation which then affected the solution in the interior. Essentially, this equation was used to introduce wall effects via boundary conditions, rather than by prescribing wall-cell centroid values in terms of wall-normal distance and flow conditions. It may be noted at this point that this method requires the solution of as many elliptical equations as there are independent components of the redistributive terms, ie 6, which constitutes a large increase in computational cost. Comparisons for this model were made with experimental and DNS data,

for channel flow and boundary layers with and without adverse pressure gradients, and the model performed well at just about every point of comparison. The most significant discrepancies were seen against the boundary layer data of [70], in a region of adverse pressure gradient. As the flow moved downstream, under-predictions in velocity of up to 9% were seen in the outermost regions of the boundary layer, and very close to the wall it was overpredicted by roughly the same amount. This was only in the regions farthest downstream after a pressure increase due to volume expansion. Another feature of the [16] model is that it is by nature independent of co-ordinate system. This was tested by simulating flow over a convex curved surface and comparing with [21], using exactly the same empirical constants as in the plane channel flow. The model successfully predicted a drop in skin friction after the bend. Shear stress profiles, kinetic energy and mean velocity profiles matched reasonably well, although some discrepancies were seen throughout the curved section. Based on [16], a new method was proposed in [47] that retains many of the advantages of the model, while reducing the number of additional equations that needed solving. It is able to take into account wall-effects on the pressure-strain term, dependent on an elliptical relaxation equation of the same form as in [16]. However, it only solved one of them rather than six, greatly reducing model complexity. The authors tuned the model such that such that predictions of the anisotropy of the dissipation tensor ε_{ij} fitted better to DNS results of [52].

In the limit $y \sim 0$, the new model had strictly the same behaviour for $\phi^*_{ij} - \varepsilon_{ij}$ as the model from [16], although not necessarily for either of the two tensors individually. The choice of different modelling for each component of ϕ^w_{ij} necessitated the calculation of the wall-normal direction for reference. The authors were able to produce a wall-normal unit vector from the blending parameter field. This vector could be calculated at any point in the domain and it depends on the local properties of turbulence. As it does not necessarily align itself with the solid boundaries away from the wall surface, it could be aptly renamed a "wall-effect" orientation vector; the geometry has an indirect effect on it by way of the calculated solution. Results compared with DNS channel flow [52] showed excellent mean velocity predictions up to $y^+ \sim 10$, and fairly good results beyond this, with some discrepancies between this value and $y^+ > 100$. The new model reproduced the anisotropy in the Reynolds Stress tensor quite well near the wall, the results were similar to that of [16]. Predictions of $\overline{u'u'}$ were too small and were inferior to those of

[16], but $\overline{v'v'}$ predictions were very good near the wall. The $\overline{w'w'}$ components were not well predicted, but were no worse than those of [16]. The new model did not predict the near-wall budgets of $\overline{u'v'}$ and $\overline{u'w'}$ components as accurately as [16], although the shape of the profile was very similar and the discrepancies were only important close to the wall. The ε predictions were also not a good match with the DNS results for $y^+ < 50$, those of [16] were a little better overall, but neither of the models matched well for $y^+ < 1$. In summary, predictions were nearly as accurate as those of [16], retaining the ability to predict wall effects on the Reynolds Stress tensor with a significantly reduced computational cost.

5.5.2 Final Reynolds Stress Model

The final model used, as implemented in Star-CCM+, was the Elliptic Blending Reynolds Stress Model, or *EBRSM* of [38]. It is based on that of [47] with some changes made by authors including [46] and [13]. The resultant model was reported to be numerically robust with improved convergence capabilities. The equation governing the transport of Reynolds stresses may be written as:

$$\frac{\partial \overline{u_i' u_j'}}{\partial t} + \frac{\partial U_k \overline{u_i' u_j'}}{\partial x_k} = P_{ij} + D_{ij}^t + \phi_{ij}^* - \varepsilon_{ij} + \frac{\partial}{\partial x_k}\left(\nu \frac{\overline{u_i' u_j'}}{\partial x_k}\right) \quad (51)$$

where P_{ij}, ε_{ij}, D_{ij}^t, denotes terms responsible for production, dissipation, and turbulent diffusion of the Reynolds stress components. It employs a different blending function for the pressure-strain rate and dissipation:

$$\phi_{ij}^* = \left(1 - \alpha^3\right) \phi_{ij}^w + \alpha^3 \phi_{ij}^h \quad (52)$$

$$\varepsilon_{ij} = \left(1 - \alpha^3\right) \varepsilon_{ij}^w + \alpha^3 \varepsilon_{ij}^h \quad (53)$$

which makes use of a blending parameter α, the solution of an elliptic equation:

$$\alpha - L_\alpha^2 \nabla^2 \alpha = 1 \quad (54)$$

The lengthscale is given by:

$$L_\alpha = C_L max\left(\frac{k^{3/2}}{\varepsilon}, C_\eta \frac{\nu^{3/4}}{\varepsilon^{1/4}}\right) \tag{55}$$

with $C_\eta = 80.0$, taken from [47] (Equation 55). However, the lengthscale coefficient is given by $C_L = 0.133$. The cubic dependency on α is due to [42]. That author argued that it would lead to a better prediction of $\overline{u'v'}$ throughout the majority of the boundary layer, and that it was worth sacrificing some accuracy in a very small region near the wall to do so. The pressure-strain far from the wall is taken from [77]:

$$\begin{aligned}\phi_{ij}^h = &-\left(C_1 + C_1^* \frac{P_{kk}}{2\varepsilon}\right)\varepsilon a_{ij} + \left(C_3 - C_3^* \sqrt{a_{kl}a_{kl}}\right) k S_{ij} \\ &+ C_4 k\left(a_{ik}S_{jk} + a_{jk}S_{ik} - \frac{2}{3}a_{lm}S_{lm}\delta_{ij}\right) + C_5 k\left(a_{ik}W_{jk} + a_{jk}W_{ik}\right)\end{aligned} \tag{56}$$

Here, S_{ij} and W_{ij} are the strain and rotation rates of the Reynolds-Averaged velocity field, and a_{ij} is the anisotropy tensor defined as:

$$a_{ij} = \frac{\overline{u_i'u_j'}}{k} - \frac{2}{3}\delta_{ij} \tag{57}$$

ϕ_{ij}^w, the near-wall part of the pressure strain term, is originally from [47]:

$$\phi_{ij}^w = -5\frac{\varepsilon}{k}\left(\overline{u_i'u_k'}n_j n_k + \overline{u_j'u_k'}n_i n_k - \frac{1}{2}\overline{u_k'u_l'}n_k n_l\left(n_i n_j - \delta_{ij}\right)\right) \tag{58}$$

The [38] model actually includes an extra additive term to the rotation rate W_{ij}, but it is equal to zero in non-rotating systems such as the one studied in the current work so it is omitted for simplicity.

The tensor for the dissipation rate is:

$$\varepsilon_{ij}^w = \frac{\overline{u_i'u_j'}}{k}\varepsilon \tag{59}$$

in the near-wall region and:

$$\varepsilon_{ij}^h = \frac{2}{3}\varepsilon\delta_{ij} \tag{60}$$

far away from the wall. The scalar value of the turbulent dissipation rate ε used in these

$C_{\varepsilon 1}$	$C_{\varepsilon 2}$	C_1	C_1^*	C_3	C_3^*	C_4	C_5	C_T	A_1	C_L	C_η	C_μ
1.44	1.83	1.7	0.9	0.8	0.65	0.625	0.2	6.0	0.085	0.133	80	0.07

Table 9: Coefficients used for $EBRSM$ model

equations comes from the transport equation:

$$\frac{\partial \varepsilon}{\partial t} + u_j \frac{\partial \varepsilon}{\partial x_j} = \frac{1}{T_t}\left(C_{\varepsilon 1}\frac{P_{kk}}{2} - C_{\varepsilon 2}\varepsilon\right) + E + D_\varepsilon^t + \frac{\partial}{\partial x_k}\left(\nu \frac{\partial \varepsilon}{\partial x_k}\right) \tag{61}$$

following [47]. However, the term E is taken from [4]:

$$E = A_1 \nu \overline{u_k' u_l'} n_k n_l \frac{k}{\varepsilon}\left(1-\alpha^3\right)\left(\frac{\partial ||S_{ij} n_i|| n_k}{\partial x_k}\right)^2 \tag{62}$$

with $A_1 = 0.085$, calibrated to channel flow for a range of Reynolds numbers. The turbulent timescale is identical to that in[47] (Equation 64). The diffusion terms D_{ij}^t and D_ε^t given in Equations 51 and 61 are calculated using a "Simple Gradient Diffusion Hypothesis", which was introduced by [38], citing reasons of numerical robustness. These authors used the following equation for the turbulent viscosity:

$$\nu_t = \left[\left(1-\alpha^3\right)\overline{u_i' u_j'} n_i n_j + \alpha^3 k\right] C_\mu T_t \tag{63}$$

with $C_\mu = 0.07$. The turbulent timescale is given by:

$$T_t = max\left(\frac{k}{\varepsilon}, C_T\left(\frac{\nu}{\varepsilon}\right)^{1/2}\right) \tag{64}$$

with $C_T = 6.0$. The second term was introduced because in regions far away from the wall the gradients of α are not well-defined, which was reported to produce spurious oscillations. Model constants are summarised in Table 9, some of the origins of these are discussed throughout this section, but others are presented without comment. This model was tested by the authors [38] in a broad range of conditions. In curved pipe flow, it was compared with DNS results. For its ability to predict a wing-tip vortex, it was compared with experiments, at high Reynolds number. Finally, it was tested for flow around a two-dimensional airfoil with a complex geometry, a "Coanda airfoil". In all three test cases, it was compared with a $k-\varepsilon$ model and also the $SSTk\omega$ model. It outperformed these other models at every point of comparison within the pipe and for the wing-tip. For the flow

around the "coanda" airfoil, it did not perform as well in some respects. It gave better predictions of the size and shape of the recirculation region behind the airfoil. However, both the $k-\varepsilon$ and the $SST\ k\omega$ predicted a more realistic lift coefficient, and the $k-\varepsilon$ also predicted a more accurate separation angle behind the airfoil. Predictions from the $k-\varepsilon$ and the $SST\ k\omega$ models for the pressure coefficient around the surface of the airfoil were better than the $EBRSM$, particularly that of the $SST\ k\omega$. The authors remarked that there was a low degree of turbulence around the leading edge of the low pressure side of the foil. This tendency towards relaminarisation of the flow entailed a further drop in pressure, which meant that the overall lift was overpredicted. In summary, the $EBRSM$ performed much better in internal flows, but not necessarily as well for the external flow around the airfoil. This was associated with a tendency for unwanted relaminarisation around bluff bodies.

The configuration used in the current study is likely to introduce issues related to those seen in both internal and external flows; the flow will be fully-developed and constrained within a thin channel before reaching the cube, but in the cube region sudden changes in geometry will induce separation and shedding. However, unlike some of the test cases used to validate the models, the separated flow will be subject to strong shear due to walls parallel to the bulk flow and largest shedding component. In the test cases considered throughout the validation process of some of the models discussed, large-scale unsteady physics was not featured. The $EBRSM$ model has its origins partly in [77], which investigated the ability of the model to represent the time-evolution of the Reynolds Stress Tensor, but this seems far separated from the large-scale unsteady shedding from a vortex cylinder. Nevertheless, reasonably successful application of RSM models to vortex shedding around long cylinders has been demonstrated, for example [64], and it is therefore hoped that they will perform well for the current case.

5.6 URANS Computational Methodology

All simulations used methods designed for incompressible flows. URANS computations were carried out using Star-CCM+, and what follows is based on the details given in [10]. A second-order upwind spatial differencing scheme that employs a Gauss type method was used to compute the gradients, necessary to project onto the cell faces. These gradi-

ents are limited using a Venkatakrishnan type scheme [80], essentially ensuring that face values are bracketed by those at the neighbouring cells. The method is more dissipative than a central-difference one, which is advantageous for flows where low Peclet numbers occur. It is of course more accurate than a first-order upwind treatment, and pays for this only in inferior convergence properties due to a reduced numerical dissipation; this is an acceptable trade-off when residuals may be monitored and convergence is scrutinised for each time-step. As such, it is considered suitable for a wide range of flow conditions. The velocity components and pressure were first solved for in an uncoupled manner on a colocated grid. Pressure-velocity coupling used a Rie and Chow pressure correction approach [63] based on a SIMPLE type predictor-corrector algorithm [57]. The temporal scheme was implicit and 2nd-order with respect to time, making use of the current timestep and the previous two in its formulation. Computational grids were all of Cartesian form, with grid refinement in selected regions where gradients were high.

5.6.1 Meshing

5.6.1.1 Unblocked Channel

Inlet conditions were designed based on the criteria that the flow was fully-developed before meeting with the obstacle. Firstly, steady-state RANS simulations were set up with periodic boundary conditions, where the mass flow rate was imposed in the streamwise direction and the solution from the exit fed back into the inlet. One such "infinitely long" simulation was set up for each combination of turbulence model and mass flow rate. Mesh independence was tested for these unblocked channel simulations, at both $Re_D = 5600$ and $Re_D = 15600$, using steady-state RANS simulations. Near wall cell heights were chosen such that y^+ values were approximately equal to 1 for each case. A hyperbolic expansion was used to stretch the mesh in the y direction such that there was a smooth, gradual increase in cell size towards the channel centre. In order to make comparisons between the different meshes, profiles of streamwise velocity and turbulent kinetic energy were plotted in the domain centre far from the recycling inlet/outlet planes and channel sides. Simulations were left to run until all globalised residuals had stopped changing; by this point channel pressure drop, u and k at the channel centre had already reached a steady state. Plots were made as a function of y, from one wall to another. At

$Re_D = 5600$ (Figures 33a, 33b), $n_y = 33$ cells was sufficient to achieve mesh independence whereas at $Re = 15600$ $n_y = 49$ cells were necessary (Figures 33a, 34a). Near the small walls at the extremes of z, a similar hyperbolic stretching was used to resolve the near-wall gradients, although this was found to affect the results much less at the centre-line. Solutions were taken from the unblocked channel simulations having $n_y = 65$ at all three Reynolds numbers, and were used to set the inlet profiles for the simulations of flow around a blockage. These blocked channel simulations used the unblocked channel meshes as a boundary point for the minimum required mesh resolution; all results presented for flow around the blockage used a higher number of cells in the y direction. The mesh used at $Re_D = 10400$ was the same as that used at $Re_D = 15600$.

As part of this process, pressure drop predictions in the unblocked channel were compared. In particular, the effect of changing wall-cell heights and wall-treatments was investigated. This was to ensure that the pressure drop predictions were not drastically changed by, for example, applying the two-layer $k-\varepsilon$ model with low y^+ values as opposed to the Standard-$k-\varepsilon$ with high y^+ values. As a result of this process, the Menter-SST-$k-\Omega$ model [51] was discounted. When the normalised wall-cell height was reduced to $y^+ \sim 5$ or less, pressure predictions were significantly different to all the $k-\varepsilon$ models and $EBRSM$ models tested, particularly at the highest Reynolds number. They were also very different to those of the same Menter-SST-$k-\Omega$ model when y^+ values were greater than 15, which were in agreement with the $k-\varepsilon$ and $EBRSM$ models. Similar issues were encountered when using another version of the $k-\Omega$ approach with a wall-treatment that was suitable across a range of y^+ values. It is not known whether this was due to problems of model implementation within Star-CCM+, or to issues inherent in the combination of the models with the wall-treatment. It was desirable to refine meshes in the region of the cube, necessitating a model/wall-treatment combination that could deal with low y^+ values, and it was also desirable that the model could also deal with changing y^+ values. As a result, the $k-\Omega$ models were not deemed suitable.

In addition to the pressure drop and to the solution spanning the small dimension from the duct floor to the duct ceiling, the effect of modelling on the prediction of secondary corner flows was investigated. The Standard-$k-\varepsilon$ model could not predict the formation of these, nor could the two-layer $k-\varepsilon$. Non-linear versions of the $k-\varepsilon$ model could, for example that of [44], although they vastly under-predicted them. Several Reynolds Stress

models were tested, and were able to better reproduce the secondary flows, although they too underpredicted their strength. Due to the small size of these (the secondary velocities are approximately 1% of the bulk velocity), and the width of the duct, they had very little effect on the flow near the duct centre. In addition to this, they were found to make an inconsequential difference to the prediction of temperature within a rectangular nuclear sub-channel. Setup parameters were chosen to reflect those of [68], and the solution at the outlet was used to define inlet conditions so as to allow turbulence-induced secondary flows to develop to their maximum possible strength. more. Despite this, there was a maximum change in temperature of only $\sim 1.5C$, confined mostly to very small regions the regions near the corners. Results of this study were presented at the 2015 University Nuclear Technology Forum, under the title "Modelling of turbulence-induced secondary flows in non-circular channels". However, since this point their prediction has been disregarded as it was considered unimportant to flow around blockages located far from the duct corners.

5.6.1.2 Blocked Channel

A fully Cartesian grid with localised refinement near the cube was used to mesh the domain for the blocked channel simulations. The mesh far from the cube was equivalent to that in the unblocked channel simulations. Firstly, a "base mesh" was generated in a domain comprising the central plane at $y = 0$, that only extended a small distance in the y direction, and this base mesh was extruded using a stretching function in order to resolve the boundary layers on the large channel walls at $y = \pm{}^{D}/_{2}$ (Figure 35). Within the base mesh, gradients in the x and z directions were well resolved due to a refinement strategy that focussed on the blockage, the finest areas were immediately adjacent to it and. Four areas were selected near the cube, one at each face, within which cells were anisometric and y_w distances were selected in order to resolve the sharp gradients near the surface (Figure 36). In total, six different levels of refinement were used passing from the bulk to the cube faces (Figure 37). The cells were in general isometric with respect to x and z within a rectangular region containing the cube, the near upstream and side regions and the downstream recirculation region. Rather than adaptive mesh refinement, large sections of the mesh were refined; regions where velocity gradients were large were well resolved all the way through the moving velocity field at each point in the cycle.

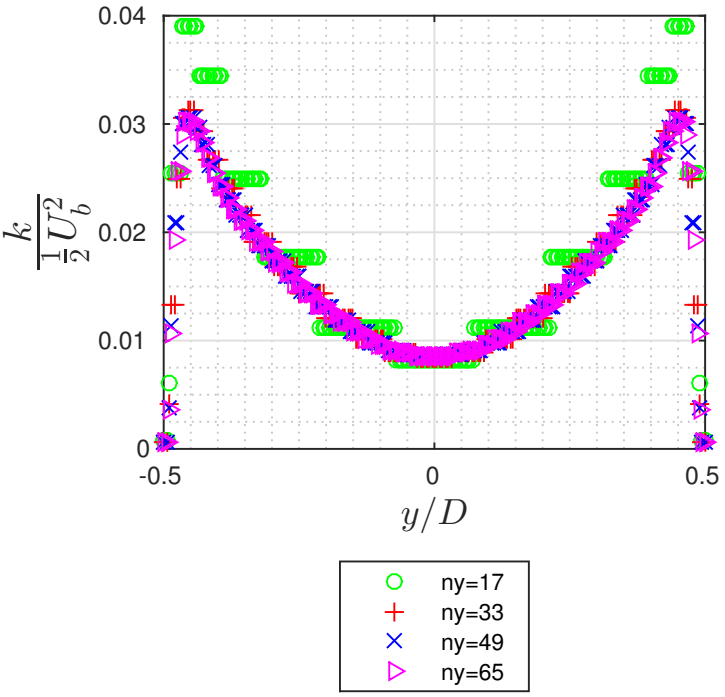

(a) $k - \varepsilon$

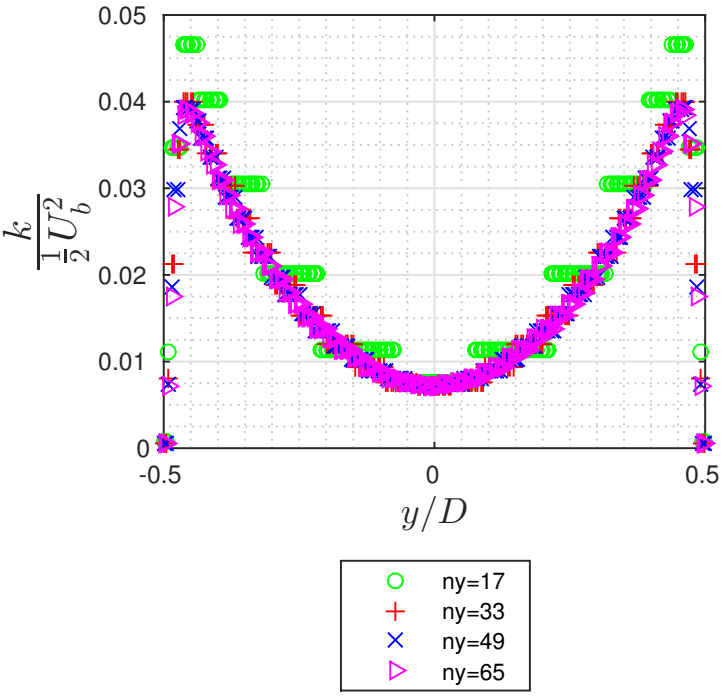

(b) *EBRSM*

Figure 33: Turbulent kinetic energy spanning the channel in the y direction, $Re_D = 5600$

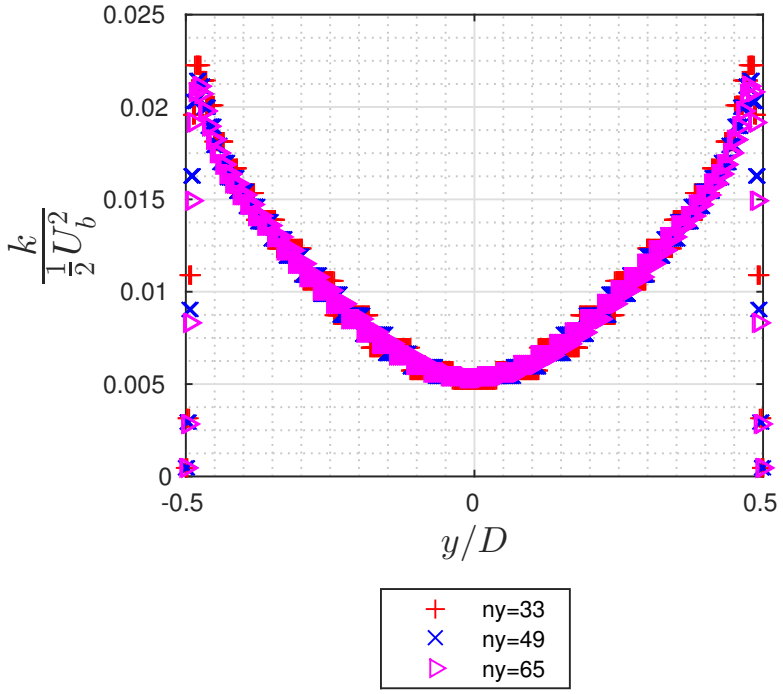

(a) $k-\varepsilon$

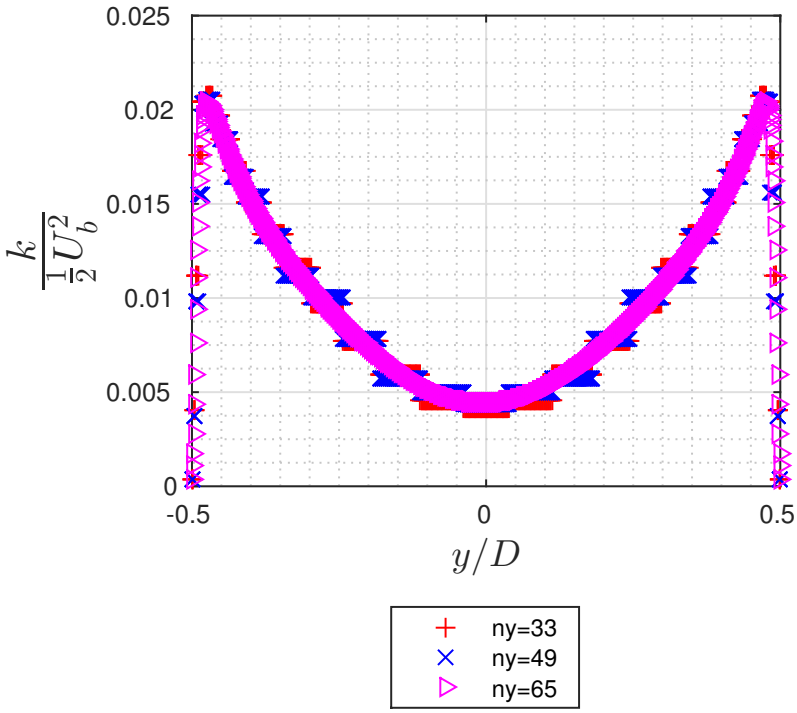

(b) $EBRSM$

Figure 34: Turbulent kinetic energy spanning the channel in the y direction,$Re_D = 15600$

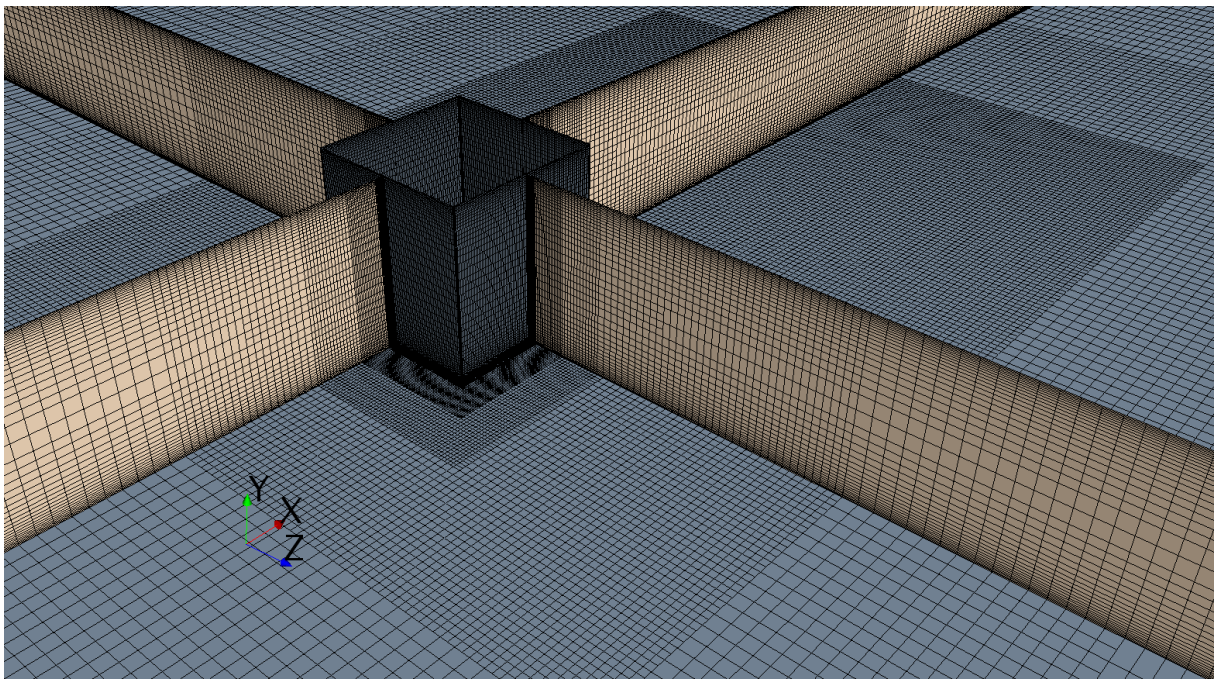

Figure 35: 3D mesh showing stretching in y direction, Mesh 4

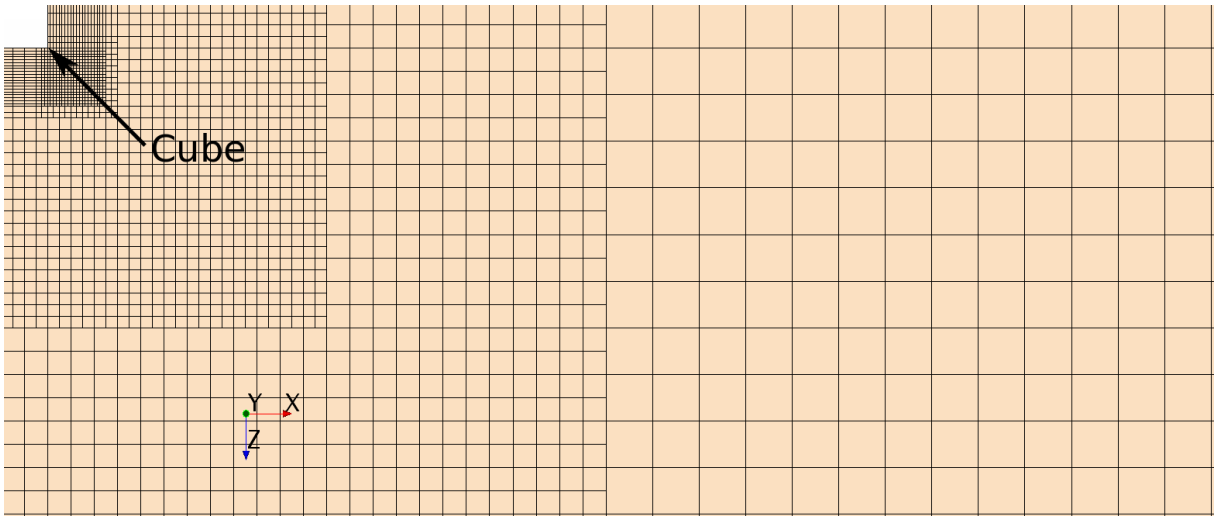

Figure 36: 2D base mesh showing x, z refinement strategy in near-cube region, Mesh 4

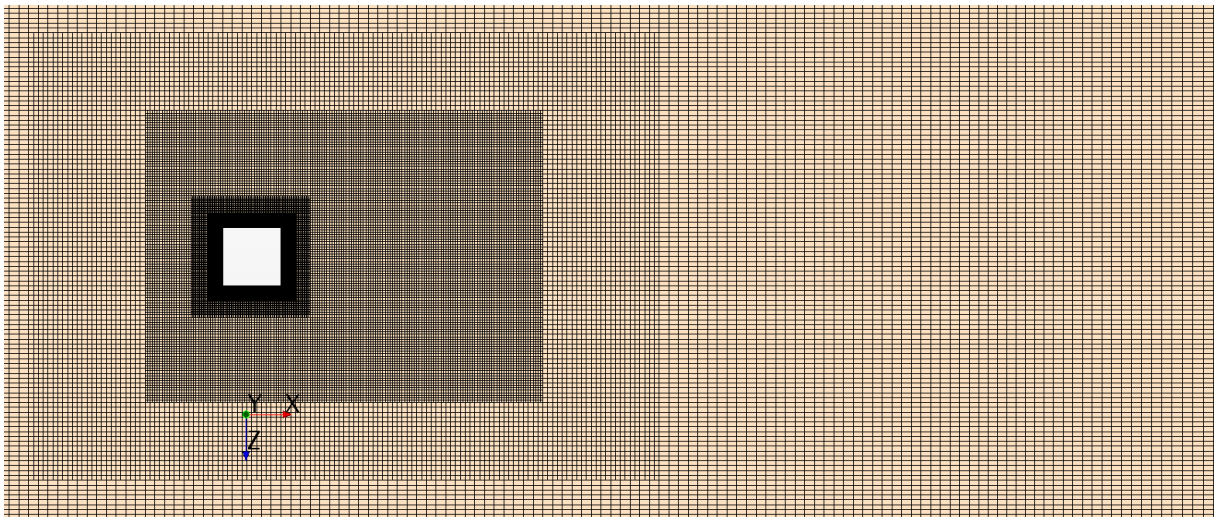

Figure 37: 2D base mesh showing x, z refinement strategy across domain, Mesh 4

$Mesh$	2	3	4	5	6
N_c	424k	930k	4.9M	16.8M	45M

Table 10: Total number of cells on different meshes

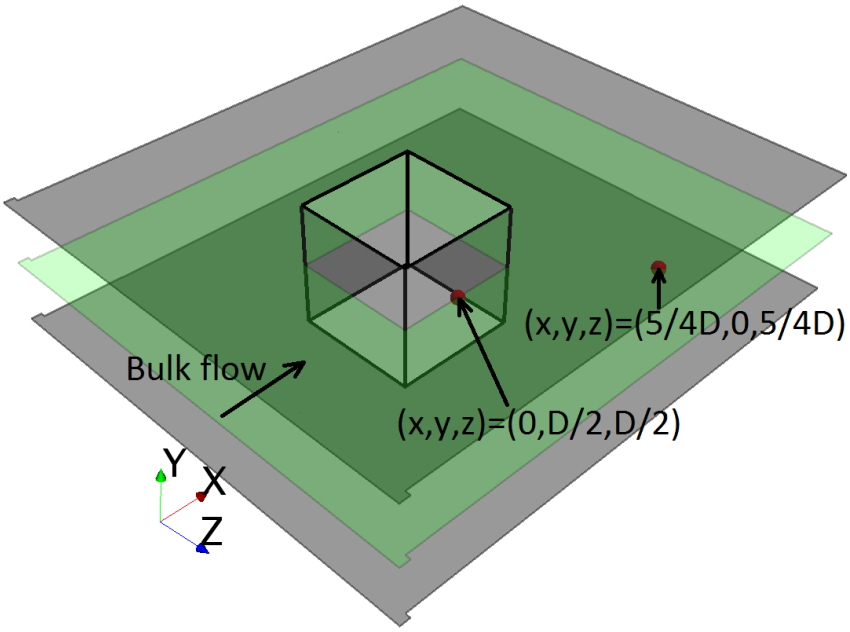

Figure 38: Location of pressure probe on cube side face and velocity probe offset from trailing corner. Probes contained within plane $y = 0$, highlighted in green

Rather than taking a purely pragmatic approach, the cell number was pushed to an extreme in order to completely eliminate the effects of grid spacing (Table 10), at $Re_D = 10400$ using the $EBRSM$.

Six different meshes were tested, ranging from very coarse (Mesh 1) to extremely well refined (Mesh 6). Mesh 1 was used to quickly generate initial conditions for the more refined meshes. In order to quantify the effect that mesh refinement had on the near-cube solution, the pressure at the cube side face was monitored along with the streamwise velocity at $(x = 1.25D, y = 0, z = 1.25D)$ (Figure 38). The velocity probe location was chosen as a large variation in velocity was seen at this point.

Results are presented for all but the coarsest mesh and the most refined at $Re_D = 10400$. They are not included for the very large Mesh 6 as results from this mesh overlaid those of Mesh 5 perfectly. Pressure at the cube side is displayed (Figure 39b), and velocity at $(x = 1.25D, y = 0, z = 1.25D)$ in (Figure 39a). Based on these comparisons, the solution had become independent of the grid spacing by Mesh 5. Differences between the solutions on Meshes 4 and 5 were very small, such that the maximum difference in pressure was less than 2% of the amplitude of the fluctuations. These differences were

much smaller still for velocity. Differences between the solutions on Meshes 3 and 4 were no more than 14% of the amplitude of the fluctuations for pressure, and less than 8% for velocity. Meshes 4 and 5 were also tested at $Re_D = 5600$ and $Re_D = 15600$; the solutions for the two meshes were found to match similarly well at these Reynolds numbers, that is to say that the difference between the solutions on Meshes 4 and 5 were no more than $2 - 3\%$ of the amplitude of fluctuations.

In conclusion, Mesh 3 was probably well-refined enough for many engineering purposes, and Mesh 5 was useful as a reference point showing the limits of the modelling strategies. Mesh 6 was excessive and served only to prove that Mesh 5 was suitable as a limiting case. Finally, Mesh 4 was sufficiently well refined for the purposes of this study and has a significantly smaller number of cells than Mesh 5. As a result, it has been used to generate the solutions used for comparisons between the models.

5.6.2 Convergence Criteria

The number of internal iterations within each timestep over which the predictor-corrector algorithm ran was limited according to the progression of global residuals, which were used to judge the state of the solution across the whole domain, hence providing a good estimate of the degree of convergence. This global residual may be calculated for a scalar ϕ as the RMS value of the local residuals across all N_c computational cells in the domain.

$$R^{\phi}_{global} = \sqrt{\frac{1}{N_c}\sum_{n=1}^{N_c}\left(r^{\phi}_{n}\right)^2} \tag{65}$$

where each r^{ϕ}_{n} is the local residual at cell n for the scalar value ϕ. The largest time-dependent fluctuations observed were aligned in the spanwise direction, and the residuals for the spanwise momentum were therefore monitored alongside those of the streamwise momentum and continuity. In order to gain some intuitive idea of their relative size, particularly when changing between different Reynolds numbers, the residuals for continuity were normalised by the value of the mass flux at the inlet. Residuals for the streamwise and spanwise momentum were both normalised by the streamwise momentum flux at the inlet, which was dominant among the three components due to the fully-developed inlet flow conditions. Allowing the simulations to run for 100 inner iterations per timestep, it

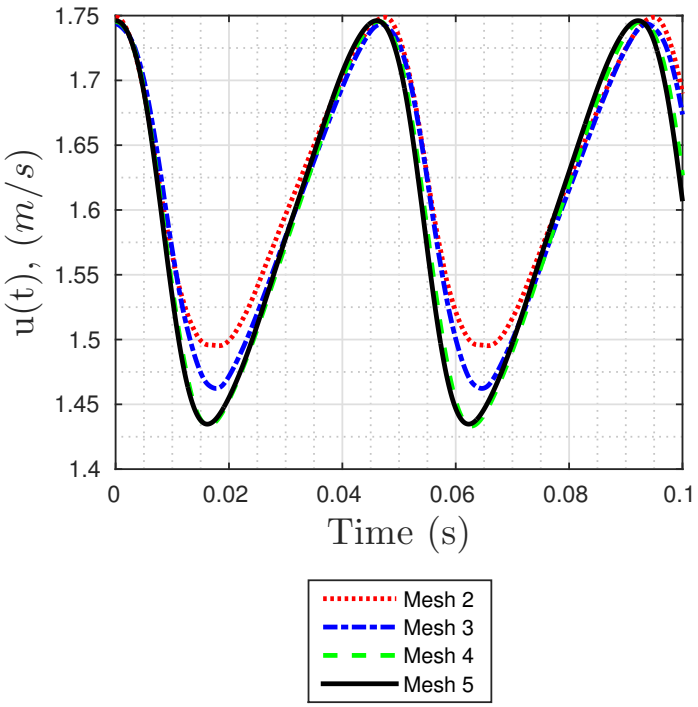

(a) Velocity near trailing edge of blockage at $(x = 1.25D, y = 0, z = 1.25D)$

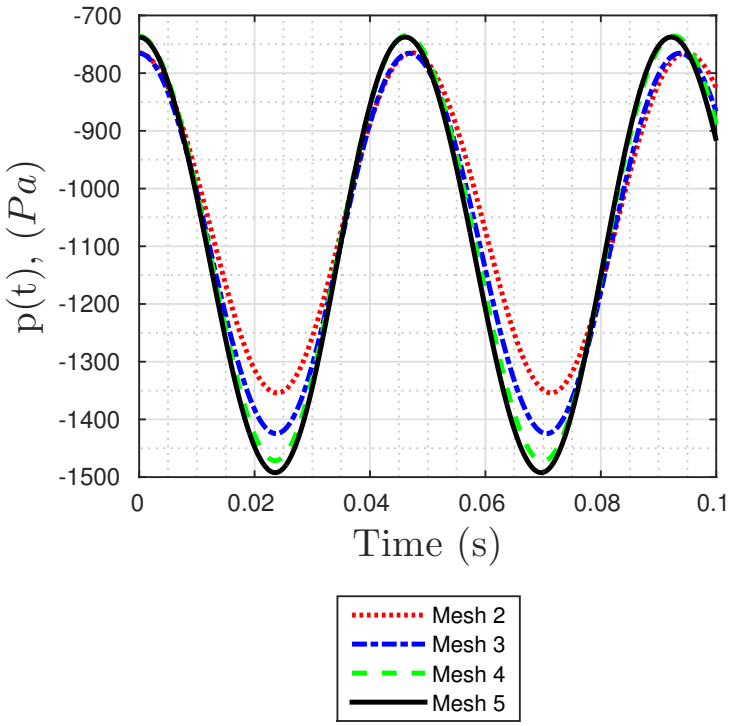

(b) Pressure at centre of cube side face at $(x = 0, y = 0, z = 0.5D)$

Figure 39: Change in fluctuating solution with mesh refinement, $EBRSM$, $Re_D = 10400$

was evident that these normalised residuals had ceased to change after a much smaller number of timesteps, where they fluctuated slightly around a steady value. Moreover, this steady value did not change from timestep to timestep. The criteria for convergence were then set at values near the end of the steep drop in magnitude for each residual, just as they reached their fully converged values. Time dependent fluctuations of the solution were found to be periodic and roughly sinusoidal in form; the solution was allowed to reach a statistically steady state where both the frequency and the amplitude of the oscillations remained constant.

5.6.3 Boundary Conditions

The solution from the unblocked channel simulations (Section 5.6.1.1) was extracted over a cross section of the domain, normal to the flow. This method allowed the fully-developed values for all solved-for variables to be fed in directly at the inlet, such that any change with progression into the domain was certainly due to effects introduced by the blockage downstream. Pressure on the inlet face was extrapolated from the nearest cell-centroids. Both velocity and pressure values on the outlet face were extrapolated from the nearest cell-centroid values using the reconstruction gradients. A no-slip condition was imposed on the velocity at each side wall and also on the blockage faces, where wall treatments were dependent on the particular model used. Pressure on these no-slip faces was extrapolated from the near-wall cells. The reference point for pressure was set at the centre of the inlet face in each case, where fluctuations were extremely small, typically less than 0.1% of the size of the fluctuations near the cube.

5.6.4 Domain Size

In order to estimate the streamwise domain lengths needed to eliminate boundary effects on the solution in the near-cube region, preliminary simulations were carried out on Mesh 4, (Table 10) with extrusions of different lengths added to the mesh both upstream and downstream. When upstream extrusions were added, the distance from the centre of the cube to the outlet, or downstream length, was fixed. The different distances from the inlet to the cube centre, or upstream lengths, that were trialled were $L_u = 12.5D$, $18.75D$ and $25D$. When downstream extrusions were added, the upstream length was fixed, and

the different distances from the cube centre to the outlet were $L_d = 15D$, $20D$, $25D$ and $50D$. The $k - \varepsilon$ model was chosen for this purpose. The pressure at the cube side and the streamwise velocity near the trailing edge (Figure 38) were recorded as for the mesh refinement.

Results are presented for $Re_D = 5600$. The pressure was more sensitive to the outlet length and the velocity was more sensitive to the inlet length. Fluctuations in both pressure and velocity had become nearly independent of the downstream length for $L_d > 25D$; the difference in the solutions with $L_d = 25D$ and $L_d = 50D$ was much smaller than the differences between the solutions with $L_d = 20D$ and $L_d = 25D$ (Figures 41a 41b), and was only $\sim 3\%$ the size of the fluctuations. As a result, L_d was set at $25D$ for all "final" simulations that were used for making comparisons with other models or data. Following the same reasoning, L_u was also set at $25D$ for "final" simulations, as the solution had become nearly independent of L_u at this length (Figures 40a, 40b). These distances were chosen for accuracy more so than practicality; they eliminated the inlet and outlet lengths as contributing variables while requiring more computational resources. It is clear that in many cases shorter inlet and outlet lengths would be sufficient for engineering purposes, for example $L_u = 12.5D$ and $L_d = 20D$. However, in terms of computational resources these inlet lengths did not make the simulations infeasible as the streamwise cell length could be stretched towards the inlets and outlets where streamwise gradients were low, while having insignificant effect on the results. The same size domain was used for "final" simulations at all three Re_D numbers.

5.7 DNS

All DNS calculations presented here were carried out using Incompact3d [35], an open-source code that was first introduced and described in [36]. This code is designed specifically for high-fidelity simulations of single-phase incompressible flows, and is adapted towards use on High Performance Computing Clusters [37]. The equations solved by Incompact3d may be expressed as:

$$\frac{\partial u_i}{\partial x_i} = 0 \tag{66}$$

$$\frac{\partial u_i}{\partial t} = -\frac{1}{2}\left(\frac{\partial u_i u_j}{\partial x_j} + u_j \frac{\partial u_i}{\partial x_j}\right) - \frac{\partial p}{\partial x_i} + \nu \frac{\partial^2 u_i}{\partial x_j^2} + f_i \tag{67}$$

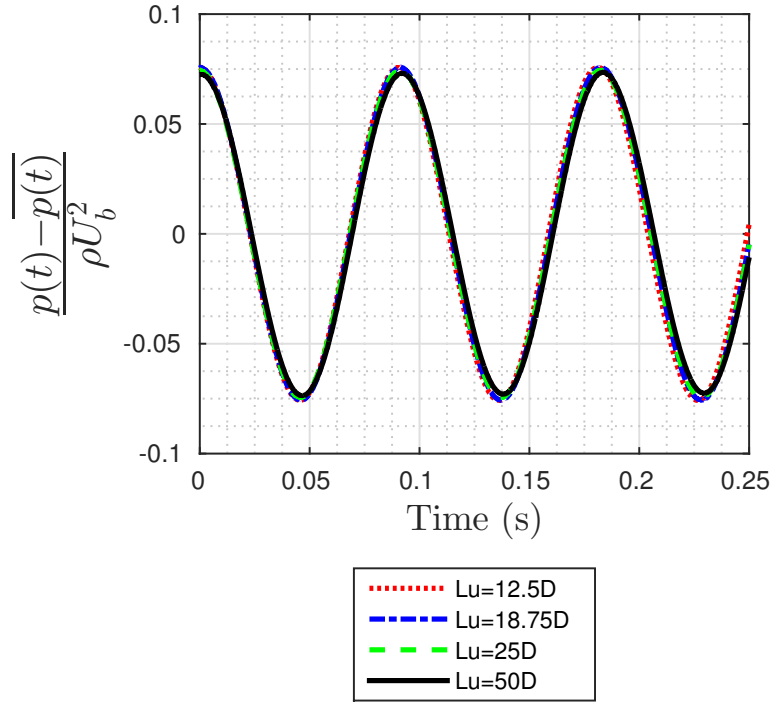

(a) Pressure at centre of cube side face at $(x = 0, y = 0, z = 0.5D)$

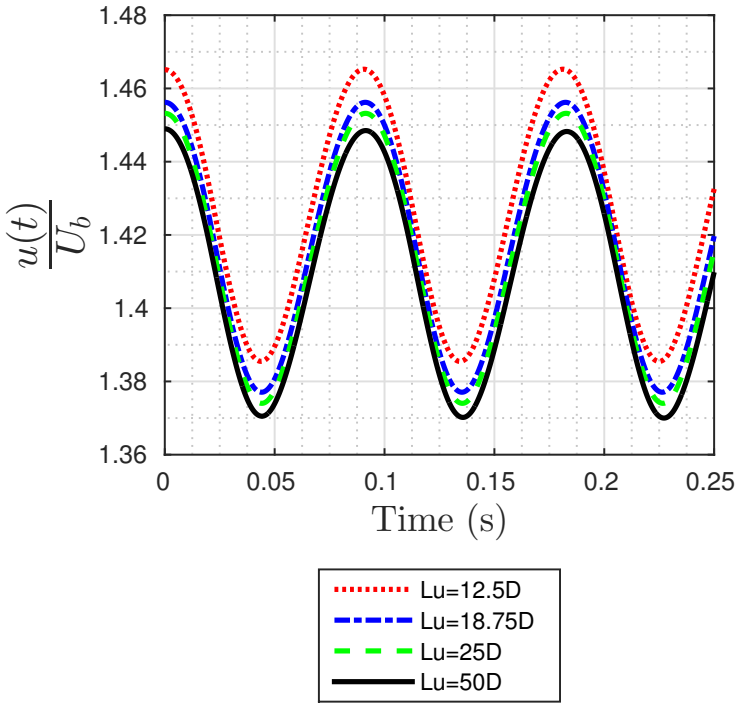

(b) Velocity near trailing edge of blockage at $(x = 1.25D, y = 0, z = 1.25D)$

Figure 40: Change in fluctuating solution with different inlet lengths, $k - \varepsilon$, $Re_D = 5600$

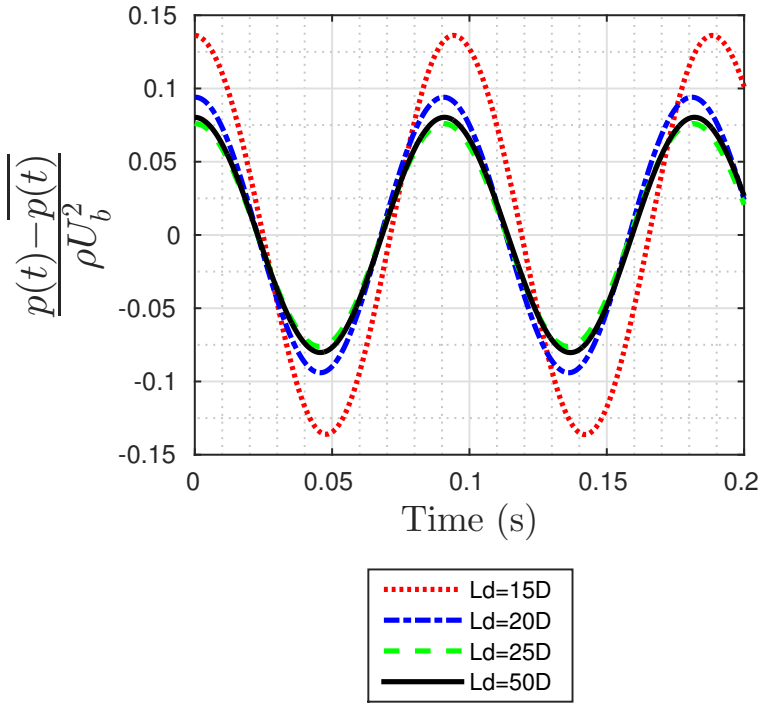

(a) Pressure at centre of cube side face at $(x = 0, y = 0, z = 0.5D)$

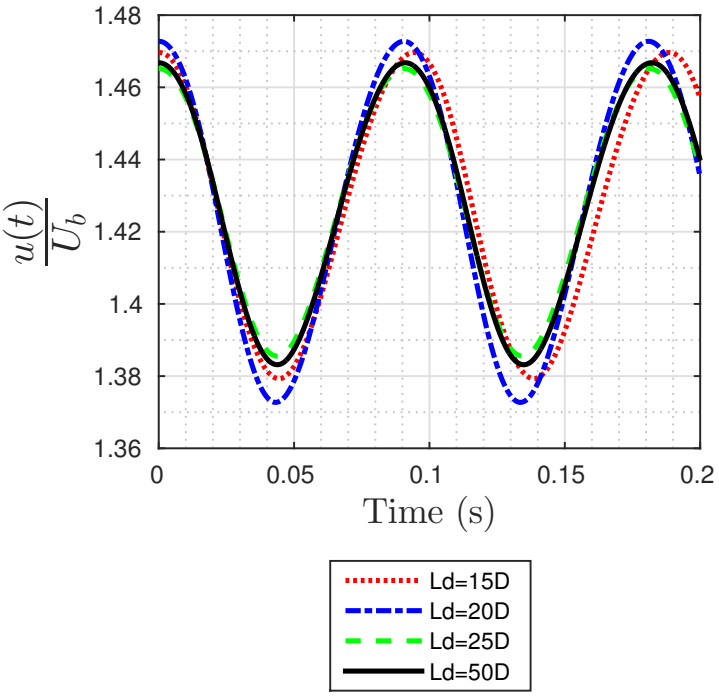

(b) Velocity near trailing edge of blockage at $(x = 1.25D, y = 0, z = 1.25D)$

Figure 41: Change in fluctuating solution with different outlet lengths, $k - \varepsilon$, $Re_D = 5600$

based on the Navier-Stokes equation in skew-symmetric form with a uniform density of $\rho = 1$ and with an external forcing function f_i. Gravitational forces are assumed to be negligible compared to the impulsive forces. Collecting together several terms to set:

$$F^k = -\frac{1}{2}\left(\frac{\partial u_i u_j}{\partial x_j} + u_j\frac{\partial u_i}{\partial x_j}\right) + \nu\frac{\partial^2 u_i}{\partial x_j^2} \tag{68}$$

the authors described the time advancement by means of a fractional step method:

$$\frac{u_i^* - u_i^k}{\Delta t} = a_k F^k + b_k F^{k-1} - c_k\frac{\partial \tilde{p}^k}{\partial x_i} + c_k \tilde{f}_i^{k+1} \tag{69}$$

$$\frac{u_i^{**} - u_i^*}{\Delta t} = c_k\frac{\partial \tilde{p}^k}{\partial x_i} \tag{70}$$

$$\frac{u_i^{k+1} - u_i^{**}}{\Delta t} = -c_k\frac{\partial \tilde{p}^{k+1}}{\partial x_i} \tag{71}$$

where the ˜ symbol overhead denotes an average value over a given sub-step:

$$\tilde{p}^{k+1} = \frac{1}{c_k \Delta t}\int_{t^k}^{t^{k+1}} p dt \tag{72}$$

$$\tilde{f}_i^{k+1} = \frac{1}{c_k \Delta t}\int_{t^k}^{t^{k+1}} f_i dt \tag{73}$$

The particular fractional step method employed was a third order Runge-Kutta type method. The scheme follows a description in [82], where a class of such methods is outlined based on criteria set on the coefficients. These criteria allow them to overwrite previously stored solution history at each sub-step while ensuring that there is no accumulation of the dominant round-off errors passing from sub-step to sub-step, hence reducing the necessary data held to one memory location for each position and velocity component. For this reason they are sometimes said to be "low-storage" methods. This is essential in the case of large simulations requiring many individual cells. The introduction of solid regions in the domain is achieved by an immersed boundary method, or IBM, where a velocity field is imposed on the solid region that satisfies the no-slip condition at the immersed boundary walls, using information obtained in the fluid region. This target velocity is set in such a way as to reduce spurious oscillations near the walls by improving the regularity of the solution in the immersed wall region [19]. Rather than continuity being strictly verified across the whole domain, the code solves a modified Poisson equation for the

pressure adjusted to allow for this modified velocity field:

$$\nabla^2 \tilde{p}_i^{k+1} = \frac{1}{c_k \Delta t} \frac{\partial (1-\varepsilon) u_i}{\partial x_i} \tag{74}$$

where ε is set to 0 and 1 outside and inside the solid body respectively. Notably, this means that continuity is still satisfied within the region that represents the physical fluid; the continuity may be violated only in the region that represents the immersed solid, which is free to act as a source/sink in the process of aiding regularity of the solution near the border between the two. In order to reduce computational cost, the pressure is obtained by solving a Poisson equation in spectral space making use of 3D FFT routines to greatly increase efficiency. Spatial discretisation follows a finite-difference method using compact schemes on Cartesian meshes that are of high order, allowing it to reduce the required number of computational cells relative to lower order methods; there is a reduction of a factor of two in each direction for the number of grid points. In the bulk, it employs a compact sixth-order formulation that requires five point stencils for both the first and second order derivatives. In the cases of symmetric, anti-symmetric and periodic boundary conditions the stencils are employed unmodified, with no ghost nodes required. They are not added in the case of no-slip boundaries either - rather single-sided formulations are used that are third order accurate for both first and second derivatives - making use of three and four stencil points respectively. At the second near most cells, fourth order accurate schemes are used before passing to full sixth order accuracy by the third cell.

5.7.1 Domain Size

The domain size was chosen based on a balance between the need to represent the same physics encountered in the experiments and practicality, as a great deal of computational resources were required. Based on the channel height $L_y = D$, the domain streamwise length was $L_x = 43D$, and the domain width was $L_z = 25D$, as in the experiments (Figure 42).

In order to achieve near-fully-developed flow conditions upstream of the blockage, there was a distance of $27D$ from the inlet to the upstream cube face. At each timestep, the velocity across the "recycling plane" $7D$ from the inlet was fed back into the inlet as

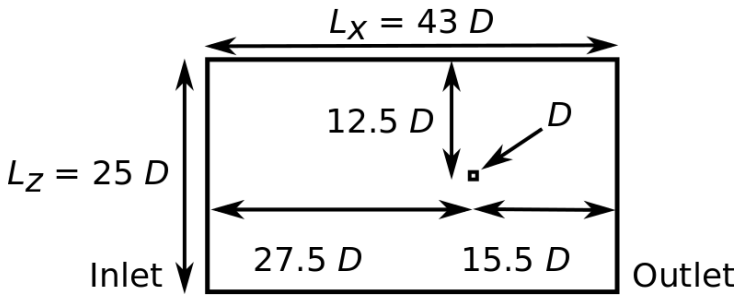

Figure 42: Channel dimensions and cube location for DNS simulation

the inlet boundary condition. This first $7D$ long "recycling region" part of the domain was used in order to simulate fully-developed flow as an inlet condition. Fully-developed turbulent channel flow in a wide rectangular duct at a similar Re was carried out in [34], where the outlet velocity at $x = 2\pi D$ was recycled on each timestep to provide the inlet velocity. These authors found that two-point correlations for all three velocity components were near zero $3.5D$ downstream of the inlet.

In the current study, initialisation of turbulence was provided by first running a coarser solution on a smaller domain. In this preliminary simulation, the solution was taken $5D$ downstream of the cube where turbulence had been triggered by interaction with the cube, and the turbulent flow was fed back into the inlet. Once this initial turbulent flow had passed once through the domain, a recycling plane was set $5D$ from the inlet and the solution was fed back into the inlet at each timestep. This simulation was allowed to develop until the entire field appeared turbulent, after the turbulence had spread to the domain edges. By this point, it had passed through the domain many times. This preliminary solution was then taken and interpolated onto the grid of the larger domain, and copied where necessary to fill the domain with turbulent flow. The simulation was then allowed to develop with the recycling plane set $7D$ from the inlet. The flow passed many times through the domain until the turbulence had spread throughout, such that the entire field appeared turbulent. From this point on, probes were employed to monitor the solution at various points in the domain, and statistics were collected to monitor development of the solution. It was not known a priori what effect the blockage would have on the solution in the recycling region; a small effect of the blockage on the solution at the recycling plane could feasibly become magnified as it is repeatedly fed back in at the inlet. The distance from the recycling plane to the blockage was $20D$; this was long enough to ensure that a URANS solution was nearly independent of inlet length in

a similar case (Section 5.6), when a fixed inlet profile was applied. After a number of shedding cycles, a mean velocity profile could be read at the recycling plane along the line $(x = 7D, y = 0, z)$. In a completely unblocked channel having the same boundary conditions this would be expected to be a simple straight line, but there was a very slight dip near the centre directly upstream of the block; mean velocity was plotted within the recycling plane, $7D$ from the inlet. As the dip was only approximately 1.4% of U_b, the upstream length was considered sufficient. From the downstream cube face to the outlet there was a distance of $15D$; there were no negative streamwise velocities at the outlet. URANS models at $Re_D = 5600$ had required slightly more than this for the fluctuating pressure at the cube side to become unaffected by the outlet boundary (Section 5.6), but the fluctuating velocity near the cube did not change much with a greater outlet length. Ideally, a larger outlet length would have been used, but it was necessary to control the domain length to reduce the cost of the simulation.

5.7.2 Meshing

The mesh used was Cartesian, having $n_x = 1025$, $n_y = 129$ and $n_z = 1024$, a total of 135M cells. Grid points were arranged in a regular fashion following x and z and the mesh was stretched in the y direction such that the mesh was very fine near the large channel walls.

5.7.3 Boundary Conditions

Boundary conditions for velocity in the streamwise direction were of the inflow/outflow type. At the inlet, the velocity was recycled as explained in the above section. At the outlet, streamwise velocity gradients were set to zero. At $y = \pm L_y/2$, a no slip Dirichlet condition was imposed on the velocity via u^* (Equation 69). At $z = \pm L_z/2$, a periodic boundary condition was applied on the velocity. For the pressure at the external boundaries, homogeneous Neumann conditions were imposed throughout. Within the immersed boundary region itself, a pressure field is calculated from the modified Poisson equation (Equation 74), where the right hand side is zero everywhere but right near the boundary.

5.7.4 Timestep

The CFL condition, necessary but not sufficient to guarantee stability of the numerical scheme, would have been met with a timestep of ~ 0.04, defined by $\Delta t = D/U_b$. However, a trial and error process was followed before settling on the final timestep size of 0.000625, as the timestep requirements were difficult to estimate a priori. Larger timesteps resulted in instabilities developing in the solution. The solution was monitored at several points within the domain and even the smallest fluctuations appeared very well resolved in time at the final chosen timestep, so it was considered that there was no need to further reduce it.

6 Computational Results

6.1 URANS

6.1.1 Fluctuating Pressure

The pressure at the centre of the side cube face, located at $(x = 0, y = 0, z = D/2)$, was used to make comparisons between the unsteady predictions of the two models, like in the experimental setup. All pressures were negative relative to the reference point which was set at the centre of the channel inlet $25D$ upstream of the blockage. Basic trends with respect to Re_D number were all as expected, that is to say that the amplitude, the magnitude of the mean value and the frequency of the oscillations increased with increasing flowrate for both models (Figures 43a, 43b, 43c). At $Re_D = 5600$ the results matched quite well in every respect. At $Re_D = 10400$ the frequencies matched quite well but the amplitudes and mean values did not. Again, at $Re_D = 15600$ the frequencies matched quite well but the amplitudes and mean values did not. At first glance, the graphs tend to follow an odd pattern; at $Re_D = 5600$ they overlay each other to a large extent with similar mean values, at $Re_D = 10400$ the $k-\varepsilon$ overlays the upper part of the $EBRSM$ plot with a higher mean, and yet at $Re_D = 15600$ the $k-\varepsilon$ appears to move back towards the mean value of the $EBRSM$ plot, overlaying a more central part of it. This apparent discrepancy is down to the great increase in amplitude of the $EBRSM$ fluctuations between the second highest and the highest Re_D numbers; the means carry on diverging from each other with increasing Re_D number but the $k-\varepsilon$ plot is nonetheless covered by the $EBRSM$ plot due to this huge increase in amplitude, that is to say that the $EBRSM$ peaks are much higher than those of the $k-\varepsilon$ and the troughs are also much lower.

6.1.2 Fluctuating Velocity

In order to compare the ability of the two unsteady models to predict the unsteady velocity fields, the streamwise velocity was monitored at $(x = 5D/4, y = 0, z = 5D/4)$. The same general trends were evident as in the fluctuating velocity, that is to say that frequency, mean values and amplitudes all increased with increasing Re_D (Figures 44a,

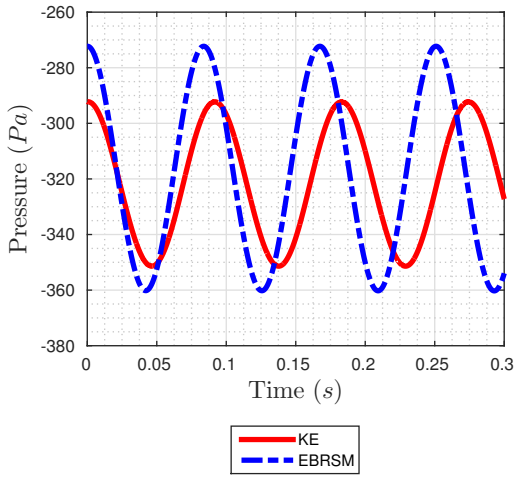

(a) $Re_D = 5600$

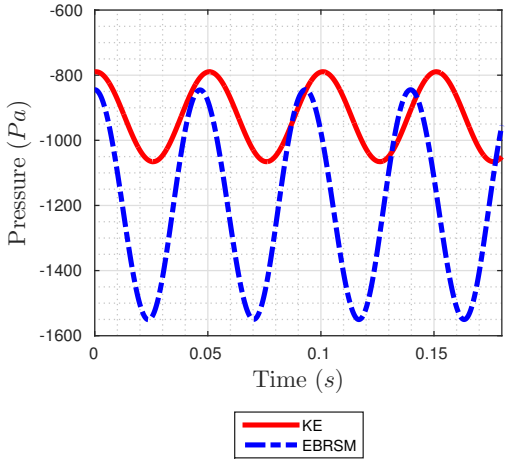

(b) $Re_D = 10400$

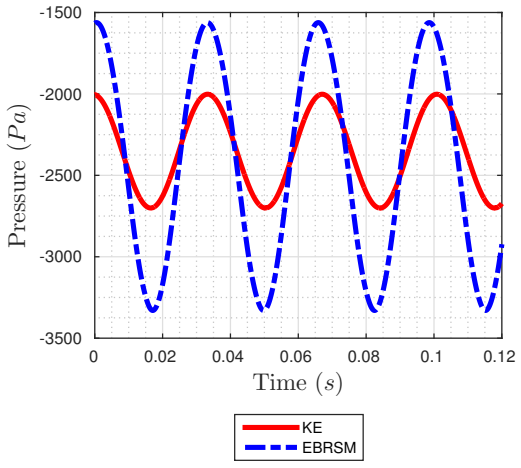

(c) $Re_D = 15600$

Figure 43: Fluctuating pressure at cube side $(x = 0, y = 0, z = 0.5D)$

Re_D	5600	10400	15600
ρU_b^2	520	1791	4030
Pressure Amplitude $k-\varepsilon\,(Pa)$	59	277	602
Pressure Amplitude $EBRSM\,(Pa)$	88	305	1769
Mean Pressure $k-\varepsilon\,(Pa)$	-322	-928	-2088
Mean Pressure $EBRSM\,(Pa)$	-316	-998	-2446
Period $k-\varepsilon\,(s)$	0.091	0.050	0.036
Period $EBRSM\,(s)$	0.084	0.047	0.033

Table 11: Fluctuating pressure at cube side ($x=0, y=0, z=D/2$), $k-\varepsilon$ vs $EBRSM$

Re_D	5600	10400	15600
U_b	0.722	1.34	2.01
u amplitude $k-\varepsilon\,(m/s)$	0.0499	0.118	0.186
u amplitude $EBRSM\,(m/s)$	0.0879	0.311	0.645
Mean $u\,k-\varepsilon\,(m/s)$	0.887	1.62	2.27
Mean $u\,EBRSM\,(m/s)$	0.912	1.58	2.17

Table 12: Fluctuating streamwise velocity behind trailing edge, $k-\varepsilon$ vs $EBRSM$

44b, 44c). Unlike in the case of the pressure discussed above (Section 6.1.1), the relative trends in mean value were clear; the mean predicted by the $EBRSM$ was slightly lower at the lowest flowrate, slightly higher at the central flowrate and higher still at the highest flowrate (Table 12). The scale on the graph was chosen in order to make clear the relative size of the fluctuations, which make the differences in the mean values appear exaggerated; the relative difference in the means was 5%, 2.4% and 11% at $Re_D = 5600$, 10400 and 15600 respectively.

6.1.3 Flow Structure Overview

The mean flow structure in the immediate cube vicinity consists of several key features, centred around vortex cores, which may be loosely grouped into upstream, side and downstream sections (Figure 45). The particular method used to find the vortex cores is that introduced in [67]. This work makes use of the "jerk vector" $\mathbf{b}$, the components of which are defined by:

$$b_i = \frac{D^2 u_i}{Dt^2} \tag{75}$$

The author summarised the methodology in the following manner: "the core line is the location of all points where $\mathbf{b}$ is parallel to $\mathbf{u}$". One of the principal advantages of defining vortex core lines in this manner is that second-order derivatives of the velocity are sufficient

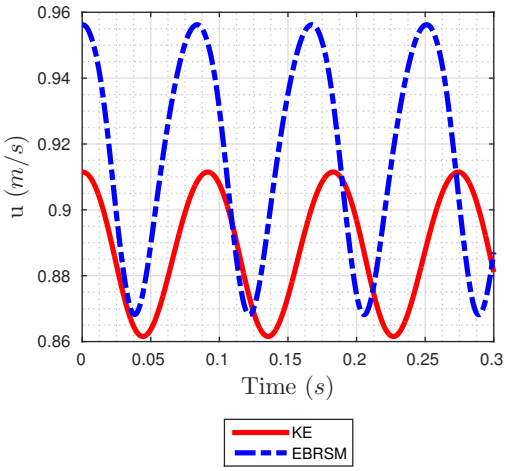

(a) $Re_D = 5600$

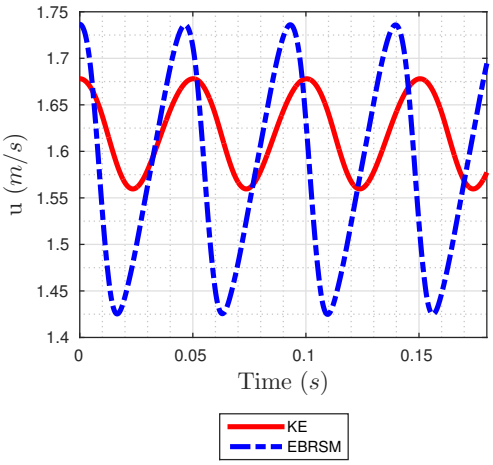

(b) $Re_D = 10400$

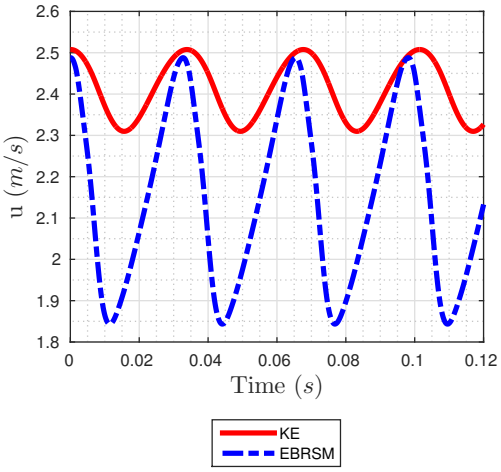

(c) $Re_D = 15600$

Figure 44: Fluctuating streamwise velocity behind trailing edge at $(x = 1.25D, y = 0, z = 1.25D)$

as opposed to the the third-order derivatives needed for a more mathematically rigorous approach. The inaccuracy inherent in this methodology is only present where core lines are strongly curved. Core lines are near-straight where quantitative comparisons are made between the various simulations and/or experiments. Upstream of the cube, the mean flow impinges on the block and flows out to the sides in the z direction, but is constrained by the channel walls at $y = \pm\frac{D}{2}$, causing it to flow back on itself near the channel walls, resulting in "upstream vortices". The upstream vortices are therefore roughly analogous to those observed upstream of the cube in [49], that is to say they consist of flow moving down from the centreline and back out along the channel floor. However, due to the extra degree of symmetry about $y = 0$ they appear in pairs. The "side vortices" may be viewed as the result of simultaneous shear within two perpendicular planes. Firstly, sharp velocity gradients in the xz planes just behind the leading edges create the beginnings of a recirculation bubble similar to that shown in [48]. Secondly, shear in the xy planes due to the channel walls deforms what would otherwise be a vortex aligned in the y direction, such that the vortex cores follow a horseshoe shape with a break in the centre, attached near the upper and lower corners at the leading edges of the cube. These side vortices that appear separated in the mean velocity field appear to be joined at certain parts of the cycle such that the vortex core passes the $y = 0$ plane. At other parts of the cycle, this critical point does not appear as the fast moving flow washes away the recirculation bubble. The "rear vortices" may be viewed as representing the statistically preferential locations of vortices behind the cube that are separated in time, rather than the location of two vortices separated in space that appear simultaneously. This is evident in the instantaneous velocity (Figure 46), where often only one vortex core appears behind the cube at one time; this vortex location tracks from side to side and moves away downstream following the dominant shedding period. There is a small part of the shedding cycle during which two weak individual vortices are present (Figure 47) but one of these is soon dissipated as it is washed downstream. As this process takes place twice per cycle, on opposite sides of the symmetry plane at $z = 0$, there are two mean vortices.

Some differences in the overall structure of the calculated flow field may be highlighted by plotting contours of the mean velocity, beginning from near the leading edges, passing the cube, and throughout the recirculation region together. In the $y = 0$ plane that is $\pm\frac{D}{2}$ from the large channel faces, the shape of the contour $U = 0$ is different in the $k - \varepsilon$

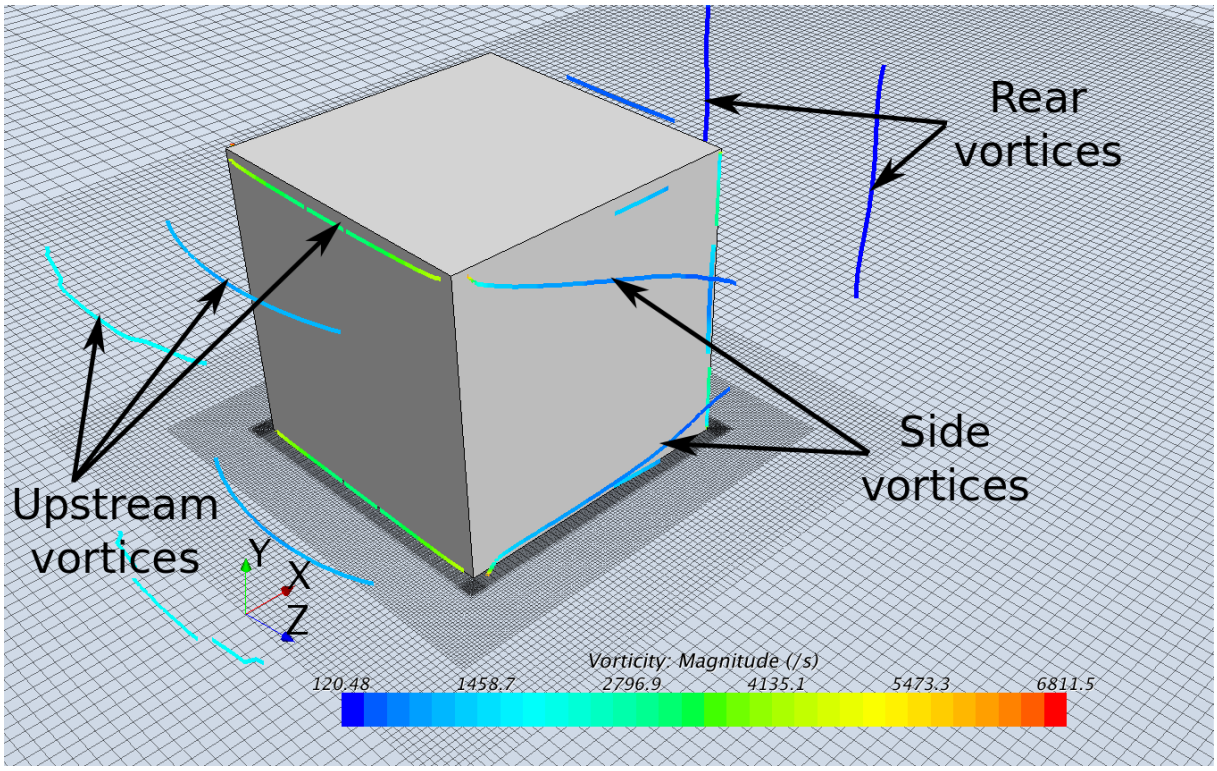

Figure 45: Mean vortex cores in the cube vicinity

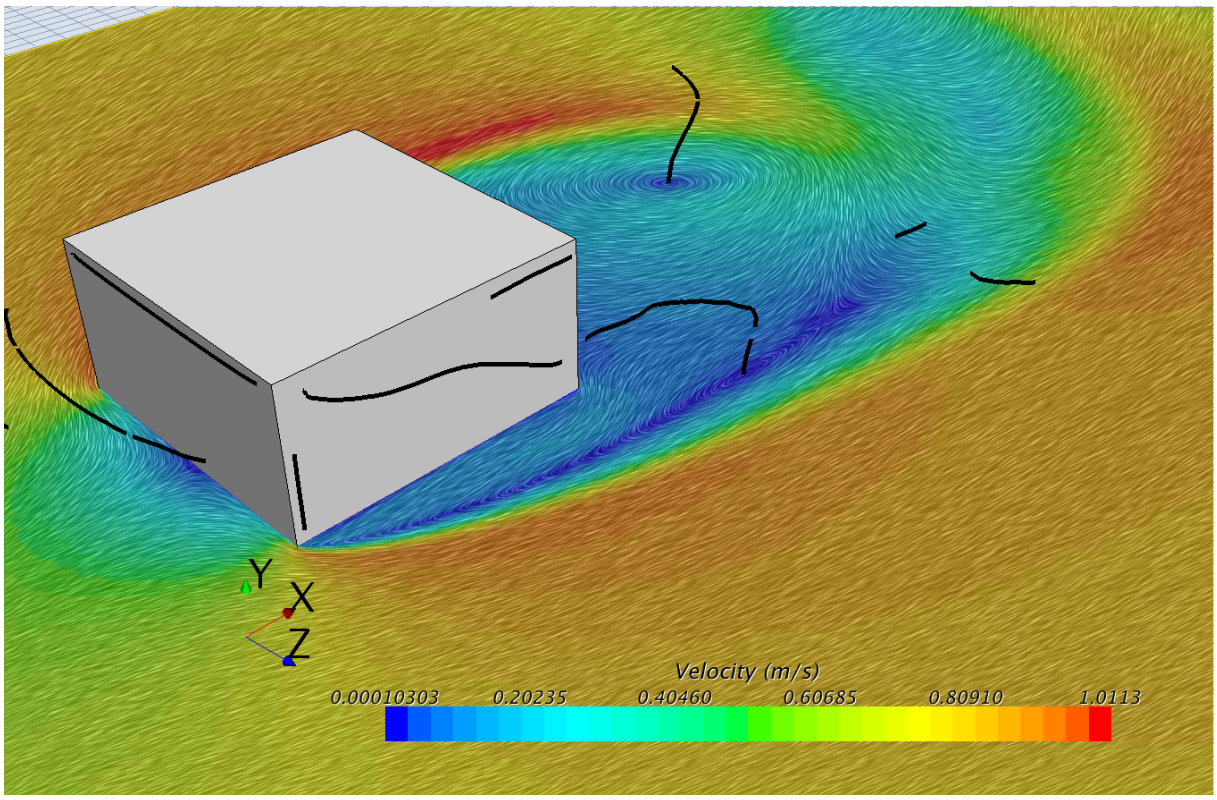

Figure 46: Instantaneous flow in the cube vicinity, showing vortex cores and their intersection of the velocity field in the plane parallel to the large faces that bisects the duct at $y = 0$

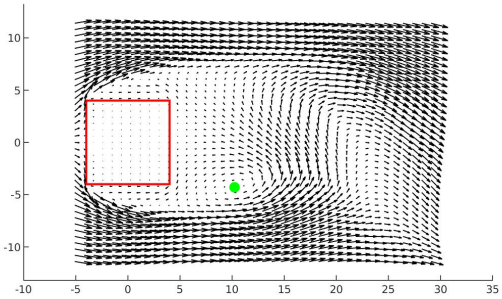

(a) Snapshot 1

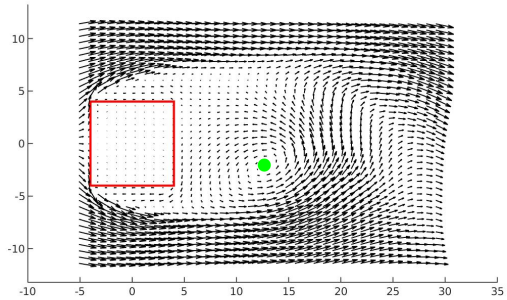

(b) Snapshot 2

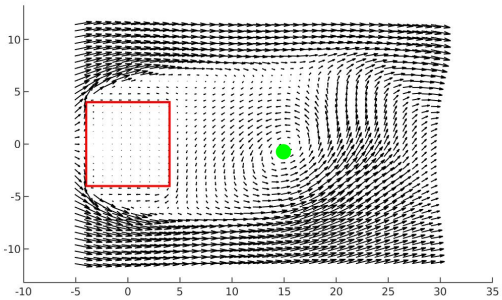

(c) Snapshot 3

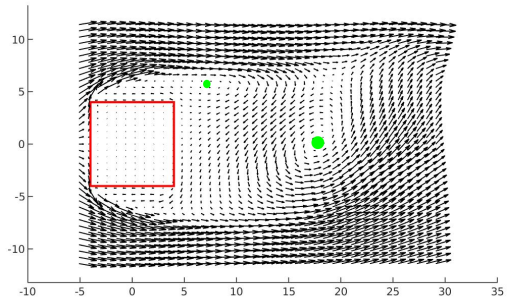

(d) Snapshot 4

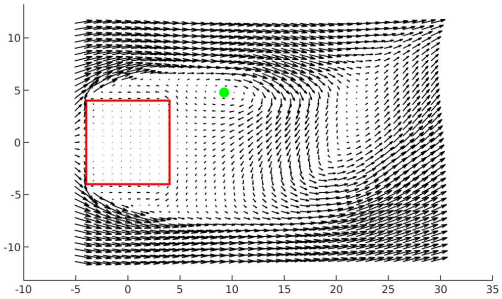

(e) Snapshot 5

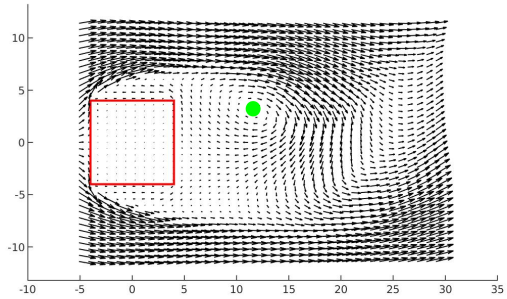

(f) Snapshot 6

Figure 47: Snapshots of instantaneous velocity showing location of main vortex cores at different phases, from beginning of period to halfway through. $EBRSM$, $Re_D = 5600$

Re_D	5600	10400	15600
L_{rexp}	$20.2mm \pm 0.1mm$	$18.7mm \pm 0.1mm$	$17.8mm \pm 0.1mm$
$L_{rk-\varepsilon}$	$22.1mm$	$20.3mm$	$19.6mm$
L_{rEBRSM}	$19.2mm$	$11.3mm$	$9.8mm$

Table 13: Recirculation length, $k - \varepsilon$ vs $EBRSM$

simulations (Figures 48a, 49a) to the $EBRSM$ simulations (Figures 48b, 49b). One way of quantifying this is to look at the recirculation length, L_r, defined as the length along the centreline at $(y = 0, z = 0)$ at which the mean streamwise velocity drops to 0 (Figure 48a). Results for L_r are summarised in Table 13. At $Re_D = 5600$, the recirculation length predicted by the $k - \varepsilon$ model is longer than that predicted by the $EBRSM$ model; the difference is more noticeable at $Re_D = 10400$ and even more so at $Re_D = 15600$. Both models follow the general trend of a decreasing L_r with increasing Re_D. The shapes of the recirculation region, bounded by $U = 0$ are also noticeably different, with the $k - \varepsilon$ model showing a sharp return of the contour towards the centreline just after the cube before a longer, more slender recirculation region appears, whereas the $EBRSM$ predicts a smoother overall shape.

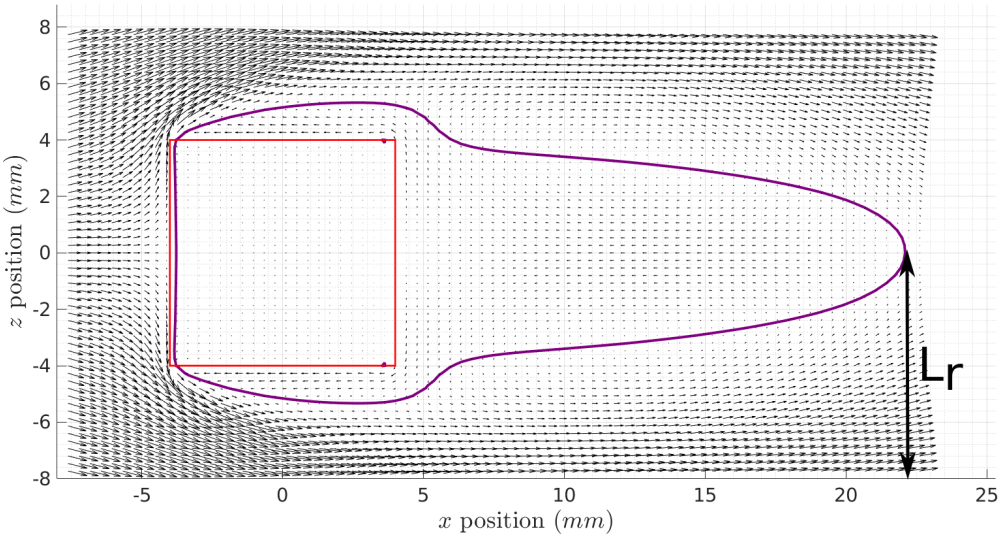

(a) $k - \varepsilon$

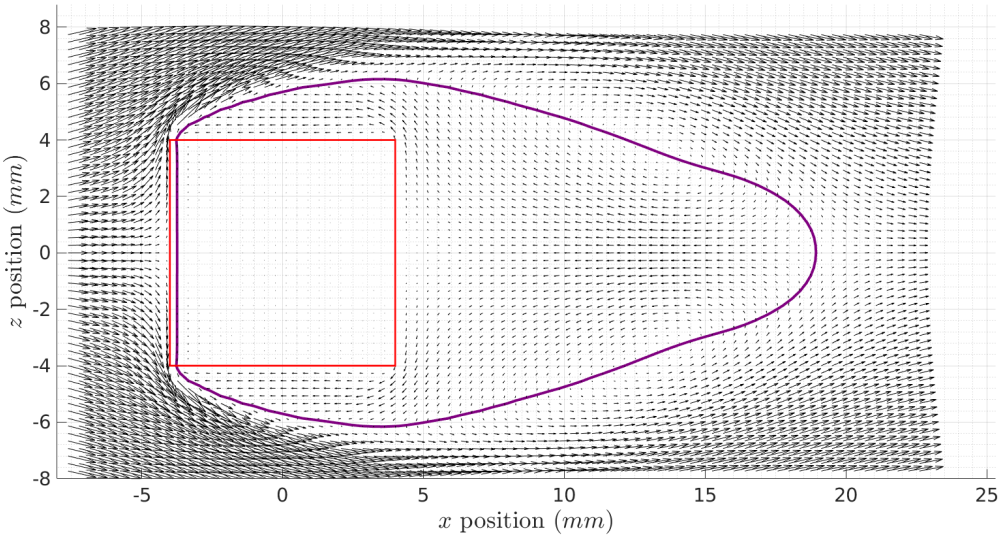

(b) $EBRSM$

Figure 48: Contour $U = 0$ within plane $y = 0$, $Re_D = 5600$

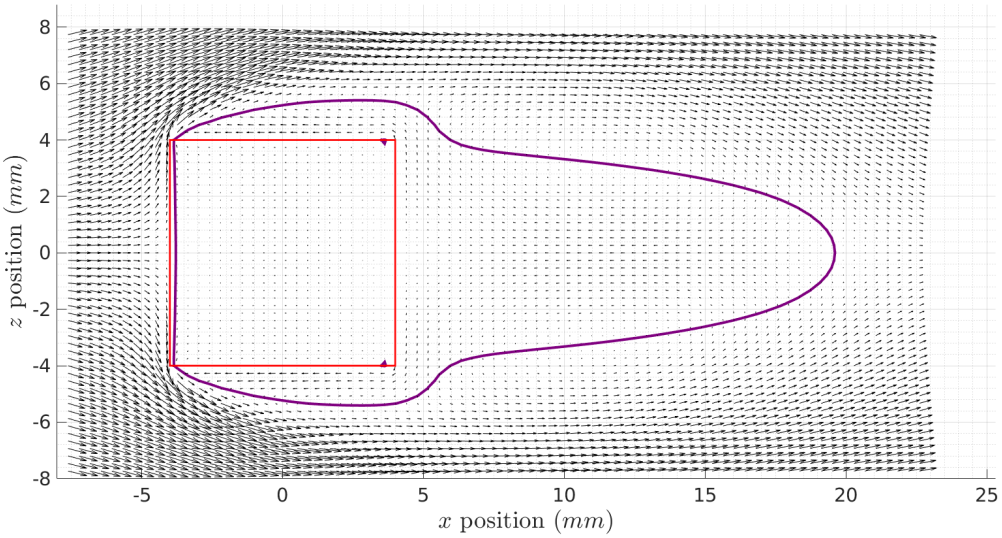

(a) $k - \varepsilon$

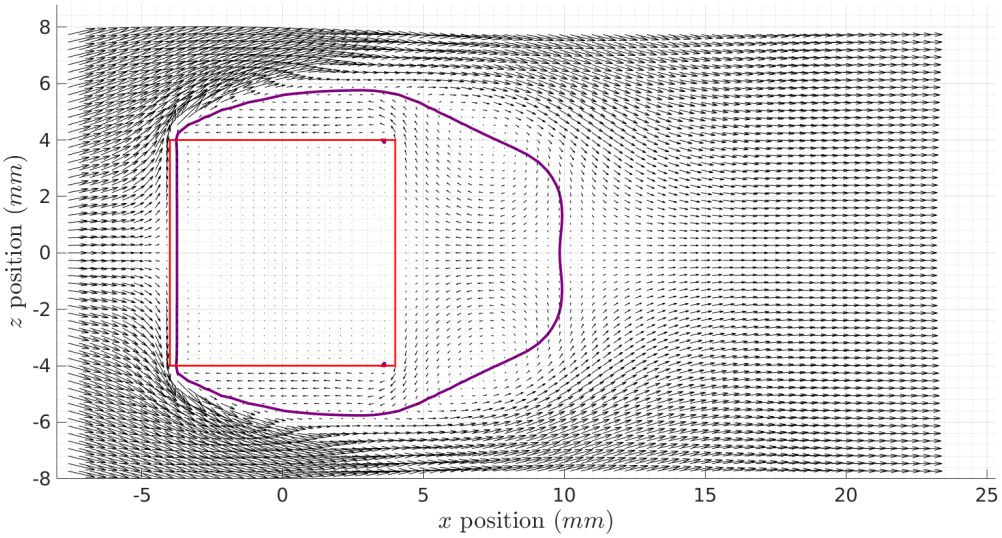

(b) $EBRSM$

Figure 49: Contour $U = 0$ within plane $y = 0$, $Re_D = 15600$

6.1.4 Solution Upstream

Upstream of the blockage, there are already differences between the $k-\varepsilon$ and $EBRSM$ models. The fully developed solutions showed differences of only $\sim 1.4\%$ in the centreline velocity at $(y = 0, z = 0)$. Vector plots of velocity upstream of the cube in the plane $y = 0$ show very little difference in the solutions. However, velocity in the plane $z = 0$ (Figures 50a and 50b) shows clear differences in the size of the z aligned vortices.

This is not surprising given that the $k-\varepsilon$ model used does not account for anisotropy in the Reynolds stress field. For illustration, in fully developed duct flow, an inability of a model to allow for Reynolds stress anisotropy in planes normal to the flow results in an inability to predict corner vortices that are aligned with it, [58], which motivated the development of Explicit Algebraic Reynolds Stress methods [28] and non-linear $k-\varepsilon$ models [76]. In 3D flow regions of high shear and highly anisotropic fields for both velocity and Reynolds stresses, this effect should also be expected to result in different predictions for vorticity. One way of highlighting this is to compare the results for turbulent kinetic energy (Figures 51a and 51b), where k for the $EBRSM$ model is calculated as the trace of the Reynolds stress tensor; the three diagonal elements involved are not in general equal. Differences in the value of k in the boundary layer exist already in unblocked channel flow (Section 5.6.1.1), but not at the centre line. Just upstream of the cube, a large increase in k is predicted by the $k-\varepsilon$ near the centreline which does not appear in the $EBRSM$ simulation. This is due to the well-known "stagnation point anomaly" [17], an issue that results in high values for k at stagnation points.

Unlike the comparison made in the plane $z = 0$, the $k-\varepsilon$ and $EBRSM$ mean velocity fields appear to show very good qualitative agreement on the $y = 0$ plane(Figures 52a, 52b). This is to be expected as transport in this faster-moving fluid is dominated by convection, whereas in the the $z = 0$ plane slower-moving fluid and high k values near the channel walls induces the Reynolds stresses to play a larger part.

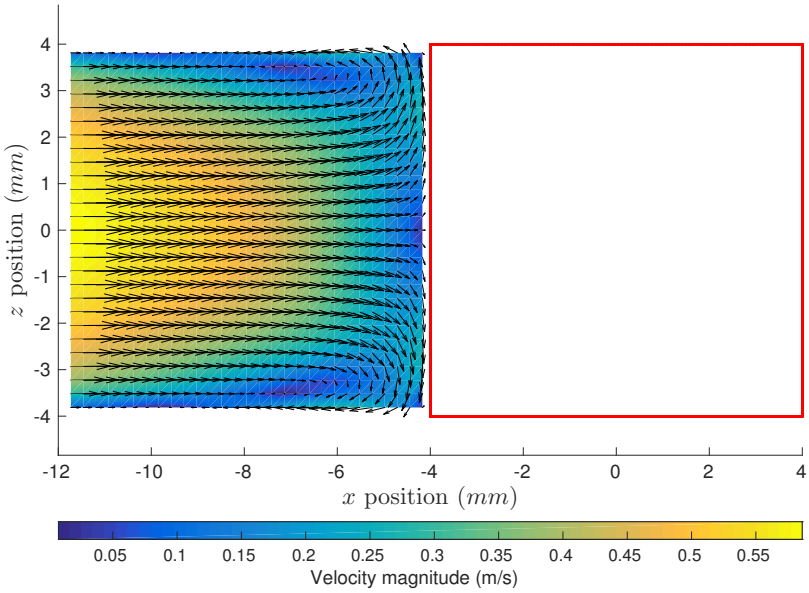

(a) $k - \varepsilon$

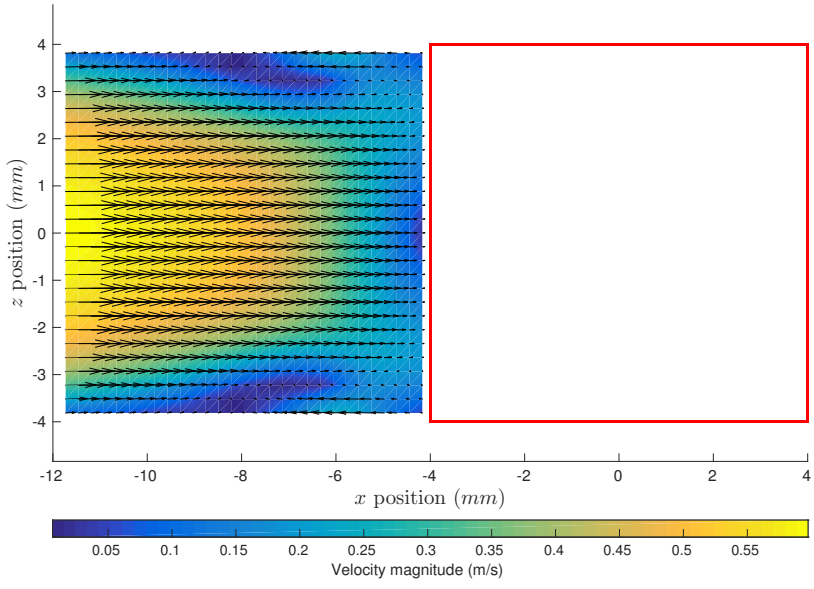

(b) $EBRSM$

Figure 50: Mean velocity upstream of the blockage in the plane $z = 0$,$Re_D = 5600$

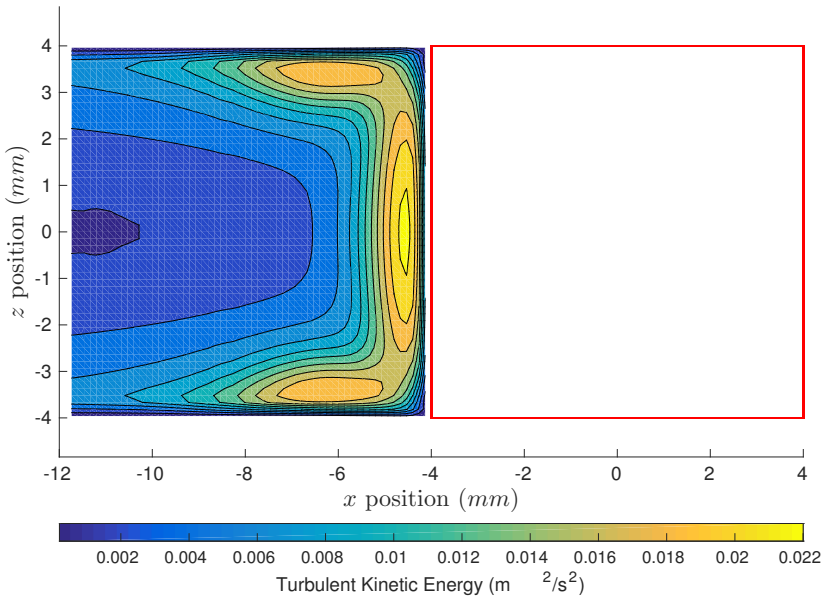

(a) $k - \varepsilon$

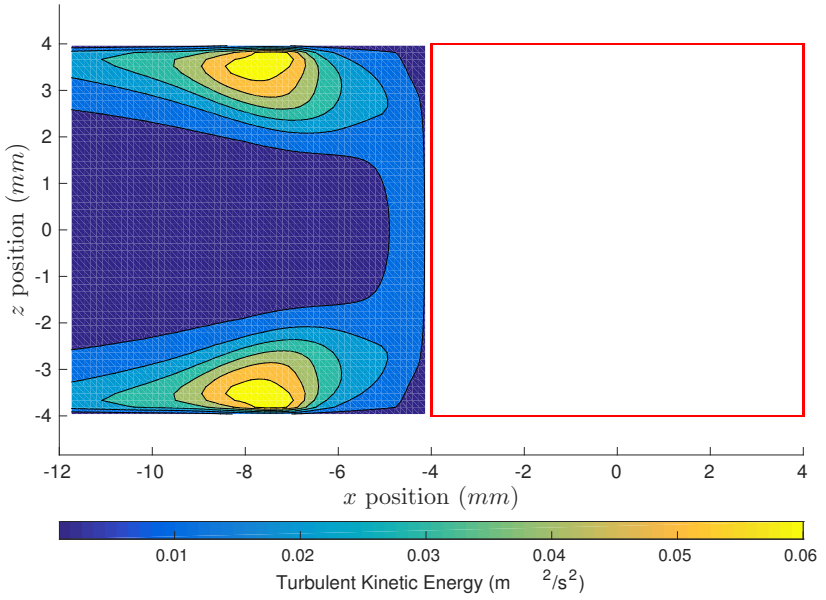

(b) $EBRSM$

Figure 51: Mean Turbulent Kinetic Energy upstream of the blockage in the plane $z = 0$, $Re_D = 5600$

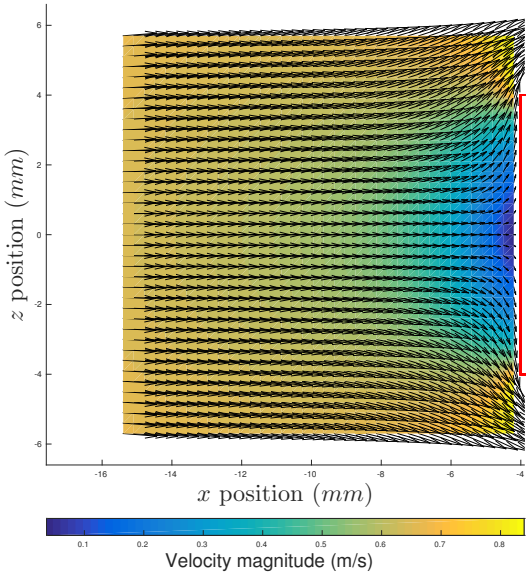

(a) $k - \varepsilon$

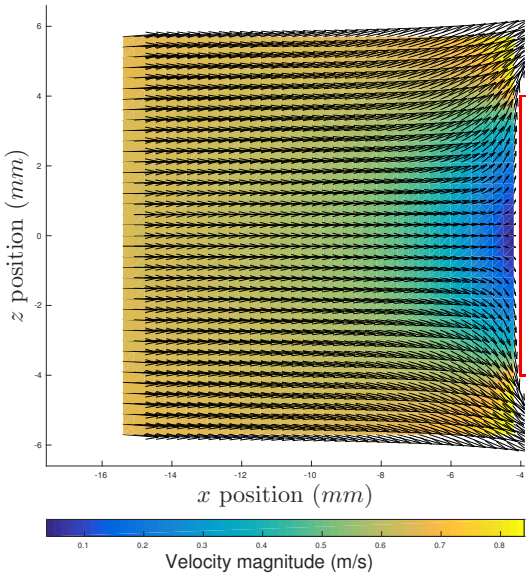

(b) $EBRSM$

Figure 52: Mean velocity upstream of the blockage in the plane $y = 0$,$Re_D = 5600$

Re_D	5600	10400	15600
$k-\varepsilon$	$(\pm 2.8mm, \pm 5.1mm)$	$(\pm 2.75mm, \pm 5.1mm)$	$(\pm 2.9mm, \pm 5.1mm)$
$EBRSM$	$(\pm 2.95mm, \pm 4.85mm)$	$(\pm 2.7mm, \pm 4.9mm)$	$(\pm 3.15mm, \pm 4.70mm)$

Table 14: (y, z) location of intercept between mean vortex cores of side vortices and plane $(x = 0, y, z)$, to nearest $0.05mm$

6.1.5 Solution near the Cube Sides

The vortex cores associated with the mean "side vortices" (Figure 45) extend from the leading corners downstream and towards the plane $y = 0$ where they approach each other but do not meet. As such, there is no clear point in this plane that may be said to characterise their location. Contrarily, comparison of the mean velocity in the plane $x = 0$ (Figures 53a, 53b) yields the locations of the two vortex strands and provides information regarding gradients due to the combined effects of both the cube sides and the channel walls. The coloured mean velocity magnitudes highlight how the flow may be separated into two main cells; one cell consists of slow moving fluid through which the side vortices pass and the other is fast moving where streamwise motion dominates the flow. Within the slow region, a zone of near-stagnant fluid stretches from near the uppermost corner to the lowermost, following a curved horseshoe form, maintaining it's distance from the wall near the central plane region. This basic pattern is unchanged at the highest Reynolds number (Figures 55a, 55b). However, at each Reynolds number the horsehoe forms appear slightly different for the $k-\varepsilon$ and $EBRSM$ models. A pocket of faster moving fluid sandwiched between near-stagnant fluid and the cube flows in the anti-streamwise direction back past the cube faces (Figure 54).

As outlined above (Section 6.1.4, the velocity predictions from the $k-\varepsilon$ and $EBRSM$ in general match quite well upstream of the cube in the central $y = 0$ plane. Much larger differences are seen in the region of the cube side, and may be seen to have a knock-on effect in the recirculation region. Contours of $U = 0$ from near the cube's leading edges to the recirculation region (Figures 48a and 48b) show a side recirculation bubble that extends much further downstream for the EBRSM model at $Re_D = 5600$.

The same comparison made at $Re_D = 15600$ shows better agreement in one respect, essentially the recirculation bubble tucks in behind the cube at a shorter distance downstream for the $EBRSM$ model, bringing it more in line with the $k-\varepsilon$ model (Figures

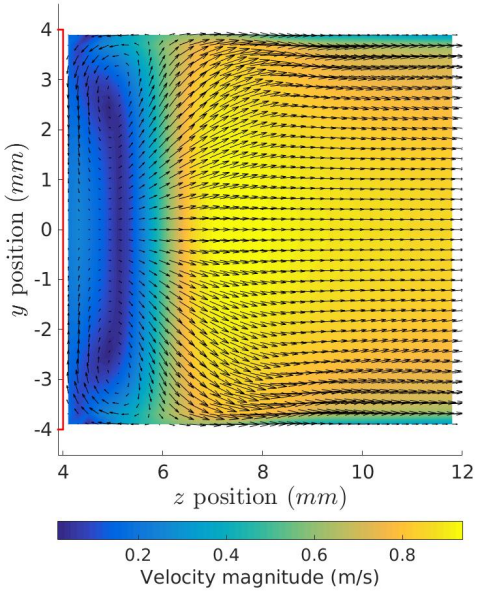

(a) $k - \varepsilon$

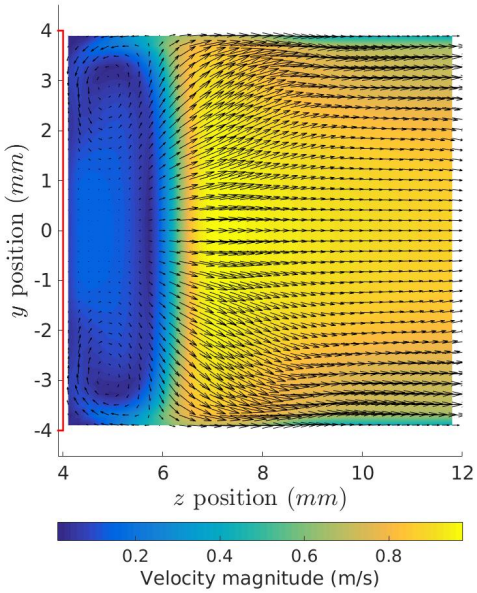

(b) $EBRSM$

Figure 53: Mean velocity to the cube side in the plane $x = 0$, $Re_D = 5600$

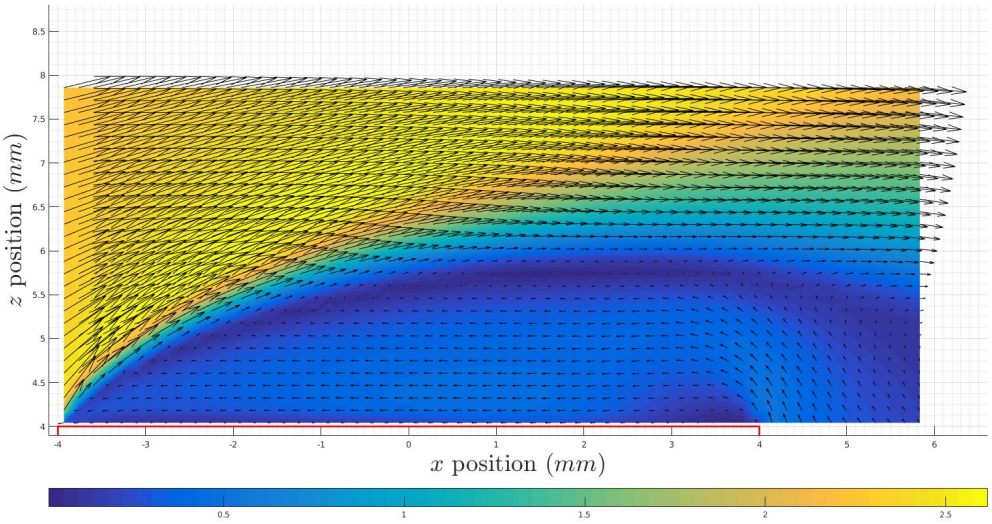

Figure 54: Mean velocity to the cube side in the plane $y = 0$, $EBRSM$, $Re_D = 15600$

49a and 49b). However, beyond this the downstream solution is quite different.

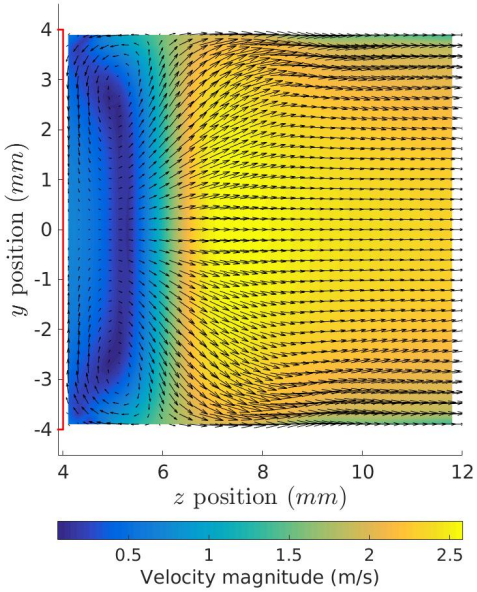

(a) $k - \varepsilon$

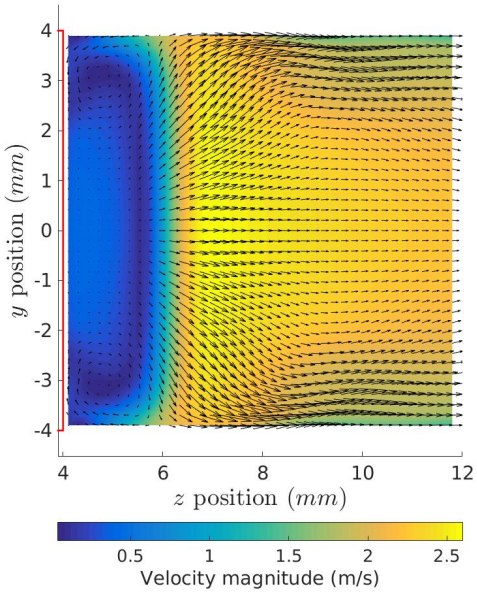

(b) $EBRSM$

Figure 55: Mean velocity to the cube side in the plane $x = 0$, $Re_D = 15600$

6.1.6 Solution in the Recirculation Region

Whereas upstream of the cube, the mean flow was very similar in structure, in the flow past the cube differences appeared. This is particularly evident in the $z = 0$ plane within the recirculation zone. This region is bordered in each case by a crescent shaped pocket of slow moving fluid, downstream of which streamwise components are all positive (Figures 56a,56b,57a,57b). Within the recirculation zone, the $k - \varepsilon$ model predicts the separation of the fastest-moving flow into two separate cells above and below the central $y = 0$ plane, whereas the $EBRSM$ predicts a single fast moving pocket of fluid that forms a crescent shape with the largest velocity magnitudes found near the central plane.

In order to further highlight these differences, contours of the mean velocity magnitude may be plotted (Figures 58a,58b, 59a,59b). The basic structure is the same for each model at the two different Reynolds numbers, although each feature is closer to the cube at $Re_D = 15600$. Due to the very short recirculation zone predicted by the $EBRSM$ at $Re_D = 15600$, the zone of high velocity magnitude is smaller and the magnitude not so high.

6.2 DNS

The DNS simulations required large computational resources to run and as a result not many shedding cycles could be captured in time to form a fully statistically converged dataset; mean values for the velocity showed unexpected asymmetry. This means that the quantitative comparisons that can be made are limited in accuracy, but it is nonetheless possible to see certain basic patterns in the solution that may serve to compare the URANS models with. All positions are converted to mm, and the velocities are presented in normalised form.

6.2.1 Flow Structure Overview

Contours of the time-averaged streamwise velocity $U = 0$ in the near cube region within the plane $y = 0$ are sufficiently well formed to compare the URANS solution with (Figure 60). The recirculation length L_{rDNS} is equal to $19.7mm \pm 0.1mm$, which is closer to that predicted by the experiments and the $EBRSM$ model than it is to the $k - \varepsilon$ calculation (Table 13). The general shape of the recirculation region in $y = 0$ matches better with

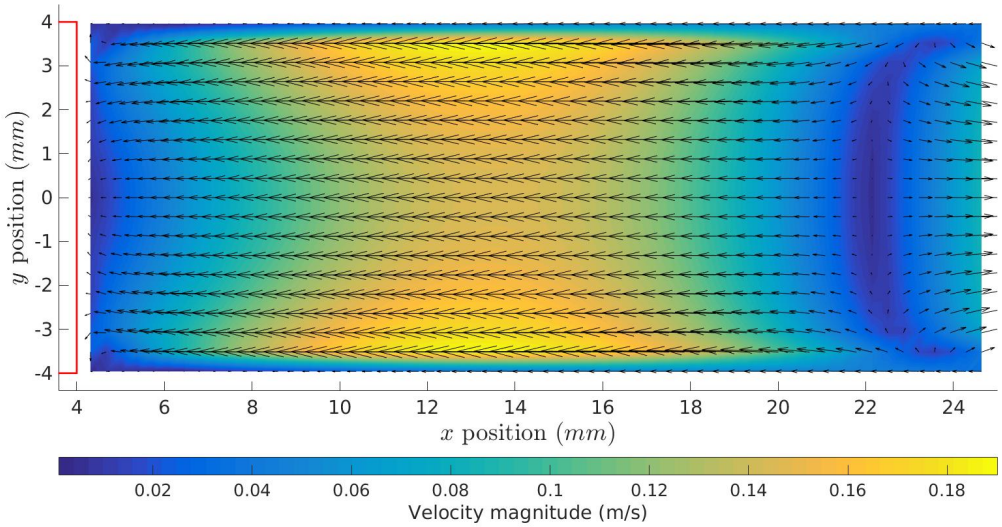

(a) $k - \varepsilon$

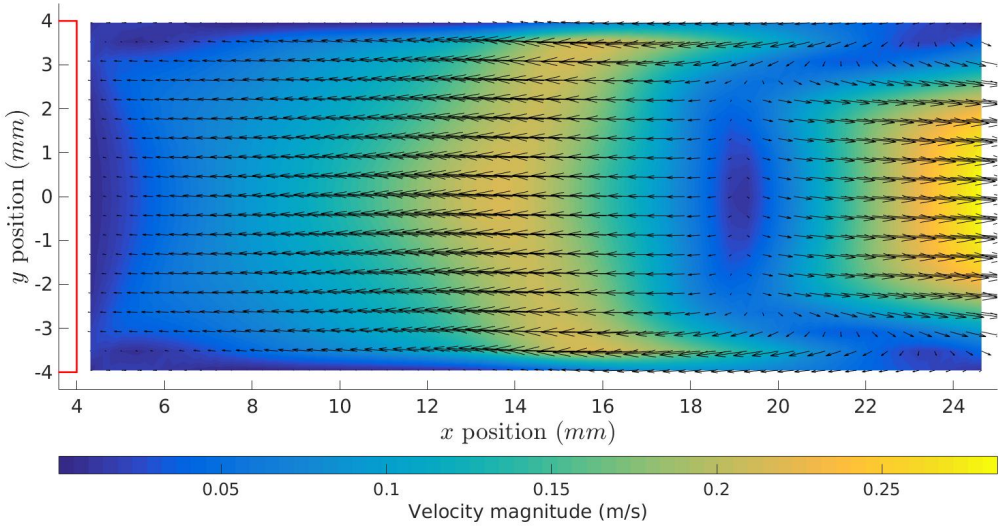

(b) $EBRSM$

Figure 56: Mean velocity downstream of the blockage in plane $z = 0$, $Re_D = 5600$

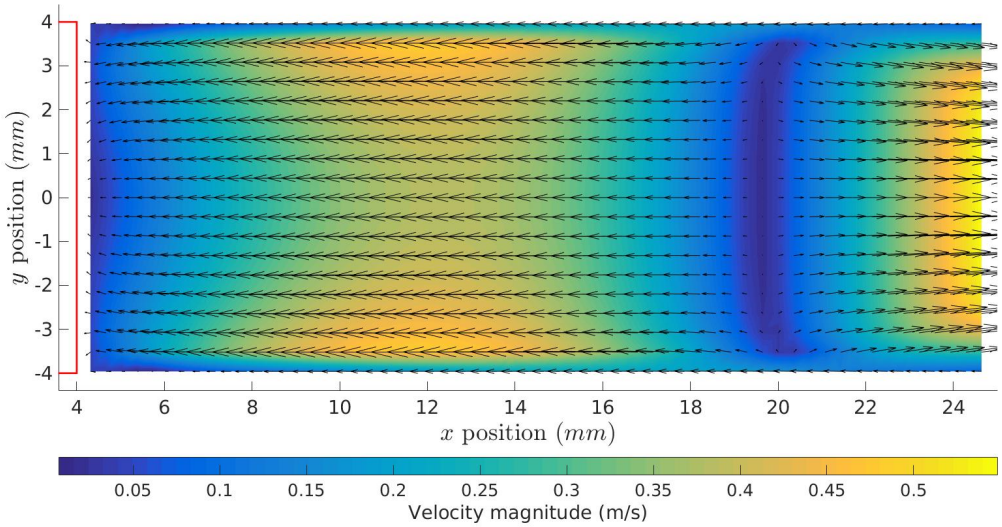

(a) $k - \varepsilon$

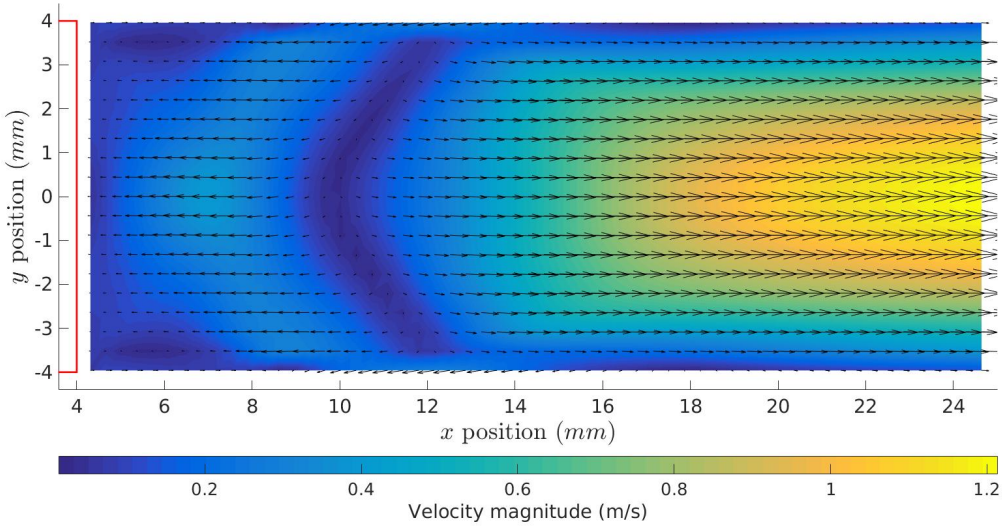

(b) $EBRSM$

Figure 57: Mean velocity downstream of the blockage in plane $z = 0$, $Re_D = 15600$

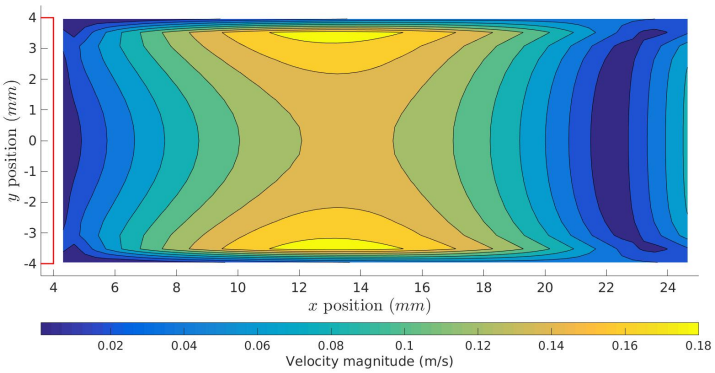

(a) $k - \varepsilon$

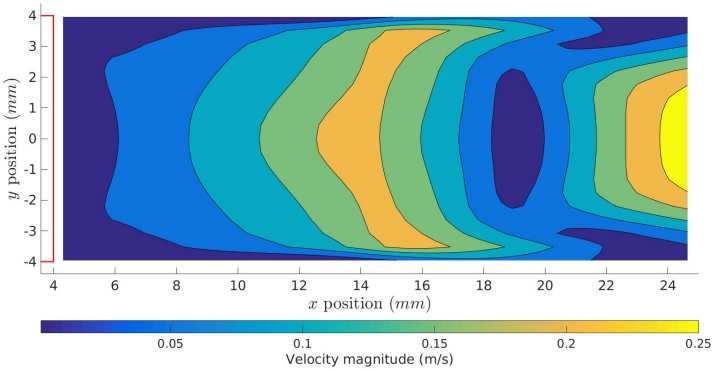

(b) $EBRSM$

Figure 58: Mean velocity contours downstream of the blockage in the plane $z = 0$, $Re_D = 5600$

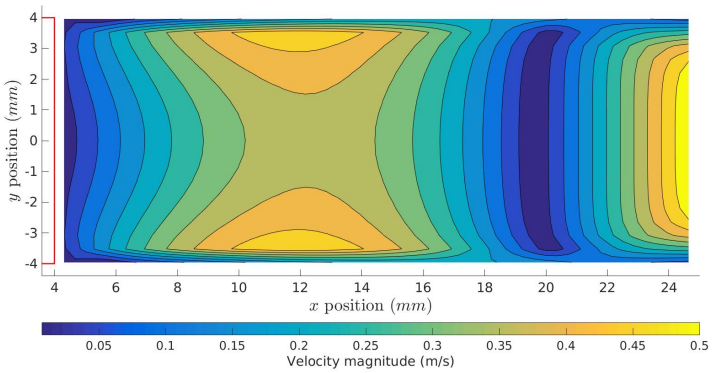

(a) $k - \varepsilon$

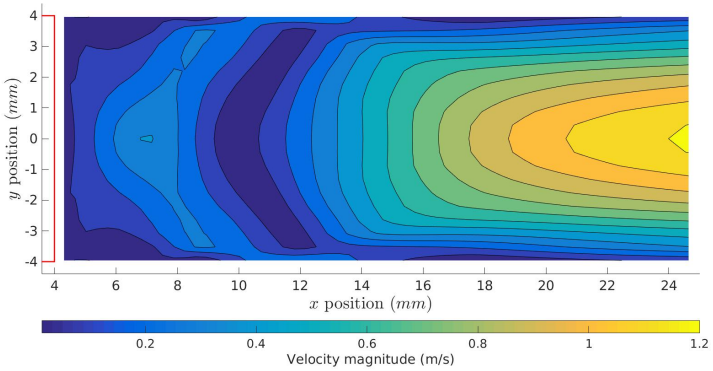

(b) $EBRSM$

Figure 59: Mean velocity contours downstream of the blockage in the plane $z = 0$, $Re_D = 15600$

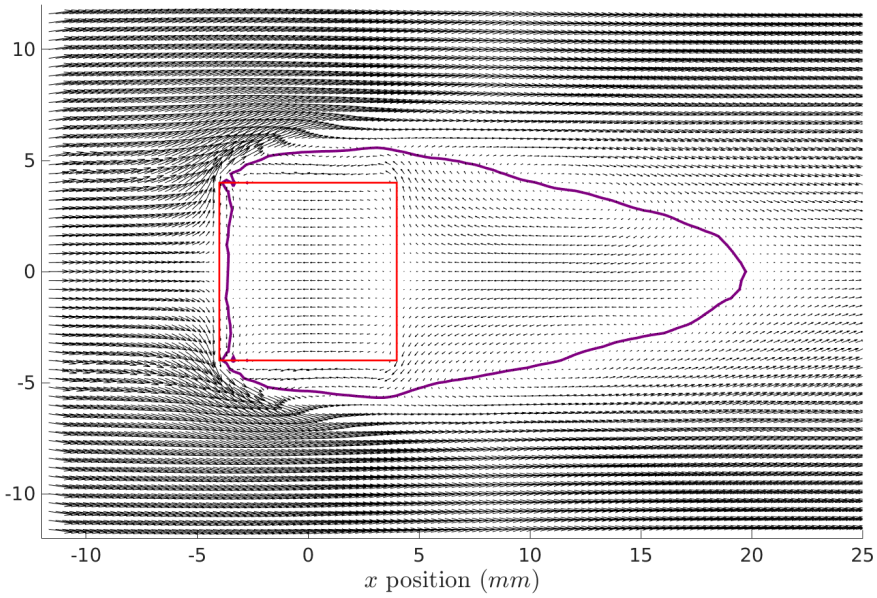

Figure 60: Contour $U = 0$ within plane $y = 0$, DNS, $Re_D = 5600$

the $EBRSM$ (Figure 48b) than it does with the $k-\varepsilon$ (Figure 48a); the contour follows a smooth curve as it extends downstream past the cube sides rather than suddenly tucking in behind the cube.

6.2.2 Solution Upstream

Upstream of the block in the plane $z = 0$, two very clear vortices may be seen (Figure 61) near the upper and lower channel faces as observed in the URANS simulations, but not enough data has been collected for a clear symmetrical pattern to form. In the plane $y = 0$, the mean flow-field appears more symmetrical (Figure 63a); upstream velocity fluctuations in this plane appear to be smaller than those in $z = 0$, and the flow is dominated by the streamwise component until right near the cube where it sweeps out equally to both sides 63a). This dominance of the main flow is evident in (Figures 63a and 63b); the flow does not appear significantly different from snapshot to snapshot, nor does any given snapshot appear very different from the mean.

It is tempting to describe the well-known shedding mechanism for flow around a long cylinder as a 2D phenomenon although it has been shown that there is a strong third component to it [8]. Following this thinking, one might erroneously expect that any large-scale unsteadiness in the instantaneous upstream flow should be aligned with the $y = 0$ plane, being triggered by the shedding downstream of it, but this is not the case.

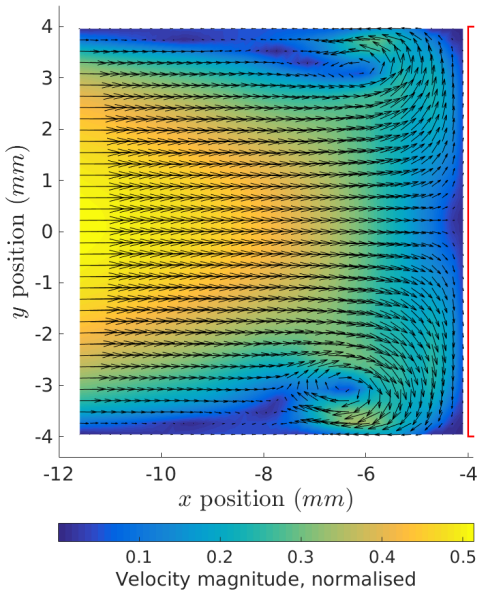

Figure 61: Mean velocity upstream of the blockage in the plane $z = 0$, DNS, $Re_D = 5600$

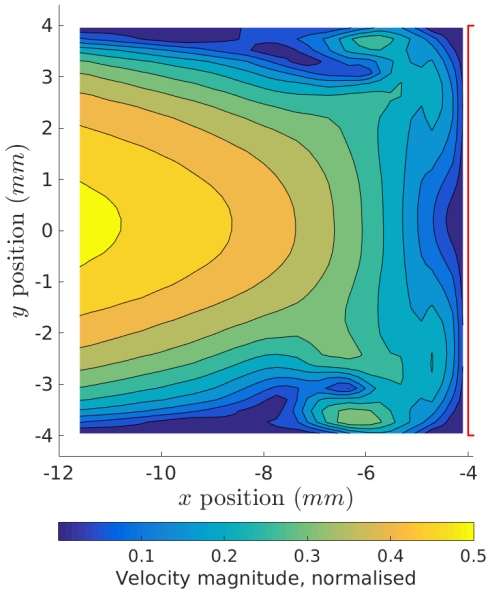

Figure 62: Mean velocity contours upstream of the blockage in the plane $z = 0$, DNS, $Re_D = 5600$

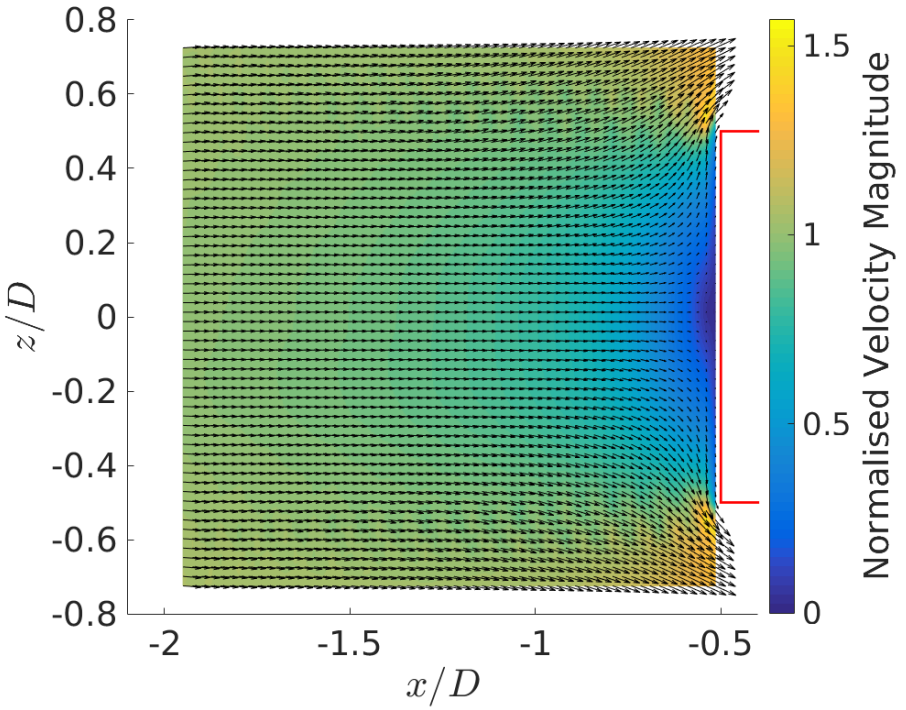

(a) Mean

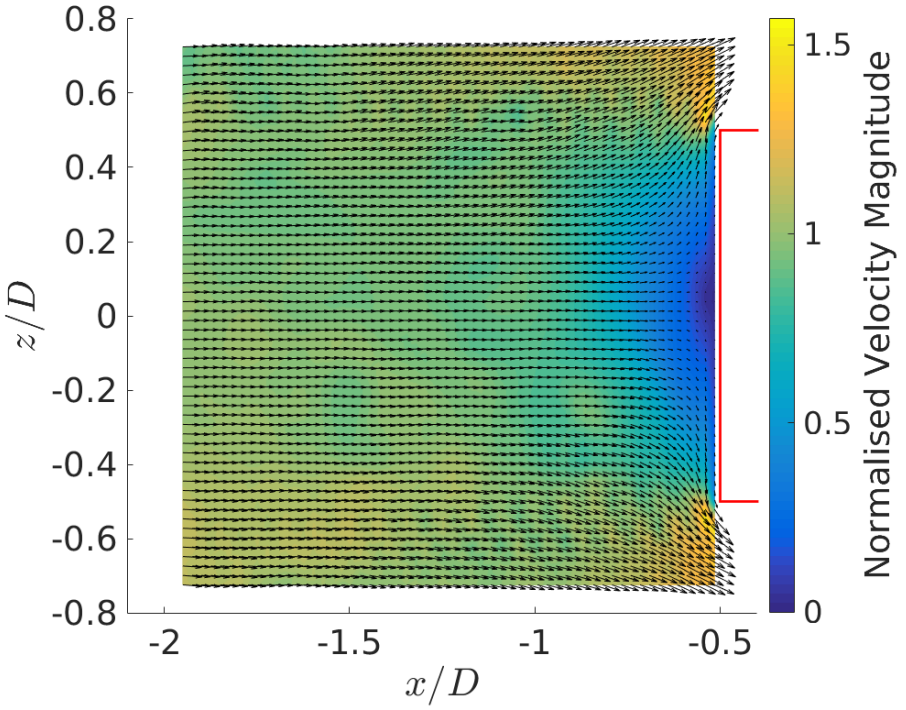

(b) Instantaneous

Figure 63: Mean and Instantaneous velocity upstream of the blockage in the plane $y = 0$, DNS, $Re_D = 5600$

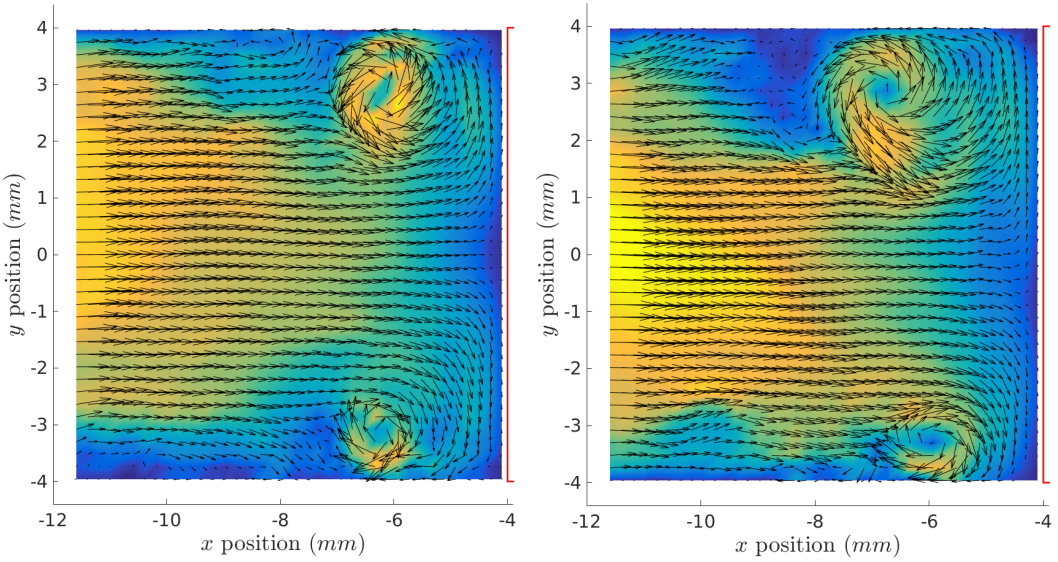

(a) Vortices equal strength, same streamwise location

(b) Top vortex stronger and further upstream

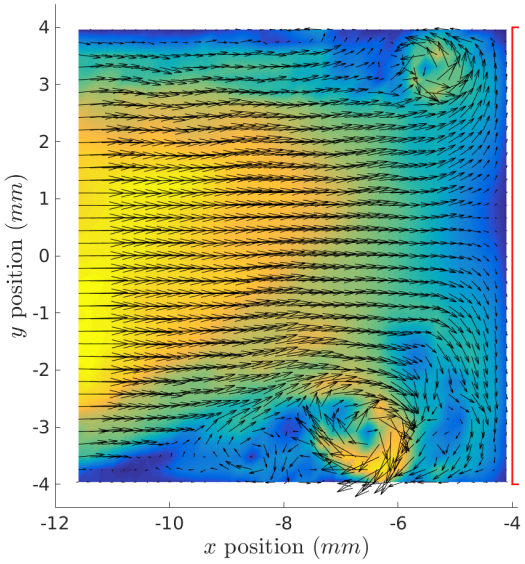

(c) Bottom vortex stronger and further upstream

Figure 64: Instantaneous snapshots illustrating different vortex locations and strengths, upstream of the cube in $z = 0$ plane, DNS at $Re_D = 5600$

The upstream vortices may be found in different positions, having different strengths (Figure 64). On average, they are located approximately $2mm$ upstream of the cube near the duct floor and ceiling and are approximately of the same strength, others are sometimes found $\sim 0.5mm$ upstream of that location and are stronger. Flow in these corner regions is loosely analogous to that in [39], and has the same structure, albeit with an extra degree of symmetry. These authors reported a bi-modal distribution for velocity in the upstream corner zone, so it is possible that the same mechanism is responsible for the fluctuation in movement and strength of the upstream vortices in the current case. In the current DNS results, the fluctuations of the two vortices seemed to be out of phase; when one was strong the other was weak and when one moved upstream the other did not. The mean velocity (Figure 61) appears to show smaller, much less prominent vortices further upstream of the primary ones, although these are hard to discern. These may be due to the knock-on effect of the primary ones; (Figure 64c) appears to show a small counter-rotating vortex immediately upstream of the larger one. Despite the unsteadiness of the incoming flow, and the tendency for these vortices to move back and forth, changing in strength, they were strong enough to appear clearly in every snapshot without exception.

6.2.3 Solution near the Cube Sides

The mean velocity at the cube side is presented as before in the plane $x = 0$ (Figure 65). The basic structure is similar to that predicted by both the $k - \varepsilon$ model (Figure 53a) and the $EBRSM$ model (Figure 53b). It is not immediately clear by viewing the vector map (Figure 65) which of the two models give the better match, this will be further investigated in (Section 7.4). Due to incomplete convergence to self-repeating sheding, there is an anomaly on the location of the intersection of the side vortices with the plane. There is a slight degree of asymmetry, the upper of the two is located at $(y = 3.14mm, z = 5.14mm)$ and the lower is located at $(y = -3.43mm, z = 5.17mm)$. Of the two URANS models, neither is clearly a better match with the DNS solution.

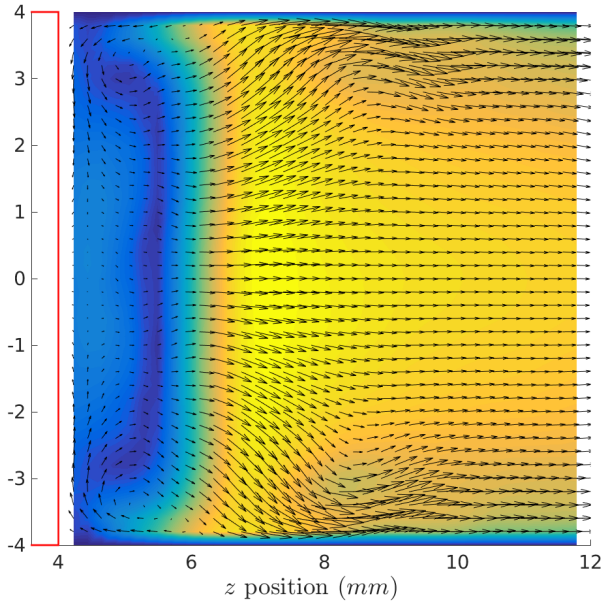

Figure 65: Mean velocity to the cube side in the plane $x = 0$, DNS, $Re_D = 5600$

6.2.4 Solution in the Recirculation Region

In the downstream recirculation zone, the mean flow does not appear to be completely symmetrical, probably due to the limited dataset. However, patterns in the mean flow are clear enough to discern which of the two URANS models matches better. The recirculation region, bounded in the plane $z = 0$ by a crescent shaped patch of low mean velocity magnitude, shows a clear patch of high velocity near the central plane, returning towards the cube rear (Figure 66). This is the general form predicted by the $EBRSM$ model (Figure 56b), as opposed to the separated cells of high velocity predicted by the $k - \varepsilon$ model (Figure 56a). As mentioned previously, the recirculation length $L_{rDNS} = 19.7mm$ matches well with the experiments and the $EBRSM$ model, but not so well with the $k - \varepsilon$. The instantaneous solution in the plane $y = 0$ may be used to illustrate the shedding phenomenon (Figure 67). The snapshots were chosen equally spaced in time, and roughly in phase with the $EBRSM$ simulation (Figure 47). Due to the high degree of turbulence, it is harder to clearly distinguish the precise location of vortex cores. It is not clear that the shedding follows a perfectly regular period, this is not necessarily to be expected. In fact the experimental results for pressure at the cube side face (Section 4) suggest that this is not the case. Nonetheless, it is clear that vortices aligned with y are generated and sweep downstream in qualitatively the same way as predicted by the

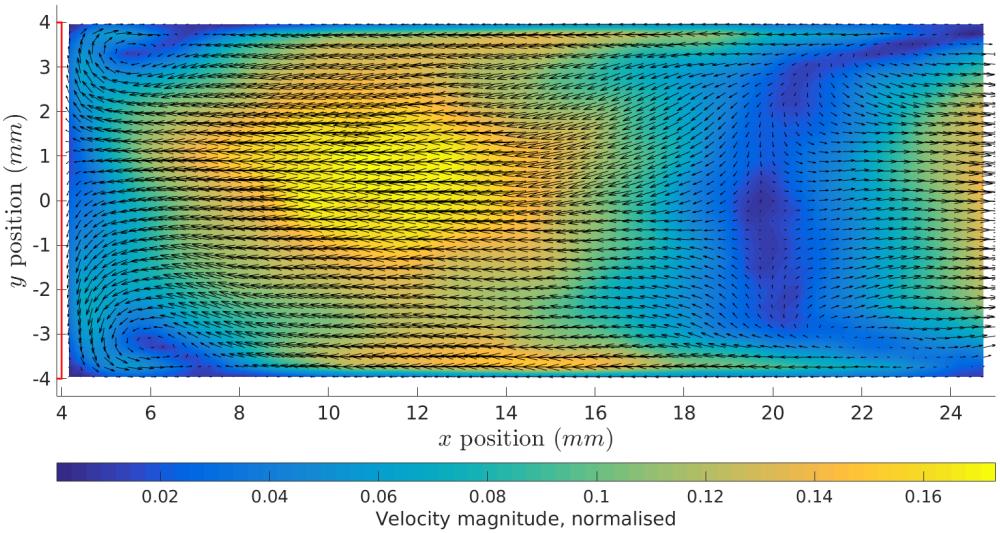

Figure 66: Mean velocity downstream of the blockage in the plane $z = 0$, DNS, $Re_D = 5600$

URANS simulations.

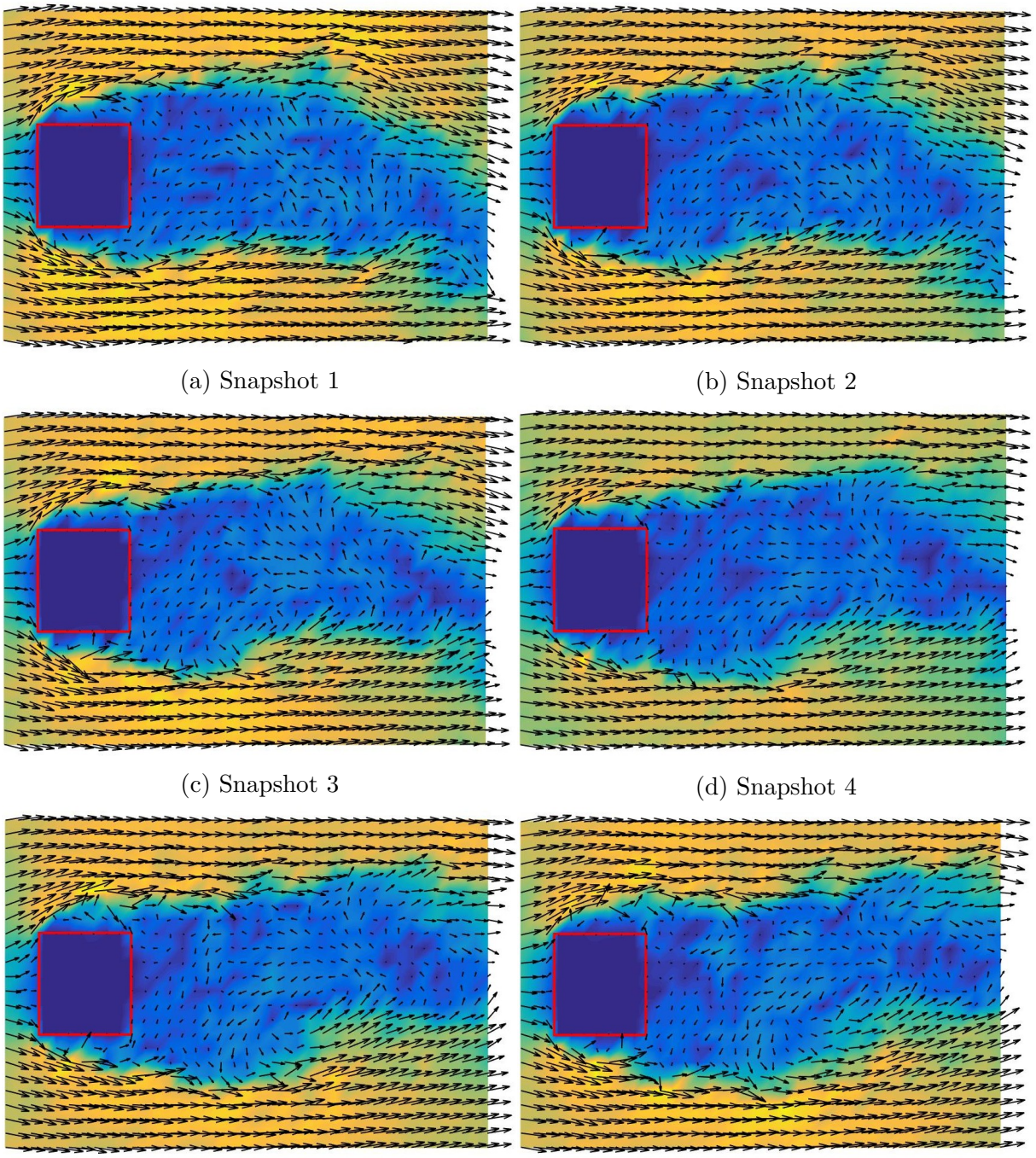

(a) Snapshot 1

(b) Snapshot 2

(c) Snapshot 3

(d) Snapshot 4

(e) Snapshot 5

(f) Snapshot 6

Figure 67: Snapshots of instantaneous velocity from DNS simulation, from the beginning of the period to halfway through

7 Comparisons and Validation

In order to make fair comparisons between the different instances of experimental results and numerical simulation, it is necessary to non-dimensionalise the results by appropriate characteristic dimensions. In what follows throughout this section, lengths will be non-dimensionalised by D, which is the cube dimension and also the channel height. Velocities will be non-dimensionalised by U_b, the duct bulk velocity, and pressures will be normalised by ρU_b^2. The turbulent kinetic energy k is non-dimensionalised by U_b^2. Reference data are provided both by experiments and a DNS simulation, and the two are compared where possible; DNS data are available at $Re_D = 5600$ only and the PIV measurements are only available in the wake. Experimental results from the pressure tapping are available at all three Reynolds numbers, and are compared with the URANS calculations.

7.1 Fluctuating Pressure at Cube Side

The phase-averaging technique carried out previously (Section 4) provides an estimation of the magnitude and frequency of the periodic shedding; it averages out chaotic turbulent fluctuations and is able to adjust to slow changes in phase and frequency so as to allow for irregularities in flow rate. The phase-averaged pressure signals from the experiments are plotted together with the URANS results at the three Re_D numbers (Figures 68a, 68b, 68c). Due to the small size of the fluctuations, which are of the order of tens of Pa, the error bars appear large at $Re_D = 5600$. The amplitude of the phase-averaged pressure fluctuations predicted by the URANS models are in agreement with the experiments at this flow rate; the $k - \varepsilon$ model matches extremely well the phase-averaged data and the $EBRSM$ matches the "adjusted amplitude" very closely too. However, due to the size of the error it can not be demonstrated that this is not coincidence. At the higher Re_D numbers, the models both predict a pressure amplitude far higher than that extracted from the data via the phase-averaging technique.

The phase-averaged pressure is calculated from the original signal based on periods that are extracted from the filtered signal (Section 3), and that are used to produce a phase-averaged pressure signal with a certain amplitude. The process is designed to allow for small deviations in frequency and phase, but it is likely that the reported amplitude

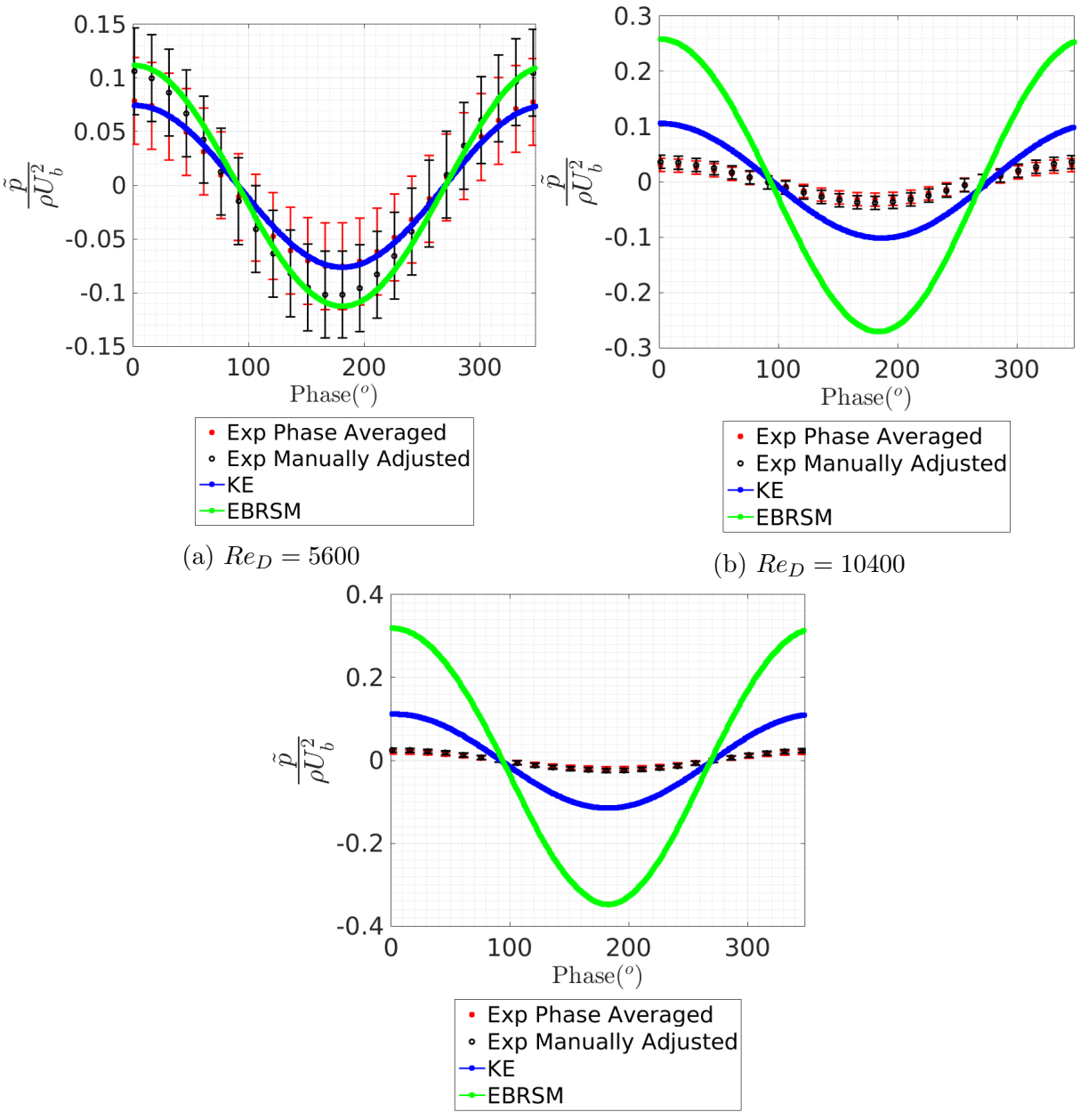

(a) $Re_D = 5600$

(b) $Re_D = 10400$

(c) $Re_D = 15600$

Figure 68: Normalised pressure at the cube side, experiments vs URANS. Plotted with experimental error bars, including adjusted pressure amplitudes

was reduced during this process. The spectrum of the fluctuations at the higher two Re_D numbers was much richer than at $Re_D = 5600$; the peaks were much less clear and a lot more was filtered out to leave the signal that eventually defined the period cut-off times. One result of this was that the peaks in amplitude of the phase-averaged pressure appeared lower than those present in the raw signal. The data for phase-averaging was collected from the original signal so as to mitigate this effect, and resulted in an amplitude slightly higher than that of the filtered signal, but differences in phase between the peaks in the filtered signal and the large, slow fluctuations meant that these latter components might be expected to corrupt the process. This was thought to be a possible explanation for the lower amplitude found. In an attempt to allow for this, the heights of the peaks in the original signal were collected visually for hundreds of periods, until their mean height had ceased to change. The slightly higher average peak heights obtained by this method are then used to scale up the phase-averaged amplitudes and are presented as "Exp Manually Adjusted" points. (Figures 68a, 68b, 68c). These scale-up ratios were 0.35, 1.18 and 1.19 at $Re_D = 5600$,10400 and 15600 respectively. At $Re_D = 5600$ (Figure 68a) this process shifted the experimental result towards the $EBRSM$ prediction; before adjustment it closely matched the $k - \varepsilon$ result. However, the movement of the phase-averaged values is within the range of the error bars, so this does not lead to a firmer conclusion as to which model gives a superior prediction. At the higher two Reynolds numbers (Figures 68b, 68c), this adjustment was largely irrelevant considering the size of the differences between the computations and the experiments. It may be noted that both of the URANS methodologies show an increase in normalised pressure amplitude when passing from the lowest Reynolds number to the highest whereas the experimental results show a decrease. There is no reason to presume that the phase-averaged experimental results did not represent well the amplitude of the fluctuations captured by the transducer, as the manual peak-finding process was a second check regarding this point. It is possible that despite the efforts made, there were some bubbles in the small hole of the pressure tapping, that could have led to some damping, which would lead to a reduction in captured amplitude. However, there were also preliminary tests made using a different cube with a hole diameter of $1mm$ rather than $0.5mm$, which would be less prone to blockage. These were analysed using the trial-and-error "constant period method" (Section 3). By this approach, the amplitudes at the three Reynolds numbers 5,800, 10,900 and 15,500

Re_D	5600	10400	15600
Normalised pressure amplitude, experimental	0.154	0.062	0.04
Normalised pressure amplitude, adjusted	0.208	0.074	0.05
Normalised pressure amplitude,$k-\varepsilon$	0.150	0.208	0.227
Normalised pressure amplitude, $EBRSM$	0.224	0.530	0.664

Table 15: Fluctuating pressure at cube side ($x = 0, y = 0, z = D/2$), $k-\varepsilon$ vs $EBRSM$

Re_D	5600	10400	15600
St, $k-\varepsilon$	0.140	0.138	0.136
St, $EBRSM$	0.152	0.147	0.149
St, experimental	0.122	0.123	0.143

Table 16: Fluctuating pressure at cube side ($x = 0, y = 0, z = D/2$), $k-\varepsilon$ vs $EBRSM$ vs Experiments

were 0.07, 0.03 and 0.02. These Reynolds numbers are very close to those of the final experiments. As the amplitudes produced in these preliminary experiments are lower than those of the final experiments, and are not as good a match, it seems that the larger hole may not have improved anything. One other uncontrolled factor that might have affected the amplitude of shedding was fluctuations in the duct flow rate, it was not possible to verify how steady the flow was over time periods of the order of a shedding cycle. The higher flow rates at the higher two Re_D and the greater movements in free surface height in the overhead reservoir may have been responsible for the entrainment of more air into the feed circuit, which may have obstructed flow in the pipework somewhat; vibrations and noise in the pipes suggested that there was some unsteadiness. In order to completely eliminate this effect a sturdier flow-rig with a larger overhead tank would have been required; this was beyond the scope of the study for practical reasons. Over the three cases, there was a large discrepancy between the amplitude predictions from the two models (Table 15), and the $k-\varepsilon$ model matched better with the data to a certain extent.

In conclusion, both the $k-\varepsilon$ and the $EBRSM$ models show quite good agreement with the experimental results at the lower flow rate; the amplitude predicted by the $k-\varepsilon$ matches the phase-averaged value to within $\sim$ 4% and the $EBRSM$ matches the "adjusted" amplitude to within $\sim$ 4% also. The bounds of experimental error are very large, and are based on the error quoted by the manufacturers, who calibrated it before shipping. The error is $\pm$50% of the phase-averaged amplitude of the signal read at $Re_D = 5600$. This is very large, and makes conclusions about relative accuracy of the

two models necessarily limited; the $EBRSM$ prediction is $\sim 40\%$ higher than that of the $k-\varepsilon$. The predictions do not match well at the higher two Reynolds numbers, but it is unclear how much of this is down to limitations in the experimental setup and how much is a result of limitations in the modelling process. Nevertheless, the $k-\varepsilon$ model appears to match better over the three flowrates. It is worth reiterating at this stage that the major model developments that were introduced (Section 6) were designed to fit data from steady flows. The extension to unsteady flow predictions is conceptually simple; an unsteady term is introduced and a quasi-steady state is attained before marching forward at each timestep. However, despite the great deal of effort made to accurately model each element contributing to the steady-flow simulation, the thinking process was largely decoupled from considerations of unsteadiness in the physics, this will addressed further in "Conclusions" (Section 8).

7.2 Upstream

In order to compare quantitatively the values of mean velocity upstream of the cube, plots have been made at a fixed value of $x = -1.5D$, $1D$ upstream of the leading face (Figure 69). In the plane $z = 0$, the mean streamwise velocity U/U_b is plotted from the lower duct face to the upper face. In the plane $y = 0$, the streamwise U/U_b and spanwise W/U_b velocities are plotted from $z = -1.5D$ to $z = +1.5D$, one cube height farther out to the side than the respective cube faces. Not enough data has been collected to completely smooth out the velocity profiles from the DNS results, but it is nonetheless clear that a reasonably good match is found between all three of the methods, across each of the comparisons made. A perturbation is seen in the mean spanwise velocity W/U_b, where a small region of fluctuations is predicted by the DNS, upstream of the cube. In the same place, a small, localised perturbation in mean streamwise velocity may be seen. These perturbations are likely to be numerical in nature, and have an amplitude of no more than $0.05U_b$. The DNS solution quickly moves closer towards the URANS solutions beyond these regions, which are $\sim 0.3D$ in size. It is not certain if these had a major effect on the mean solution downstream, but they may have had some significance so they will be considered in the discussion of the flow further downstream.

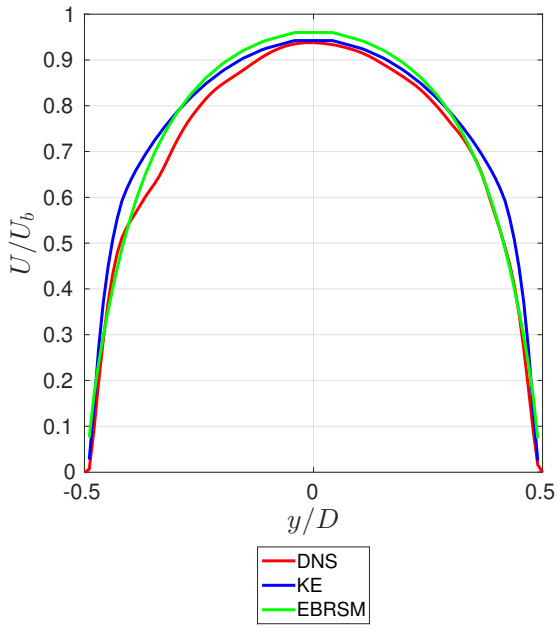

(a) $U(y, z = 0)$

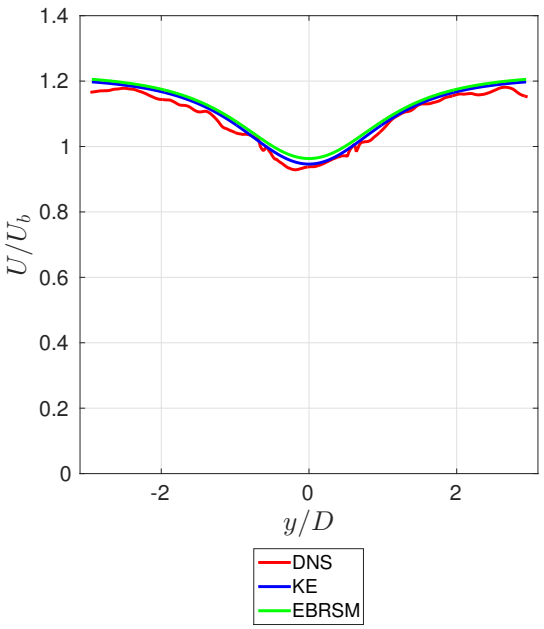

(b) $U(y = 0, z)$

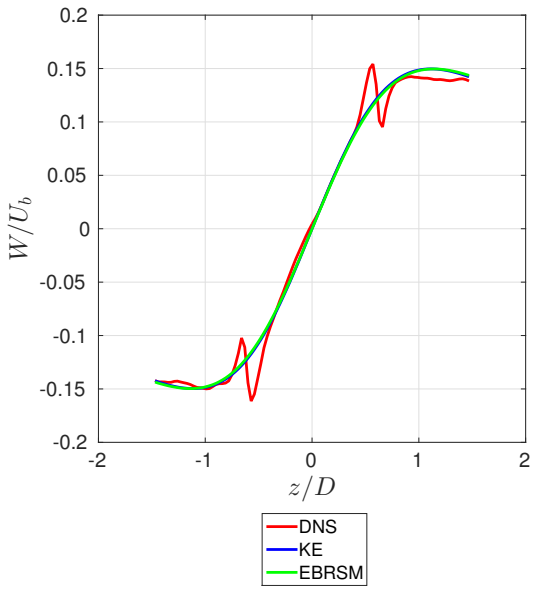

(c) $W(y = 0, z)$

Figure 69: Comparison of mean velocity profiles upstream of the cube at $x = -1.5D$

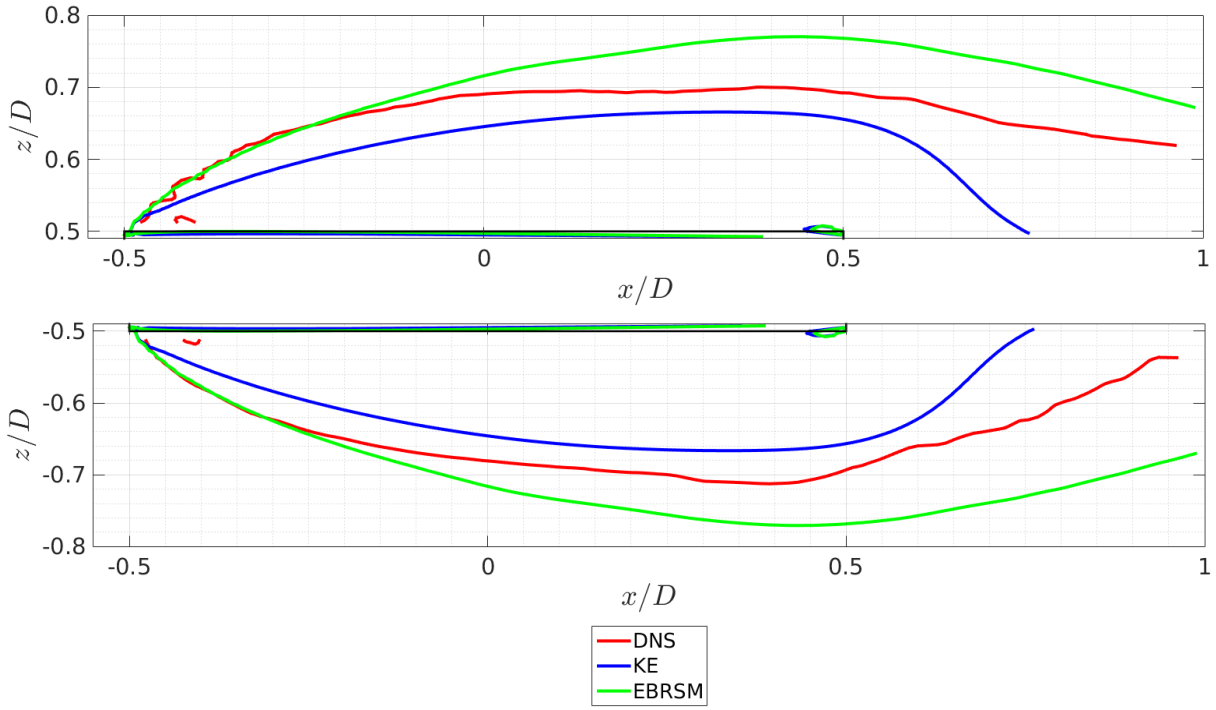

Figure 70: Contours of $U = 0$ within the plane $y = 0$ near the cube sides

7.3 Cube Side

Contours for $U = 0$ in the plane $y = 0$ by the cube sides show a clear trend in the shapes of the "side bubble" (Figure 70). Due to laser light reflections from the cube sides, results from the PIV experiments were not helpful in this regard; only the DNS results at $Re_D = 5600$ are useful as a reference. These show a better agreement with the $EBRSM$ model near the leading edge, the "side bubble angle" formed by the contour and the cube edge is a very good match near the leading edge. The side bubble angle remains more or less fixed during the periodic fluctuations predicted by the $URANS$ models, the large scale unsteadiness begins downstream of it. Therefore, the relative performance of the URANS models near the leading edge depends more on their ability to deal with steady physics and is not too strongly affected by the periodic shedding motion. That the $EBRSM$ prediction of side-bubble angle should be so much better than that of the $k-\varepsilon$ might be taken as an indicator that predictions downstream should be better, as in this region of very high shear near the leading edge the model is more successful. However, downstream, the DNS contour moves back towards the centreline more quickly than that of the $EBRSM$, approaching the $k-\varepsilon$ prediction. At all three Reynolds numbers, the $k-\varepsilon$ predicts a lower side bubble angle and moves in behind the cube at a shorter distance

downstream. It is also worth remembering that there was some discrepancy in the results upstream of the cube (Figure 69); perhaps these affected the results.

In order to further investigate this, it is logical to compare velocity profiles from the cube side face outwards in the z direction at different x locations (Figure 71). In all four of the x locations, the $k-\varepsilon$ model predicts a velocity trough that is lower than that of the $ERSM$, and this trough is closer to the wall. In terms of an overall match along the length of the profile, the $EBRSM$ shows better agreement at $x = -0.25D$. By $x = 0$, closest to the cube centre, neither of the two models is clearly better over the length of the profile, although the $k-\varepsilon$ has a trough value which matches well with that of the DNS. By $x = 0.25D$, halfway between the cube centre and the trailing edge, the $k-\varepsilon$ clearly matched the DNS more closely. At $x = 0.5D$, in line with the cube's rear face, the $k-\varepsilon$ still matches the DNS more closely. In conjunction with the $U = 0$ contours (Figure 70), this serves to demonstrate model performance from the cube's leading edge, where the $EBRSM$ matches better, to the trailing edge, where the $k-\varepsilon$ matches better.

In Section 6, vector maps were presented showing the mean velocity in the plane $x = 0$, which may be seen as cutting the domain into an upstream and a downstream section. In the $k-\varepsilon$, $EBRSM$ and DNS results, the two branches of the "side vortices", as defined by the vortex cores, were shown to pass through this plane. These were manifest as two vortices apparent near the corners formed by the cube sides and the duct walls, roughly aligned in the streamwise direction. The z coordinate of each of these vortices was about $\pm 0.625D$. Plots of the mean streamwise velocity U/U_b are shown along profiles which pass roughly through these mean vortices (Figure 72); also, profiles of W/U_b are shown (Figure 73). The maximum size of the normalised V/U_b components was $\sim 4\%$ (results are not presented for these here). It is clear from the DNS results that there are insufficient data to reach a statistically steady state, but certain rough conclusions can nonetheless be drawn. Firstly, the DNS results for streamwise velocity along this profile match better to those of the $EBRSM$ model than the $k-\varepsilon$, when the entirety of the profile is considered. Secondly, the $EBRSM$ successfully predicts a dip in W near the central plane that is present in the DNS data, and this dip is not seen in the $k-\varepsilon$ predictions. The $k-\varepsilon$ and $EBRSM$ solutions for W are actually close, but when the entirety of this profile is considered it is fair to say that the $EBRSM$ gives a better match despite the uncertainty in the final converged result.

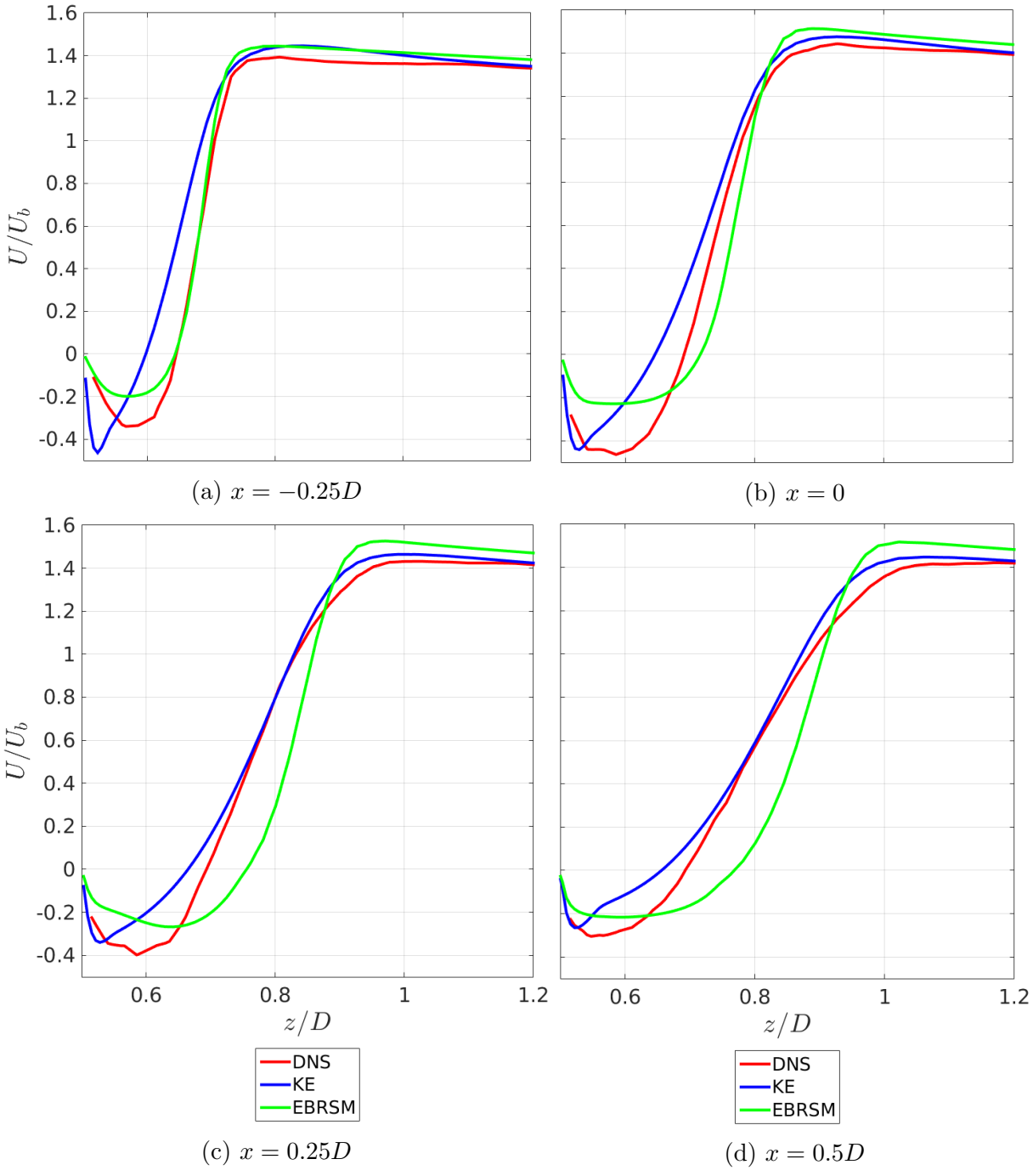

(a) $x = -0.25D$

(b) $x = 0$

(c) $x = 0.25D$

(d) $x = 0.5D$

Figure 71: $U(z)$ extending out from the cube side in the plane $y = 0$, at different x locations, x increasing from top-left to bottom-right

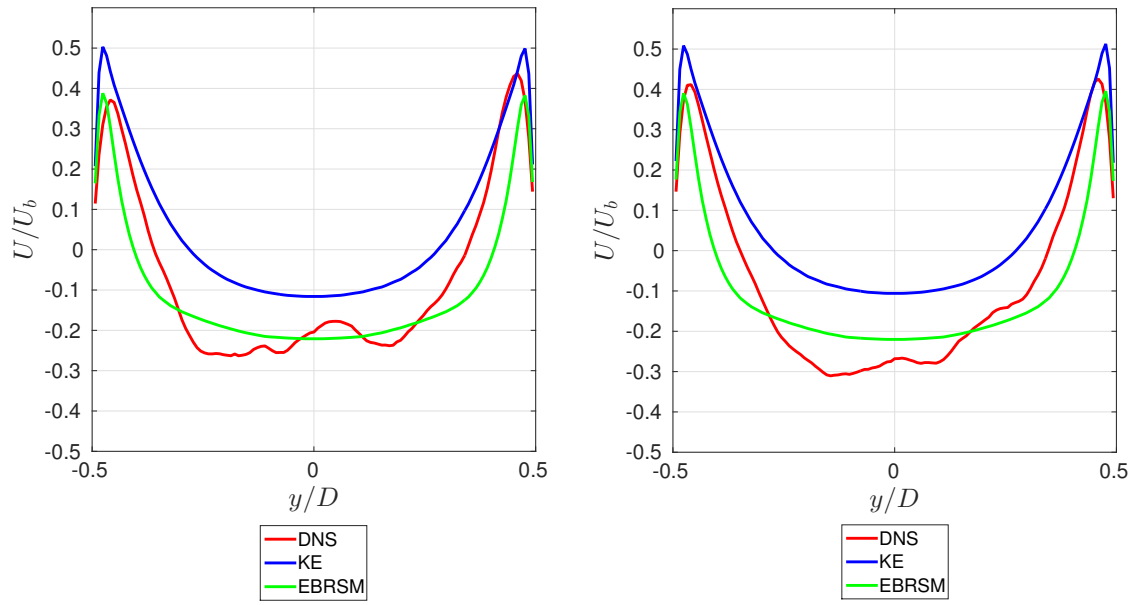

(a) $(x = 0, y, z = 0.625D)$ (b) $(x = 0, y, z = -0.625D)$

Figure 72: U near the cube side from the floor to the ceiling

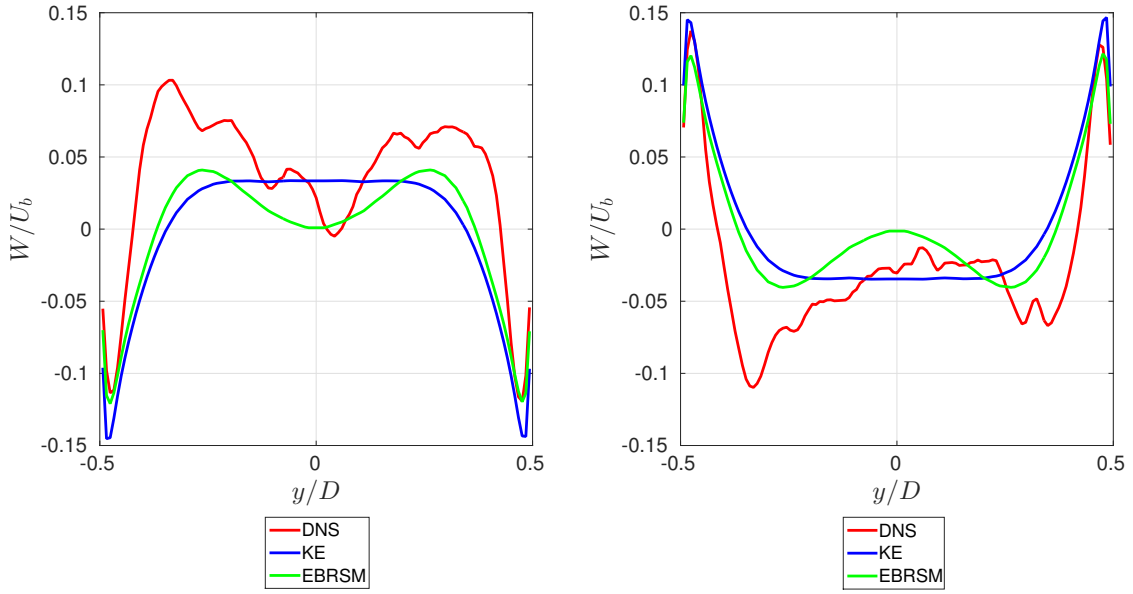

(a) $(x = 0, y, z = 0.625D)$ (b) $(x = 0, y, z = -0.625D)$

Figure 73: W near the cube side from the floor to the ceiling

One might view the recirculation bubble as being the result of two different flows; the first flow is entrained by the faster moving fluid in the bulk which tends to sweep fluid away and the second replenishes the bubble by feeding fluid in from behind the cube. As a result of this, the overall prediction of the side bubble is also dependent on the prediction of the flow in the recirculation region, as will be discussed further on.

In order to further illustrate this, velocity "visualisation streamlines" have been produced that end inside the side bubble region in a small constrained "seeding plane" located at $x = 0$. These "visualisation streamlines" are constructed by stepping forward a small increment in the direction of the the instantaneous velocity vector, determining the alignment of the instantaneous velocity vector in the new location, and so on. It is through the small "seeding plane" that the recirculating flow passes as it moves back upstream close to the cube side, as may be seen by following the visualisation streamlines. The seeding plane extends from the duct floor to the duct roof, and from $z = 0.5D$ at the cube side to $z = 0.55D$, an area in which the flow direction is principally opposed to that in the channel bulk. Results are shown for $k - \varepsilon$ and $EBRSM$ (Figure 74) at the same phase within the shedding cycle. The phase was determined by reference to the fluctuating velocity at $(x = 1.25D, y = 0, z = 1.25D)$ and the fluctuating pressure at the cube side face as before. The length of the visualisation streamlines was also equal in terms of number of incremental steps aligned with the velocity vector. The flow is highly three-dimensional in nature in the cube vicinity, it is subject to shear in two planes and detaches from the trailing edge. Therefore, it is not surprising that the predictions from the two models are different, given the ability of the $EBRSM$ to calculate the transport of the Reynolds Stresses whereas the $k-\varepsilon$ can not; as discussed above the $EBRSM$ gives superior predictions close to this region. These differences are manifest in the streamlines given in (Figures 75, 76). It seems that the fluid that passes through this area has its origins in slightly different regions in the two simulations. As the flow is unsteady, following visualisation streamlines in the reverse direction does not strictly reveal the origins of a fluid particle; they are not equivalent to streamlines in steady flow. However, it may be assumed that they tell us qualitatively something about the regions of the flow from which the fluid came, as long as this assumption is only made in regions where the solution is relatively steady. Under this assumption, there is some proportion of the flow that comes from upstream, past the leading edge near the duct ceiling and floor. In the

$k-\varepsilon$ simulation, these visualisation streamlines encroach further in towards the channel centre, whereas in the $EBRSM$ case they are confined to a smaller region right near the duct ceiling and floor. The tendency of the flow to be slowed down as it becomes closer to the the duct floor and ceiling allows it to become entrained, and this effect takes hold closer to the central $y = 0$ plane in the $k-\varepsilon$ case. At the part of the shedding cycle that is displayed, the maximum value of streamwise velocity, as predicted by the $EBRSM$ model, is slightly higher than that of the $k-\varepsilon$ (Figure 77). The relatively fast-moving flow immediately downstream of the leading edge appears to sweep past the side bubble in the $EBRSM$ predictions as opposed to becoming entrained into it. The side bubble predicted by the $EBRSM$ is larger on both sides of the cube in this instantaneous snapshot as well as in the mean, suggesting that its larger size would persist even if the mean flow were steady downstream of it. As a result, it seems that the differences in the model predictions within this region of the flow are down to differences in the steady flow predictive qualities, as opposed to differences in prediction of unsteady flow components.

Following the visualisation streamlines back from the central part of the seeding plane at $y \sim 0$ (Figures 75, 76), it seems that some of the flow that passes the point $(x = 0, y = 0, z = 0.5D)$ may originate from the other side of the cube in the $k-\varepsilon$ case, although caution must be taken as the visualisation streamlines align with instantaneous vectors as opposed to acting like tracer particles. In the $EBRSM$ case, some of the visualisation streamlines that pass by the pressure tapping point at $(x = 0, y = 0, z = 0.5D)$ suggest that the fluid was recently in a different y plane; the visualisation streamlines follow a path from near the duct floor in towards the pressure tapping point, having passed along the cube surface near the trailing edge. The instantaneous structure of the flow is quite different from the two model predictions, it is highly 3D. Given the complexity of this flow, and its dependency on the ability of the models to predict strongly 3D structures, it is not surprising that the fluctuating pressure here at the cube side face is strongly dependent on model choice. Due to the fact that some of the fluid passing by the pressure tap comes from downstream behind the cube, pressure predictions are also likely to be affected by the solution in the recirculation region.

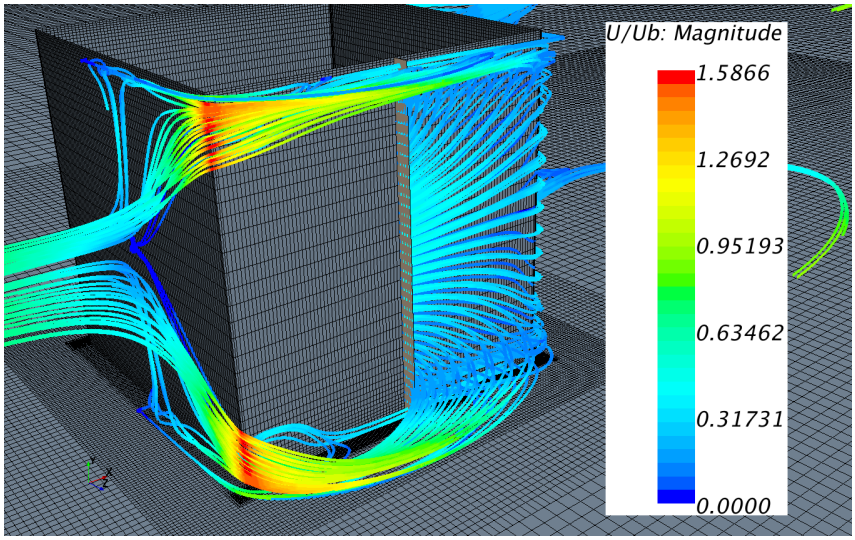

(a) $k - \varepsilon$

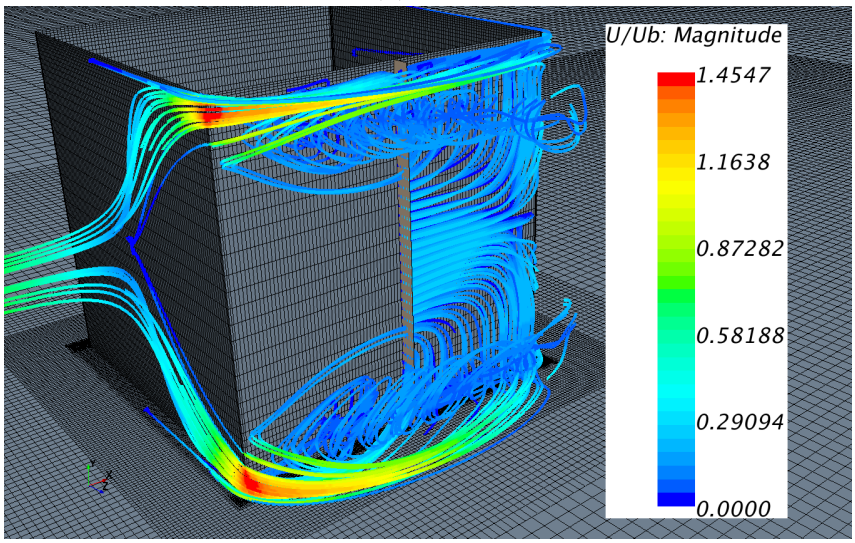

(b) $EBRSM$

Figure 74: Velocity visualisation streamlines in the cube vicinity in the plane $y = 0$ at the same point within a shedding cycle

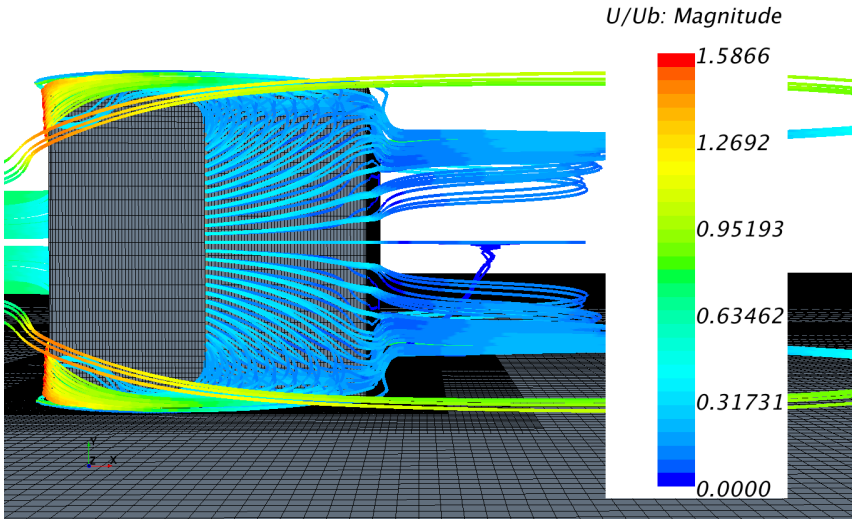

(a) Facing cube side

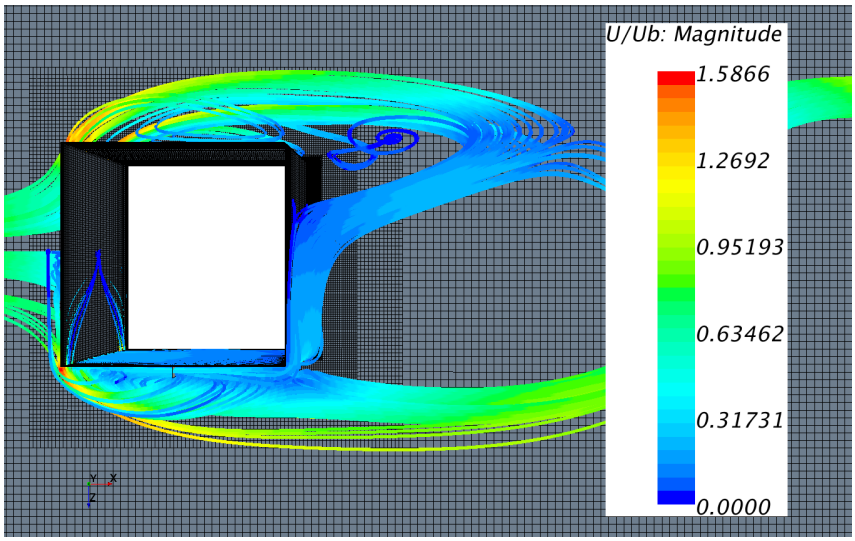

(b) Facing top of cube

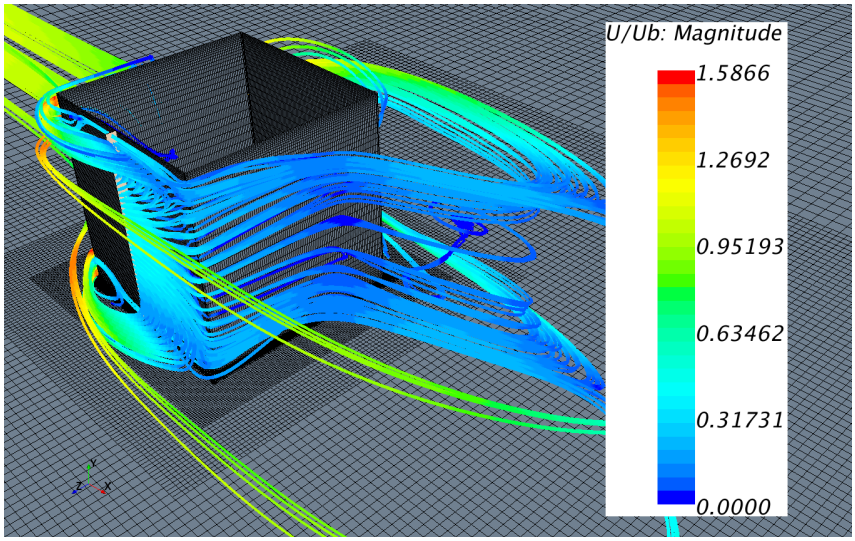

(c) Isometric projection facing cube from behind and to side

Figure 75: Visualisation streamlines leading into the plane $(x = 0, -0.5 < y < 0.5, 0.5 < z < 0.55)$, $k - \varepsilon$, $Re_D = 5600$

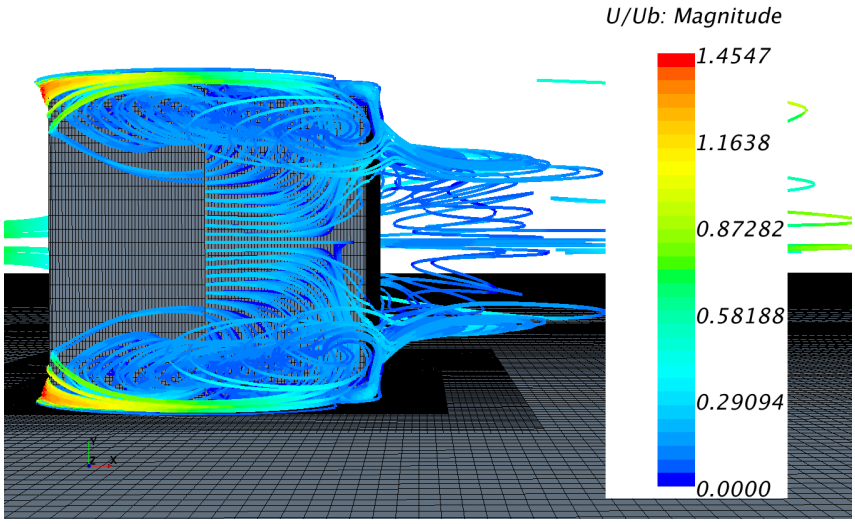

(a) Facing cube side

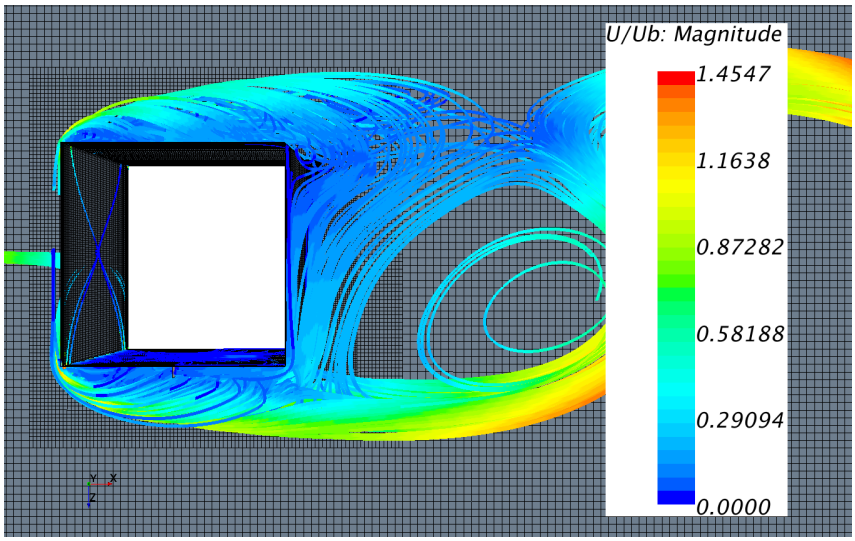

(b) Facing top of cube

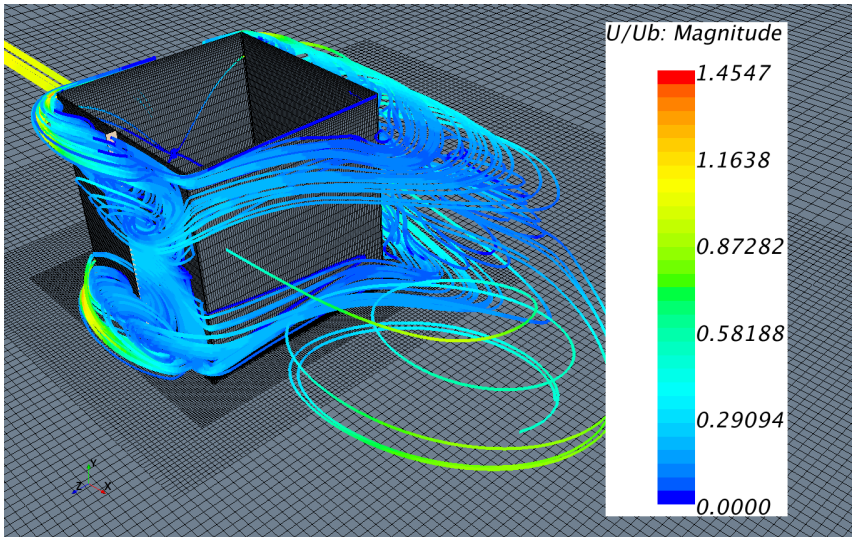

(c) Isometric projection facing cube from behind and to side

Figure 76: Visualisation streamlines leading into the plane $(x = 0, -0.5 < y < 0.5, 0.5 < z < 0.55)$, $EBRSM$, $Re_D = 5600$

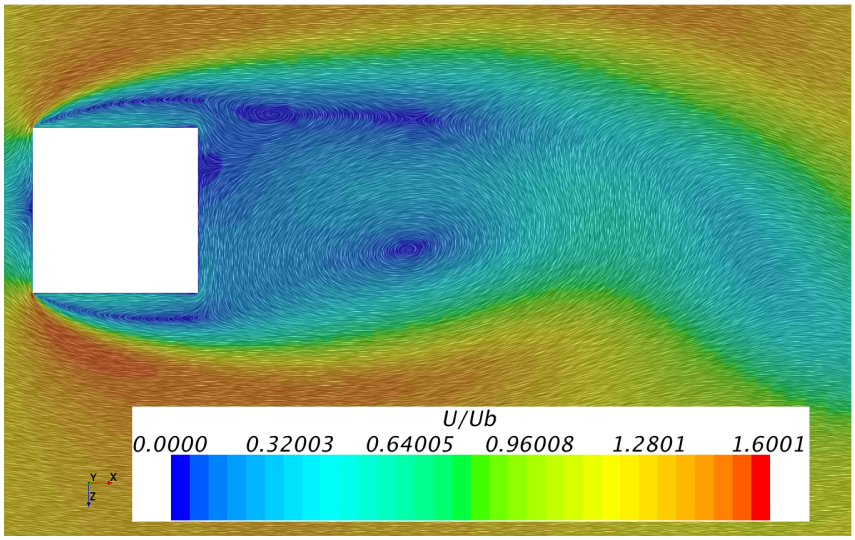

(a) $k - \varepsilon$

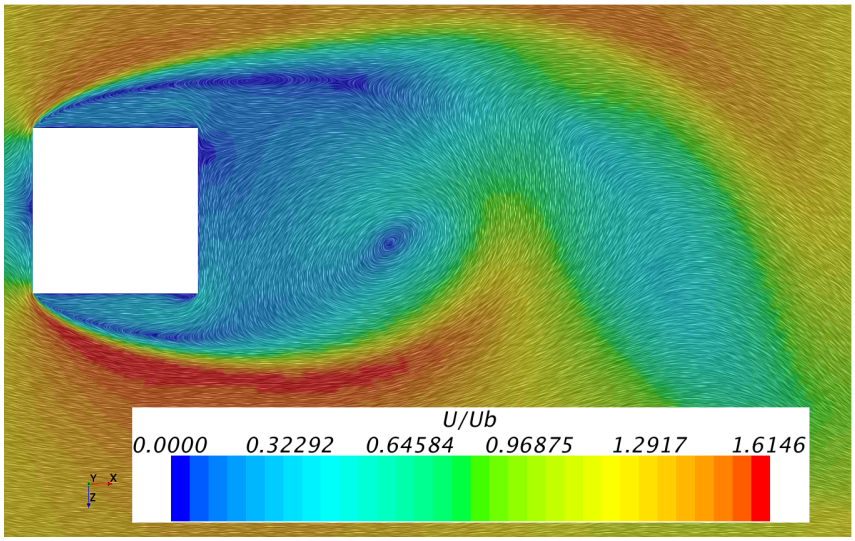

(b) *EBRSM*

Figure 77: Velocity in the cube vicinity in the plane $y = 0$ at the same phase within a shedding cycle

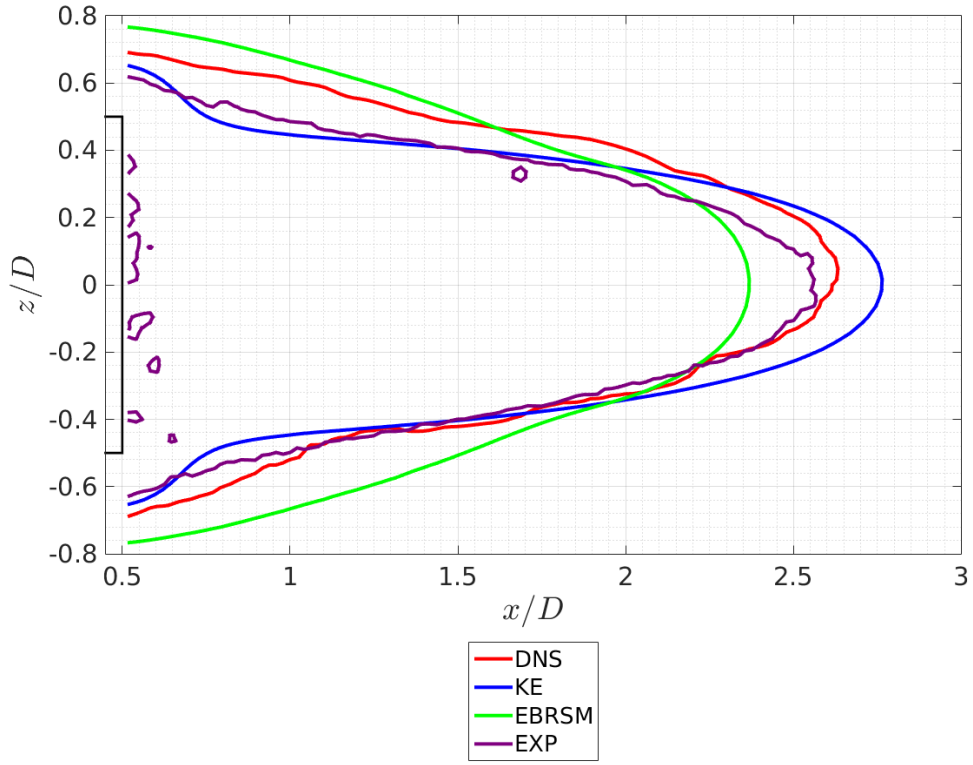

Figure 78: Contours of $U = 0$ downstream of the cube in the plane $y = 0$, $Re_D = 5600$

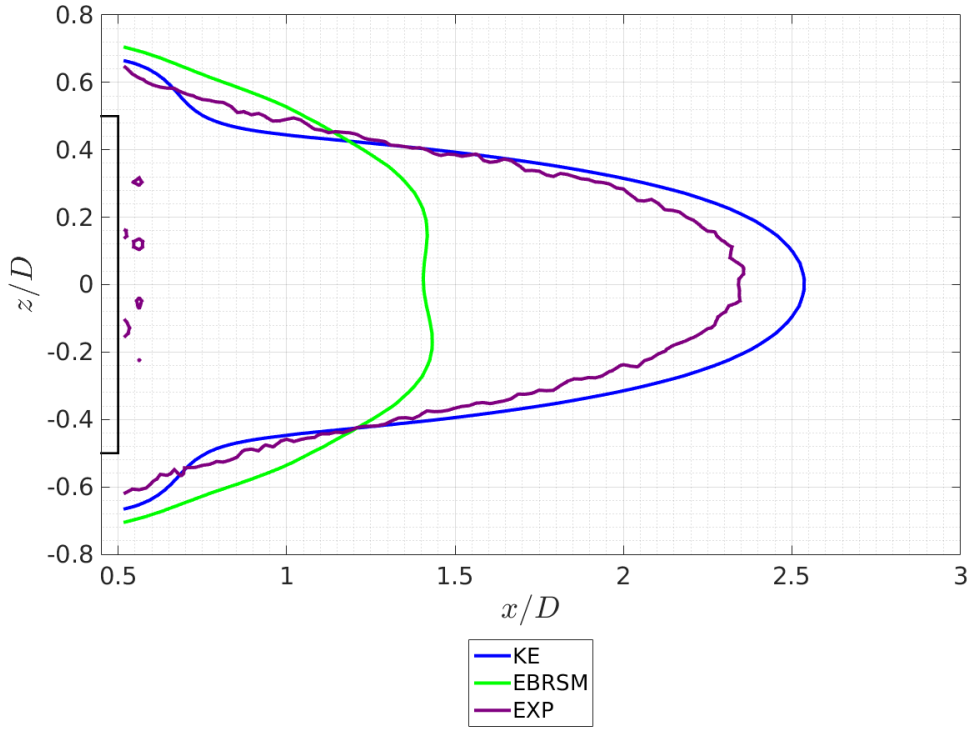

Figure 79: Contours of $U = 0$ downstream of the cube in the plane $y = 0$, $Re_D = 10400$

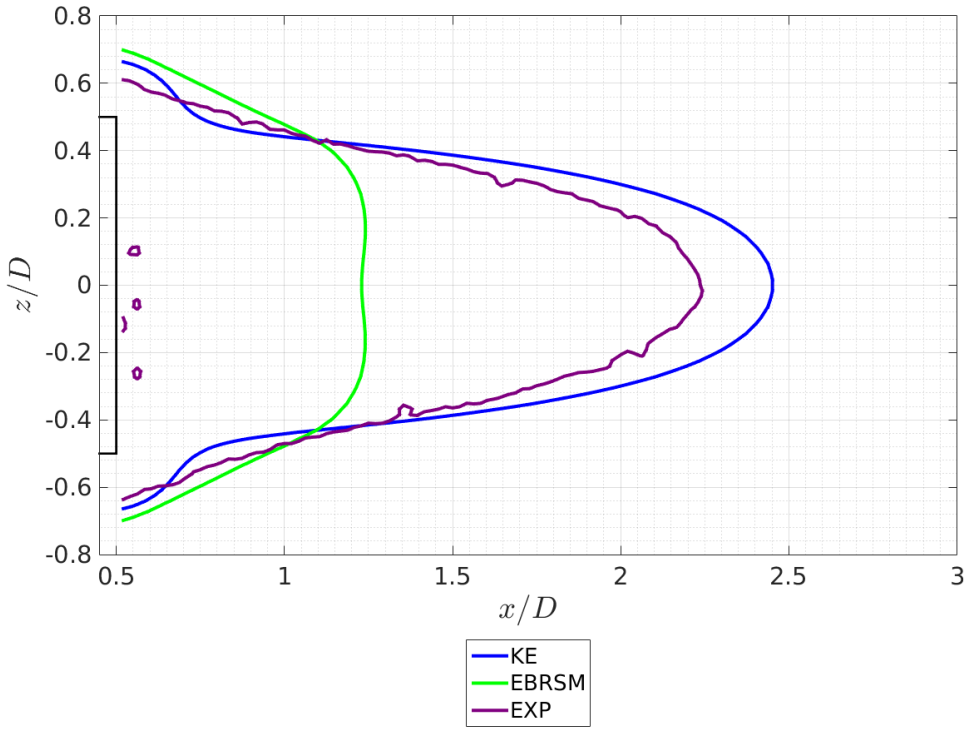

Figure 80: Contours of $U = 0$ downstream of the cube in the plane $y = 0$, $Re_D = 15600$

7.4 Recirculation Region

Downstream of the cube, contours of zero streamwise velocity in the plane $y = 0$ are overlaid in (Figures 78, 79, 80). The length of the recirculation regions is summarised by the "recirculation length" L_r in (Table 17). Across all Reynolds numbers, the $k-\varepsilon$ model L_r predictions match better with the experiments and DNS than those of the $EBRSM$. They are a much better match with the experiments at $Re_D = 10400$ and $Re_D = 15600$, where the $EBRSM$ under-predicts the recirculation length by a large amount, it is only about 45% of the experimental one. The contours of $U = 0$ from the $k-\varepsilon$ quickly tuck in behind the cube between $x = 0.5$ and $x = 0.75$ at all three Reynolds numbers, but do not do so for the $EBRSM$ model. At $Re_D = 5600$, the DNS results show a fairly good match with the experiments, the basic shape and size of the contour is similar although the match is not perfect. This may be as a consequence of an insufficient degree of statistical convergence, if not enough shedding cycles were captured.

It is perhaps surprising that the $k-\varepsilon$ model shows more accurate predictions for L_r than the $EBRSM$. The flow is highly 3D and there are strong shear forces acting within more than one plane, so the ability of the $EBRSM$ model to transport the Reynolds Stresses in three dimensions might be expected to result in superior predictions, but this

Re_D	5600	10400	15600
$L_{rk-\varepsilon}$	2.76 ± 0.01	2.54 ± 0.01	2.45 ± 0.01
L_{rEBRSM}	2.40 ± 0.01	1.41 ± 0.01	1.24 ± 0.01
L_{rexp}	2.55 ± 0.02	2.35 ± 0.02	2.24 ± 0.02
L_{rDNS}	2.47 ± 0.01	–	–

Table 17: Recirculation length normalised by D, behind cube in plane $y = 0$

is not the case. [64] compared predictions from a two-layer $k-\varepsilon$ and from Reynolds Stress models, plotting the mean streamwise velocity behind a rectangular cylinder alongside experimental results. The same basic pattern of differences in recirculation length was found; the Reynolds Stress models showed a return to high positive velocities much closer to the cylinder than the $k - \varepsilon$ did. It is possible that this was due to differences in the overall strength of the organised cross-stream fluctuations; a lower degree of momentum transfer from the faster-moving fluid far away from the centreline would result in a longer recirculation zone. The instantaneous velocity in the plane $y = 0$ (Figure 77) shows this difference in strength quite clearly; the snapshots were taken at identical parts of the shedding cycle. The plots for fluctuating velocity in (Section 6) showed a clear pattern of higher amplitude for the $EBRSM$ predictions than the $k - \varepsilon$, and the difference in amplitude increases with Reynolds number, which is consistent with this hypothesis.

Following from the discussion on the overall length of the recirculation bubble, the mean streamwise velocity is compared along the line $(x, y = 0, z = 0)$ throughout the recirculation region in (Figures 81a, 82a, 82b). At $Re_D = 5600$, the results from the DNS do not match as closely as might be expected with the experiments, possibly due to a low degree of statistical convergence. There are two clear spikes at $x \sim 1.2$ and $x \sim 1.45$ which are in the same location at all three flowrates, despite the dependency of overall flow structure on Reynolds number. This suggests that they might be due to unwanted reflections from the cube and/or aberrations in the perspex duct wall. As a result, they are ignored in the analysis.

For the region immediately behind the cube the $EBRSM$ model matches better with the experiments than the $k - \varepsilon$ does, particularly at $Re_D = 10400$ and $Re_D = 15600$. However, further downstream the $k - \varepsilon$ gives a better prediction, such that the overall match is better across all x values within the recirculation region. Further downstream still, the $k - \varepsilon$ matches better with the DNS right up to the point where the $k - \varepsilon$

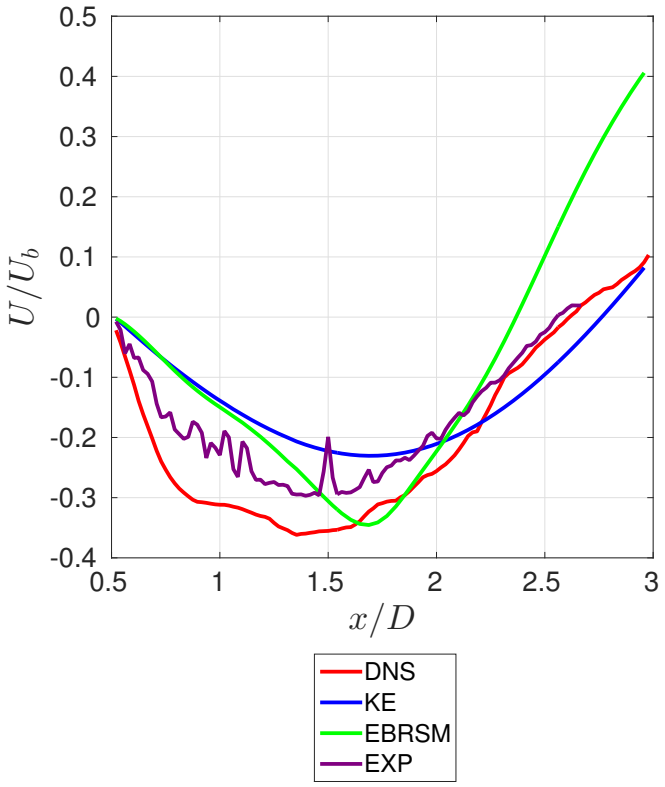

(a) Zoomed in, from $x = 0.5D$ to $x = 3D$

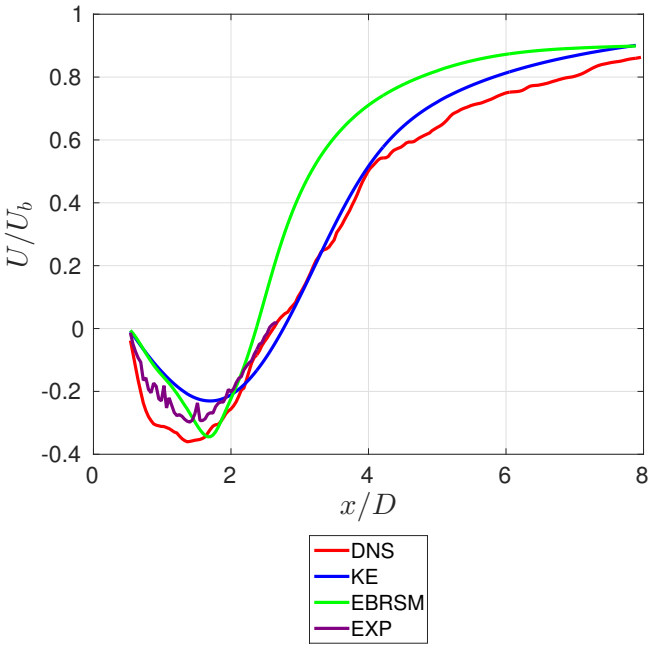

(b) Zoomed out, from $x = 0.5D$ to $x = 8D$

Figure 81: U along line $(x, y = 0, z = 0)$ downstream of the cube, $Re_D = 5600$

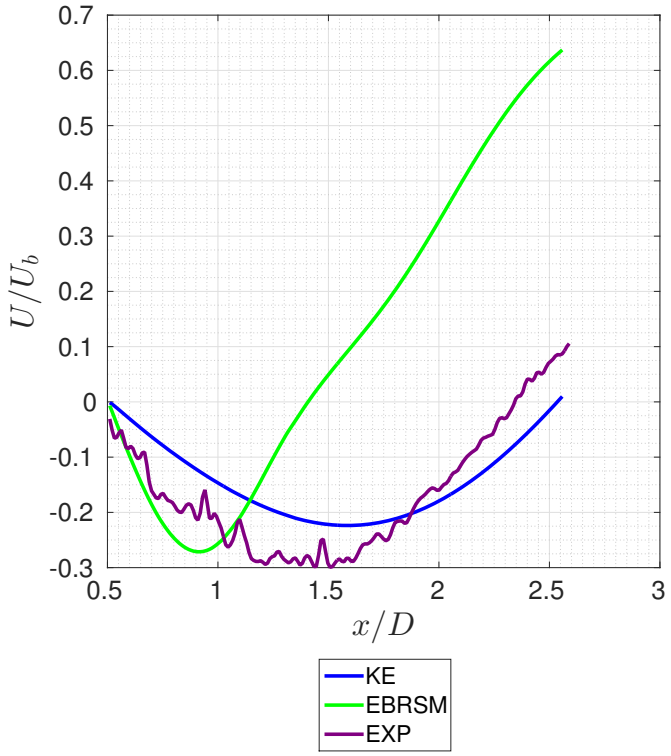

(a) $Re_D = 10400$

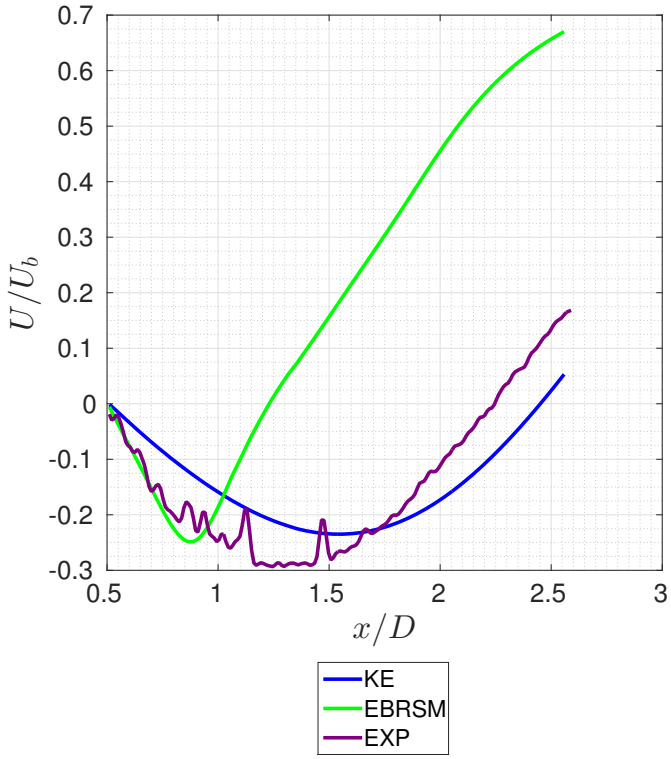

(b) $Re_D = 15600$

Figure 82: U along line $(x, y = 0, z = 0)$ downstream of the cube, from $x = 0.5D$ to $x = 2.6D$

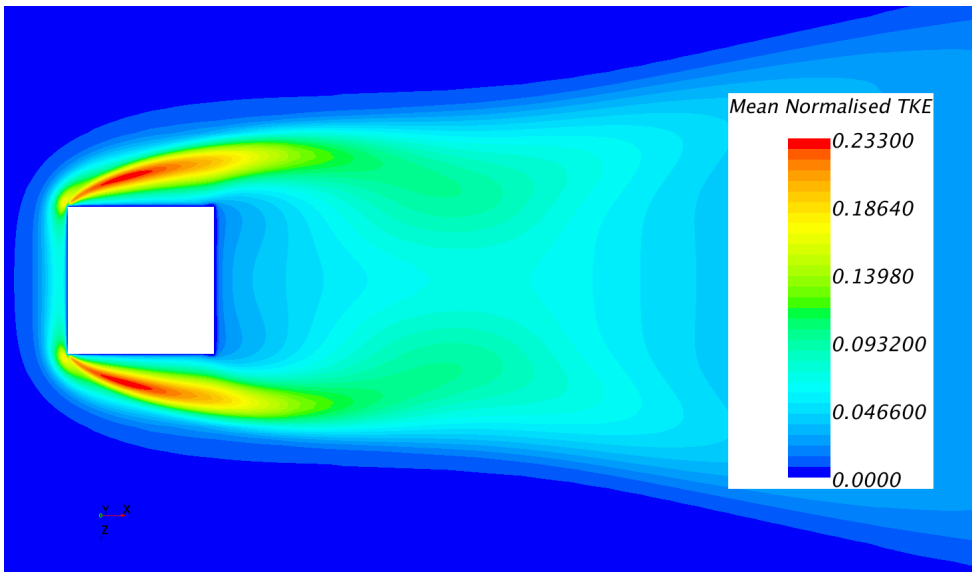

(a) KE

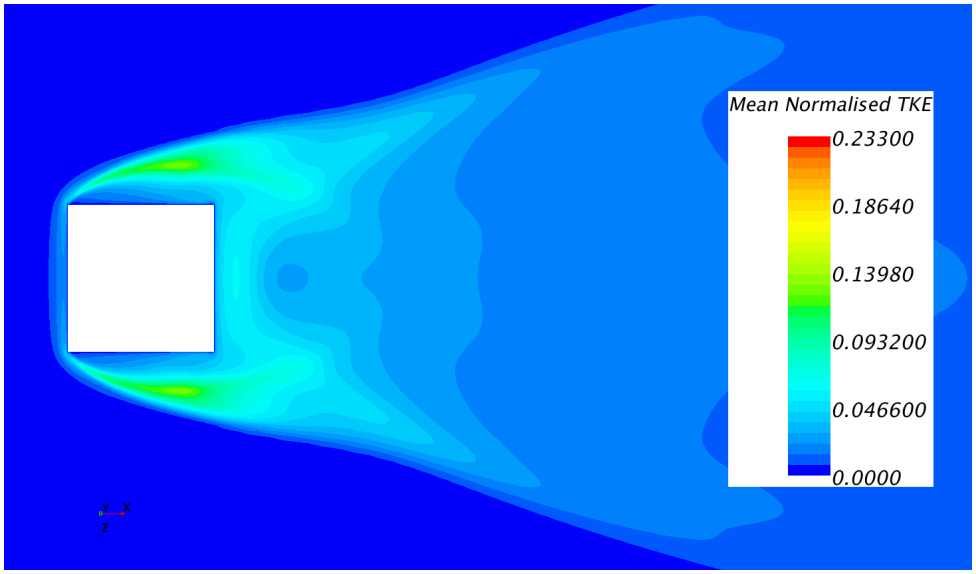

(b) $EBRSM$

Figure 83: Mean turbulent kinetic energy in the near-cube and wake region, $Re_D = 15600$, normalised by U_b^2

and $EBRSM$ plots rejoin (Figure 81b). Following [64], one might expect the $k - \varepsilon$ to predict smoother changes in mean velocity along this centreline than the $EBRSM$, which shows a sharper trough that rapidly rises again such that the recirculation region is shorter; this is the case with a long cylinder at high Reynolds numbers. It could also be expected to predict a longer overall recirculation length, as discussed above. Also in [64], the predictions did not clearly show which was better, the $k - \varepsilon$ or the Reynolds Stress models, when compared along the equivalent profile. However, in the present comparison the $k - \varepsilon$ predictions clearly are.

Differences in the mean turbulent kinetic energy in the central plane (Figure 83)

could go some way to explaining this. They are much higher for the $k-\varepsilon$ model than they are for the $EBRSM$, the ratio in the peak values between the two models being ~ 1.3. The well-known "stagnation point anomaly" alluded to previously (Section 6) is part of the reason for this discrepancy and as a result, it may be expected that the predictions in organised fluctuating kinetic energy tend to be lower for the $k-\varepsilon$. This train of thought was developed by referring to [23], in which flow around a rectangular cylinder was simulated using three different variants of the $k-\varepsilon$ model, and compared to data from [15]. In [23], the fluctuating kinetic energy was separated into two parts; the organised, periodic velocity fluctuations and the modelled turbulent fluctuations, which are parcelled together in k. The fluctuating velocity was directly recorded as was the modelled turbulent kinetic energy k. Time-means were taken of both and a time-mean total fluctuating kinetic energy $\overline{E}$ was reconstructed which characterised the totality of the fluctuations around the time-mean. This was used to make comparisons between the model variants considered in the study. Firstly, modifications were made to the Standard-$k-\varepsilon$ model in order to allow for anisotropy in the Reynolds Stress tensor. As a result, the predictions for $\overline{E}$ were found to be a better match with experiments, as were results for the time-mean velocity. As a knock-on effect, the recirculation length prediction was more accurate. Secondly, production of the modelled turbulent kinetic energy k was suppressed at the stagnation point upstream of the cylinder, leading to a lower k further downstream in the recirculation region. As a result of this modification, total fluctuating kinetic energy $\overline{E}$ predictions were better still, entailing a further improvement in mean velocity predictions. However, this is not the whole story, as ultimately it is the viscosity that damps out the fluctuations, which is also dependant on the turbulent dissipation rate ε. As described above (Section 5), the turbulent viscosity is calculated as a function of k and ε in both the $k-\varepsilon$ and the $EBRSM$ model, with a slightly different formulation. As illustrated in Figure 84, the turbulent viscosity resultant from these two formulations is very different. In these images, the ratio between the turbulent viscosity and the molecular viscosity, μ_t/μ is presented. From this, two relevant conclusions may be drawn; the $k-\varepsilon$ predicts a higher turbulent viscosity and the turbulent viscosity is large compared to the molecular one. Peak values of the turbulent viscosity ratio as predicted by the $k-\varepsilon$ are very roughly twice as large as those of the $EBRSM$. It is this high turbulent viscosity which is responsible for damping out the velocity fluctuations more in the $k-\varepsilon$ case, and

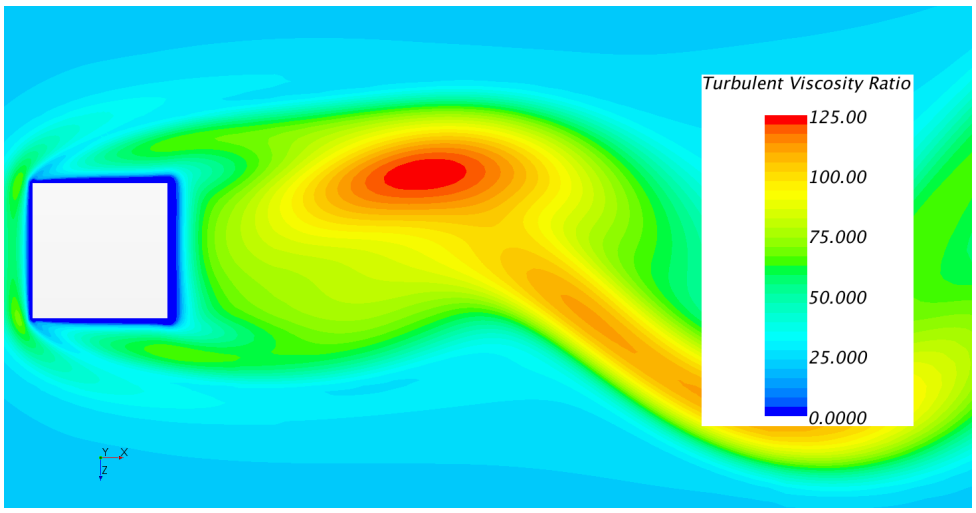

(a) KE

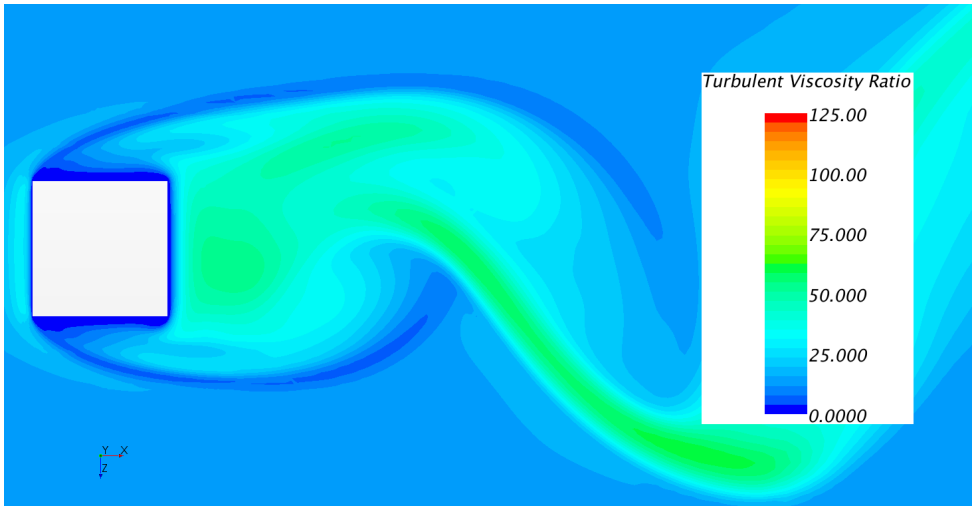

(b) $EBRSM$

Figure 84: Turbulent Viscosity Ratio μ_t/μ

which ultimately brings the $k-\varepsilon$ mean velocity predictions closer to the experimental results than those of the $EBRSM$.

8 Conclusions

8.1 Summary of Work Carried Out

This project has provided a detailed study of single-phase flow within a thin, wide rectangular channel, in the vicinity of a cubic blockage which spanned the smaller of the two dimensions. To the knowledge of the present author this geometry has not been studied within the scientific literature. Such a case is of interest in the context of using CFD for partially blocked ducts, for example when reinforcement struts might be used.

Several similar configurations had been studied where similar physics are manifest, for example the strong separation and unsteady vortex shedding around long, square cylinders and the highly 3D, unsteady flow around a wall-attached cube. The first of these is characterised by a large degree of unsteadiness, in which 3D effects are present but less dominant. The second is characterised by large changes in three dimensions, with unsteady physics that are significant but are less dominant.

In the scientific literature, various modelling strategies have been employed to deal with the challenges presented by such configurations, to varying degrees of success. A rationale has been followed that success in these related cases is likely to lead to success in the current case. Conversely, failure to represent accurately the physics in those relevant cases was considered good reason to ignore a given model, as similar physical conditions were likely to be encountered. In addition to this, various models were scrutinised for their ability to predict flow within an unblocked channel. Testing the various models within an unblocked channel highlighted an issue with the Menter-SST-$k-\Omega$ model; when combined with certain wall-treatments it gave pressure drop predictions that were significantly different to all other model/wall-treatment combinations, it was discarded on this basis. Various URANS models were tested for their ability to predict secondary corner flows, but these were found to have little effect on the solution throughout most of the channel, their effects remaining confined to the corner regions. As a result, the considered list of models was greatly narrowed down.

Following on from this, variants of two of the most popular modelling approaches have been considered in more detail; the two-layer $k-\varepsilon$ model [64] and the elliptic-blending Reynolds Stress model, or $EBRSM$ [38]. These models were applied using a

leading commercial CFD code, Star-CCM+, with care taken to understand the details of the modelling process that was used. The effects of boundary conditions, mesh spacing, timesteps and the number of inner iterations were all controlled to ensure that the final results were a fair representation of the capabilities of models. Hence, useful comparisons could be drawn with experiments and DNS.

The experimental setup used was designed from scratch, in the light of similar designs in scientific literature. Fluctuating pressure was recorded at the cube side, in order to provide time-resolved data that could be used to characterise the unsteady physics. Laser PIV data was captured in a two-dimensional plane directly behind the cube encompassing the mean recirculation region, where organised unsteadiness in the velocity was at its highest. This provided detail of the instantaneous spatial structure and allowed mean velocities to be constructed. Experiments were run at three separate Reynolds numbers, $Re_D = 5600$, $Re_D = 10400$ and $Re_D = 15600$. In addition to this, a DNS simulation was run with the open-source code Incompact3d at the lowest Reynolds number, $Re_D = 5,600$. This enabled the capture of data in the cube vicinity, although run-time was insufficient at the time of writing to make many firm conclusions based on mean statistics.

8.2 Findings

To begin with, it was not known how strong organised periodic shedding would be in the current setup. Although it was considered quite likely that some shedding would occur, the degree to which it would be suppressed by shear due to the channel walls at $y/D = \pm 0.5$ was not entirely clear. Firstly, URANS simulations predicted that strong periodic shedding would be present. This was confirmed to be the case early on in the experimental process; a periodic component was present in the pressure fluctuations. Further to this, dye flow visualisation demonstrated clearly that vortex shedding was occurring, in a fashion which resembled the classical Von-Karmann vortex shedding. This shedding was roughly periodic, and occurred at about the same frequency as the observed pressure fluctuations, establishing their presence beyond doubt. What is more, this shedding occurred at a rate that was similar to that found in literature for flow around long square cylinders; comparisons were based on the Strouhal number and this matched reasonably well at all three flow rates. However, there was a large amount of pressure fluctuation at

frequencies other than the shedding frequency which complicated the picture.

The difference between the URANS pressure predictions and the experimental ones was large, giving reason to question the accuracy of the pressure measurements. A lengthy data treatment process was followed to isolate the effects of periodic shedding from the other fluctuations in the pressure data. This process necessarily involved some arbitrary choices, for example the filtering parameters employed. However, the appearance of organised shedding in the dye-flow visualisation, and the fact that it occurred at a frequency close to that seen in the pressure measurements gave credence to choices made during the data-treatment process. Possible explanations for the additional fluctuations that were measured included uncontrolled pressure fluctuations in the circuit and blockage of pressure transmission to the transducer; neither of these could be ruled out and both may have contributed to the discrepancies.

The pressure signal was used as a reference for phase, defining the large-scale shedding motion; imprecision in the definition of phase may therefore have contributed to a failure to produce plausible phase-averaged velocity results. Phase-blurring may only be reduced by separating the data into a high number of phase-bins, and convergence of an ensemble average for each individual phase requires a high number of samples; these two constraints are at odds with each other. A far greater number of PIV snapshots would have perhaps allowed reasonable accurate phase-averaged velocity results to be generated despite the difficulties experienced with the pressure phase-reference. It was not possible to determine whether the difficulty in generating phase-averaged velocity results was mostly due to difficulties experienced with the pressure recording or to the limited number of snapshots. A higher number of snapshots may at least have made this clear.

It was possible to confirm using the DNS data that a periodic flapping motion was present. Precise control of the inlet and outlet boundary conditions did not eliminate this behaviour, it remained clearly visible by simple inspection of successive instantaneous velocity snapshots. This confirmed that the phenomenon was not merely an artefact of some other effect in the experimental setup. DNS data was insufficient to improve the phase-averaging analysis over that of the experiments; the number of shedding cycles that were simulated made phase-averaging impossible. Mean values were not fully converged, so comparisons made were necessarily imprecise. However, the DNS simulation was still useful as a tool by which quantitative information could be extracted in regions where

the flow was largely steady. In these regions, enough data was generated to draw some conclusions regarding the relative performance of the URANS models.

One of the key aspects of the turbulence modelling that was called into question during this study was the applicability to flows with strong, organised, unsteady behaviour. All the validation cases presented during the development of the models in question were based on flows that were largely steady, for which the RANS modelling framework was appropriate. The coefficients used in these models have been tuned towards accurate representation of mean flow structure in steady cases. Validation of them involved testing the ability of the boundary layer predictions to adapt to local turbulence conditions, the ability of the models to reproduce corner vortices that are purely turbulent in origin, and the ability of the models to predict recirculating flows with sharp geometry changes. These situations did not require the simulations to adjust to large scale, time-dependent changes. Although this seems like a natural approach within the RANS modelling framework that has been used, it does not allow for the large variety of flows within which strong, organised fluctuations are present in addition to small-scale turbulence and a steady mean. Therefore, perhaps different tuning of the models could improve their predictions of such flows without changing their basic formulation. If this were the case, such flows could be simulated effectively without turning to higher cost approaches such as LES. The most notable failures found in the literature were in the case of shedding around a long cylinder; mean velocities in the recirculation region were not very well matched by any URANS model for which results were presented. It is likely that this inability to deal with highly unsteady flow was also the cause of much of the disagreement between the URANS models and reference data in the current study.

In addition to this, some of the details of the model implementation in Star-CCM+ are not made clear in the user manual, nor is the justification for some choices. For example, many of the original papers cited regarding the origins of the models applied them in two-dimensional flow. In the case of the $EBRSM$ model, certain changes made were designed to increase numerical robustness and to speed up convergence, and possible effects on accuracy were not discussed in detail.

Nonetheless, the time-averaged velocity results from the experiments, DNS and URANS were in reasonable agreement at $Re_D = 5600$. For example, the DNS and experiments predicted a recirculation length that was within agreement to within 4%; this small dis-

crepancy could be explained by a combination of experimental error and insufficient DNS data. The $EBRSM$ predicted a recirculation length of $\sim 10\%$ less than this and the $k-\varepsilon$ prediction was $\sim 6\%$ higher. Mean velocity DNS results upstream and to the side of the cube did not prove that either of the two URANS models was better; they showed better agreement in different places. Overall, across all three Re_D, the main spatial features of the flow were arguably better represented by the $EBRSM$ model, and the size of the recirculation zone was better predicted by the $k-\varepsilon$ model. As a result, it can not be concluded that either of the two models was superior.

8.3 Suggestions for Further Work

This study has illustrated a limitation in the applicability of URANS models to a particular set of unsteady flows. Performance in an intuitively similar case, flow around a wall-attached cube, does not seem to have been a good predictor of performance in the current case. The issues discussed in the literature when applying the models to flows around a long cylinder seem to be present, and to have been consequential in the current study. The validation of Unsteady RANS models for flows where organised, large scale fluctuations make up a significant part of the flow physics is clearly an area where more work is required, particularly for the $EBRSM$ model used.

Perhaps the most useful extension that could be made to the current study would be the collection of more DNS data, which was made impossible by time and resource constraints. This could have been carried out in a smaller domain, if equivalence with the very wide, thin channel of the experiments was considered unimportant. The collection of statistically converged means, and also higher order statistics could provide a very useful point of reference for the validation of the URANS models. In addition to this, with a sufficient number of shedding cycles, phase-averaged results could be produced. Finally, additional DNS data at a higher Reynolds number would also be very useful for model validation, although this would require much more computational resources.

Improvements to the experimental study could be made with the collection of pressure data in different locations. Perhaps a better reference point could have been found where the signal was more clean. Alternatively, multiple taps could provide a better means to define the shedding period by characterising the pressure change across more of the cube

surface, shedding of the boundary layer as a whole may have been more clearly defined in this manner. In addition to this, information could be gleaned from such an experiment regarding pressure distributions across the cube surface, and the correlation between the individual signals.

Further to this, the PIV experiments would be greatly improved by collecting more snapshots from which to form phase-averaged velocity fields. Perhaps a higher number of snapshots would be sufficient to form the phase-averages without improvements to the pressure measurement. Certainly, in tandem with an improved means of defining phase, this would yield useful information for validation of the URANS models; their ability to predict the large scale unsteady components of the physics could be scrutinised. Alternatively, with a suitably high frame-rate, phase-angles could be inferred directly from the PIV velocity data. However, this would necessitate the storage and processing of a great deal of data, so it may not be the most practical route.

Finally, with better reference data and a clearer knowledge of the modelling details, it would be useful to compare a broader range of models. For example, there are many variants within the $k-\varepsilon$ and RSM families which could be tested to see if any among them are better suited to the current case without modification. It is not known why the $k-\Omega$ models tested gave pressure drop predictions that were inconsistent when combined with certain wall-treatments. This issue could have also been investigated, and it would be useful to know if there were any implementation problems which could be addressed. The uncertainty regarding implementation of the turbulence models would be best reduced by using code that could be easily accessed and modified, so that the fine details of the modelling could be more explicitly known. For this purpose, an open source code such as OpenFOAM would be ideal. This would also provide the possibility of making modifications beyond changing coefficients, to better tailor the models towards unsteady flow prediction.

9 References

References

[1] IAPWS Industrial Formulation 1997 for the Thermodynamic Properties of Water and Steam. Technical report, International Association for the Properties of Water and Steam, 1997.

[2] H An, L Cheng, M Zhao, and F Tong. Numerical simulations of flow around a circular cylinder at high Reynolds number. In *Proceedings of the Twelfth (2016) Pacific-Asia Offshore Mechanics Symposium*. International Society of Offshore and Polar Engineers, 2016.

[3] J H Bell and R D Mehta. Design and calibration of the mixing layer wind tunnel. Technical Report JIAA TR-89, Stanford University, 2013.

[4] F Billard and D Laurence. A robust K-E $\overline{v^2}$/K elliptic blending turbulence model applied to near-wall, separated and buoyant flows. *International Journal of Heat and Fluid Flow*, 33:45–58, 2012.

[5] M Braza, R Perrin, and Y Hoarau. Turbulence properties in the cylinder wake at high Reynolds numbers. *Journal of Fluids and Structures*, 22:757–771, 2006.

[6] M L Brown, M Parsheh, and C K Aidun. Turbulent flow in a converging channel: effect of contraction and return to isotropy. *Journal of Fluid Mechanics*, 560:437–448, 2006.

[7] E Brundett and W D Baines. The production and diffusion of vorticity in duct flow. *Journal of Fluid Mechanics*, 19(3):375–394, 1964.

[8] L Bruno, D Fansos, N Coste, and A Bosco. 3D flow around a rectangular cylinder: A computational study. *Journal of Wind Engineering and Industrial Aerodynamics*, 98:263–276, 2010.

[9] B Cantwell and D Coles. An experimental study of entrainment and transport in the turbulent near wake of a circular cylinder. *Journal of Fluid Mechanics*, 136:321–374, 1983.

[10] CD-ADAPCO. *STAR-CCM+ user guide, v10.02*, 2017.

[11] F H Champagne, V G Harris, and S Corrsin. Experiments on nearly homogeneous turbulent shear flow. *Journal of Fluid Mechanics*, 41(1):81–139, 1970.

[12] P-Y Chou and R-L Chou. 50 years of turbulence research in China. *Annual Review of Fluid Mechanics*, 27:1–15, 1995.

[13] F Dehoux, Y Lecocq, S Benhamadouche, R Manceau, and L Brizzi. Algebraic modeling of the turbulent heat fluxes using the elliptic blendingapproach - application to forced and mixed convection regimes. *Flow Turbulence and Combustion*, 88:77–100, 2012.

[14] Z Duan, M M Yovanovich, and Y S Muzychka. Pressure drop for fully developed turbulent flow in circular and noncircular ducts. *Journal of Fluids Engineering*, 134, 2012.

[15] D F G Durao, M V Heitor, and J C F Pereira. Measurements of turbulent and periodic flows around a square cross-section cylinder. *Experiments in Fluids*, 6:298–304, 1988.

[16] P A Durbin. A Reynolds stress model for near-wall turbulence. *Journal of Fluid Mechanics*, 249:465–498, 1993.

[17] P A Durbin. On the K-E stagnation point anomaly. *International Journal of Heat and Fluid Flow*, 17:89–90, 1996.

[18] R Franke. *Numerische Berechnung der instationaren Wirbelablosung hinter zylindrischen Korpern*. Phd thesis, University of Karlsruhe, 1991.

[19] R Gautier, S Laizet, and E Lamballais. A DNS study of jet control with microjets using an immersed boundary method. *International Journal of Computational Fluid Dynamics*, 28(6-10):393–410, 2014.

[20] F B Gessner. The origin of secondary flow in turbulent flow along a corner. *Journal of Fluid Mechanics*, 58(1):1–25, 1973.

[21] J C Gillis, J P Johnston, W M Kays, and R Moffat. Turbulent boundary layer on a convex curved surface. Technical Report HMT-31, Department of Mechanical Engineering, Stanford University, 1980.

[22] S E Haaland. Simple and explicit formulas for the friction factor in turbulent pipe flow. *Journal of Fluids Engineering*, 105:89–90, 1983.

[23] A Hadid, M M Sindir, and R Issa. A numerical study of 2D vortex shedding from rectangular cylinders. *Computational Fluid Dynamics Journal*, 1(2):207–214, 1992.

[24] K Hanjalic and B E Launder. A Reynolds stress model of turbulence and its application to thin shear flows. *Journal of Fluid Mechanics*, 52(4):609–638, 1972.

[25] D P Hart. Super-resolution PIV by recursive local-correlation. *Journal of Visualization*, 3:187–194, 2000.

[26] H J Hussein and R Martinuzzi. Energy balance for turbulent flow around a surface mounted cube placed in a channel. *Physics of Fluids*, 8:764–780, 1996.

[27] G Iaccarino, A Ooi, P A Durbin, and M Behnia. Reynolds averaged simulation of unsteady separated flow. *International Journal of Heat and Fluid Flow*, 24:147–156, 2003.

[28] M K Ibragimov, V S Petrishchev, and G I Sabelev. Calculation of secondary flow in a turbulent fluid stream. *Mekhanika Zhidkosti I Gaza*, 4(4):166–170, 1969.

[29] G V Iungo, L M Pii, and G Buresti. Experimental investigation on the aerodynamic loads and wake flow features of a low aspect-ratio circular cylinder. *Journal of Fluids and Structures*, 28:279–291, 2012.

[30] W P Jones and B E Launder. The prediction of laminarization with a two-equation model of turbulence. *International Journal of Heat and Mass Transfer*, 15:301–314, 1972.

[31] T Jongen. *Simulation and Modelling of Turbulent Incompressible Fluid Flows*. Phd thesis, Ecole Polytechnique Federale de Lausanne, 1998.

[32] V Kalro and T Tezduyar. Parallel 3D computation of unsteady flows around circular cylinders. *Parallel Computing*, 23:1235–1248, 1997.

[33] G E Karniadakis and G STriantafyllou. Three-dimensional dynamics and transition to turbulence in the wake of bluff objects. *Journal of Fluid Mechanics*, 238:1–30, 1992.

[34] J Kim, P Moin, and R Moser. Turbulence statistics in fully developed channel flow at low Reynolds number. *Journal of Fluid Mechanics*, 177:133–166, 1997.

[35] S Laizet. Incompact3d user guide version 2.0. `http://www.incompact3d.com/uploads/5/8/7/2/58724623/__user_guide_incompact3d_v2.pdf`, 2015.

[36] S Laizet and E Lamballais. High-order compact schemes for incompressible flows: A simple and efficient method with quasi-spectral accuracy. *Journal of Computational Physics*, 228:5989–6015, 2009.

[37] S Laizet and Li Ning. Incompact3d: A powerful tool to tackle turbulence problems with up to $O(10^5)$ computational cores. *International Journal for Numerical Methods in Fluids*, 67:1735–1757, 2011.

[38] S Lardeau and R Manceau. Computations of complex flow configurations using a modified Reynolds-stress model. ETMM 10, 10th International ERCOFTAC Symposium on Engineering Turbulence Modeling and Measurements, September 2014.

[39] A Larousse, R Martinuzzi, and C Tropea. Flow around surface-mounted, three-dimensional obstacles. In *Eighth Symposium on Turbulent Shear Flows*. Technical University of Munich, 1991.

[40] B E Launder, G J Reece, and W Rodi. Progress in the development of a Reynolds-stress turbulence closure. *Journal of Fluid Mechanics*, 68(3):537–566, 1975.

[41] B E Launder and D B Spalding. The numerical computation of turbulent flows. *Computer Methods in Applied Mechanics and Engineering*, 3:269–289, 1974.

[42] Y Lecocq. *Contribution a l'analyse et a la modelisation des ecoulements turbulents en regime de convection mixte : application a l'entreposage des dechets radioactifs.* Phd thesis, Universite de Poitiers, 2009.

[43] M J Lee and Reynolds W C. Numerical experiments on the structure of homogeneous turbulence. Technical Report TF-24, Stanford University, 1985.

[44] F S Lien, W L Chen, and M A Leschziner. Low-Reynolds number eddy-viscosity modelling based on non-linear stress-strain/vorticity relations. Proceedings of the 3rd Symposium on Engineering Turbulence Modelling and Measurements, May 1996.

[45] D A Lyn and W Rodi. The flapping shear layer formed by flow separation from the forward corner of a square cylinder. *Journal of Fluid Mechanics*, 267:353–376, 1994.

[46] R Manceau. Elliptic blending model: a new near-wall Reynolds-stress turbulence closure. Proceedings of the 4th International Symposium on Turbulence and Shear Flow Phenomena, January 2005.

[47] R Manceau and K Hanjalic. Elliptic blending model: A new near-wall Reynolds-stress turbulence closure. *Physics of Fluids*, 14:744–754, 2002.

[48] C Mannini, A Soda, and G Schewe. Unsteady RANS modelling of flow past a rectangular cylinder: Investigation of Reynolds number effects. *Computers and Fluids*, 39:1609–1624, 2010.

[49] R Martinuzzi and C Tropea. The flow around surface-mounted, prismatic obstacles placed in a fully developed channel flow. *Journal of Fluids Engineering*, 115:85–92, 1993.

[50] A Melling and J H Whitelaw. Turbulent flow in a rectangular duct. *Journal of Fluid Mechanics*, 78:289–315, 1976.

[51] F R Menter. Two-equation eddy-viscosity turbulence models for engineering applications. *AIAA JOURNAL*, 32(8):1598–1605, 1994.

[52] R D Moser, J Kim, and N N Mansour. Direct numerical simulation of turbulent channel flow up to Re_τ 590. *Physics of Fluids*, 2(4):943–945, 1999.

[53] C Norberg. An experimental investigation of the flow around a circular cylinder : influence of aspect ratio. *Journal of Fluid Mechanics*, 258:287–316, 1994.

[54] A Okajima. Strouhal numbers of rectangular cylinders. *Journal of Fluid Mechanics*, 123:379–398, 1982.

[55] A V Oppenheim and R W Schafer. *Discrete-Time Signal Processing*. Pearson, 3rd edition, 2010.

[56] S V Patankar and D B Spalding. *Heat and Mass Transfer in Boundary Layers*. Morgan-Grampian Press, 1967.

[57] S V Patankar and D B Spalding. A calculation momentum procedure for heat, mass and momentum transfer in three-dimensional parabolic flows. *International Journal of Heat and Mass Transfer*, 15:1787–1806, 1972.

[58] H J Perkins. The formation of streamwise vorticity in turbulent flow. *Journal of Fluid Mechanics*, 44(4):721–740, 1970.

[59] A Pinelli, M Uhlmann, A Sekimoto, and G Kawahara. Reynolds number dependence of mean flow structure in square duct turbulence. *Journal of Fluid Mechanics*, 644:107–122, 2010.

[60] Pipeflow.com. K factor databases. `https://www.pipeflow.com/pipe-pressure-drop-calculations/pipe-fitting-loss-calculation`, 2013.

[61] S B Pope. A more general effective-viscosity hypothesis. *Journal of Fluid Mechanics*, 72(2):331–340, 1975.

[62] M Raffel, C E Willert, S Wereley, and J Kompenhans. *Particle Image Velocimetry - A Practical Guide*. Springer, 2nd edition, 1998.

[63] C M Rie and W L Chow. Numerical study of the turbulent flow past an airfoil with trailing edge separation. *AIAA JOURNAL*, 21(11):1525–1532, 1983.

[64] W Rodi. Experience with two-layer models combining the K-E model with a one-equation model near the wall. 29th Aerospace Sciences Meeting, American Institute of Aeronautics and Astronautics, January 1991.

[65] W Rodi. Comparison of LES and RANS calculations of the flow around bluff bodies. *Journal of Wind Engineering and Industrial Aerodynamics*, 69-71:55–75, 1997.

[66] W Rodi, J H Ferziger, M Breuer, and M Pourquie. Status of Large Eddy Simulation: Results of a workshop. *Journal of Fluids Engineering*, 119:248–262, 1997.

[67] M Roth. *Automatic Extraction of Vortex Core Lines and Other Line-Type Features for Scientific Visualization*. Phd thesis, ETH Zrich, 2000.

[68] A Salama, M F El-Amin, and S Sun. Three-dimensional, numerical investigation of flow and heat transfer in rectangular channels subject to partial blockage. *Heat Transfer Engineering*, 36:152–165, 2015.

[69] A Salama and S E D El-Morshedy. CFD simulation of the IAEA 10 MW generic MTR reactor under loss of flow transient. *Annals of Nuclear Energy*, 38:564–577, 2011.

[70] G B Schubauer and W B Spangenberg. Forced mixing in boundary layers. *Journal of Fluid Mechanics*, 8(1):10–32, 1960.

[71] International Atomic Energy Agency Physics Section. Research reactor core conversion from the use of highly enriched uranium to the use of low enriched Uranium fuels guidebook. Technical Report 233, International Atomic Energy Agency, 1980.

[72] A Sergis. *Experimental and numerical heat transfer studies of nanofluids with an emphasis on nuclear fusion applications*. Phd thesis, Imperial College London, 2013.

[73] K B Shah and J H Ferziger. A fluid mechanicians view of wind engineering : Large eddy simulation of flow past a cubic obstacle. *Journal of Wind Engineering and Industrial Aerodynamics*, 67 & 68:211–224, 1997.

[74] T H Shih, W W Liou, A Shabbir, Z Yang, and J Zhu. A new $k - \varepsilon$ eddy viscosity model for high Reynolds number turbulent flows. *Computers Fluids*, 24:227–238, 1995.

[75] C Speziale. Analytical methods for the development of Reynolds stress closures in turbulence. Technical Report 182017, 90-26, Institute for Computer Applications in Science and Engineering, NASA, 1990.

[76] C G Speziale. On nonlinear K-l and K-E models of turbulence. *Journal of Fluid Mechanics*, 178:459–475, 1987.

[77] C G Speziale, S Sarkar, and T B Gatski. Modelling the pressure-strain correlation of turbulence : an invariant dynamical systems approach. *Journal of Fluid Mechanics*, 227:245–272, 1991.

[78] S Szepessy and P W Bearman. Aspect ratio and end plate effects on vortex shedding from a circular cylinder. *Journal of Fluid Mechanics*, 234:191–217, 1992.

[79] F X Trias, A Gorobets, and A Oliva. Turbulent flow around a square cylinder at Reynolds number 22,000 : A DNS study. *Computers and Fluids*, 123:87–98, 2015.

[80] V Venkatakrishnan. On the accuracy of limiters and convergence to steady state solutions. In *31st Aerospace Sciences Meeting & Exhibit*. American Institute of Aeronautics and Astronautics, 1993.

[81] R Vinuesa, P Schlatter, J Malma, C Mavriplis, and D S Henningson. Direct numerical simulation of the flow around a wall-mounted square cylinder under various inflow conditions. *Journal of Turbulence*, 16:555–587, 2015.

[82] J H Williamson. Low-storage Runge-Kutta schemes. *Journal of Computational Physics*, 35:48–56, 1980.

[83] M Wolfshtein. The velocity and temperature distribution in one-dimensional flow with turbulence augmentation and pressure gradient. *International Journal of Heat and Mass Transfer*, 12(2):301–318, 1969.

10 Acknowledgements

Firstly, I would like to thanks Dr Raad Issa, my primary supervisor. The technical advice, wisdom and experience he offered was absolutely invaluable throughout my PhD. His support and kindness was not limited to that which should be expected, and I may simply not have managed without it.

Also, I thank Dr Simon Walker for his huge input. As well as providing technical advice, he facilitated a great many practical solutions throughout my project, acting as my primary supervisor in the early stages. In addition to this, he made it possible for me to take a break from my studies when unfortunate outside events made it difficult for me to continue.

I thank Professor Yannis Hardalupas and Professor Alex Taylor for their help regarding the experimental side of the project, providing technical and practical advice as well as access to experimental resources and suggestions on how to best analyse the experimental data.

Dr Antonis Sergis made a large contribution to the experimental study. I have no doubt that it would have been much more difficult without him, he made it possible to obtain results within a very short timeframe by helping with the equipment setup and operation, particularly the PIV. In addition to this, he suggested solutions for data analysis.

My former colleague Dr Frederic Sebilleau was of great help regarding the DNS study, providing me with a copy of the Incompact3d code in which he had already found some bugs and written routines for data visualisation. Along with the code he passed me, he had initiated a working Immersed Boundary case that represented my geometry. In addition to this, he showed me how to run jobs on the High Performance Computing cluster. Talks with him over coffee often proved to be as fruitful as those within the office.

Max Nussbaum, a visiting student from TU Berlin, took the DNS case and adjusted various parameters, allowing the solution to develop while checking progress along the way. His input was very useful, and brought the test case part way to the point where data could be generated.

The staff within the Mechanical Engineering workshop were of great assistance when adjustments needed to be made to experimental equipment, particularly regarding the use of workshop equipment. In particular, Stuart Marchant installed the experimental flow rig, and provided very useful practical advice that fed into the experimental design.

I greatly appreciate Professor Rodriguez y Baena for his pastoral support and advice during a difficult time which affected my work and necessitated that I take a break from studies.

I would like to gratefully acknowledge the financial support of Rolls-Royce.